Evolution of Flux Transfer Events at the Magnetopause:
MMS Observations and Global Hybrid-Vlasov Simulations

by

Mojtaba Akhavan-Tafti

A dissertation submitted in partial fulfillment
of the requirements for the degree of
Doctor of Philosophy
(Climate and Space Sciences and Engineering)
in the University of Michigan
2020

Doctoral Committee:

      Professor James A. Slavin, Chair
      Dr. Guan Le, NASA Goddard Space Flight Center
      Professor Minna Palmroth, University of Helsinki, Finland
      Professor Tuija Pulkkinen
      Research Professor Gábor Tóth
      Assistant Professor Louise Willingale

Mojtaba Akhavan-Tafti

akhavant@umich.edu

ORCID iD: 0000-0003-3721-2114

Dedication

This dissertation is humbly dedicated to the space science community whose commitment to uncovering the innerworkings of the universe continuously advances our technological and scientific boundaries.

Acknowledgements

It is with immense honor and pleasure that I recognize the citizenry of the United States of America and Europe whose direct contributions made this research using spacecraft observations and computational global simulations attainable.

I would also like to recognize and appreciate the contributions and the support of my doctoral advisor, Prof. James A. Slavin. Jim encouraged and supported me in tailoring my unique graduate experience. Jim empowered me to explore freely and to think critically.

I am also grateful and acknowledge the support of Prof. Minna Palmroth and the Vlasiator team at the University of Helsinki, Finland who enriched my graduate experience and propelled me to look deeper.

I am also indebted to Prof. Nilton Renno for his mentorship and scholarly role in pushing me to step beyond convention.

Lastly, I am truly grateful for my family and for my partner, Grace, whose supports and sacrifices enabled this dissertation.

Table of Contents

List of Tables

List of Figures

flux rope. The Closest Approach is indicated by Y_0 and R_0 and X_0 are the flux rope radius and the distance from the closest approach to the edge of the flux rope, respectively. X_i and R_i increase incrementally as the spacecraft travels farther toward the edge of the flux rope. j) Chi-square profile of the second Eastwood et al. (2016) event. The estimated FTE radius is comparable to that previously reported ($\sim$ 550 km).

parameter inside each individual bin, $\sigma_{mean} \equiv \sigma / \sqrt{n}$; where σ and n are the standard deviation and the number of events in each bin, respectively. Note that the primary and secondary y-axes are different in range and, in the case of plasma temperature, unit.

local extrema (except #2 & 5) are selected and labeled as '1'-'5'. c) VDF cuts at the five selected E_x values in $\mathbf{V_B}$ - $\mathbf{V_{B \times V}}$ (left column) and $\mathbf{V_{B \times V}}$ - $\mathbf{V_{B \times (B \times V)}}$ (right column) diagrams, where $\mathbf{V_B}$ represents the velocity along the magnetic field orientation. $\mathbf{V_{B \times V}}$ and $\mathbf{V_{B \times (B \times V)}}$ are along $(\mathbf{B \times V})$ and $\mathbf{B \times (B \times V)}$ directions, respectively, where $\mathbf{V}$ is the ion bulk velocity. A video illustrating the temporal evolution of ion VDFs as a function of E_x and position with respect to the X-point is included as **Video S1**.

magnetic field, b) magnetic field components in the Geocentric Solar Ecliptic (GSE) coordinates, c) ion plasma density, d) ion velocity components, e) electron velocity components, f) parallel (red solid line) and perpendicular (black solid line) current density components, g) parallel (red solid line) and perpendicular (black solid line) ion temperature components, h) plasma beta, β, defined as the ratio of plasma thermal pressure to magnetic pressure. The frozen-in condition of the ions and electrons at 00:59:13-19 UT are also represented as observed by MMS1 in the following panels: i) magnetic field total, and the components of the electric field measured directly using the EDP instrument (black solid line) and derived from the cross product of the bulk FPI electron (blue) and ion (red) velocities and the FGM magnetic field vectors (red solid line) along the j) X_{GSE}, k) Y_{GSE}, and l) Z_{GSE}.

List of Appendices

Abstract

Magnetic reconnection is the underlying physical process responsible for the release of energy stored in magnetic fields that powers plasma heating and acceleration. Flux transfer events (FTEs) are transient signatures of magnetic reconnection at the magnetopause. FTEs are twisted open flux tubes associated with the transfer of plasma from the magnetosheath into the magnetosphere and the ionosphere. FTEs play an important role in transporting mass, momentum, and magnetic flux from the solar wind into and across the magnetospheres. Determining the magnetic field structure, electric currents, and plasma distributions within FTE-type flux ropes is critical to the understanding of their origin, evolution, and dynamics. In agreement with the multiple X-line reconnection model, FTEs at the subsolar magnetopause, as observed by the Magnetospheric Multiscale (MMS) spacecraft, are found to have an exponential size distribution with an average diameter, $\lambda \sim 35\ d_i$, where $d_i = c/\omega_{pi} \sim 70$ km is the local ion inertial length at the magnetopause. The exponential size distribution of FTEs indicates that magnetic reconnection is likely the main source of their generation and evolution. The residual net forces inside FTEs are evaluated using multi-spacecraft techniques. It is found that the residual net force causes the evacuation of plasmas from the stressed region, resulting in the observed reduced plasma density near the central axes of FTEs. We further show that the average plasma pressure inside FTEs decreases at a sub-adiabatic rate with increasing FTE diameter, suggesting the presence of significant plasma heating inside FTEs. To further examine the presence of plasma energization and heating inside FTEs, the relative roles of parallel electric fields and the betatron and first-order Fermi processes in accelerating plasmas were evaluated. It is found that parallel electric fields are the dominant energization mechanism for both ions and electrons in the leading edge of FTEs, indicating that FTEs convecting along the magnetopause away from the subsolar reconnection region likely interact with the ambient environment via magnetic reconnection. It is also revealed that the observed strong net-heatings inside FTEs are proportional to $\lambda^{-1/2}$, therefore, concluded that reconnection-driven heating continues inside FTEs far from the subsolar electron and ion diffusion regions. The

hybrid-Vlasov Vlasiator simulations were then employed to study the temporal and spatial evolutions of FTEs at the magnetopause in two spatial and three velocity dimensions. Based on the simulation results and the MMS measurements, it is estimated that an MMS-observed ion-scale FTE may grow Earth-sized within ~10 minutes, which is comparable to the average transport time for FTEs formed in the subsolar region to the high-latitude magnetopause, based on previous ground-based measurements. The FTE coalescence process is further investigated using MMS observations in conjunction with the 2D global Vlasiator simulations. In particular, in an ion-scale current sheet between the merging, oppositely-directed field lines, plasmas are found to drift due to a pressure difference across the current sheet in the presence of a strong background magnetic field, causing the formation of a self-closing diamagnetic current. This diamagnetic current is perpendicular to the background magnetic field and generates magnetic field perturbations that are comparable with the reconnection Hall signatures. The Vlasiator simulations further reveal that the reconnection current sheet between the coalescing islands expands at a rate comparable to the local Alfven speed. The analyses and conclusions can further be applied to other collisionless plasma regimes, such the planetary magnetotails and the interplanetary medium.

Chapter 1: Introduction

Space physics is to a large part plasma physics. This became evident when geomagnetic phenomena were discovered to be driven by processes in the swirling ionized gases (plasmas) of the upper atmosphere, the ionosphere, and interplanetary magnetic field. These processes were later revealed to take place at time scales much shorter than those of the dynamical processes in the Earth's interior.

High-ionization matter is susceptible to electric and magnetic fields and, thus, behaves differently from other states of matter (solids, liquids, and gases). In this introduction, the basics of plasmas are introduced. This is followed by geophysical plasma concepts including the physics of the interaction between the geomagnetic and interplanetary magnetic fields. The chapter is concluded by the three main objectives of this dissertation.

1.1 Physics of Magnetized Plasmas

A plasma is a hot and highly-ionized gas. Plasmas are ubiquitous and are the dominant building block of our universe. Plasmas consist typically of equal numbers of free positive and negative charge carriers. This characteristic is defined as 'quasi-neutrality.' For a classical non-relativistic plasma to behave quasi-neutral, there must be very large numbers of particles whose macroscopic parameters such as number density, n, bulk velocity, v, and temperature, T, can be defined.

1.1.1   Single Particle Motion

The kinetic theory is concerned with defining a distribution function, $f_s(x, v, t)$ for each species (s; ions and electrons) in the plasma. The distribution function gives the probability of finding a certain number of particles in the phase-space interval [$x, v; x+dx, v+dv$]. Charged particles in a dilute collisionless and hot plasma can move independent of the Coulomb fields of other charged particles located over a distance, known as the Debye length, λ_{Ds}:

$$\lambda_{Ds} = \left(\frac{\epsilon_0 \, k_B \, T_s}{n_e \, q^2}\right)^{1/2},$$

where k_B is the Boltzmann constant, ϵ_0 is the permittivity of free space, and q is the particle charge.. Within this distance, the particle orbit in the presence of an external magnetic field, $\boldsymbol{B}$, and electric field, $\boldsymbol{E}$, is described by Lorentz force, $\boldsymbol{F}_L$:

$$\boldsymbol{F}_{Ls} = m_s \frac{dv_s}{dt} = q_s \, (\boldsymbol{E} + \boldsymbol{v}_s \times \boldsymbol{B}),$$

where m represents the particle mass. Lorentz force implies that the only parameter impacting the parallel motion of a single particle is the parallel component of electric field, $E_\parallel$. On the other hand, the transverse (perpendicular) particle motion is influenced by both the magnetic field and electric field and can be split into a number of independent velocities.

The particle motion in a uniform magnetostatic field and in the absence of an external electric field ($\boldsymbol{E} = 0$), has a component parallel to the magnetic field that is constant ($v_\parallel = constant$). The magnitude of the perpendicular component of velocity (speed) is also constant ($v_\perp^2 = v_{\perp 1}^2 + v_{\perp 2}^2$ = $constant$). However, the direction of motion in the plane perpendicular to B is a function of time. The particle motion is then a helical orbit and is described in the following form:

$$x_\parallel = v_\parallel \, t,$$

$$x_{\perp 1} = r_g \, sin \, (\omega_g \, t),$$

$$x_{\perp 2} = r_g \, cos \, (\omega_g \, t),$$

where $r_g = \frac{v_\perp}{\omega_g}$ defined as the gyro-radius and $\omega_g = \frac{q \, B}{m}$ is the gyrofrequency, i.e., the cyclotron frequency. Here, the particle motion is described along ($\hat{x}_\parallel$) and in a plane perpendicular to B ($\hat{x}_{\perp 1}$ and $\hat{x}_{\perp 2}$).

The motion of a single particle whose gyromotion is sufficiently fast compared to the variation times of the fields ($\omega_g \gg \frac{\partial \boldsymbol{B}}{\partial t}$ & $\frac{\partial \boldsymbol{E}}{\partial t}$) can be averaged over the circular gyromotion and replaced by its guiding center (*Northrop*, 1963). The velocity of the guiding center can be decomposed into a number of particle drifts. The guiding center drift velocity of a charged particle for any arbitrary force, $\boldsymbol{F}$, acting on the particle in a magnetic field is obtained from a general form:

$$\boldsymbol{v}_{Fs} = \frac{1}{\omega_g} \, \left(\frac{\boldsymbol{F}_s}{m_s} \times \frac{\boldsymbol{B}}{B}\right).$$

The difference between guiding-center drift velocities for ions and electrons results in a transverse current, $\mathbf{j}_F$:

$$\mathbf{j}_F = q\, n_e\, (\mathbf{v}_{Fe} - \mathbf{v}_{Fi})\,.$$

Table 1-1 lists a summary of the expressions of the guiding-center drift velocities and associated transverse currents. Here, magnetic moment of a species, μ, is defined as the ratio of perpendicular energy, $W_\perp$, and field:

$$\mu_s = \frac{mv_\perp^2}{2\,B} = \frac{W_{\perp s}}{B}\,.$$

Table 1-1: Summary of guiding-center drifts.

Type	Drift Velocity	Transverse Current
$E \times B$ *Drift*	$\mathbf{v}_E = \dfrac{\mathbf{E} \times \mathbf{B}}{B^2}$	0
Polarization Drift	$\mathbf{v}_P = \dfrac{1}{\omega_g\, B}\, \dfrac{d\mathbf{E}_\perp}{dt}$	$\mathbf{J}_P = \dfrac{n_e(m_i + m_e)}{B^2}\, \dfrac{d\mathbf{E}_\perp}{dt}$
Gradient Drift	$\mathbf{v}_{\nabla B} = \dfrac{mv_\perp^2}{2\,q\,B^3}\,(\mathbf{B} \times \nabla B)$	$\mathbf{J}_{\nabla B} = \dfrac{n_e(\mu_i + \mu_e)}{B^2}\,(\mathbf{B} \times \nabla B)$
Curvature Drift	$\mathbf{v}_R = \dfrac{mv_\parallel^2}{q\,R_c^2\,B^2}\,(\mathbf{R_c} \times \mathbf{B})$	$\mathbf{J}_R = \dfrac{2\,n_e(W_{i\parallel} + W_{e\parallel})}{R_c^2\,B^2}\,(\mathbf{R_c} \times \mathbf{B})$
Diamagnetic Drift	$\mathbf{v}_D = \dfrac{(\mathbf{B} \times \nabla_\perp P)}{q\,n_e\,B^2}$	$\mathbf{J}_D = \dfrac{(\mathbf{B} \times \nabla_\perp(P_e + P_i))}{B^2}$

1.1.1.1 Adiabatic Invariants

Here, three characteristic constants of a particle motion are introduced. These quantities are called adiabatic invariants and are not absolute constants such as particle charge or mass. In fact, adiabatic invariants may slowly change both as a function of time and space. It is the slow change compared to typical particle motion characteristics that merits adiabatic invariants to be considered as constant quantities.

The first adiabatic invariant is the magnetic moment, μ, and, as discussed above, is associated with the particle gyromotion in the presence of an external magnetic field. In other words, magnetic moment is conserved as the particle moves into stronger or weaker magnetic fields resulting. This prompts a change in the particle's perpendicular energy, in particular, a change in $v_\perp$.

Conservation of magnetic moment along converging magnetic fields forces a change in the particle's perpendicular velocity. Furthermore, total energy is a constant of motion which prohibits a change in the magnitude of particle velocity. Together, these constant quantities require a particle moving into regions of stronger fields to change its direction of parallel motion with respect to the field. In other words, the particle's pitch angle, defined as the ratio of between the perpendicular and parallel velocity components, $\alpha = tan^{-1}(v_\perp/v_\parallel)$, will increase. In this case, a particle drifting (e.g., $E \times B$ drift) into a region of increased field strength will gain perpendicular energy. This phenomenon is known as adiabatic heating and is associated with the so-called betatron acceleration.

A particle trapped inside a magnetic mirror, which is a magnetic geometry where the field lines converge on both sides, can reflect from regions of strong magnetic field intensity due to the conservation of magnetic moment. In this system, a second adiabatic invariant is also conserved. The longitudinal invariant, J, is defined as:

$$J = \oint m \, v_\parallel \, ds,$$

where ds is an element of the guiding center path and the integral is taken over a full oscillation between the mirror points.

Conservation of longitudinal invariant may lead to a change in the particle's parallel energy. Therefore, in a system where stretched field lines straighten causing the total length of the

field line to shrink the parallel velocity and energy of the particle increases. This type of parallel energization is also known as Fermi acceleration.

The third invariant involves the conservation of magnetic flux encircled by an orbiting trapped particle inside an axisymmetric mirror magnetic field configuration. This type of invariant is also known as the drift invariant and is defined as:

$$\Phi = \oint v_d \, r \, d\psi .$$

Here, v_d denotes the cumulative drift velocity (sum of all perpendicular drift velocities), ψ is the azimuthal angle, and r indicates the distance between the center of the symmetry. The closed integral incorporates the full drift path.

1.1.1.2 Magnetic Induction

The transport of magnetic field lines and plasma is described by the magnetic induction equation which is, to a first-order, defined as:

$$\frac{\partial \boldsymbol{B}}{\partial t} = \nabla \times (\boldsymbol{v} \times \mathbf{B}) + \frac{1}{\mu_0 \sigma_0} \nabla^2 \mathbf{B},$$

where σ_0 denotes uniform plasma conductivity in free space. Magnetic induction equation indicates that the change in magnetic field in a plasma can be describes with two terms: *i)* the motion of the plasma with velocity $\boldsymbol{v}$, and *ii)* magnetic diffusion. Other terms such as the Hall and pressure gradient term are not included here.

In a uniformly resistive medium (collisional plasma with finite σ), magnetic fields can diffuse across the plasma. This condition will allow magnetic flux to transport without moving the plasma which can smooth out any local magnetic field inhomogeneities. Therefore, magnetic diffusion in a stationary plasma ($\boldsymbol{v} \sim 0$) is expressed as:

$$\frac{\partial \boldsymbol{B}}{\partial t} = \frac{1}{\mu_0 \sigma} \nabla^2 \mathbf{B} .$$

This equation can also be written more generally as:

$$\frac{\partial \boldsymbol{B}}{\partial t} = D_\eta \nabla^2 \mathbf{B},$$

where $D_\eta \equiv \frac{\eta}{\mu_0}$ denotes magnetic diffusivity and η is the resistivity and is assumed constant. In highly-conductive media (collisionless plasma with infinite σ), where magnetic diffusion is

5

negligible ($D_\eta \nabla^2 \mathbf{B} \sim 0$), plasmas are bound to a specific field line. This condition is referred to as the frozen-in condition and is described as:

$$\frac{\partial \mathbf{B}}{\partial t} = \nabla \times (v \times \mathbf{B}) \ .$$

1.1.2 Kinetic Equations

In a plasma, the dynamics can often be described in terms of the collective bulk motion of the particles under the forces of the electromagnetic fields.

1.1.2.1 Maxwell Equations

In general, plasma dynamics are governed by Maxwell equations:

$$\nabla \times \mathbf{B} = \mu_0 \, J + \frac{1}{c^2} \frac{\partial E}{\partial t} \ ,$$

$$\nabla \times \mathbf{E} = - \frac{\partial B}{\partial t} \ ,$$

$$\nabla \cdot \mathbf{B} = 0 \ ,$$

$$\nabla \cdot \mathbf{E} = \frac{Q}{\epsilon_0} \ ,$$

where μ_0 is the magnetic permeability of free space, Q is the total charge per unit volume, and c denotes the speed of light.

1.1.2.2 Vlasov Equation

In collisionless plasmas, plasma dynamics are described by the Vlasov equation, taken separately for each species:

$$\frac{df}{dt} \equiv \left[\frac{\partial}{\partial t} + v \cdot \nabla + \frac{q_s}{m_s} (E + v \times \mathbf{B}) \cdot \frac{\partial}{\partial v} \right] f_s(x, v, t) = 0 \ ,$$

where f_s represents the particle's six-dimensional phase-space distribution (PSD) function and describes how the particle's dynamics vary in space, velocity, and time.

1.1.2.3 Velocity Moments

The moments of the distribution function are used to determine plasma density, bulk velocity, and temperature, as solution of the Vlasov equation:

$$n_s = \int f_s(\boldsymbol{x}, \boldsymbol{v}, t) \, d^3v \,,$$

$$\boldsymbol{v}_s = \frac{1}{n_s} \int \boldsymbol{v} f_s(\boldsymbol{x}, \boldsymbol{v}, t) \, d^3v \,,$$

$$T_s = \frac{m_s}{3 \, n_s \, k_B} \int (v^2 - v_s^2) f_s(\boldsymbol{x}, \boldsymbol{v}, t) \, d^3v \,.$$

1.1.2.4 Velocity Distributions

As discussed in the previous section, many characteristic features of a plasma including density and temperature can be derived from the function's velocity dependence. In plasmas where the particles are distributed homogenously (isotropic) and that are stationary, the PSD function can be simply presented as a function of velocity only. This function is known as the velocity distribution function (VDF) and is represented as $f(\boldsymbol{v})$. One general equilibrium in collisionless space plasma is the Maxwellian VDF and is described as:

$$f(v) = n \left(\frac{m}{2\pi k_B T}\right)^{3/2} exp\left(-\frac{\varepsilon}{k_B T}\right),$$

where $\varepsilon = \frac{m v^2}{2}$ and represents particle's energy. A Maxwellian plasma is in thermal equilibrium. This indicates that the plasma does not contain any free energy to exchange between particles in the plasma.

Not all velocity distributions are isotropic and stationary. For instance, isotropic plasmas streaming at a common non-zero velocity are referred to as the drifting Maxwellian velocity distribution. A drifting Maxwellian is asymmetric with respect to $v = 0$. The asymmetry in velocity distribution is called anisotropy.

Anisotropic velocity distributions are common in the presence of magnetic fields because of the different parallel and perpendicular velocities discussed in previous sections. One common distribution often observed in space plasmas has the form $f(v_\parallel, v_\perp)$. These distribution functions are two-dimensional and gyrotropic velocity distributions. They are also independent of the phase

angle of the gyromotion.

1.1.3 Magnetohydrodynamics

Detailed description of plasmas requires knowledge of the evolution of particle distribution functions in phase space (e.g., Vlasov equation in collisionless plasmas). However, the exact evolution of the distribution functions is not always essential in understanding the dynamics of a plasma system. In fact, it is often sufficient to determine the spatial and temporal development of the macroscopic moments of the distribution such as plasma density, bulk velocity, and pressure to describe the state of the plasma.

Magnetohydrodynamics (MHD) is the theory of electrically conducting fluids (not necessarily plasmas) subject to the presence of external and internal magnetic fields. The continuity equation for the total fluid is the first MHD equation and is the zeroth moment of the collisionless Vlasov equation:

$$\frac{\partial n}{\partial t} + \nabla \cdot (n\,\boldsymbol{v}) = 0,$$

The continuity equation states that the fluid mass is conserved as its center of mass moves with velocity $\boldsymbol{v}$. Similarly, the momentum conservation equation has the following form:

$$\frac{\partial (nm\boldsymbol{v})}{\partial t} + \nabla \cdot (nm\,\boldsymbol{v}\boldsymbol{v}) = -\nabla \cdot \mathbf{P} + \rho \mathbf{E} + \boldsymbol{j} \times \mathbf{B},$$

where P represents the pressure tensor and the net charge density is defined as $\rho = q\,(n_i - n_e)$.

1.1.4 Force-Free Magnetic Fields

At equilibrium, the equation of motion for a quasi-neutral fluid becomes:

$$\frac{\partial (nm\boldsymbol{v})}{\partial t} + \nabla \cdot (nm\,\boldsymbol{v}\boldsymbol{v}) = -\nabla \cdot \mathbf{P} + \boldsymbol{j} \times \mathbf{B} = 0.$$

At this point all forces, the right-hand terms, cancel. In some particular environments, the structure may become force-free. In this case both, the first and the second terms on the right-hand side become negligible, i.e., $\nabla \cdot \mathbf{P} = \boldsymbol{j} \times \mathbf{B} = 0$. In the case where $\boldsymbol{j} \times \mathbf{B} = 0$, current density j is completely parallel to the sum of the ambient and induced magnetic fields. In other words, $\boldsymbol{j} \propto \mathbf{B}$, where based on the Ampere's law, $\boldsymbol{j} \propto \nabla \times \mathbf{B}$. Therefore, the magnetic force-free condition requires that $\mathbf{B} \times (\nabla \times \mathbf{B}) = 0$ or that $\nabla \times \mathbf{B} = \alpha_L\,\mathbf{B}$, where α_L is a scalar to make sure that the current density

remains parallel to B throughout the structure.

Figure 1-1 illustrates a schematic view of a magnetically force-free structure. The outer field lines become helical due to a poloidal B induced by a sufficiently-strong current density flowing parallel to straight field lines at the center of the structure. The helical structure can then compensate for the residual net Lorentz force.
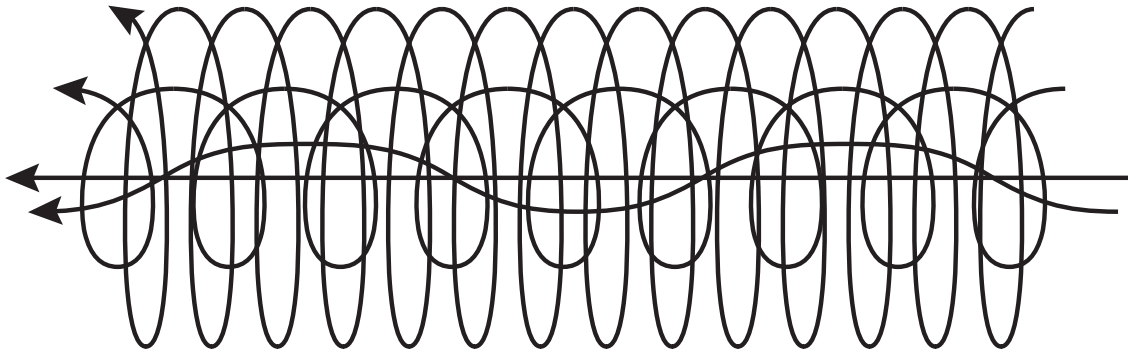
Figure 1-1: A typical magnetic force-free structure in which current density j is parallel to the sum of external and induced magnetic field B.

1.2 Geophysical Plasmas

The terrestrial plasma environment is under a continuous plasma flow from the Su, the solar wind. The solar wind interacts with the bodies of the solar system including planets, moons, and comets. The properties of the bodies govern the extent to which the interplanetary magnetic field (IMF) interacts with the body. In particular, the solar wind interaction with the magnetized bodies such as the Earth and Mercury results in the formation of a magnetosphere. A thin outer boundary of the magnetosphere is called the magnetopause representing a sudden transition from the solar wind plasma to the planetary magnetic field. The shape and extent of magnetosphere is controlled by the solar wind conditions.

1.2.1 Solar Wind

Originated from the solar corona, the solar wind, which is a stream of high-speed particles, blows out into the interplanetary space with speeds ranging between 300 to 1400 km/s. The solar wind extends far beyond the orbit of the planets and terminates in the interstellar space where the weakly-ionized interstellar gaseous medium dominates.

The solar wind originates from coronal holes where the field lines are stretched from the solar atmosphere out into the interplanetary space. The solar atmosphere is characterized by its quiescent low-speed and low temperature ($\sim$ 6000 K). Therefore, strong particle acceleration mechanisms are required to energize particles to its high interplanetary streaming velocities in the hot solar corona ($\sim$1.6 MK). The proposed solar wind heating mechanisms include wave heating and magnetic reconnection. Upon formation, the solar wind radially propagates into the interplanetary space. The solar wind's magnetic field intensity, plasma density, and temperature drop as a function of distance from the origin.

Solar wind properties control its dynamics and interactions with interplanetary bodies. One important plasma parameter is the Alfven velocity which is the fundamental speed at which magnetic signals in a plasma propagate by waves and is defined as:

$$v_A^2 = \frac{B^2}{\mu_0 \rho}.$$

Therefore, Alfvenic Mach number, which is the ratio of plasma velocity to Alfven velocity, can be written as:

$$M_A^2 = \left(\frac{v}{v_A}\right)^2.$$

Another important plasma property of the solar wind is the state at which it is magnetized. This can be inferred by examining plasma beta, defined as the ratio of thermal ($P_{th} = n\, k_B\, T$) to magnetic ($P_m = \frac{B^2}{2\mu_0}$) pressures:

$$\beta = \frac{P_{th}}{P_m}.$$

Figure 1-2 shows the radial profiles of solar wind Alfvenic Mach number, plasma beta, and dynamic pressure which depends on the plasma density and bulk velocity ($P_{dyn} = \rho\, v^2$).
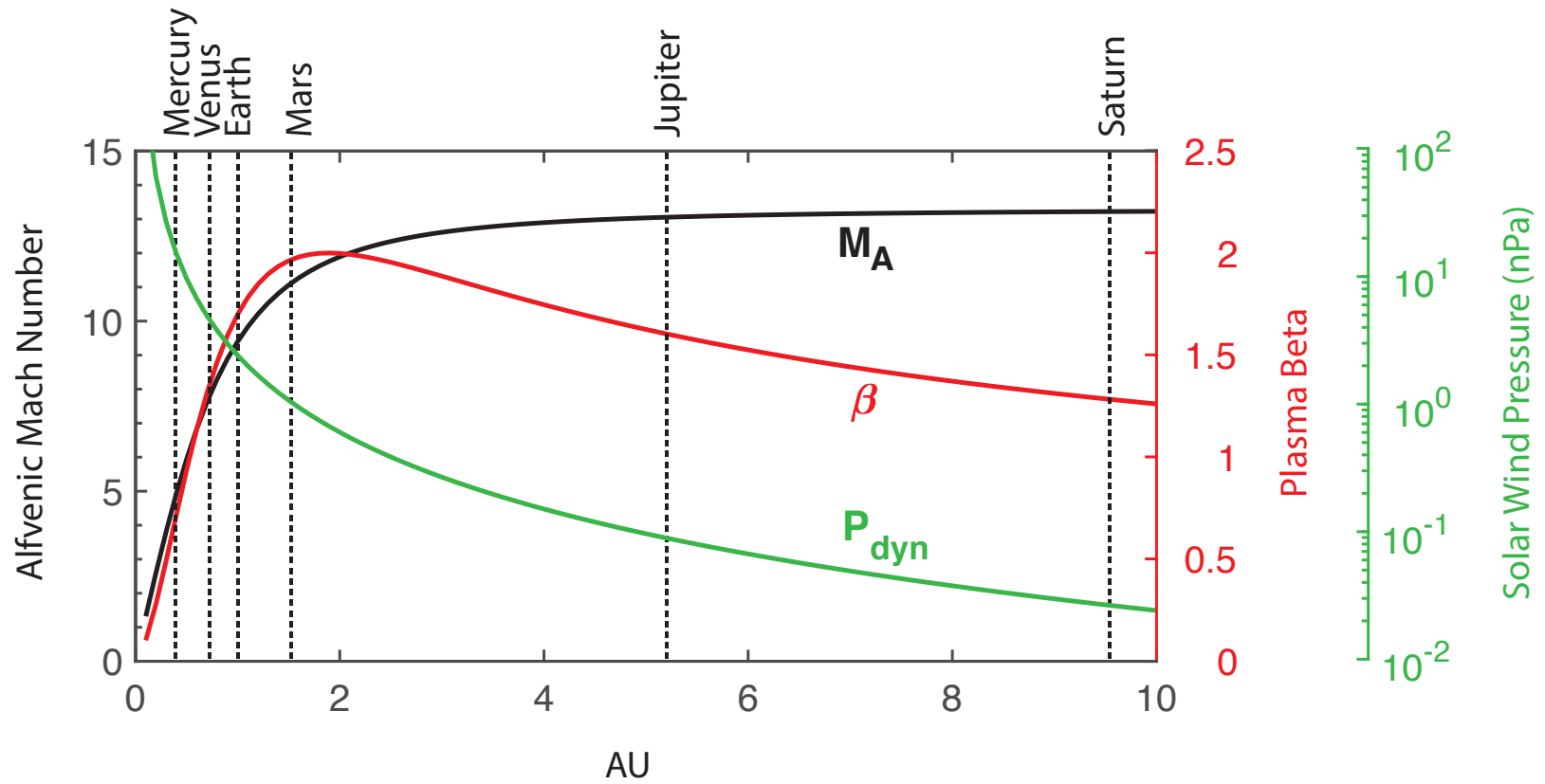
Figure 1-2: Radial profiles of solar wind plasma beta, Alfvenic Mach number, and dynamic pressure.

1.2.2 Magnetosphere

Due to its supersonic and super-Alfvenic velocity, the solar wind flow at Earth's orbit ($v \sim$ 500 km/s and $T_e \sim 10^5$ K) is subject to the formation of a shock when interacting with an obstacle in its path. Earth's bow shock is an example of a plasma shock and develops as a result of the interaction of Earth's magnetosphere with the super-magnetosonic solar wind ($c_{ms}^2 = c_{sound}^2 + c_A^2$; where c_{sound} represents sound speed and is a function of plasma temperature).

Frozen-in, collisionless solar wind plasma is slowed down substantially at the bow shock where much of the particles' kinetic energy is converted into thermal energy. These particles form a region known as the magnetosheath, which is the boundary between the bow shock and the planetary magnetic field. Magnetosheath is populated with subsonic plasmas at the dayside magnetosheath that are hotter and denser than those in the solar wind.

Due to the frozen-in condition, shocked solar wind plasmas do not penetrate the terrestrial magnetic field. Instead, the particles are deflected and move around the terrestrial magnetic field. The solar wind plasma pressure compresses the terrestrial dipole field resulting in a distorted magnetic field geometry whose frontside is compressed while the backside stretches outward into a long magnetotail, as shown schematically in Figure 1-3. The cavity generated by the terrestrial magnetic field is known as the magnetosphere. The boundary separating the magnetosphere from the magnetosheath is called the magnetopause.
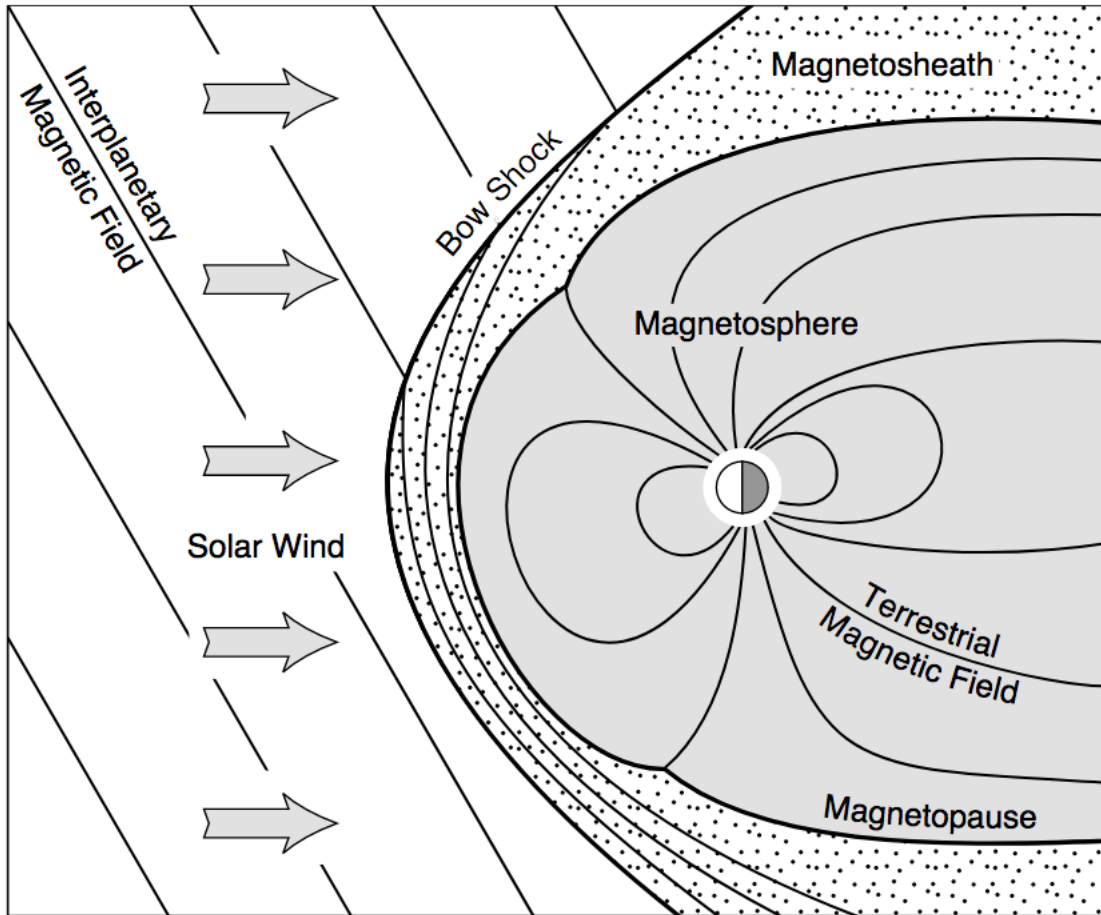
Figure 1-3: Topography of the solar-terrestrial environment (from *Baumjohann and Treumann*, 2012).

1.2.3 Magnetic Reconnection

In classical mechanics, a stable condition is referred to the state in which the system is stable and can return quickly back to equilibrium in the presence of small external perturbations. In Figure 1-4, stable equilibrium is depicted as a heavy ball situated at the bottom of a deep potential trough. In this case, external perturbation leads to the heavy ball oscillating alongside the potential walls before slowing down by the counteracting resistive force and coming to rest at the bottom of the well.

The remaining three configurations are unstable. In the case where the heavy ball is located at the top of a potential hill, the ball will roll down due to slightest displacement. This configuration is known as linear unstable and characterizes linear instabilities in plasmas. The ball in the metastable configuration, on the other hand, can wander along the plateau before rolling down the hill. Finally, in the case of non-linear unstable configuration, the ball experiences local stability. For small-amplitude perturbations, the ball will return to rest. However, beyond a threshold, the ball will roll down the potential hill. Instabilities of this category are referred to as non-linear instabilities.

MHD instabilities are divided into two major categories: ideal and non-ideal instabilities. Ideal instabilities include the bending and deformation of magnetic flux tubes while plasmas remain frozen-in. In contrast, non-ideal instabilities are present in plasmas where the frozen-in condition breaks down. Magnetic flux in non-ideal (collisional) plasmas can diffuse across the plasma and be exchanged between different plasma regimes in mutual contact.

During diffusion, magnetic flux is often slowly re-arranged. However, the process can become comparably faster if the re-ordering of field lines is restricted to a region of small spatial extent, as it is the case in magnetic reconnection. Magnetic reconnection (merging) is the process through which magnetic field lines marge and are cut and reconnected to other field lines resulting in a change in magnetic topology. Magnetic reconnection is a key mechanism in driving local and global phenomena at the magnetopause, in the magnetotail, and beyond.

The oppositely-directed magnetic field lines ($\pm B_z$) between two approaching ideal MHD flows ($\pm v_x$) may annihilate one another at the plane of contact. Figure 1-5 depict the processes involved in two approaching oppositely-directed magnetic fields annihilating each other and re-
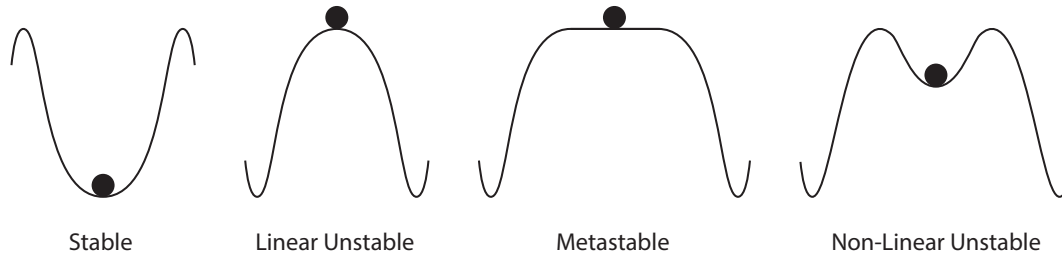
Figure 1-4: Different non-equilibrium configurations leading to instability.

arranging into a new configuration. Figure 1-5*a* shows two magnetic field lines moving toward each other while pointing in opposite directions. The four colored balls represent particles. The bent field lines, shown in Figure 1-5*b*, will be the initial point of contact between the two bundles. The interaction region is localized and has a scale length *L*.

According to the Maxwell equations, in particular Ampere's law, an out-of-plane (j_y) current layer will form between the two magnetized flows. The initial instability between the two non-ideal bent field lines is a transverse current instability. The instability leads to diffusion of magnetic flux and to increased concentration of current at the neutral point. In three dimensions, the neutral point extends out of the page into a neutral line or an X-line, as shown in Figure 1-5*c*. These dynamics are described by the general induction equations and the diffusion time, τ_d, which is the characteristic time of the magnetic field diffusion, can be written in terms of the bent magnetic field length, *L*, and the constant electrical constant, σ:

$$\tau_d = \mu_0 \, \sigma \, L^2,$$

and the diffusion velocity is described as:

$$v_d = L \, / \, \tau_d = 1 \, / \, \mu_0 \, \sigma \, L \, .$$

At the X-line, inside the diffusion region, magnetic field diffuses across the flow and annihilate. The annihilation process cuts the anti-parallel field lines in halves. Consequently, the field-line halves from one side are reconnected with those from the other side. At this point, the merged field lines are expelled from the diffusion region ($\pm v_z$) by the tension force ($\mathbf{F}_c \propto \mathbf{B} \cdot \nabla \mathbf{B}$) stored in the highly-bent reconnected field lines. More importantly, the newly-reconnected field

lines will be populated by a mixture of plasmas from both sides of the current sheet (even without any necessity of diffusion). The outflowing plasma in the downstream of the X-line is perpendicular to the original inflow and is characterized as enhanced plasma flow or reconnection jets.
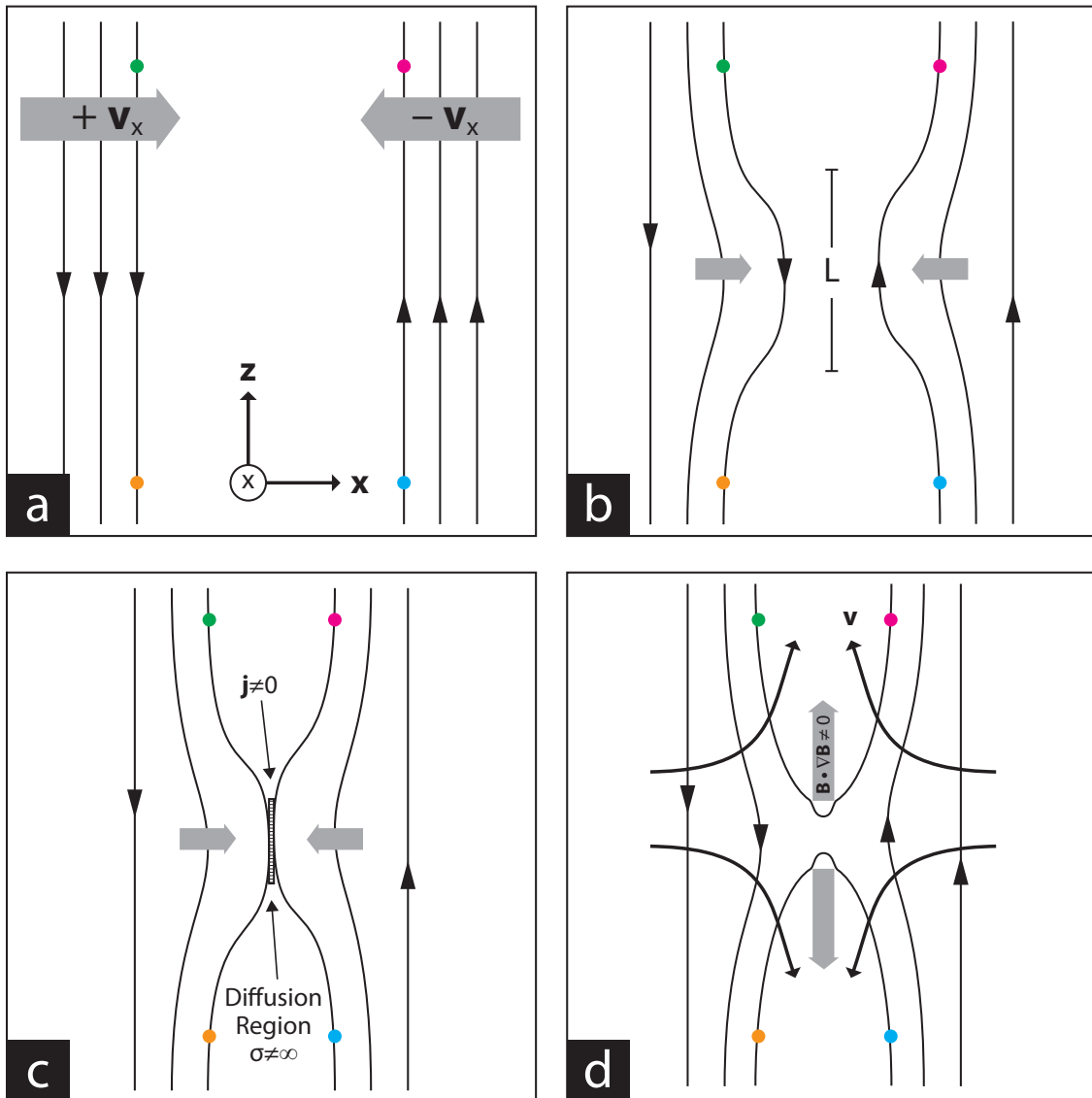
Figure 1-5: Counter-streaming flows leading to the merging of oppositely-directed field lines, formation of current sheet, and neutral point leading to re-arrangement of field lines.

1.2.3.1 Reconnection Rate

In the case of stationary reconnection, shortly after the formation of a current layer at the interface of oppositely-directed field lines, diffusion becomes stationary. At this point, the inflowing mass and magnetic flux, the magnetic diffusion, and the outflowing mass and magnetic flux reach an equilibrium. Reconnection rate is the rate at which the magnetic field can diffuse in and through the diffusion region and is a key parameter in determining the efficiency of the different models of reconnection.

The Sweet-Parker reconnection model relies on the conservation of mass, momentum, energy, and magnetic flux in the flow upstream, inside, and downstream of the diffusion region. The model involves steady flow and diffusion of magnetic field across a long and narrow diffusion region of length, $2L$, and width, $2d$. The conservation requirements suggest that:

$$B_{0z} / L \approx B_{dx} / d,$$

where B_{0z} and B_{dx} represent the strength of the inflowing and outflowing magnetic fields, respectively. The outflow (diffusion) velocity is:

$$v_{dz}^2 \approx v_{A0}^2.$$

where v_{A0} the Alfvén speed in the upstream inflowing plasma. Therefore, the Sweet-Parker model reconnection rate (efficiency), which is the defined as the ratio of the plasma (magnetic field) outflow and inflow through the diffusion region, is described as:

$$R = v_{dz} / v_{0x} = M_{A0},$$

where v_{0x} can be described independent of the diffusion region width, d, as:

$$v_{0x}^2 \approx v_{A0}^2 / \mu_0 \sigma L.$$

The Sweet-Parker reconnection rate can be re-written as:

$$R_{SP} = M_{A0} = R_{m0}^{-1/2},$$

where $R_{m0} = \mu_0 \sigma L v_{A0}$ is the magnetic Reynolds number and is the ratio of the convective to the diffusive terms of the magnetic induction equation. The reconnection rate is, therefore, inversely related to the magnetic Reynolds number indicating that in collisionless plasmas (infinite σ), such as that at the magnetopause, the reconnection process proceeds very slowly ($R_m > 1$).

The elongated diffusion region yields the slow reconnection process in the Sweet-Parker reconnection model. When the finite conductivity is restricted spatially into a localized region, the reconnection process becomes much faster. The Petschek reconnection model relies on a short and narrow diffusion region, hence, limiting the amount of plasma crossing the diffusion region. The model also requires the formation of a shock to mediate the necessary change in plasma flow direction, since most of the plasma will have to turn around before reaching the interface between the two counter-streaming flows. Table 1-2 summarizes the reconnection rates and the ratio at which the inflowing magnetic energy is converted to the outflowing kinetic energy of the plasmas for both the Sweet-Parker and Petschek reconnection models. The ratio of magnetic-to-kinetic energy conversion is derived from the conservation of magnetic flux through the diffusion region. The Petschek model of reconnection is much faster (and violent) than the Sweet-Parker model. Also, in the Petschek model, 60% of the inflowing magnetic energy is converted into flow energy and thus accelerating plasmas to higher kinetic energies while the remaining 40% of the incoming energy is used to heat the plasma.

At very large Reynolds numbers, $R_m \gg 1$, the resistive term becomes dominant (collisional) and cascading islands are formed (e.g., *Ji & Daughton*, 2011). The Sweet-Parker and the Petschek reconnection theories, which rely on constrained diffusion regions, do not apply in highly-collisional plasma regimes.

Table 1-2: Reconnection rates and magnetic-to-kinetic energy conversion ratios for the Sweet-Parker and Petschek reconnection models.

Type	SP model	Petschek model
Reconnection rate	$R_{m0}^{-1/2}$	$\pi\,(8\,ln(R_{m0}))^{-1}$
Conversion ratio	1/2	3/5

1.2.3.2 Steady Collisionless Reconnection

Reconnection in collisionless space plasmas cannot be explained using resistive MHD. Instead, kinetic models which rely on particle dynamics to initiate reconnection can be used. In the following sections, the role of tearing mode instability in the onset of reconnection and the possibility of reconnection reaching a steady collisionless state are presented.

1.2.3.2.1 Linear Regime

In a collisionless system, where the ambient magnetic field, $B_0(x, z)$, is two-dimensional (independent of y-component), the initial vector potential, A_0, can be simplified as:

$$A_0 = B_0 / [(2L)(x^2 - z^2)],$$

where L is the system size and is represented in Figure 1-6. In this system, $\mathbf{E} = E_y\,\hat{e}_y$, since steady reconnection. The system can be categorized into two regions: *i)* adiabatic, and, *ii)* non-adiabatic. In the adiabatic region, particles drift adiabatically into and out of the system (along the z and x-axes, respectively). Adiabaticity is violated inside the non-adiabatic region in the vicinity of the neutral point, shown as a gray circle in Figure 1-6, where the conversion of magnetic energy into flow energy takes place.
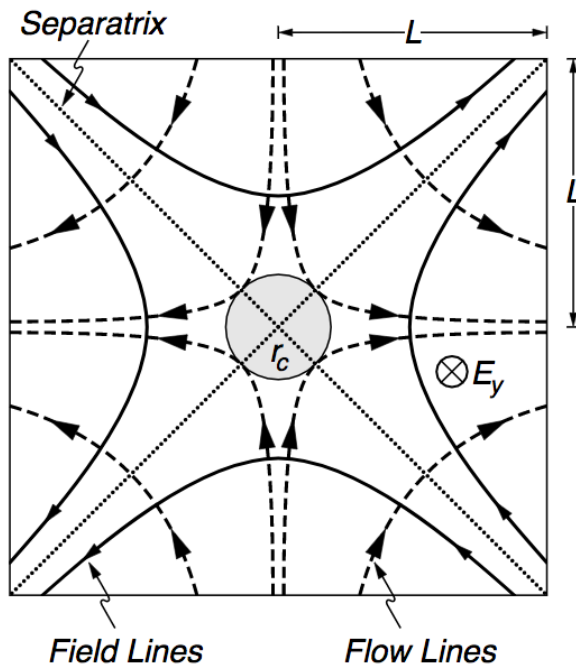
Figure 1-6: Collisionless reconnection in a two-dimensional magnetic field system.

A particle entering the X-point is subjected to three force fields: *i)* the particle is accelerated out of the page (in the *y*-direction) by the electric field, *ii)* the particle is forced along the *x*-direction by B_z, and *iii)* B_x leads the particle to oscillate along *z*:

$$v_y (t) = q\, E_y\, t\, /\, m,$$

$$t_c = (m^2\, L\, /\, q^2\, B_0\, E_y)^{1/3},$$

$$\omega_b(t) = (q^2\, B_0\, E_y\, t\, /\, m^2\, L)^{1/2},$$

where t_c and $\omega_b(t)$ are the critical acceleration time along *x* and the oscillation frequency in *z*, respectively. These equations suggest that a particle ejected from the X-point reaches the edge of the dissipation region, r_c ($\sim L\, (m\, E_y\, /\, q\, B_0^2\, L)^{1/3}$), quickly (at an exponential rate of $exp\, (t\, /\, t_c)^{3/2}$). The particle energy gain is proportional to the particle mass, $m^{1/3}$, and the total magnetic energy dissipation is proportional to the third power of the electric field, E_y^3.

The linear approximation breaks down when the induced magnetic field strength created due to the dominantly-ion current away from the X-line becomes comparable to the initial ambient magnetic field, B_0. The linear limit can be expressed as:

$$M_{A0} = \widetilde{R}_{m0}^{-1/4},$$

where the Reynolds number is approximately defined as the ratio of the total length to the external ion inertial length, $\widetilde{R}_{m0} = (L\, \omega_{pi}\, /\, c)^{1/2}$, indicating that the reconnection rate is determined by the ion inertia. The linear regime also has a more restrictive limit on E_y ($\leq E_{yc} = m_i\, v_{A0}^2\, c\, /\, q\, L^2\, \omega_{pi}$) which can be readily violated resulting in $M_{A0} = \widetilde{R}_{m0}^{-1}$. Beyond this limit, the reconnection process transforms into the non-linear regime.

1.2.3.2.2 Non-Linear Regime

In environments where $E_y > E_{yc}$, magnetic reconnection enters the non-linear regime during which large reconnection rates occur. In this case, the reconnection site for a normalized vector potential, $A_0 = (x^2 - z^2)\, /\, 2$, is elongated with length 2L and width 2*d*. The geometry is shown in Figure 1-7. Under these conditions and constant current density *j*, the normal component of the magnetic field variations along *x* can be assumed negligible, $dB_z\, (x)/dx \propto d\, /\, L \ll 1$. This

indicates that the reconnection site is nearly a one-dimensional current sheet and that magnetic field spatial variations are only in the x-component $B_x(z)$. Therefore, the critical acceleration time along x and the oscillation frequency in z in the non-linear regime can be written as:

$$t_c \sim (E_y \, \frac{dB_z}{dx})^{-1/3},$$

$$\omega_b(t) \sim (E_y \, t \, \frac{dB_x}{dz})^{1/2}.$$

where the time scale t_c for the non-linear regime is much longer than that of the linear regime. Furthermore, the bounced-averaged motion of the ions is decoupled from the oscillation along the z-axis. In particular, the ion motion can be expressed in two forms: 1) $t < t_c$ wherein ions with a zero-average normal velocity component entering the dissipation region will be accelerated out of the plane along y. Within this period, these ions also experience an explosive thrust from the neutral line. 2) During $t > t_c$, the motion is dominated by the ExB drift which defines the edge of the dissipation region along the x axis, $x_c \sim E_y \, t_c^2 \sim L$. The determination of the edge of the dissipation region along the z-axis is a function of the amplitude of the ion bounce motion at t_c and is expressed as, $d \sim E_y^{-4/3} \sim n_0^{-1} \sim j^{-7/4}$. Interestingly, as the expression suggests, plasma moments in the dissipation region are dependent on the out-of-plane electric field E_y, i.e., reconnection rate. Finally, the reconnection rate in the non-linear regime is approximately inversely proportional to the square root of the ion inertial Reynolds number $\widetilde{R}_{A0}$:

$$R_{CL} \sim \widetilde{R}_{A0}^{-1/2},$$

noting that, while the scaling here is similar to the Sweet-Parker scaling R_{SP}, the ion inertial Reynolds number $\widetilde{R}_{A0}$ may help to increase the reconnection rate.
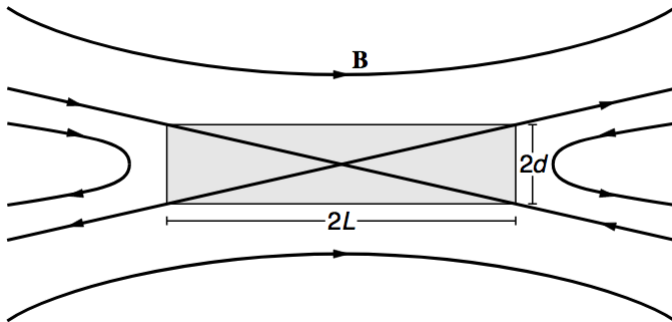
Figure 1-7: An elongation reconnection site where electric field $E_y \gg 1$ is far above the critical field, E_{yc}.

1.2.3.2.3 Tearing Instability

The reconnection onset has been associated with a plasma instability observed in a plasma with inhomogeneous magnetic field and current density, i.e., non-zero normal magnetic field component B_{0z}. This plasma instability requires the presence of a dissipative region around the magnetic neutral point, where oppositely-directed magnetic fields cancel each other out. Inside the dissipative region, plasmas are collisional, i.e., resistive dissipation, or that the magnetic field diffusion occurs via a collisionless dissipation mechanism. In a two-dimensional collisional dissipative diffusion region, the onset of reconnection is linked to the interaction of a series of magnetic islands and neutral points that are formed in a current layer due to *resistive tearing instability*. The resistive tearing mode is believed to play a decisive role in solar physics. On the other hand, when the plasma is collisionless, 2D reconnection can only evolve as a kinetic instability. In this case, the ion inertia supports the *collisionless tearing instability* which causes the diffusion of magnetic fields and the generation of a succession of magnetic islands and neutral points. In Figure 1-8, a current layer thins and breaks into a chain of magnetic islands, i.e., O-points, and magnetic neutral points, i.e., X-points. The collisionless tearing mode is believed to play a key role in collisionless magnetospheric environments. The electron-scale processes are shown particularly important in the magnetosphere.
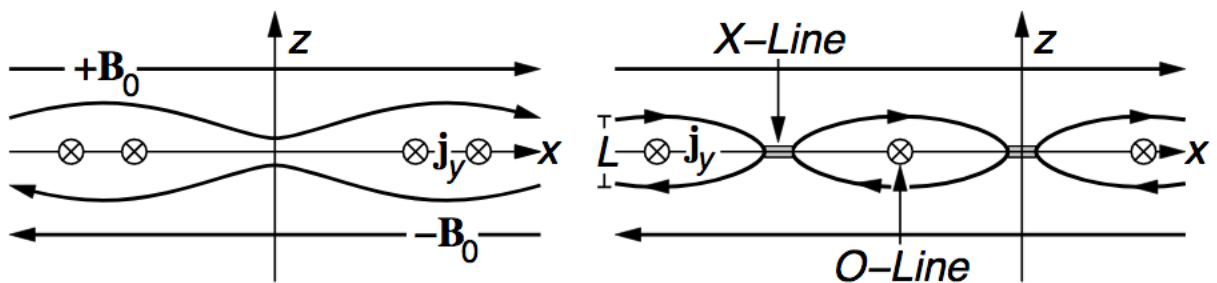
Figure 1-8: Tearing-mode instability giving rise to the formation of magnetic islands and neutral points in a two-dimensional dissipative diffusion region.

1.2.4 Magnetic Flux Ropes

A *flux tube* is defined as the volume enclosed by a set of field lines that intersect a simple closed curve. The frozen-in condition of ideal MHD describes a parcel of plasma threaded by magnetic field lines as a conserved entity, whose motion can be followed by accounting for all the Newtonian forces acting on the magnetized plasma. Flux tubes are universal objects in the plasma universe ranging from laboratory magnetic fusion experiments to astrophysical plasmas. Flux tubes can form inside reconnecting current sheets. The flux tubes generated inside current sheets wherein a magnetic field component parallel to the current is present are deformed due to an induced poloidal magnetic field component. The resulting twisted flux tubes are called *flux ropes*. Flux ropes are observed on the Sun, in the solar wind, and in the magnetospheres of the magnetized planets. At the magnetopause, flux ropes penetrating the boundary layer are referred to as flux transfer events (FTEs). FTEs have a wide range of scale sizes and play an important role in transporting mass, momentum, and magnetic flux from the solar wind into and across the magnetospheres.

Solar observations indicate that solar flux ropes can form due to various processes including the emergence of twisted magnetic fields from the convection zone inside the Sun and the interaction between neighboring active regions. Magnetic reconnection is also thought to play an important role in the formation of new solar flux ropes and the energization of solar plasmas. Magnetic reconnection in the solar corona can give rise to the production of and the ejection of magnetic flux ropes, also known as magnetic clouds. Coronal mass ejections often show flux rope structures. The flux ropes signatures observed in the solar wind with in-situ spacecraft measurements are referred to as interplanetary coronal mass ejections (ICMEs). ICMEs are identified by their low-variance, enhanced magnetic fields and counter-streaming electron signatures, i.e., closed field lines.

Magnetic flux ropes are also observed in the Earth's current sheet. Upon formation due to magnetic reconnection in the current sheet, magnetic flux ropes convect earthward or tailward. Magnetic flux ropes convecting tailward are known as plasmoids and have diameters of many tens of Earth radii R_E and are strongly correlated with geomagnetic substorms and high-speed tailward flows. On the other hand, the earthward-moving flux ropes experience an strengthening ambient magnetic field environment near the planet and are often recombined with the geomagnetic field.

1.2.4.1 Flux Transfer Events

At the dayside magnetopause, FTEs are often formed due to magnetic reconnection between the southward interplanetary magnetic field (IMF) and the northward geomagnetic field. Upon formation, FTEs convect away from the reconnection site along the magnetopause toward the high-latitude magnetopause or the flanks, as part of the so-called Dungey cycle. As shown in Figure 1-9, *Dungey* (1961) proposed that proposed that reconnection drove plasma convection via the ExB drift in the magnetosphere. The numbered field lines show the succession of configurations a geomagnetic field line assumes after reconnection with an IMF field line (1') at the front of the magnetosphere. Field lines 6 and 6' reconnect at a second X-line in the magnetotail, after which the field line returns to the dayside at lower latitudes. The inset shows the positions of the feet of the numbered field lines in the northern high-latitude plasma flows, an anti-sunward flow in the polar cap, and a return flow at lower latitudes.

As flux ropes, FTEs are identified with their bipolar signature in the normal component ($\boldsymbol{B}_n$) of magnetic field in the magnetopause boundary normal coordinates (e.g., *Russell & Elphic*, 1978). The bipolar signature is coincident with an enhancement in both the axial component and the total magnetic field, |B|. FTEs have been observed in various planetary environments, from Mercury to Jupiter (*Russell & Elphic*, 1979; *Walker & Russell*, 1985; *Briggs et al.*, 2011; *Slavin et al.*, 2012; *Jasinski et al.*, 2016). FTEs are believed to contain plasmas from both the magnetosphere and the magnetosheath (e.g., *Klumpar et al.*, 1990).
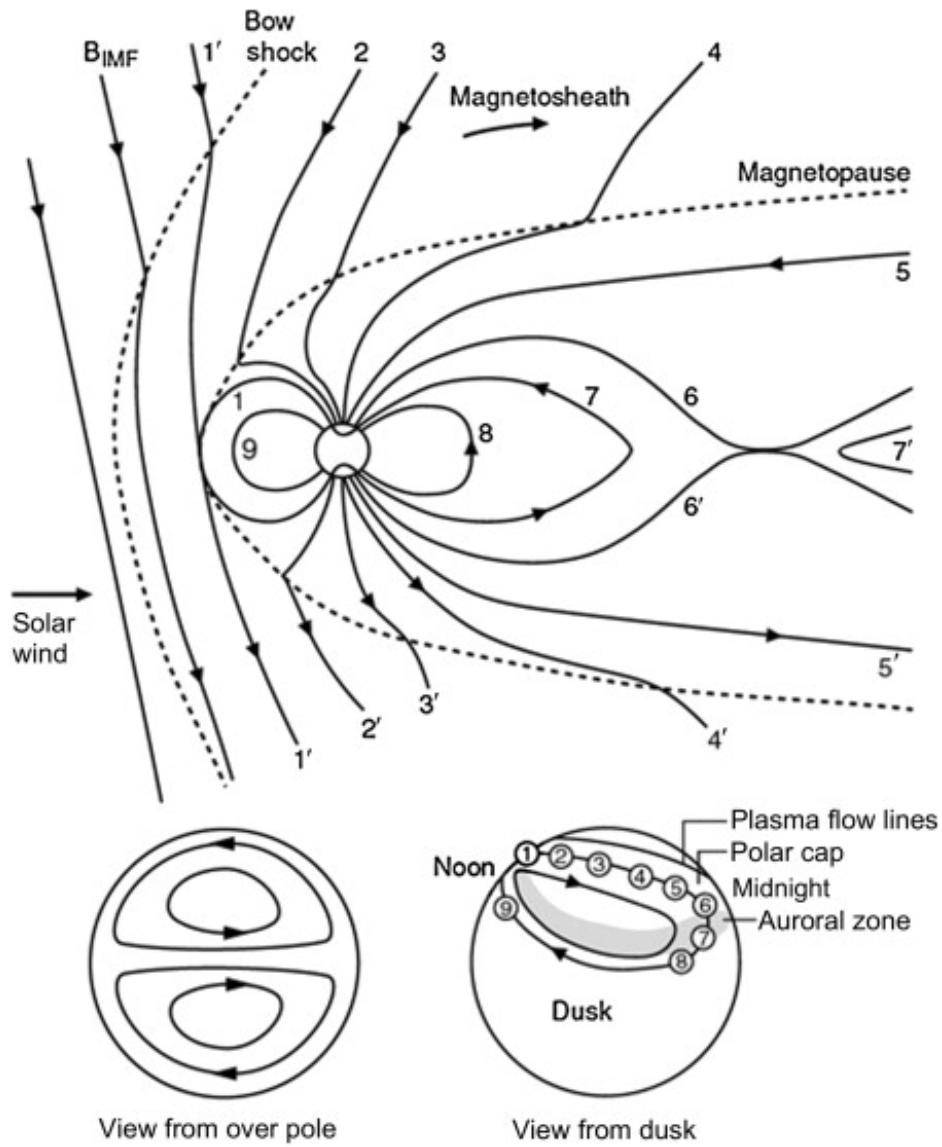
Figure 1-9: Illustration of convection of magnetic fields and the frozen-in plasma within the magnetosphere driven by magnetic reconnection.

Previous observational studies have hypothesized three FTE generations mechanisms:

1) Transient bursty reconnection (elbow-shaped flux bundle), wherein a transient X-line is formed at the dayside magnetopause giving rise to the generation of two bundles of flux tubes convecting in opposite directions in the X-line's frame of reference (*Russell & Elphic*, 1978; *Dunlop et al.*, 2005). The elbow-shaped, spiral magnetic fields, as shown in Figure 1-10, are spatially constrained in their azimuthal extent. They are connected to the high-altitude ionosphere through the northern and southern cusps. The resulting FTEs are believed to contain bidirectional electron population at their outer magnetic layers near the reconnection site. Ions at the region of enhanced |B| are found to become dominantly unidirectional (*Varsani et al.*, 2014).

2) Continuous reconnection at a single X-line with a modulating reconnection rate (e.g., *Scholer*, 1988; *Southwood et al.*, 1988; *Phan et al.*, 2004) can generate FTEs with a wide azimuthal extent. The dominantly-field aligned plasmas in the exhaust region of the X-line are thermalized farther inside the FTE (*Lockwood & Hapgood*, 1998).

3) Multiple X-line reconnection involves the simultaneous (*Lee & Fu*, 1986) and/or sequential (*Raeder*, 2006) occurrence of a plurality (n) of X-lines giving rise to the generation of multiple (n-1) FTEs (e.g., *Fuselier et al.*, 2018; *Hwang et al.*, 2018). In this scenario, the reconnection exhausts from the adjacent X-lines converge inside the embedded FTE (e.g., *Hasegawa et al.*, 2010; *Øieroset et al.*, 2011, 2016). The resulting FTEs may contain magnetic fields and plasmas originated in the magnetosheath, magnetopause, or a combination thereof (*Lee & Fu*, 1985).

Earlier observations of FTEs at the Earth's magnetopause have suggested average diameter ~1-2 R_E (*Wang et al.*, 2005). However, theory and simulations have indicated that FTEs of the order of 1 to few ion inertial lengths (d_i) should also be present (*Drake, Swisdak, Schoeffler, et al.*, 2006; *Fermo et al.*, 2011). *Eastwood et al.* (2016) reported the observation of d_i-scale FTEs at the magnetopause, in agreement with theory. The size distribution of FTEs can give us insight into their generation mechanism(s) and evolution. Therefore, this dissertation will focus on the size distribution, cross-sectional profiles of physical properties, and size dependence of thermal pressure and plasma energization mechanisms inside FTEs at the Earth's subsolar magnetopause. The overarching goal of this dissertation is to shed light on the significance and the extent of

reconnection-driven plasma heating in the Earth's dayside magnetosphere. The findings of this dissertation are applicable to other comparable plasma environments, such as in the magnetospheres of magnetized planets/exoplanets, solar/stellar flux ropes, and laboratory magnetic reconnection.
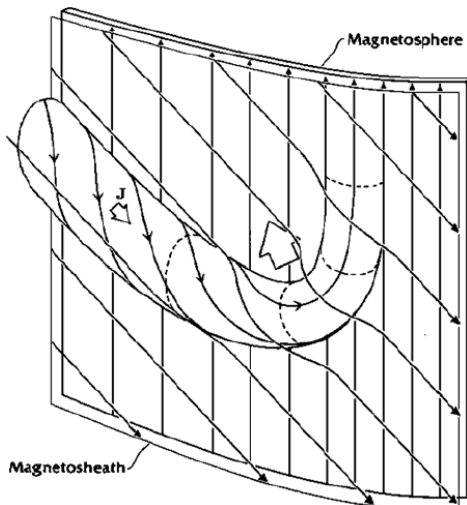
Figure 1-10: Illustration of elbow-shaped FTEs. Courtesy of *Russell & Elphic* (1978).

1.3 Science Objectives

1.3.1 To investigate the size distribution of FTEs at the subsolar magnetopause

Determining the magnetic field structure, electric currents, and plasma distributions within FTE-type flux ropes is critical to the understanding of their origin, evolution, and dynamics. Previous theoretical investigations have suggested that FTE-type flux ropes whose cross section is smaller than or equal the local ion inertial length ($d_i = c/\omega_{pi} \sim 70$ km) should be generated inside thin magnetopause reconnecting current layers (e.g., *Drake, Swisdak, Schoeffler, et al.*, 2006). While capturing some small-scale FTEs with average size <2000 km, Cluster observations at high-latitude magnetopause and flanks were not able to detect ion-scale FTEs (*Fermo et al.*, 2011). Therefore, it is important to investigate the subsolar magnetopause to examine the occurrence (e.g., *Eastwood et al.*, 2016) and the size distribution of FTEs (e.g., *Wang et al.*, 2005). Chapter 4 focuses on the size distribution of FTEs at the subsolar magnetopause, wherein FTEs are identified using reproducible and objective selection criteria (e.g., *Slavin et al.*, 2003). The size distribution of FTEs can indicate the processes through which FTEs are generated and evolve. It is also possible to study the physical characteristics of subsolar FTEs as a function of diameter.

1.3.2 To study the radial profiles of physical characteristics inside subsolar FTEs and to examine the FTE growth mechanisms

Previous studies have indicated that FTEs grow as they convect away from the reconnection site along the magnetopause. This increase in FTE diameter may occur via adiabatic expansion in response to decreasing external pressure away from the subsolar region or due to a continuous supply of magnetic flux and plasma to the FTEs' outer layers by magnetic reconnection. The net forces inside and at the outer layers of FTEs can 1) contribute to the evolution of FTEs, and 2) energize plasmas. In Chapter 5, the residual net force inside FTEs at the subsolar magnetopause are investigated using multi-spacecraft techniques (*Harvey*, 1998). The magnitude and the radial profiles of the components of the net residual force are examined to determine the growth of subsolar FTEs as they convect away along the magnetopause. The Chapter further explores the thermodynamics of FTE evolution. In particular, average plasma properties inside FTEs are investigated as a function of FTE size to determine the likely processes through

which FTEs evolve.

1.3.3 To evaluate plasma energization and heating mechanisms inside FTEs

Upon formation, flux transfer events (FTEs) in the subsolar magnetosheath are shown in Chapter 4 to grow in diameter, λ, while convecting along the magnetopause. In Chapter 5, plasma pressure has also been found to decrease sub-adiabatically with increasing λ, indicating the presence of internal plasma acceleration and heating processes. Chapter 6 further examines the relative roles of parallel electric fields and betatron and first-order Fermi processes in energizing plasmas inside and at the outer layers of subsolar FTEs. The relative contributions of different plasma energization mechanisms can further enable us to determine how FTEs interact with the ambient environment while convecting along the magnetopause. The energization mechanisms are further studied as a function of FTE diameter.

1.3.4 To verify reconnection theory using hybrid-Vlasov simulations and to provide a holistic view of reconnection-driven FTE evolution mechanisms

The Vlasiator hybrid-Vlasov code was developed to investigate global magnetospheric dynamics at ion-inertial scales. As discussed in Chapters 4 and 5, FTEs can evolve via magnetic reconnection. Spacecraft observations are limited in theory ability to study the temporal and spatial evolutions of a magnetic structure. Therefore, global simulations can be used to provide a wholistic view of the mechanisms through which FTE-type flux ropes evolve. In Chapter 7, two dimensional magnetic islands, which are analogous to flux ropes in three dimensions, are investigated at the magnetopause. First, hybrid-Vlasov simulations are examined to insure that the ion kinetics associated with magnetic reconnection are well resolved. Next, the simulations are used to classify and evaluate the relative contributions of the different reconnection-driven magnetic island evolution mechanisms. The simulations results are further used to guide our understanding of the FTE growth at the magnetopause and to enrich spacecraft observations by providing a global context.

1.3.5 To investigate the microphysics of the FTE coalescence using MMS observations and to study the temporal and spatial evolutions of coalescing magnetic islands at the magnetopause using hybrid-Vlasov simulations

FTEs at the dayside magnetopause are found to grow via FTE coalescence. During the coalescence process, two neighboring FTEs merge and reconnect to create one larger FTE. While merging, a current sheet is formed between oppositely-directed field lines. The current sheet soon becomes unstable to reconnection. In Chapter 8, we extend the coalescence process, as discussed in Chapter 7, to further examine the microphysics of the coalescence process. In particular, the electron and ion behaviors inside the thin and reconnecting current sheet are investigated. Spacecraft observations of the coalescence process are limited in determining the temporal and spatial evolution of the coalescence process, therefore, hybrid-Vlasov simulations are further employed to provide a global view of the magnetic island coalescence process.

In summary, this dissertation explores the role of magnetic reconnection in controlling the evolution and thermodynamics of magnetic fields and plasmas through the lens of FTE-type flux ropes. In-situ observations are used to study the temporal and spatial evolution of FTEs. To achieve this, numerous assumptions regarding the growth mechanisms and the general structure of FTEs are needed to be made. Therefore, global hybrid-Vlasov Vlasiator simulations are employed to examine our assumptions and to further provide a holistic view of the FTE evolution and its global impact. The dissertation is finally concluded in Chapter 9 and future direction is discussed.

Chapter 2: Measuring Charged Particles and Fields in Space

2.1 Particle Detectors in Space

The earliest measurement of charged particles was reported by the British physicist, William Gilbert (*Gilbert*, 1958) in the early 1600s. Gilbert constructed the first electroscope comprising a pivoted needle to detect the presence of static electric charge. Further improvements of the electroscope involved using gold leaves in a vacuum chamber, as shown in Figure 2-1, to measure electrostatic charge buildup on an object with and without (electrostatic induction) direct contact. Charles-Augustin de Coulomb reported in 1785, in his famous "Mémoires sur l'électricité et le magnétisme" (*Coulomb*, 1935), the surprising, spontaneous discharge of an electroscope by air.

Figure 2-1: The gold-leaf electroscope.

In 1910, the German scientist and priest, Theodor Wulf designed and constructed a transportable electroscope. The new design, as illustrated in Figure 2-2, replaced the gold leaves with two metalized glass strips. Wulf climbed the Eiffel tower with his improved electroscope to investigate the change in ionization rate as a function of distance from the Earth surface. Wulf's finding that the ionization rate did not change significantly with distance from the possibly-radioactive Earth surface, gave rise to one of mankind's revolutionary scientific discoveries, the cosmic rays (*De Angelis*, 2011). The discovery of charged particles with energies higher than can be generated at Earth revolutionized our understanding of fundamental physics and quantum theory.
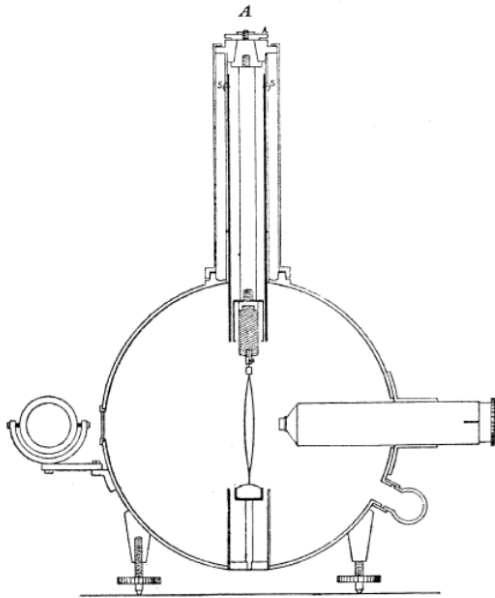
Figure 2-2: Scheme of the Wulf electroscope. On the right, there is a microscope that measures small displacement of the two silicon glass wires. The two glass wires were illuminated, for improved visibility, by a mirror, installed on the left hand side of the instrument.

The study of cosmic rays soon started the space science. Though unsuccessful to meet its defined main science objective of understating the distribution of low-energy cosmic ray, the Geiger counter aboard Explorer I (and Sputnik III, in 1958) discovered the Earth's radiation belts (*Allen*, 1958). As shown in Figure 2-3, the Geiger counters aboard the satellites 1958 alpha and gamma were saturated, marked by flat count rates at ~130 counts/s, by the high-energy radiation, hence, termed the 'radiation belts'.

The types particles in the solar system encompass electrons, charged atoms and molecules, as well as neutral atoms, molecules, and particulate matter (dust). The sources for these particles range from extra-galactic and galactic environments to solar corona and flares. Planetary bow shocks, dust rings (and cometary tails), surface, and atmospheres can also generate the observed particles in the solar system. These particles cover a large (12 orders of magnitude; 10^0 - 10^{20} eV) energy range and a wide mass range: from electron mass to hundreds of atomic mass units (amu). Therefore, particle detectors are designed to cover a wide parameter space. For instance, particle detectors at high temporal resolutions are used to study space plasmas and cometary environment explorations utilize high mass resolution particle detectors to investigate a comet's coma.

33
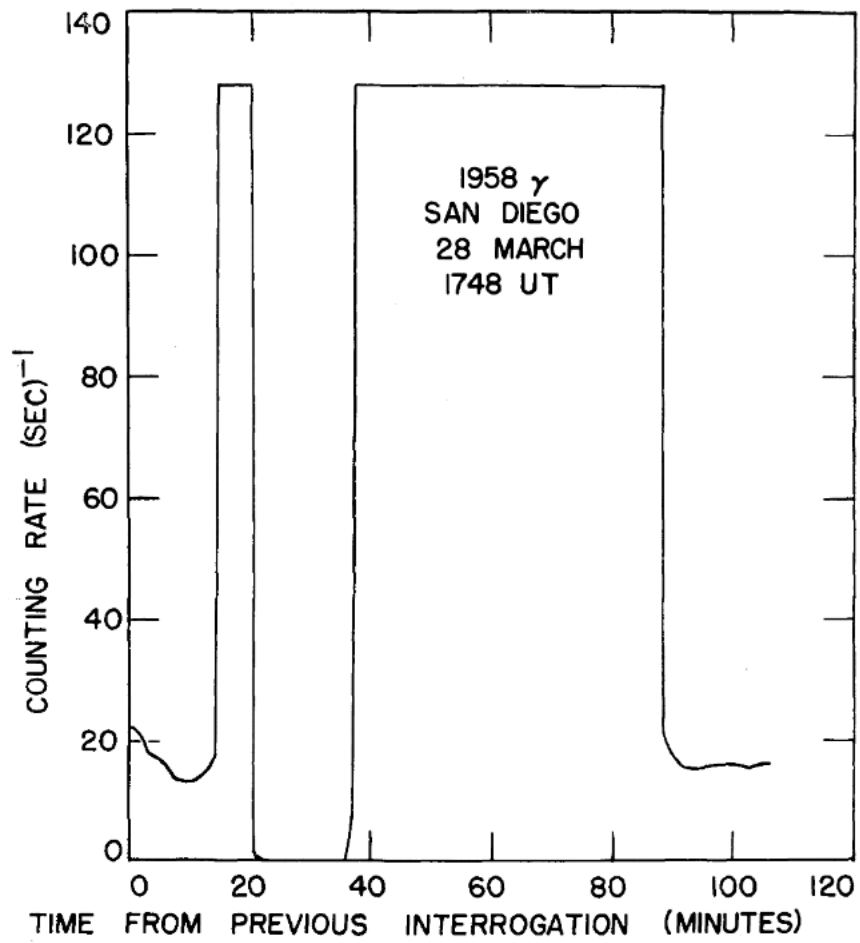
Figure 2-3: A sample of the results of a tape recorder readout by satellites 1958 alpha and gamma, near San Diego on March 28, 1748 UT. Courtesy of *Allen*, 1958.

2.2 Fields Detectors in Space

2.2.1 Magnetic Field Measurements

The outer geomagnetic field has been a subject of scientific interest and inquiry for more than 150 years (e.g., *Cahill*, 1963). The early experimental investigations measured the outer geomagnetic field using indirect methods, including the observations of magnetic fluctuations at the surface magnetic observatories. From the studies of magnetic storms and auroras, the outer geomagnetic field was found related to solar activity. In particular, in early 1930s, Chapman and Ferraro had attempted to explain the initial phase of a geomagnetic storm from the surface magnetic observations. The observations of magnetic fluctuations at the surface magnetic observatories included an enhancement in the horizontal component of the geomagnetic field.

Chapman and Ferraro attributed the field signature to the interaction of the geomagnetic fields with an electrically-conducting flow of neutral, charged gas beam originating from the Sun at the time of a solar flare. The argued that the interaction between the two environments compressed the geomagnetic field on the sunlit side of the earth and caused an increases in the horizontal component of the field (*Chapman & Ferraro*, 1931). Later studies, including those by James Wynne Dungey and Eugene Newman Parker, discovered that the geomagnetic field compression was not limited to the episodes of geomagnetic storm (e.g., *Dungey*, 1954; *Parker*, 1958). Instead, it was suggested that a steady flow of charged particles is continually emanating from the sun, streaming through the interplanetary environment, and interacting with the sunlit side of the geomagnetic field. The interaction with the geomagnetic field, during 'quiet' times, was believed to cause the compression of the sunlit side of the geomagnetic field to distances ranging from 5 to 10 earth radii. The interaction further caused a cavity in the solar wind that extend to considerable distances. The solar wind pressure also forced the dark side geomagnetic fields into an elongated tail-like structure.

Early satellite magnetic experiments were designed and set to study the structure and the boundary of the geomagnetic field. The magnetometers aboard the satellites were designed to measure within a large range of magnetic field magnitudes spanning 1 to 60, 000 nT to measure interplanetary and surface magnetic fields, respectively. The magnetometers were capable of recording at rates up to several thousand cycles per second. The instruments were further required to be light-weight and immune to environmental and launch noise. Some of the early

magnetometers include the search coil, the saturable core (fluxgate), the proton precession, and the Rubidium vapor magnetometers. Magnetometers have travelled across and beyond our solar system with discoveries, including a subsurface ocean at Europa, Jupiter's moon, with Galileo (*Kivelson et al.*, 2000) and the heliosheath with Voyager 1 (*Burlaga et al.*, 2013).

2.2.2 Electric Field Measurements

Direct measurements of electric fields in space involved measuring the potential differences between two conductors and dividing by the separation between the two conductors. The technique is termed the 'double probe.' Indirect methods measure the change in signal in potential analyzers or ion drift meters from controlled plasma releases (*Haerendel et al.*, 1967) or by tracing electron drift trajectories via the 'electron-drift technique' (*Paschmann et al.*, 1998).

Different measurement techniques provide advantages and disadvantages. Direct measurements of electric fields are made in environments, such as thin and hot plasmas, that can be easily disturbed by the measuring device. On the other hand, indirect measurements are selective in that they only measure a certain component of electric field and can only be utilized in particular environments where certain conditions are met (*Mozer*, 2016).

2.3   Magnetospheric Multiscale Mission

Magnetospheric Multiscale (MMS), a flagship NASA mission was launched on March 12, 2015. MMS is a solar-terrestrial probe constellation comprising four identically instrumented spacecraft designed to use Earth's magnetosphere as a laboratory to study the microphysics of three fundamental plasma processes: magnetic reconnection, energetic particle acceleration, and turbulence (*Burch, Moore, et al.*, 2016). These processes occur in all astrophysical plasma systems but can be studied in situ only in our solar system and most efficiently only in Earth's magnetosphere, where they control the dynamics of the geospace environment and play an important role in the processes known as "space weather."

2.3.1 Mission Objectives

MMS strives to determine the processes that cause magnetic field lines to reconnect in a collisionless plasma. The MMS results will reveal the mechanisms at play far beyond the Earth's magnetosphere from astrophysical environments such as comet-tail disconnection events, magnetar flares, supernova ejections, and dynamics of neutron-star accretion disks to magnetic-confinement fusion devices in which magnetic reconnection is a limiting factor in achieving and maintaining electron temperatures high enough to initiate fusion.

The MMS mission will focus on questions about reconnection at the Earth's magnetosphere. In particular, MMS will investigate the kinetic processes occurring in the electron diffusion region that are responsible for reconnection and that determine how it is initiated. MMS will further our understanding of the larger impacts of magnetic reconnection by placing the microphysics into the context of the broad spectrum of physical processes associated with reconnection. The MMS results will also help to inform reconnection theories and models.

2.3.2 Spacecraft Specifications

Each of the four MMS satellites has an octagonal form factor with approximately 3.5 meters in width and 1.2 meters in height. During science operations, the satellites will maintain a rotational spin of 3 rotations per minute. Each satellite contains 8 deployable booms. Four booms are 60 meter long wires extended in the spin plane to help hold in place the electric field sensors. Additional electric field sensors are mounted on two 12.5 meter booms along the axial plane. The

magnetometers are also separated from the spacecraft bus by two 5 meter booms that are extended in the spin plane.

The attitude control system insures accurate positioning of the satellites to within $\pm$ 0.5 degree error during science operations. This is achieved via the use of star sensors and sun sensors, and accelerometers which provide attitude and acceleration measurements, respectively. The actuation for both small formation maintenance maneuvers and large apogee raise maneuvers is performed by the thrusters which include a mono-propellant blowdown system with 12 thrusters. Each satellites stores up to 360 kg of propellant in four titanium tanks per spacecraft.

The spacecraft electrical operations are powered by batteries. The batteries are re-charged by 8 identical body-mounted solar array panels that are electrostatically and magnetically clean. The battery specifications are particularly selected to carry out the mission operations during the 4 hour eclipses. The thermostatically controlled heaters keep the bus and the on-board instruments at a thermally-stable status. The MMS spacecraft communicated with the ground-based data stations over a single S-Band frequency for uplink and a single S-Band frequency for downlink.

Orbit determination is performed using on-board signal global positioning system (GPS) processing. Each satellite including instruments, fuel, and margin has a mass of approximately 1,250 kg and a power budget of approximately 318 watts.

2.3.3 Scientific Instrumentation

The four MMS spacecraft carry identical instrument suites of plasma analyzers, energetic particle detectors, magnetometers, and electric field instruments. The four spacecraft are also equipped with a spacecraft charging system, called the active spacecraft potential control (ASPOC) to quantify and avoid any interference with the highly sensitive measurements required in and around the diffusion regions.

Each MMS observatory carries 11 scientific experiments developed at multiple institutions around the world. The majority of the scientific instruments are installed inside the observatory. The instruments include 25 separate sensors. The scientific instruments are divided into three suites: a) Hot plasma Suite, b) Energetic Particles Detector Suite, and c) Fields Suite.
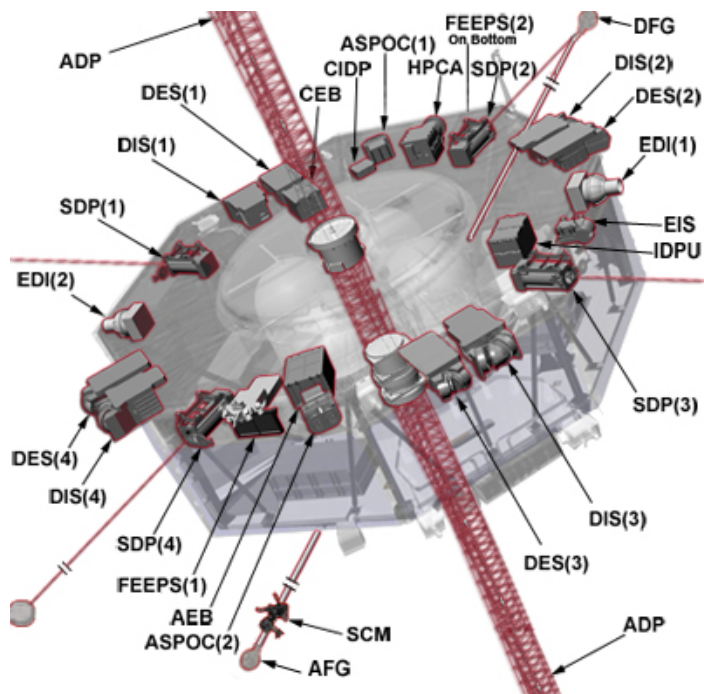
Figure 2-4: The MMS spacecraft instrument suites. The image is borrowed from the official NASA MMS website.

2.3.3.1 Hot plasma Suite

The main objective of the Suite is to observe the nature of the plasma during magnetic reconnection. The hot plasma suites includes the fast plasma investigation (FPI) and hot plasma composition analyzer (HPCA) instruments. The FPI instrument was developed to measure the differential directional flux of magnetospheric electrons and ions. The high temporal resolution electron and ion measurements are designed to resolve kinetic-scale plasma dynamics. To achieve this, four dual 180-degree top hat spectrometers for electrons (dual electron spectrometers; DES) and four dual 180-degree top hat spectrometers for ions (dual ion spectrometers; DIS) are distributed around the four MMS spacecraft. The eight spectrometers for each species provide 4pi steradians field-of-view. The energy per charge sampling provides a broad range from 10 eV/q to 30 keV/q (*Pollock et al.*, 2016). FPI is able to provide the velocity-space distribution of electrons and ions with a time resolution of 30 ms and 150 ms, respectively. As shown in Figure 2-4, each satellite also contains one HPCA instrument which measures the composition-resolved velocity-space distribution of ions from 1 eV to 40 keV with time resolution of $10 - 15$ seconds (*Young et al.*, 2016).

2.3.3.2 Energetic Particles Detector Suite

Each MMS satellite is also equipped with the energetic particle detector (EPD) including one energetic ion spectrometer (EIS) and two all-sky particle samplers called the fly's eye energetic particle sensor (FEEPS). The EDP instruments will sense remotely the regions where reconnection occurs and determine how reconnection processes produce such large numbers of energetic particles. These instruments measure the energy-angle distribution and composition of ions (20 to 500 keV) at a time resolution of < 30 seconds, the energy-angle distribution of total ions ($45 - 500$ keV) at a time resolution of < 10 seconds, and the coarse and fine energy-angle distribution of energetic electrons ($25 - 500$ keV) at time resolutions of < 0.5 and < 10 seconds, respectively (*Mauk et al.*, 2016).

2.3.3.3 Fields Suite

The fields investigation is crucial for the study of the change in magnetic field configuration during magnetic reconnection. The fields suite includes a sensor suite consisting of two axial and four spin-plane double-probe electric-field sensors (ADP and SDP), two flux-gate magnetometers (AFG and DFG), a search-coil magnetometer (SCM), and two electron drift

instrument (EDI) per MMS spacecraft. The sensors are mounted on extended booms to avoid potential measurement aliasing. The DC magnetic field measurements have a resolution of 10 ms, and the DC electric field is measured at 1 ms. The magnetic and electric plasma waves are measured up to 6 kHz and 100 kHz, respectively (*Torbert, Vaith, et al.*, 2016).

Chapter 3: Global Magnetospheric Simulations

The interaction of the sun with the planetary bodies is a complex natural system consisting of numerous interconnecting components. The transfer of solar wind's mass, momentum, and energy to the planetary magnetosphere, ionosphere, and upper atmosphere can impact the systems in non-trivial ways. The capability to model and simulate the planetary interactions with the solar wind will improve our understanding of how different components of the system response to the solar wind and will further empower us to predict space weather phenomena. The space weather phenomena can impact many aspects of our technological civilization, including determining the success, reliability, and health of manned and unmanned air and space missions.

3.1 Magnetohydrodynamic (MHD) simulations

The early multiscale magnetospheric models involved two and three-dimensional generalized magnetohydrodynamic (MHD) simulations of cometary environments and their interactions with the solar wind (*Schmidt & Wegmann*, 1981; *Gombosi et al.*, 1996). With advancements in computational capabilities and techniques, including the use of adaptive grids to improve spatial resolution in high gradient regions (*Gombosi et al.*, 1994), the global magnetospheric models became more affordable and reliable. By 2006, the MHD simulations of the cometary and terrestrial magnetospheres were expanded to encompass the sun-Earth environment with the main objective 'to develop predictive models of explosive solar activity and its effect on the near-Earth space environment.'

The Space Weather Modeling Framework (SWMF) was developed at the University of Michigan including the MHD code Block-Adaptive Tree Solar-wind Roe-type Upwind Scheme (BATS-R-US) (*Powell et al.*, 1999). The framework provides a high-performance flexible framework for physics-based space weather simulations, as well as for various space physics applications. The SWMF integrates numerical models of the Solar Corona, Eruptive Event Generator, Inner Heliosphere, Solar Energetic Particles, Global Magnetosphere, Inner

Magnetosphere, Radiation Belt, Ionosphere Electrodynamics, and Upper Atmosphere into a high-performance coupled model (*Tóth et al.*, 2005).

3.1.1 MHD with Embedded Particle-in-Cell Model

While highly efficient, computational models based on a fluid description, such as MHD neglect the kinetic effects which are important for accurately reproducing important phenomena such as magnetic reconnection at the magnetopause and in the magnetotail. To address this, BATS-R-US was coupled with an implicit Particle-in-Cell (PIC) model (iPIC3D), to create an MHD model with embedded PIC regions (MHD-EPIC; *Daldorff et al.*, 2014). The semi-implicit PIC scheme removes the numerical stability constraints of explicit PIC algorithms and, therefore, enables kinetic plasma simulations at MHD time scales (*Markidis et al.*, 2010). The early investigations of the code have been compared with the Galileo's observations of Ganymede (*Tóth et al.*, 2016).

The MHD-EPIC code has also been applied to Earth's magnetosphere, in order to reproduce some of reconnection's characteristic features, including plasma jets and crescent-shaped ions and electron distributions (*Chen et al.*, 2017). As shown in Figure 3-1, *Chen, et al.* (2017) the electric field along X_{GSM} reaches nearly 15mV/m at the magnetopause side of the X-line formed near the subsolar region. The E_x along a virtual spacecraft trajectory is presented in panel *d* wherein the electric field is shown to reach a minimum on the magnetospheric side of the X-line. This negative E_x is comparable to the PIC simulations of kinetic Larmor electric field. In addition, in *panels b* and *c*, the ion and electron phase space distributions are collected in the vicinity of the X-line and in association with the Larmor electric field to further support the hypothesis that the MHD-EPIC global simulations can resolve magnetopause reconnection at the electron and ion kinetic-scale.
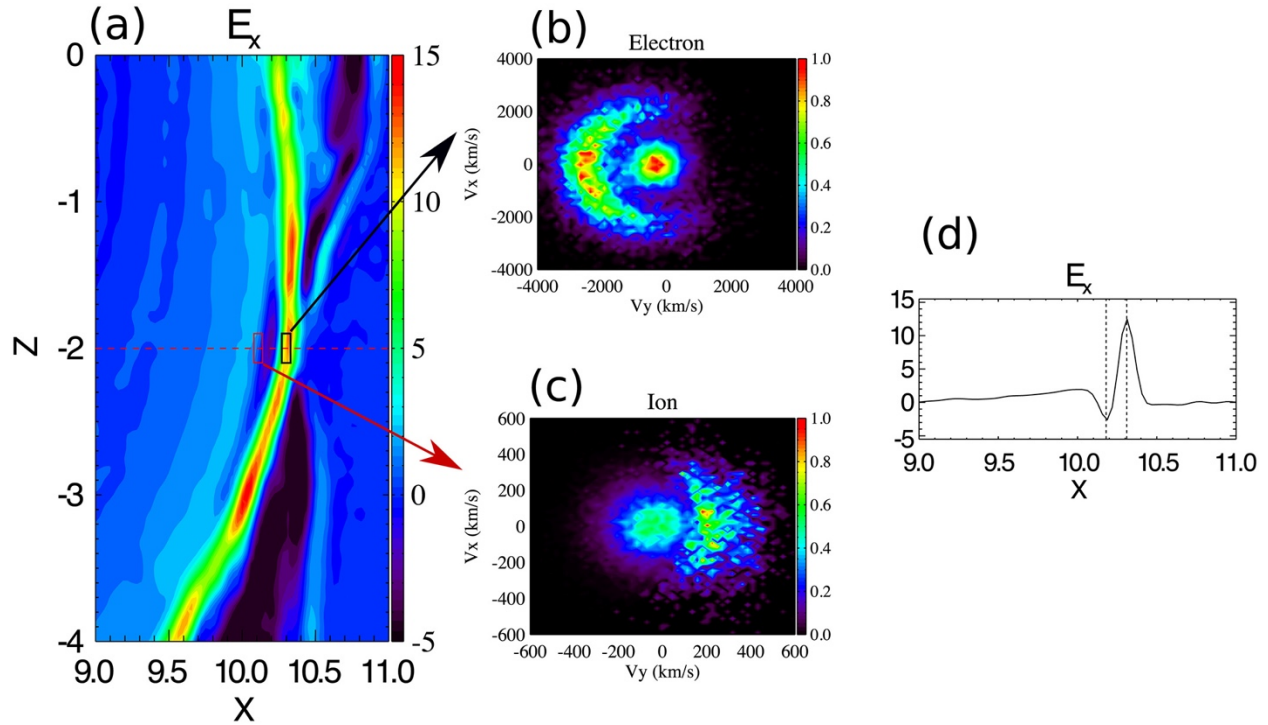
Figure 3-1: The Larmor electric field and crescent electron and ion phase space distributions (Courtesy of *Chen et al*., 2017). (a) electric field along X_{GSM}, E_x (mV/m), in the meridional plane at simulation time, t = 3,600s. (b) The normalized electron distribution in V_y−V_x phase space. The electrons are inside the black box shown in *panel a*: 10.27 R_E < X < 10.33 R_E and −0.3 R_E < Y < 0.3 R_E, and −2.1 R_E < Z < −1.9 R_E. (c) Ion phase space distribution for particles inside the red box in *panel a*: 10.08 R_E < X < 10.14 R_E and −0.3 R_E < Y < 0.3 R_E and −2.1 R_E < Z < −1.9 R_E. The phase density is normalized. (d) E_x along the red dashed line in *panel a*.

3.1.2 10-Moment Simulations to resolve electron and ion kinetics globally

Another notable attempt to resolve plasma kinetics in collisionless reconnection is the three dimensional two-fluid 10-moment simulation, which is constructed by taking velocity moments of Vlasov equations of each species, including electrons, to obtain a hierarchical set of moment equations. Conceptually, the 10-moment model is akin to a fluid version of PIC code, truncated at the second-order moment, the pressure tensor. Unlike traditional MHD simulations, the 10-moment simulations treat ions and electrons independently, and no net charge neutrality is assumed (*Wang et al.*, 2018). To achieve this, a total of 10 equations are solved for each species:

$$\frac{\partial(m_s n_s)}{\partial t} + \frac{\partial(m_s n_s u_{j,\,s})}{\partial x_j} = 0\,,$$

$$\frac{\partial(m_s n_s u_{j,\,s})}{\partial t} + \frac{\partial(P_{ij,\,s})}{\partial x_j} = n_s q_s(E_i + \epsilon_{ijk} u_{j,s} B_k)\,, \text{ and}$$

$$\frac{\partial(P_{ij,\,s})}{\partial t} + \frac{\partial(Q_{im,\,s})}{\partial x_m} = n_s q_s u_{[i,\,s} E_{j]} + \frac{q_s}{m_s}\,\epsilon_{[iml}\,_{P_{mj}]s}\,B_l\,.$$

where subscripts $s = e$, i represent the electron and ion species, respectively. The square brackets in equation the bottom equation around indices i, j, m represent the minimal sum over permutations of these indices that give completely symmetric tensors. The first-, second-, and third-order moments are defined as:

$$m\,u_{ij} \equiv m \int v_i\,f\,d\boldsymbol{v}\,,$$

$$P_{ij} \equiv m \int v_i\,v_j\,f\,d\boldsymbol{v}\,, \text{ and}$$

$$Q_{ijm} \equiv m \int v_i\,v_j\,v_m\,f\,d\boldsymbol{v}\,.$$

with f being the phase space distribution function. The code has further been used for many laboratory and space plasma physics contexts (*Wang et al.*, 2000; *Hakim*, 2008; *Dong et al.*, 2019).

     Dong et al. (2019) applied the 10-moment multi-fluid model to Mercury in three-dimensional space. The non-ideal effects, important for kinetic processes controlling the magnetic reconnection process, were resolved by including Hall effect, inertia, and tensor pressure terms in the generalized Ohm's law. A reduced ion-electron mass ratio $m_i/m_e = 25$ and a reduced speed of light c = 3000 km/s were further applied. The top panel in Figure 3-2 illustrates the simulated bow shock, magnetosheath, magnetosphere, and magnetotail under typical upstream solar wind conditions. In particular, the upstream conditions were tuned to match that of MESSENGER's second flyby on October 6, 2018 (referred to as M2). During the M2 flyby, the interplanetary magnetic field (IMF) remained steadily southward, (−15.2,8.4,−8.5) nT in Mercury-Solar-Orbital (MSO) coordinates. Other solar wind parameters include: $n = 40$ cm^{-3}, $\boldsymbol{v} = $ (−400, 50, 0) km/s, and $T = 18$ eV. In the bottom four panels (panels *a-d*), the simulation results (red) are compared with in-situ MESSENGER magnetic field observations (black). As shown, the model is able to reproduce the observed magnetic field vectors.
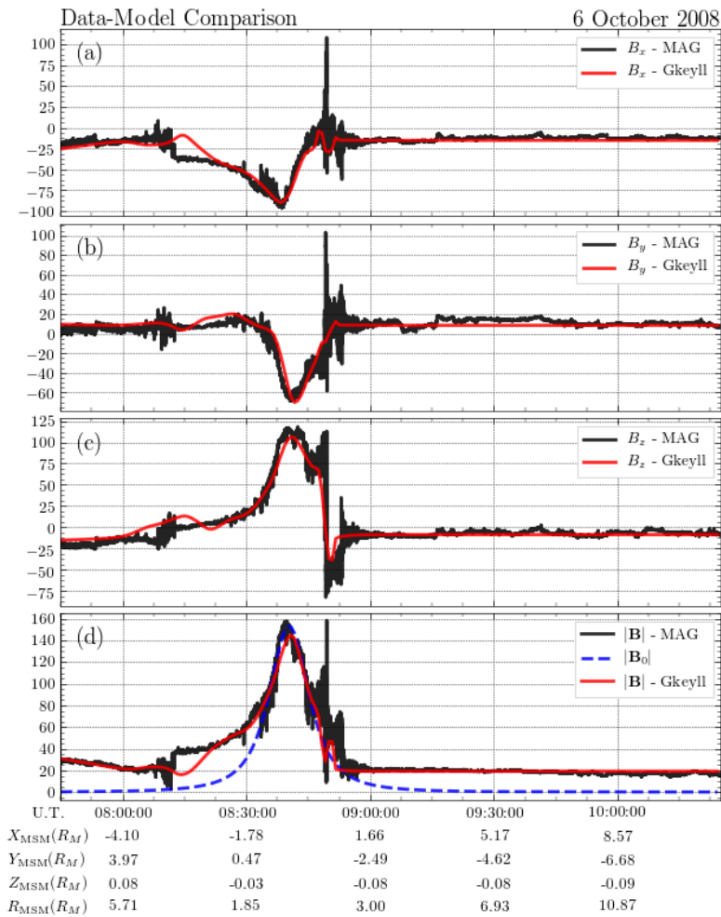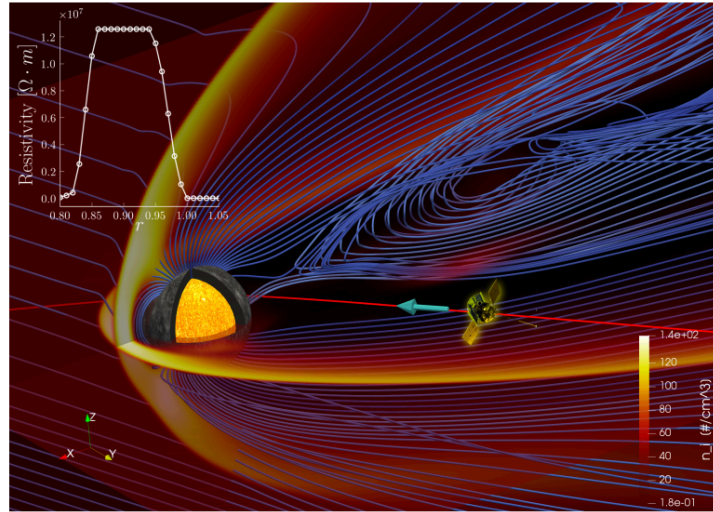
Figure 3-2: *Top*: Mercury's three-dimensional magnetosphere from the ten-moment multifluid calculation (Courtesy of *C. Dong et al.*, 2019). The color contours depict the ion density in cm^{-3}. The "hot" sphere inside Mercury represents its conducting core with a size R$_{core}$ = 0.8 R$_M$. The magnetic field lines are presented in blue. The red curve together with a cyan arrow represents MESSENGER's M2 trajectory. *Bottom*: Data-model comparison of magnetic fields along MESSENGER's M2 trajectory.

3.2 Vlasov Simulations

3.2.1 Hybrid-Vlasov Simulations to resolve ion kinetics globally

Global MHD simulations have been found to provide reliable description of large scale phenomena. However, where ion kinetics become of significance, MHD simulations become poorly-equipped to provide reliable description of the system behavior. These systems include the foreshock regions and the inner magnetosphere.

Hybrid simulations, wherein electrons are modeled as a charge-neutralizing fluid. On the other hand, ions are described by a kinetic model. Hybrid PIC simulations typically treat ions kinetically as macroparticles, while electrons are assumed to be a massless fluid (*Winske et al.*, 2003). Global scale hybrid-PIC simulations of the Earth's magnetosphere have been performed in two and three spatial dimensions (e.g., *Lin*, 2003; *Lin & Wang*, 2005). The challenge with hybrid-PIC simulations is numerical noise, particularly for deriving ion velocity distribution functions. To address the noise the number of ions introduced in the simulation frame can be increased; however, this will further drive up the computational cost of global simulations.

Instead of treating ions as particles, hybrid-Vlasov simulations use the Vlasov equation to directly model the evolution of an initial six-dimensional ion distribution function, comprising three ordinary space and three velocity space dimensions:

$$\frac{\partial}{\partial t} f(\boldsymbol{r}, \boldsymbol{v}, t) + \boldsymbol{v} \cdot \nabla_r f(\boldsymbol{r}, \boldsymbol{v}, t) + \boldsymbol{a} \cdot \nabla_v f(\boldsymbol{r}, \boldsymbol{v}, t) = 0 ,$$

where $\boldsymbol{r}$ and $\boldsymbol{v}$ are the three ordinary space and velocity space coordinates, acceleration $\boldsymbol{a}$ is given by the Lorentz force, and $f(\boldsymbol{r}, \boldsymbol{v}, t)$ is the six-dimensional phase space density of protons with mass m and charge q. The advantage of the hybrid-Vlasov method compared to hybrid-PIC simulations is the noise-free ion distribution functions. However, until recently, the cost of propagating ion distribution functions in space and time has been prohibitive.

The simulation frame consists of a three-dimensional Cartesian mesh in the ordinary space. Each ordinary-space cell contains variables describing the electromagnetic fields, as well as a three-dimensional velocity mesh describing the full six-dimensional phase-space (*Palmroth et al.*, 2013). The ion distribution function is propagated forward in time using the finite volume method

(FVM), where the volume average f is propagated forward in time by computing the fluxes at every cell face:

$$\tilde{f}(t+\Delta t) = \tilde{f}(t) - \frac{\Delta t}{\Delta r_i} \left[F_{r,\,i}\,(r_i + \Delta r_i) - F_{r,\,i}\,(r_i) \right] - \frac{\Delta t}{\Delta v_i} \left[F_{v,\,i}\,(v_i + \Delta v_i) - F_{v,\,i}\,(v_i) \right],$$

where $\boldsymbol{F_r} = (F_x, F_y, F_z) = \boldsymbol{v}\,\tilde{f}$ and $\boldsymbol{F_v} = (Fv_x, Fv_y, Fv_z) = {}^q\!/_m\,(\mathbf{E} + \mathbf{v} \times \mathbf{B})\,\tilde{f}$ are the fluxes at cell faces in ordinary and velocity spaces, respectively.

Figure 3-3 illustrates the near-Earth space in the meridional plane (XZ$_{GSE}$; *Palmroth et al.*, 2018). The upstream interplanetary magnetic field (IMF) is initialized at a 45 degree cone angle relative to the ambient plasma flow. The shocked IMF experiences a jump condition across the bow shock region, resulting in an increase in the magnetic field magnitude. The shocked plasma further generates the hot plasma population downstream of the bow shock, known as the magnetosheath. In Figure 3-4, an example non-Maxwellian ion distribution function is provided. The hybrid-Vlasov Vlasiator model can generate noise-free, non-Maxwellian ion distribution functions, unlike MHD systems wherein plasma distributions are approximated as a Maxwellian distribution.
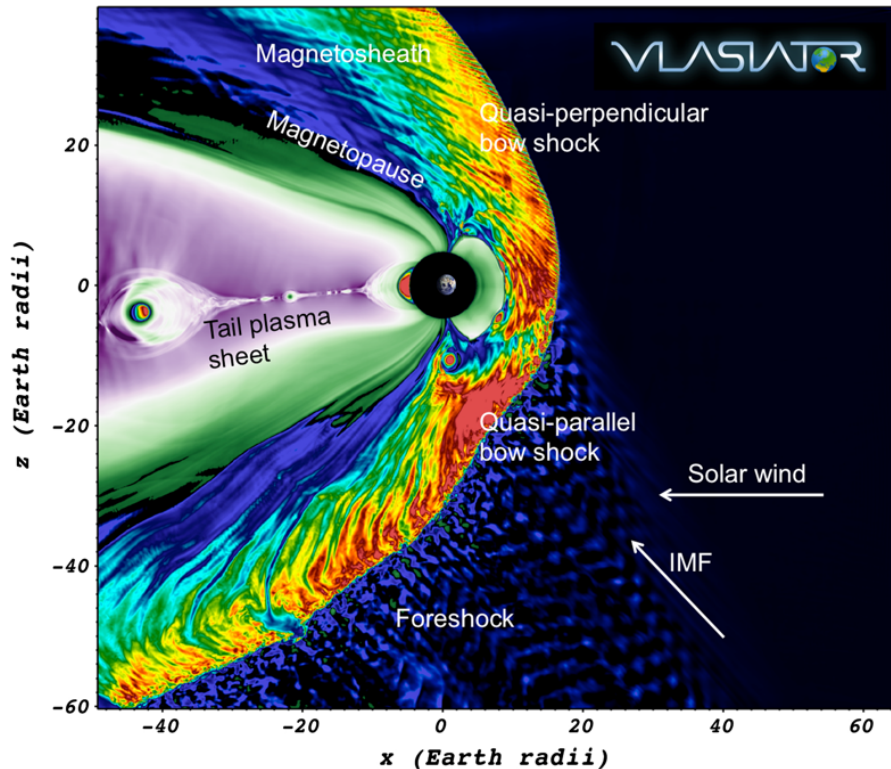
Figure 3-3: Vlasiator modelling of the magnetosphere in the noon–midnight meridian plane viewed from the morning sector (Courtesy of *Palmroth et al.*, 2018).
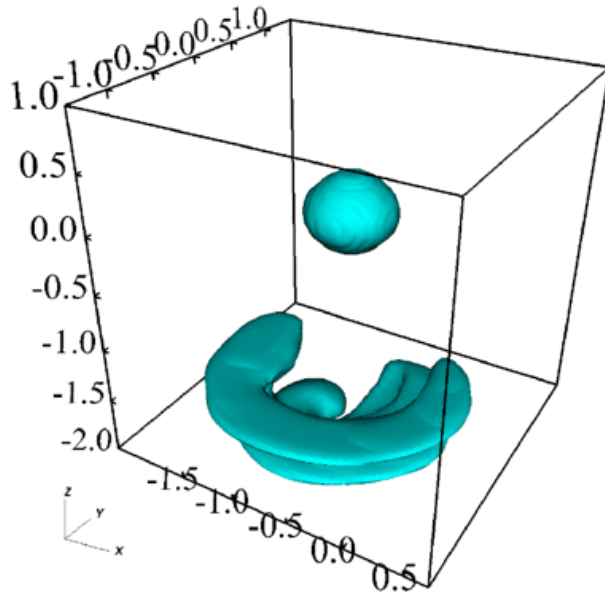
Figure 3-4: An example three-dimensional, normalized ion velocity distribution function in a transient foreshock in the magnetosheath (Courtesy of *Pfau-Kempf*, 2016). The axes indicate the velocity distribution in the Cartesian planes.

To summarize, the difference between hybrid-PIC and Vlasiator simulations is that in hybrid-Vlasov the distribution functions are evolved in time as an entity, and not constructed from particle statistics, as in hybrid-PIC simulations. This, though computationally expensive, results in the generation of noiseless distribution functions.

Chapter 4: MMS Examination of FTEs at the Earth's Subsolar Magnetopause

This Chapter is adopted from Akhavan-Tafti, M., Slavin, J. A., Le, G., Eastwood, J. P., Strangeway, R. J., Russell, C. T., et al. (2018). MMS examination of FTEs at the Earth's subsolar magnetopause. Journal of Geophysical Research: Space Physics, 123, 1224– 1241. https://doi.org/10.1002/2017JA024681.

4.1. Introduction

Magnetic reconnection is the underlying physical process responsible for the release of energy stored in magnetospheric magnetic fields that powers plasma heating and acceleration (e.g., *Masaaki Yamada et al.*, 2010; *Gonzalez & Parker*, 2016b). Flux Transfer Events (FTEs) are transient signatures of magnetic reconnection. FTEs are twisted open flux tubes associated with the transfer of plasma from the magnetosheath into the magnetosphere. FTEs are identified by a bipolar signature in the component of magnetic field normal to the magnetopause together with a maximum in the axial component of magnetic field (*Russell & Elphic*, 1979; *Rijnbeek et al.*, 1984). The *Berchem & Russell* (1984) statistical study of ISEE observations concluded that FTEs are formed at low latitudes and move to the flanks and to high latitudes and toward the flanks due to the anti-sunward magnetosheath flow and $J \times B$ magnetic tension forces (e.g., *Kawano & Russell*, 1997; *Omidi & Sibeck*, 2007).

According to the magnetohydrodynamic (MHD) model of magnetic reconnection, low reconnection rates are expected in highly elongated current sheets (*Eugene N Parker*, 1957). However, 2D kinetic simulations have argued that laminar Sweet-Parker layers such as the magnetopause become unstable to the formation of plasmoids with increasing Lundquist number, $S \propto V_A L_{SP} \eta^{-1}$, where $V_A \propto B \rho^{-1/2}$ is the Alfven speed, L_{sp} is the Sweet-Parker current sheet thickness, and η is the resistivity (*Daughton et al.*, 2009; *Huang & Bhattacharjee*, 2010, 2013). Plasmoids or magnetic islands are two-dimensional realizations of three-dimensional flux ropes.

Plasmoid instability leads to the formation of secondary plasmoids which serve to enhance the reconnection rate (*Manheimer & Lashmore-Davies*, 1984; *Dieter Biskamp*, 2000). Various studies have assessed the characteristics and the factors on which plasmoid instability, secondary island formation, and 'fast' reconnection depend (e.g., *Vishniac*, 1995; *Eastwood et al.*, 2007; *Bhattacharjee et al.*, 2009; *Cassak et al.*, 2009; *Cassak & Drake*, 2009; *Moser & Bellan*, 2012; *Su et al.*, 2013; *Luca Comisso & Grasso*, 2016).

The transition between the slow and fast reconnection regimes is predicted to take place at the ion inertial length, d_i, (*Simakov & Chacón*, 2008) where the thinning of the Sweet-Parker current layer (electron diffusion region (EDR) in the context of kinetic simulations) becomes quickly unstable to plasmoid formation leading to larger variations in the reconnection rate (*Fujimoto*, 2006; *Daughton et al.*, 2006; *Karimabadi et al.*, 2007; *Phan et al.*, 2007; *Daughton et al.*, 2009; *Wang et al.*, 2016). Theoretical kinetic models and resistive MHD simulations have been employed to investigate the dynamics and distribution of plasmoids (e.g., *Richard et al.*, 1989; *Y.-M. Huang & Bhattacharjee*, 2010, 2013).

Due to the development of tearing mode instability, multiple X-line reconnection, a series of current filaments, can occur. Tearing mode instability is a particular type of resistive instability arising from the decoupling of magnetic field lines from the fluid (*Furth et al.*, 1963). Multiple X-line reconnection gives rise to the generation of multiple flux ropes which are termed flux transfer events at the magnetopause (*Lee & Fu*, 1985). *Finn & Kaw* (1977) and *Pritchett & Wu* (1979) envisioned a configuration in which, due to finite resistivity, coalescence instability leads to a merging of multiple plasmoids into a single plasmoid via secondary reconnection (*Wang et al.*, 2016). For the purposes of this study, the magnetic reconnection occurring between two merging flux ropes is called 'secondary reconnection' (*Wang et al.*, 2016). *Fermo et al.* (2010) studied in 2D the role of coalescence in the growth of magnetic islands. Here, coalescence is the merger of two smaller magnetic islands through reconnection into a single larger island. *Fermo et al.* (2011) provided observational evidence, based on Cluster FTE observations, to support this model of magnetic island, or in 3D, flux rope growth.

Simulations and observations have indicated the existence of a more developed reconnection event in the outflow region of the primary X line (*Divin et al.*, 2007; *Sitnov et al.*, 2009). Kinetic 2D simulations of coalescence show that after the collapse of an intermediate X-line, neighboring

magnetic islands are pushed together and merge via reconnection to form larger ones (*Daughton et al.*, 2011). This resulting magnetic island in turn expands by progressively cooling down from the outer layer inwards, until pressure gradient between the internal and external plasmas is stabilized resulting in a temporarily stable condition (*Cazzola et al.*, 2015). This process is repeated and larger scale islands are formed. Similarly, at the dayside magnetopause, multiple FTEs are believed to form due to the reconnection process and evolve into larger structure over time (*Lee & Fu*, 1985). Previous studies have determined the size distribution and flux content of FTEs (e.g., *Wang et al.*, 2005; *Hasegawa et al.*, 2006, 2010; *Fermo et al.*, 2011; *Eastwood et al.*, 2012, 2016; *Pu et al.*, 2013; *Wang et al.*, 2016). These results indicate that FTEs are one to few Earth radii in size and contain 1-10 MWb in magnetic flux. However, these measurements are mostly gathered at higher altitudes and away from the subsolar region.

This study employs the Lepping-Burlaga constant-α flux rope model to determine the radius of FTEs and the impact parameter (IP) of the individual MMS trajectories through the flux ropes observed at the Earth's subsolar region and evaluates the cogency of this model using the Magnetospheric Multiscale (MMS) mission's high spatial and temporal resolution plasma and fields measurements. Physical properties of FTEs are investigated and the role of coalescence in FTE growth is emphasized. Our results indicate that 1) small-scale FTEs are observed at the magnetopause more frequently than previously reported, 2) electric currents inside growing FTEs help reduce magnetic forces over time, and 3) plasma density and core magnetic field are inversely related inside evolving FTEs.

4.2. Experimental Approach

4.2.1. Instrumentation and Data

MMS was launched in 2015, and it consists of four identical satellites with unprecedented temporal and spatial resolutions (*Burch et al.*, 2016). MMS orbits at an inclination angle of 28˚ with geocentric apogee and perigee of 12 and 1.2 R_E, respectively. The first phase of the mission targeted the Earth's dayside magnetopause at low latitudes. For this phase, regions of interest with radial distances greater than 9 R_E were identified during which all instruments are operated at their fastest cadence, producing burst-mode data.

The four spacecraft were maintained at an average tetrahedron size of ~10 km (~ 6 electron inertial lengths based on a plasma density of 12 cm^{-3}). The fast plasma experiment (FPI) data were captured at 30 ms cadence for electrons and 150ms for ions (*Pollock et al.*, 2016). FPI moments are constructed from all-sky electron and ion distributions. The fluxgate magnetometer (FGM) operates at 128 vectors per second (*Russell et al.*, 2016).

The subsolar region was targeted to investigate FTEs shortly after they are generated by reconnection (*Fuselier et al.*, 2016). In this study, the subsolar region is defined as 12 ± 22.5' Local Time and $X_{GSM} > 8$ R_E. Figure 4-1 illustrates the spacecraft trajectories (grey lines) as well as burst-mode intervals (red lines) in the Geocentric Solar Magnetospheric (GSM) equatorial plane for this region. Model magnetopause minimum and maximum boundaries are also plotted for reference (*Shue et al.*, 1998). Our study uses the measurements taken during 55 orbital passes (11/03/2015 — 12/28/2015) and a total of 279 burst-mode intervals. The average burst-mode interval was 2.25 min in duration.
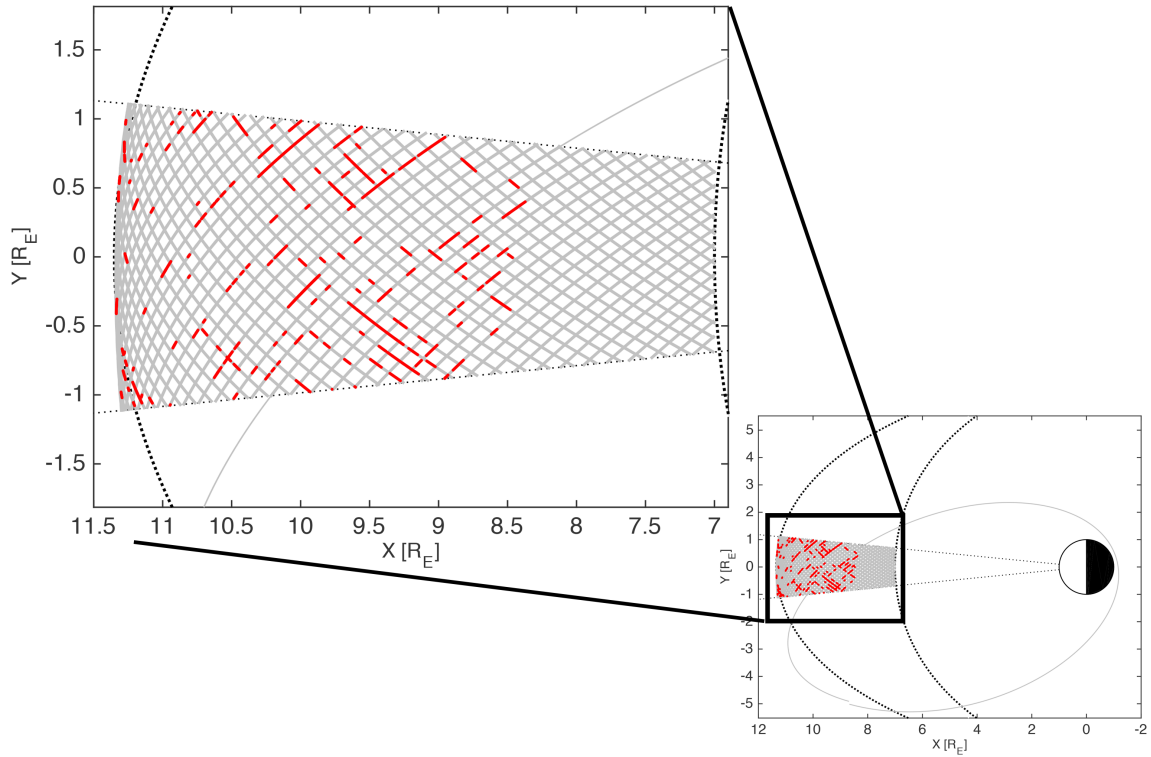
Figure 4-1: MMS Regions of interest (12 ± 22.5' MLT and X>7 R_E) in GSM coordinates (equatorial plane); shown in red are the Burst-mode intervals where the FPI time resolution is 30 ms for electrons and 150 ms for ions and FGM sample rate is 128 vectors/s. The grey lines are the spacecraft trajectories during November 03, 2015 through December 28, 2015.

4.2.2. Methods

Flux ropes are identified with their bipolar signature in the normal component of the magnetic field, corresponding to a peak in the axial component of the magnetic field. In LMN coordinates, these components translate into B_L and B_M, respectively (*Russell & Elphic*, 1978). The peak in B_M insures the presence of a strong axial magnetic field component which is the distinctive characteristic distinguishing helical flux ropes from other similar magnetic structures.

The transformation from the GSM coordinate system into the LMN coordinate system was achieved via applying minimum variance analysis (MVA) of the magnetic field (*Sonnerup & Cahill Jr*, 1967; *Sonnerup & Scheible*, 1998; *Xiao et al.*, 2004; *Teh et al.*, 2017). MVA was performed on 30s, 60s, 120s, and full intervals of burst-mode magnetic field time series data to identify FTEs. Figure 4-2 provides a sample MMS FTE observed by the four probes at 13:04:34 UTC on 16 October 2015 at (8.3, 7.1, -4.8) R_E in GSM. During this encounter, the enhancement in $|\mathbf{B}|$ correlated with bipolar perturbation of B_L (positive-then-negative). *Eastwood et al.* (2016) originally reported the observation of this ion-scale FTE several minutes before encountering an electron dissipation region (*Burch et al.*, 2016).

The high time cadence of FGM together with small-scale tetrahedron and the very accurate and precise positioning knowledge of the MMS spacecraft enable multi-dimensional spatial gradient methods (*Harvey*, 1998). Here, we investigate stress balance inside FTEs using the current density computed by curlometer technique (*Dunlop et al.*, 1990; *J. A. Slavin, Lepping, Gjerloev, Goldstein, et al.*, 2003). Current density is also calculated directly using high quality FPI data according to the formula $\mathbf{J} = e\,(n_i\,\mathbf{v}_i - n_e\,\mathbf{v}_e)$ where n and v are the zeroth (number density) and first (bulk velocity) plasma moments, respectively. Figure 4-2c-e show the plasma moment profiles. For comparison, the linear barycentric value of $\mathbf{J}_{FPI}$ is calculated with Taylor series expansion (first-order approximation) of current density with respect to a reference spacecraft α. The term barycenter refers to the center of mass of the tetrahedron:

$$\bar{\mathbf{B}} = \mathbf{B}_\alpha + [\nabla\mathbf{B} \cdot (\bar{\mathbf{r}} - \mathbf{r}_\alpha)] \qquad (1)$$

where α indicates the satellite's number (α = 1, …, 4) and $\nabla\mathbf{B}$ is the gradient of the magnetic field vector:

$$(\nabla B)_{ij} = \frac{1}{N^2} \left[\sum_{\alpha \neq \beta} (B_{\alpha i} - B_{\beta i})(r_{\alpha k} - r_{\beta k}) \right] R_{kj}^{-1} . \qquad (2)$$

Here, r and N are the position vector and the number of spacecraft, respectively, and R_{kj}^{-1} is the inverse of the *volumetric tensor*:

$$R_{kj} = \frac{1}{N} \sum_{\alpha=1}^{N} r_{\alpha k} \, r_{\alpha j} . \qquad (3)$$

The current density profile, denoted as J_{FPI} in Figure 4-2f, is derived from a single-probe plasma measurements (MMS2). The ratio of perpendicular to parallel components of current density helps analyze stress balance inside the FTE (*Y. Zhao et al.*, 2016):

$$R_J = |\mathbf{J}_\perp| / |\mathbf{J}_{//}|$$

where $J_{//} = |\mathbf{J} \cdot \mathbf{B}| / |\mathbf{B}| = J \, cos(\theta_{JB})$ and $J_\perp = \sqrt{|\mathbf{J}|^2 - (J_{//})^2} = |\mathbf{B} \times (\mathbf{J} \times \mathbf{B})| / |\mathbf{B}|^2$. In other words,

$$R_J \equiv arctan(\theta_{JB}). \qquad (4)$$

In Figure 4-2g, the blue and green lines are calculated using current densities that are computed from the curlometer technique and all four FPI measurements at the barycenter, respectively, while the red line only takes into account the FPI measurements from a single spacecraft. Small R_J along the cross section of this FTE indicates that the structure is magnetically force-free (i.e. $\mathbf{J} \times \mathbf{B} = 0$).

The force-free flux rope model (*Burlaga*, 1988; *Lepping et al.*, 1990; *Slavin et al.*, 2003) can be applied to gain quantitative information about the size and flux content of FTEs. The model assumes flux ropes to be i) cylindrically symmetric, and ii) force-free ($\mathbf{J} \times \mathbf{B} = 0$ and $\nabla P = 0$ where P denotes thermal pressure). Thus, current density, $\mathbf{J}$, is linearly proportional to magnetic field, $\mathbf{B}$, and the force law has the following solutions (*Lundquist*, 1950):

$B_R = 0,$ Radial component of **B**

$B_A = J_0(\alpha r') B_0,$ Axial component of **B**

$B_T = J_1(\alpha r') B_0 H.$ Tangential component of **B**
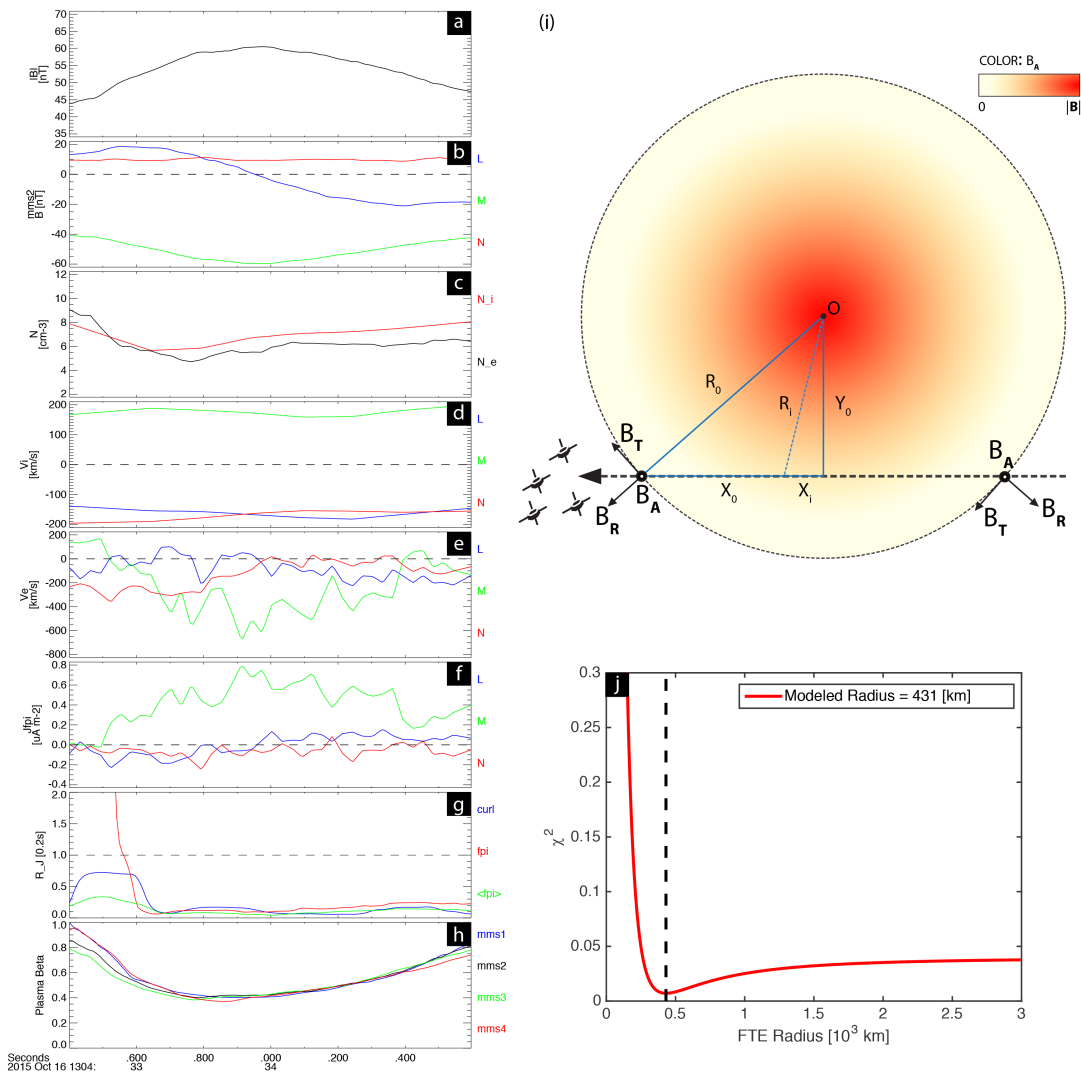
Figure 4-2. The Eastwood 2016 event. *a)* total magnetic field, *b)* Magnetic field components in the LMN coordinates, *c)* ion (red) and electron (black) number densities, *d)* ion velocity in LMN coordinates, *e)* electron velocity in LMN coordinates, *f)* current density components, *g)* R_J (curlometer technique: blue, one spacecraft FPI current density: red, FPI current density at the barycenter: green), *h)* plasma beta. *i)* a cross-sectional view of a flux rope. The dashed line represents the trajectory of the spacecraft through the flux rope. The Closest Approach is indicated by Y_0 and R_0 and X_0 are the flux rope radius and the distance from the closest approach to the edge of the flux rope, respectively. X_i and R_i increase incrementally as the spacecraft travels farther toward the edge of the flux rope. *j)* Chi-square profile of the second *Eastwood et al.* [2016] event. The estimated FTE radius is comparable to that previously reported (~ 550 km).

where J_0 and J_1 are zeroth and first order Bessel functions, respectively, and B_0 is the magnitude of the core field along the axis of flux rope, H is the handedness, and r' describes the fractional radial distance from the center of the flux rope, equal to zero at the core and one at the edge. The core of the structure is where the magnetic field magnitude is most significant and the edge of the structure refers to the outer boundary of the flux rope where magnetic field magnitude drops to a minimum and the normal component of the magnetic field peaks. The value at which J_0 reaches zero is a constant $\alpha = 2.4048$.

Previous statistical studies of the size and flux content distribution of FTEs relied on an implicit assumption that the spacecraft passes through the center of the structure (e.g., *Fermo et al.*, 2011). Here, we employ the force-free model to infer the impact parameter (i.e. distance from the center of the structure at the closest approach), radius, peak core magnetic field magnitude, and flux content of FTEs. Appendix A lists the steps for computing the size and flux content of flux ropes. Figure 4-2i provides a schematic depiction of an arbitrary pass through a flux rope by MMS spacecraft. In this figure, Y_0 is the impact parameter and R_0 is the actual flux rope radius. For more detail, see Appendix A. Figure 4-2j shows the chi-square profile of observed magnetic field components with respect to a cylindrically-symmetric constant-α flux rope model for the *Eastwood et al.* (2016) event. The modeled characteristic radius for this FTE is the radius at which the global extremum of the chi-squared profile is located.

4.3. Results and Discussion

4.3.1. FTE size distribution

During a 2-month dayside phase of MMS (11/03/2015—12/28/2015), when MMS sampled the subsolar magnetopause, 63 FTEs were identified using the visual criteria listed in the Methods section. All FTEs were required to be detected by all four spacecraft, but this was generally the case due to the small spacecraft separation. Using the force-free model described in Appendix A, the size and flux content of each FTE was determined.

Our approach takes into account the trajectory of the spacecraft with respect to the center of the FTE. Previous studies of FTEs have been limited by the uncertainty associated with assuming that the spacecraft goes straight through the center of the FTE along the surface of the magnetopause. That assumption is especially prone to error for large impact parameters (i.e. trajectories passing farther away from the center of the FTE). Here, we have constrained our selection criteria to only include FTEs with impact parameter smaller than 0.5 (IP ≤ 0.5) and the Pearson's chi-squared test value below $\chi^2 \leq 0.1$. Figure 4-3 summarizes the distributions of IP and chi-square parameters for the 63 FTEs detected in the MMS burst-mode intervals. Of these events, eight had impact parameters larger than 0.5 and chi-squared fit values larger than 0.1, thus were eliminated from our study.
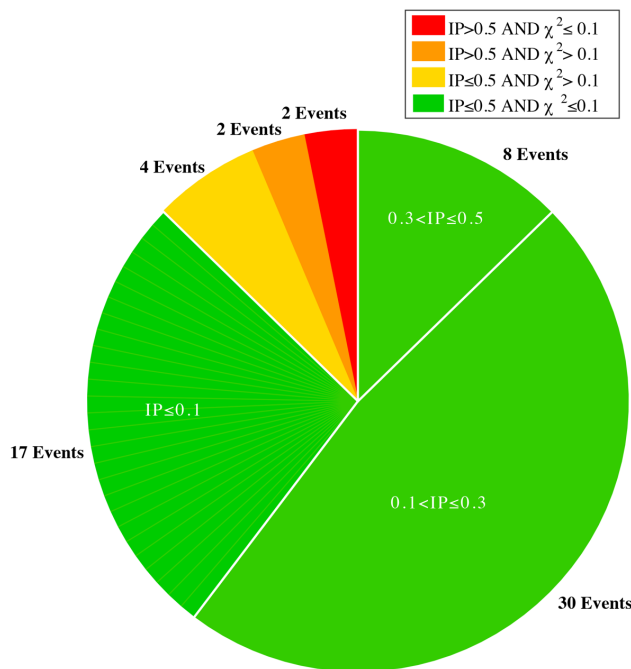
Figure 4-3. Distribution of the identified FTE data where green indicates the properties of the events included in this study: impact parameter (IP) smaller than 0.5 and chi-squared values lower than 0.1.

Figure 4-4a is a histogram of the size distribution of 1098 FTEs observed by Cluster mission between 2001 and 2003 where the assumption was that the Cluster spacecraft trajectories intersected the central axis (i.e., IP=0) (*Wang et al.*, 2005; *Fermo et al.*, 2011). The black dashed curve is an exponential fit of nominal diameter of 5300 km. Figure 4-4b demonstrates the histogram of the normalized size distribution of MMS observations of the 55 FTEs that met all our criteria. As previously indicated, the FTE size is determined using the force-free model. The red curve corresponds to an exponential fit with the nominal diameter of 1700 ± 400 km and $30 \pm 9\ d_i$, where d_i is the average ion inertial length inside each FTE. The black dashed curve represents the results from the Cluster observations. The MMS spacecraft observe small-scale FTEs at the subsolar magnetopause more frequently than Cluster satellites at high latitudes. This results in a decaying exponential fit whose mean is at least three times smaller than previously reported. It is
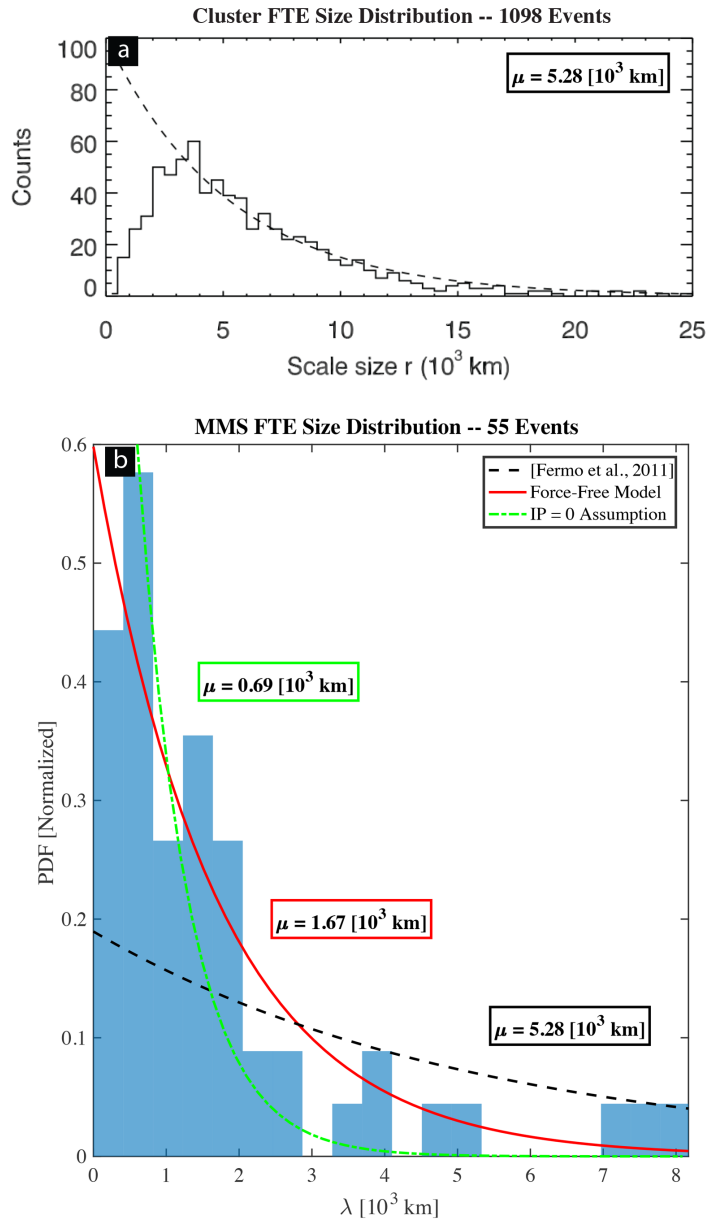
Figure 4-4: *a)* Distribution of the diameters of 1098 Cluster flux transfer events with an exponential tail fit with $\lambda_0 = 5280$ km to the tail of the distribution assuming IP = 0 for all crossings (*Fermo et al.*, 2011), and *b)* A distribution of the diameters of 55 flux transfer events with IP < 0.5 and $\chi^2 < 0.1$. The solid red line is the exponential fit of $\lambda_0 = 1670$ km. The black dashed curve corresponds to the FTEs observed by Cluster, as shown in panel *a*. The green curve is the exponential fit for the 55 events while assuming IP = 0 for all crossings.

important to note that the IP = 0 assumption underestimates both the diameter and the strength of the magnetic field in the core. The green curve corresponds to MMS observations assuming IP = 0 for all crossings. As expected, this assumption results in a mean diameter that is artificially lower than the actual value.

The relative size distribution of the 55 FTEs at the subsolar region are depicted in Figure 5a. The circles illustrate the diameter and the spatial distribution of the events in the equatorial plane. The mean diameter is 1700 km which corresponds to ~30 ion inertial lengths. Ion-scale FTEs are observed at the subsolar region shortly after they are formed by reconnection. On the other hand, massive FTEs are observed farther away from the subsolar magnetopause. Figure 4-5b shows a histogram of the magnetic flux content of all FTEs. Flux content is calculated using the modeled values of core magnetic field and FTE radius (See Appendix A-viii). The exponential decay fit (red curve) has a mean of 100 ± 30 kWb. This average flux content is nearly 3 orders of magnitude smaller than previously reported.
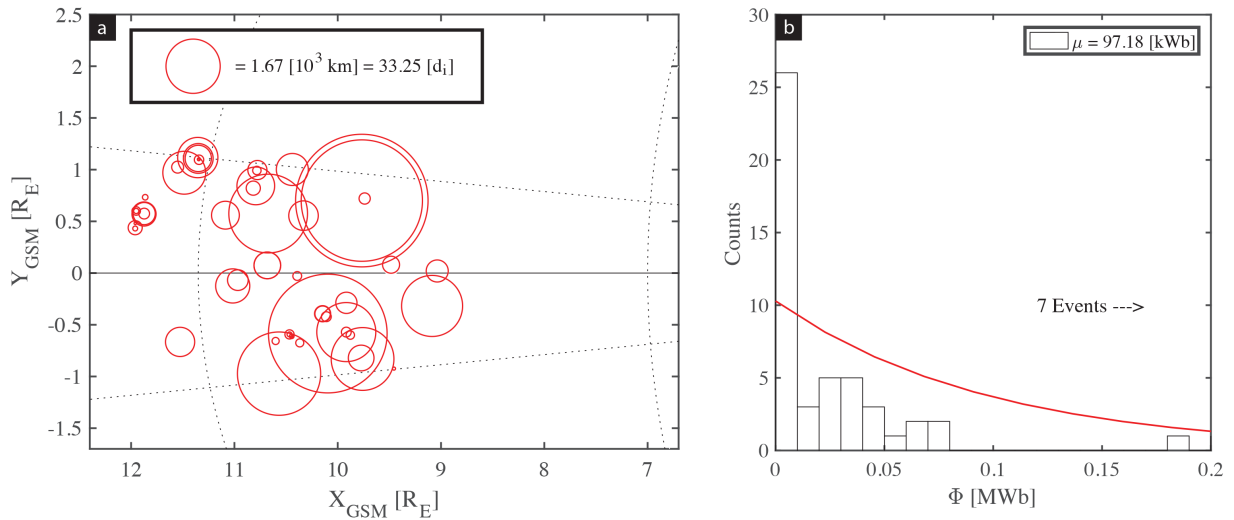
Figure 4-5: *a)* Positions and size distributions of 55 FTEs in the GSM XY-plane; *b)* The distribution of the magnetic flux content of 55 flux transfer events with IP < 0.5 and χ^2 < 0.1. The solid red line is the exponential fit of $\Phi_0 \sim 100$ kWb.

The larger FTEs, on average, contain less plasma and are likely "older". In Figure 6a, plasma density, N, is averaged across the cross section of individual FTEs and plotted against diameter. The 55 events are grouped into (bin width (BW) = 500 km) bins and the error bars are graphical representations of the variability of averaged plasma data within each bin ($\sigma_{mean} \equiv \sigma/\sqrt{n}$; where n is the number of events in each bin). Large FTEs are observed away from the subsolar magnetopause and are the result of multiple X-line reconnection (e.g., MMS: *Hwang et al.*, 2016; THEMIS and Cluster: *Hasegawa et al.*, 2006; *Zhang et al.*, 2008; *Hasegawa et al.*, 2010; *Eastwood et al.*, 2012; Double Star: *Trenchi et al.*, 2011).

The average plasma density drops with increasing core magnetic field strength inside FTEs. Figure 4-6b depicts averaged plasma density inside individual FTEs binned (BW = 1 nT) and plotted against modeled core magnetic field values (using the force-free flux rope model). The x-intercept of the linear fit in Figure 4-6b indicates that there is an upper threshold on the core magnetic field ($|B|_{core} < 120$ nT) at the dayside magnetopause. Flux ropes rely on plasmas to carry electric current for their existence, hence, flux ropes cannot exist beyond the above threshold where plasma density drops to zero. The y-intercepts in Figures 4-6a and 4-6b determine that in the absence of flux ropes (i.e. $\lambda \to 0$ or $|B|_{core} \to 0$), plasma density rises to typical subsolar magnetopause plasma density ($N \sim 30$-50 cm^{-3}; (*Escoubet et al.*, 1997)).
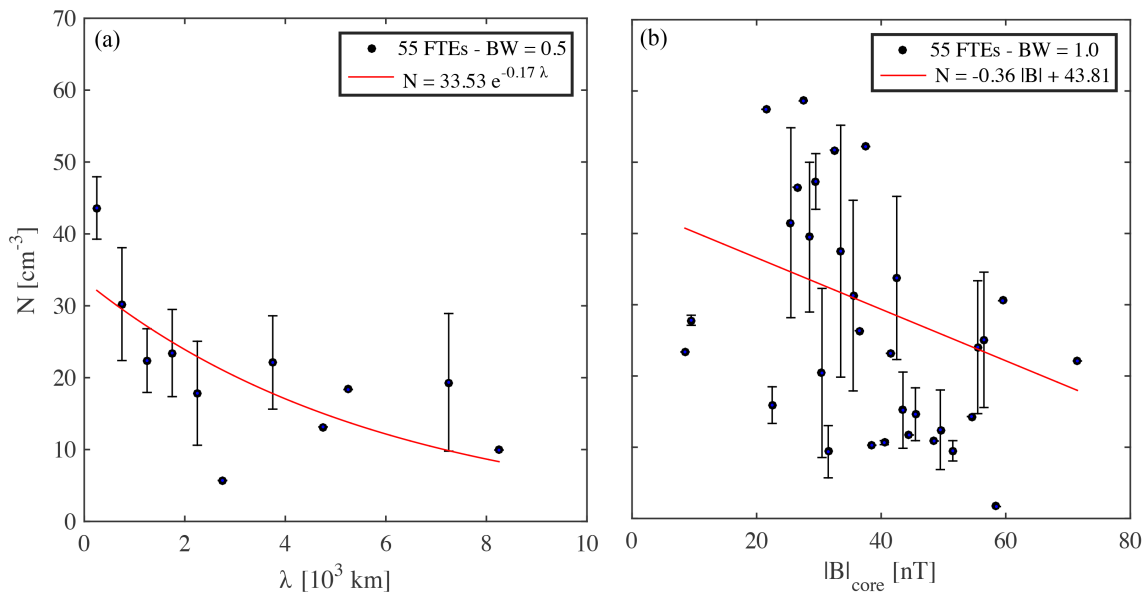
Figure 4-6: *a)* Bin-averaged (bin-width: BW=500 km) exponential fit of the FTEs' averaged number density and size; *b)* Bin-averaged (bin-width: BW=1 nT) linear regression of the FTEs' averaged number density and modeled core magnetic field.

4.1.2. Magnetic force-balance inside FTEs:

Forces across a force-free structure must balance. The MMS high resolution FPI plasma measurements complement multi-spacecraft analysis techniques in assessing our force-free selection criteria. In particular, R_J, the ratio of perpendicular component of current density to the parallel component is examined. In Figure 4-7a, the normalized probability distribution functions (PDF) of R_J computed at the barycenter from particle moments (<FPI>; green) and curlometer technique (CURL; blue) for all observed data points are plotted. Here, we assume structures with $R_J < 1$ to be force-free. This assumption is mathematically equivalent to *arctan*$(\theta_{JB}) < 1$ or $k\pi - \pi/4 < \theta_{JB} < k\pi + \pi/4$; where k is an integer (e.g., *Zhao et al.*, 2016). Figure 4-7b shows the normalized cumulative distribution function (CDF) of R_J. The ratio is calculated using the current density components from the curlometer technique at the barycenter (CURL). FPI current density components are also used to calculate the ratio at the barycenter (<FPI>), at individual spacecraft (FPI 1 S/C), and via averaging the four-spacecraft FPI measurements (AVG). The four methods unanimously indicate that, in general, 60 percent of the cross section of FTEs is force-free. Our findings indicate that all FTEs are force-free near the core and non-force-free in the outer boundary ($> 0.6 \, R_{flux \, rope}$). The ratio, R_J, from the current density calculated via averaging the four-spacecraft FPI measurements (AVG), in Figures 4-7b, is in good agreement with ratios from both CURL and <FPI>.

Figure 4-8a shows the evolution of the Hall term (i.e., net magnetic force) as a function of FTE diameter. Averaged $|J \times B|$ is computed at the barycenter of individual FTEs and binned and plotted against FTE diameter. It indicates that FTEs become more magnetically force-free as they grow larger (i.e., age). In other words, small-scale FTEs must grow via adiabatic expansion or non-adiabatic mechanisms (i.e., coalescence) in order to re-arrange magnetic field lines and reach lower energy state. Figure 4-8b illustrates a first-order approximation of magnetic pressure gradient force across each FTE:

$$\nabla P_m \sim \frac{B_{core}^2 - B_{edge}^2}{2\mu_0 R_{FR}}$$

where B_{core} and B_{edge} are the (force-free) modeled core magnetic field and the FTE boundary magnetic field magnitude, respectively, and R_{FR} is the modeled FTE radius. The plotted values are grouped into 500 km bins. Hence, the exponential fit here indicates that magnetic pressure gradient
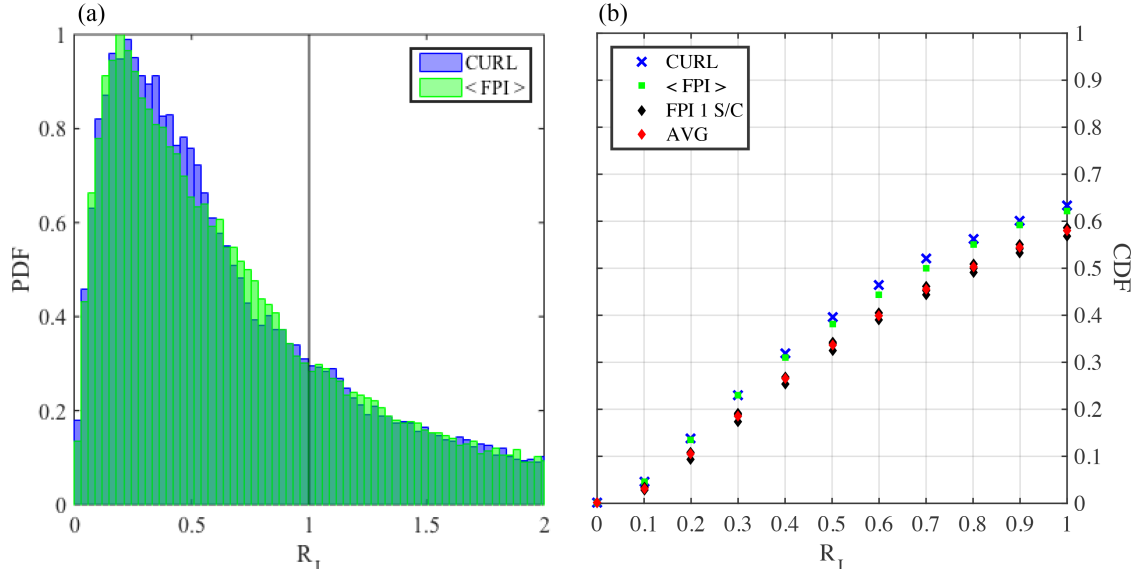
Figure 4-7: *a)* Probability Distribution Function (PDF) of R_J. Blue indicates values that are computed using the curlometer technique while green signifies FPI measurement of current density at the barycenter. *b)* Cumulative Distribution Function (CDF) of R_J from the curlometer technique (blue), FPI measurements at the barycenter (green), and single-spacecraft FPI measurements (grey). The red diamonds are the average values for the four FPI measurements.

drops with increasing FTE size. That is to say, the densely populated magnetic field lines inside ion-scale FTEs become uniformly distributed across the cross section of the FTE with time via strong (oppositely-directed) magnetic curvature force:

$$\mathbf{J} \times \mathbf{B} = -\nabla P_m + (\mathbf{B} \cdot \nabla)\mathbf{B} / \mu_0 \, .$$

Here, the second term on the right-hand side is the magnetic curvature force. Furthermore, we conclude that FTEs become magnetically force free (x-intercept in Figure 4-8a) beyond ~9000 km.

Previous studies have investigated the reliability of the curlometer technique in measuring current density in different plasma regimes (*Ergun et al.*, 2016; *Graham et al.*, 2016; *Perri et al.*, 2017). In particular, *Graham et al.* (2016) concluded that, in the absence of sharp spatial gradients (i.e. sub-proton scale structures), the parallel component of current density for both CURL and AVG are largely congruent. Figure 4-9 shows a scatter plot of all data points for parallel components of J_{CURL} and $J_{<FPI>}$ (indicated by grey +). The red line specifies the orthogonal linear regression fit and indicates that there is very good agreement (correlation coefficient ~ 0.95) between the curlometer technique current density and the current density derived from plasma

moments at the barycenter. In theory, a purely force-free structure lacks any sharp spatial gradients, therefore $J_{\parallel \text{CURL}} = J_{\parallel <\text{FPI}>}$ $= (1/N) \sum_i \{(\mathbf{J_{FPI}})_i \cdot \mathbf{B_i} / |\mathbf{B_i}|\}$, where $i =$ 1, …, N. However, our observations show that curlometer $J_\parallel$ gives slightly larger values than those computed using FPI moments at the barycenter, especially at higher magnitudes. The small y-intercept, in Figure 4-9, casts out the existence of any significant sources of (systematic or random) error in computing current density using either techniques.

4.1.3.   Case study

Figure 4-10 summarizes the physical quantities of three ion-scale FTE-type flux ropes. Table 4-1 lists the coordinate transformation (GSE to LMN) eigenvalues (λ) and eigenvectors for all events. FTE axes are all in the y-direction, consistent with *Owen et al.* (2008), indicating that FTEs move duskward (dawnward) due to J×B force exerted by magnetosheath flow. Knowledge of the impact parameter enables spatial characterization of physical properties of FTEs. Impact parameter varies between

Figure 4-8: Bin-averaged (bin-width: BW=500 km) *a)* orthogonal linear regression of the FTEs' averaged net magnetic force (**J** × **B**) and diameter; *b)* exponential fit of the FTEs' averaged magnetic pressure gradient and diameter.

zero and one, where IP = 0 at the core of the structure and IP = 1 at the edges. As listed in Figure 4-11, *Events 1-3* are classified by impact parameter: low (IP ≤ 0.1), medium (0.1< IP ≤ 0.3), and high (0.3< IP ≤ 0.5) impact parameters.
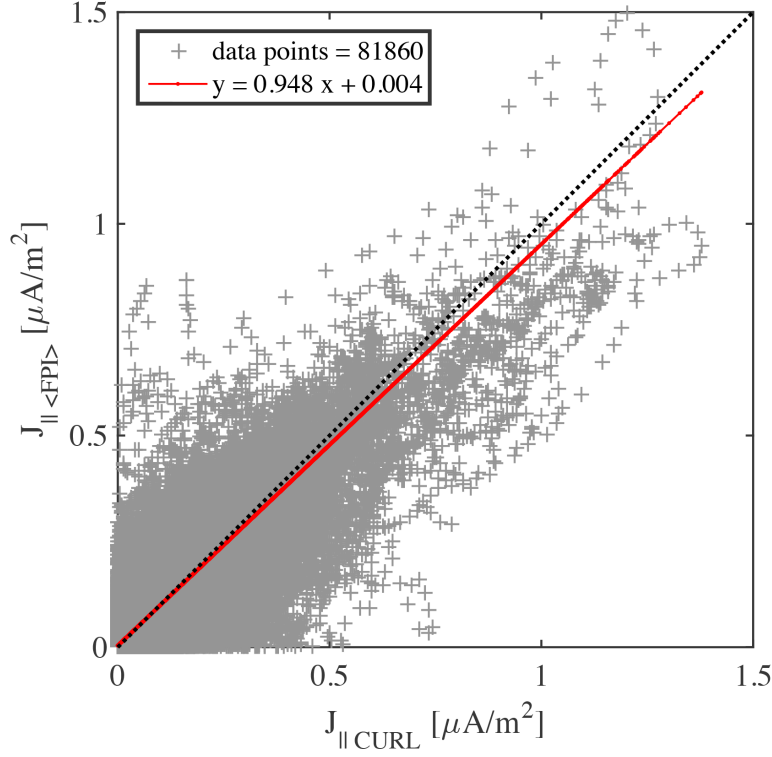
Figure 4-9: Orthogonal linear regression of the parallel components of curlometer and barycenter FPI current densities of all 70 FTE data points. Black dotted-line indicates unity correlation coefficient.

Event 1 was captured on November 16, 2015 at 02:56:31 UT. During this event, the four MMS spacecraft crossed the magnetopause into the magnetosheath with average separation of 12 km and the tetrahedron quality factor (TQF) ~0.7, which compares the structure to a regular tetrahedron (*Fuselier et al.*, 2016). The cross section of the structure was estimated to be 700 km, using the force-free model assuming an estimated local flow velocity $v_i \sim 185$ km/s. This scale length is equivalent to 10 ion inertial lengths ($d_i = c/\omega_{pi} \sim 70$ km). The spacecraft crossed nearly through the core of the structure (IP = 0.06; $\chi^2 \sim 2 \times 10^{-3}$). The core magnetic field was found to be $|B|_{core} \sim$ 49 nT which corresponds to 9 kWb total magnetic flux content.

Table 4-1. The GSE to LMN coordinate transformation for three ion-scale FTE-type flux ropes.

Event #	λ_1	λ_2	λ_3	$\hat{L}$ [GSE]	$\hat{M}$ [GSE]	$\hat{N}$ [GSE]
1	86.2	9.8	0.1	[0.723, -0.045, -0.690]	[-0.151, 0.963, -0.222]	[0.675, 0.264, -0.689]
2	270.4	20.2	0.6	[-0.997, -0.046, 0.065]	[0.061, -0.966, 0.250]	[0.051, 0.253, 0.966]
3	105.2	6.3	0.03	[-0.966, 0.135, 0.221]	[-0.086, -0.972, 0.218]	[0.244, 0.192, 0.951]
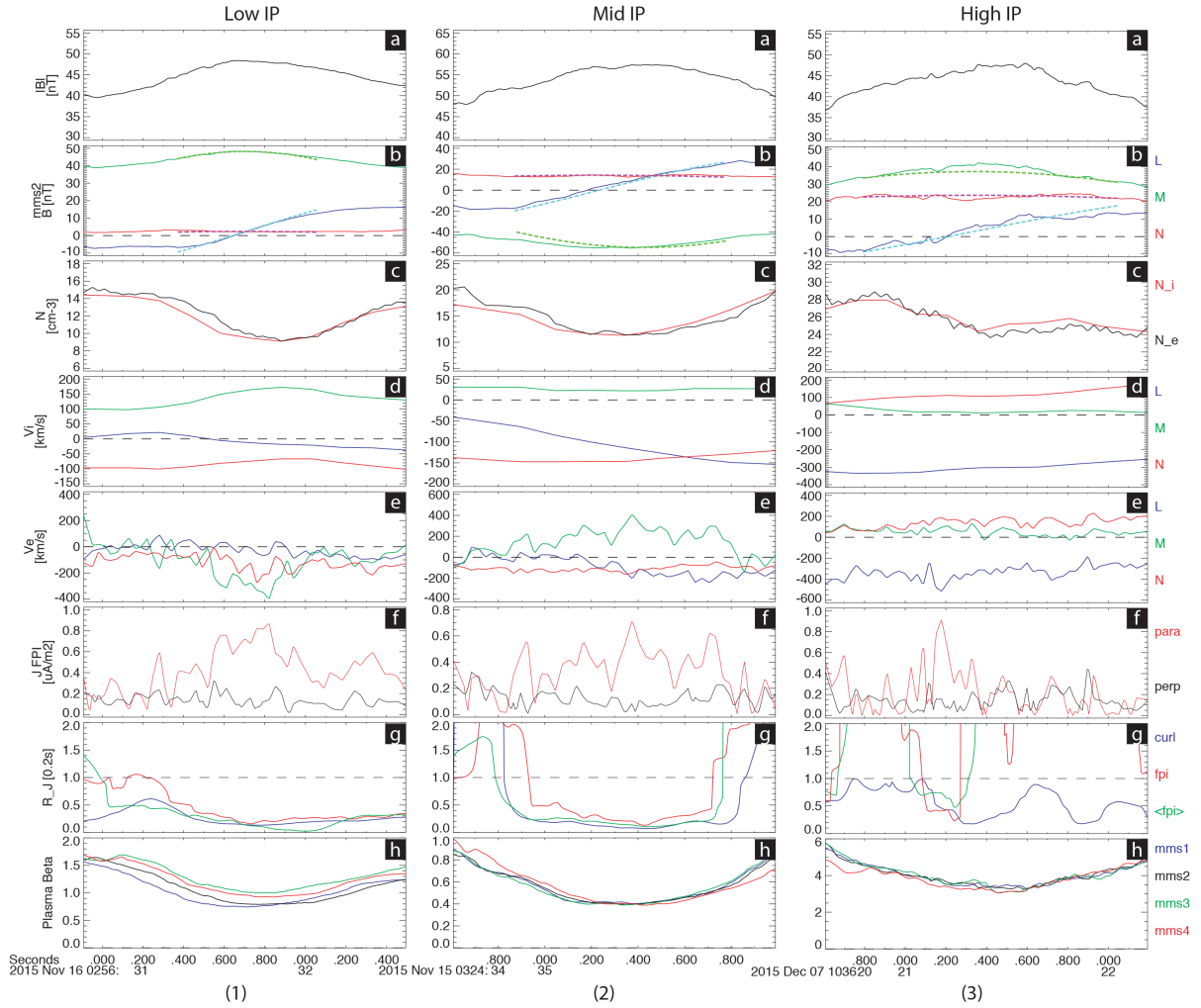
Figure 4-10: The flux rope-like FTEs (*Event1-3*): *a)* Magnetic field magnitude, *b)* observed (solid lines) and modeled magnetic field components (dashed lines) in LMN coordinates, *c)* ion density, *d)* ion parallel and perpendicular velocity components, *e)*, electron parallel and perpendicular velocity components, *f)* single spacecraft FPI current density, *g)* R_J (curlometer: blue, single-spacecraft FPI: red, and barycenter FPI: green), *h)* plasma beta (all four satellites).

On November 15, 2015 at 03:24:35 UT (*Event 2*) an ion-scale FTE was observed in the Earth's subsolar region. This event was 700 km in diameter ($v_i \sim 180$ km/s; IP=0.24; $\chi^2 \sim 9 \times 10^{-3}$). With a modeled core B strength of 56 nT, this FTE contained about 10 kWb magnetic flux.

All four satellites sampled the outer boundary of a medium-size FTE (*Event 3*) on December 07, 2015. Similar to *Events 1&2*, this structure was only 1.5 seconds in duration corresponding to 1500 km in diameter and magnetic flux content of 40 kWb (IP = 0.4; $\chi^2 \sim 2 \times 10^{-2}$). The FTE was driven by a strong anti-sunward magnetosheath flow ($v_i \sim 340$ km/s).

Plasma density and plasma beta dip at the closest approach. *Panels c* in Figure 4-10 depict plasma density profiles across the cross section of the FTE. The drop is most significant (30%) closest to the core of the structure (IP ≤ 0.1). Near the core of FTEs, strengthening magnetic field together with a dip in plasma density result in a drop in the plasma beta profile. This indicates that magnetic pressure plays a greater role in driving the evolution of the structure closer to the core (i.e. magnetic pressure gradient force) while thermal pressure is dominant at the edges of FTEs. Weaker plasma beta observed at the core of the FTE is linked to the out-of-plane guide magnetic field (*Karimabadi, Krauss-Varban, et al.*, 1999; *Liu et al.*, 2009) and is believed to inhibit the development of anisotropic velocity distributions and subsequent instabilities (i.e., Weibel instability (*Weibel*, 1959)) (*Schoeffler et al.*, 2011).
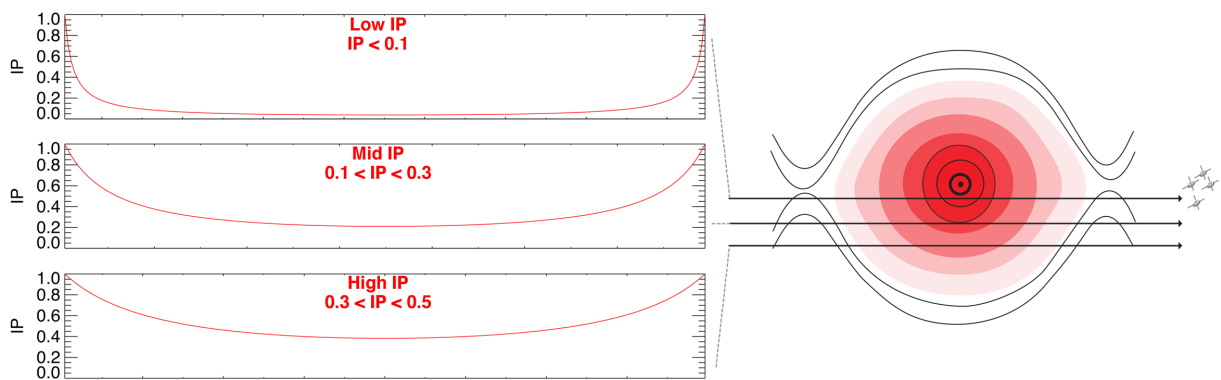
Figure 4-11: Example low, mid, and high impact parameter trajectories through the structure.

Plasma beta (the ratio of the plasma pressure to the magnetic pressure) is suggested to play a role in determining the extent of plasma energization during flux rope formation (e.g., *Phan et al.*, 2010). Magnetic reconnection is credited for spawning significant changes in the particle distribution function for $\beta < 0.1$ (*Li et al.*, 2017) and is shown to be less proficient in plasmas with relatively large β ($\beta < 0.1$) (*Hoshino et al.*, 2001; *Drake, Swisdak, Che, et al.*, 2006; *Drake et al.*, 2010; *Oka, Phan, et al.*, 2010)). Simulations have also attributed flux rope's shape, core magnetic field strengths, and evolution to plasma beta (*Karimabadi et al.*, 1999; *Schoeffler et al.*, 2011). Plasma beta drops with both increasing FTE size and FTE core magnetic field. In Figure 4-12, the mean plasma beta values are computed per FTE and are binned and plotted against both FTE diameter and the modeled core magnetic field magnitude. Here, the plasma beta dropping with increasing FTE size is an order of magnitude faster than the drop with strengthening core magnetic field. This indicates that plasma pressure must be dropping with much faster rate than the rate with which magnetic pressure increases inside evolving FTEs. This is consistent with the hypothesis that FTEs grow force-free via driving out plasma while their core magnetic field strengthens (*Ma et al.*, 1994).
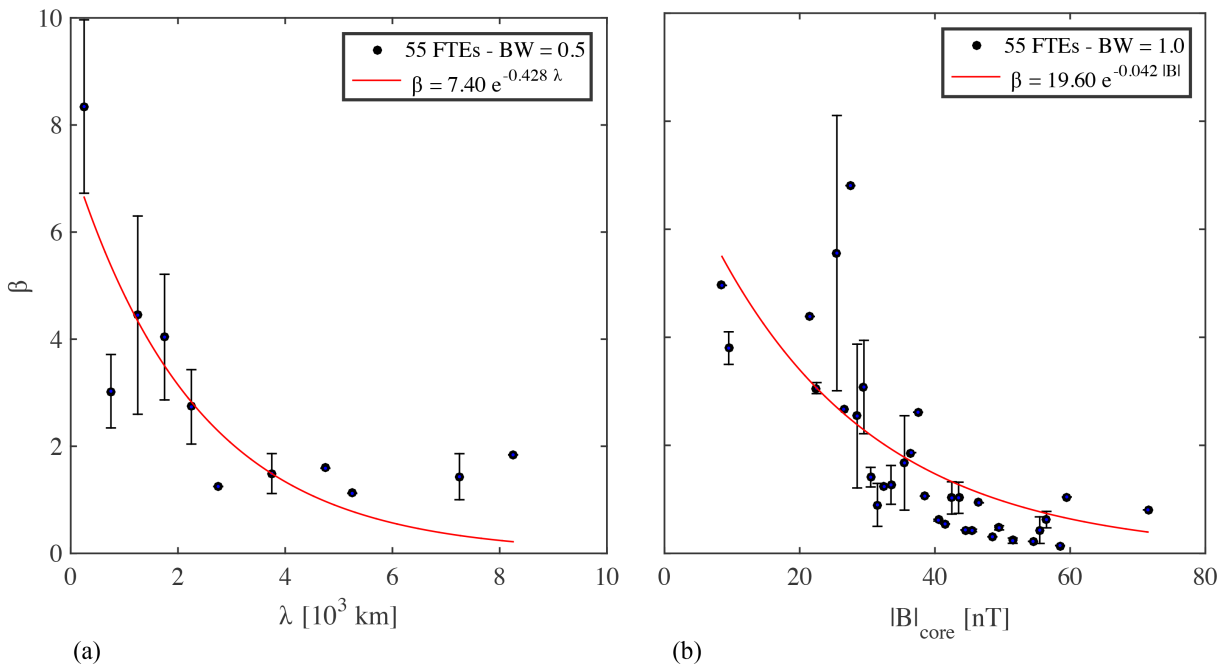
Figure 4-12: Bin-averaged exponential fit of the FTEs' averaged plasma beta and *a)* FTE size (BW=500km), and *b)* FTE modeled core magnetic field magnitude.

Ions inside densely populated FTEs are evacuated by a dominantly-parallel ion velocity while ions inside less populated FTEs remain 'trapped' (i.e. $V_{\parallel} < V_{\perp}$) due to increasing perpendicular ion velocity (*Schindler*, 1979; *Paschmann et al.*, 1982). The red shaded area in Figure 4-13 indicates that the parallel ion velocity dominates inside FTEs with larger plasma densities (see *Zhang et al.*, 2010). Inside FTEs with lower plasma density, ion velocity is prominently perpendicular to the local magnetic field configuration indicating that ions are trapped inside the flux rope (*T. W. Speiser & Williams*, 1982). This is reminiscent of the betatron acceleration inside evolving magnetic flux ropes (e.g., *Retinò et al.*, 2008; *Fu et al.*, 2011; *Fu et al.*, 2013). In this view, the internal and external forces result in a net force that can accelerate particles via betatron acceleration perpendicular to the local magnetic field (*Zhao et al.*, 2017). The population with smaller pitch angles accelerated parallel to the magnetic field upon 'opening' of the field lines have already been evacuated leaving particles with large pitch angles behind. Future study will further investigate the composition and pitch angle distribution of cold populations inside FTEs.

Current density is enhanced and is predominantly field-aligned in the core regions of FTEs. At low IP, current density reaches a peak at the closest approach at which point the parallel component of current density dominates. However, farther away from the core, current density is, in general, small with comparable parallel and perpendicular components (with localized variabilities), as shown in Figure 4-10.3.f (*Farrugia et al.*, 2016). Average current density across each FTE (BW = 500 km) is shown to be inversely proportional to FTE size. The decaying exponential fit in Figure 4-14a indicates that current density decreases with increasing FTE diameter while magnetic field strengthen has a direct relationship with FTE size (or age), as indicated in Figure 4-14b.
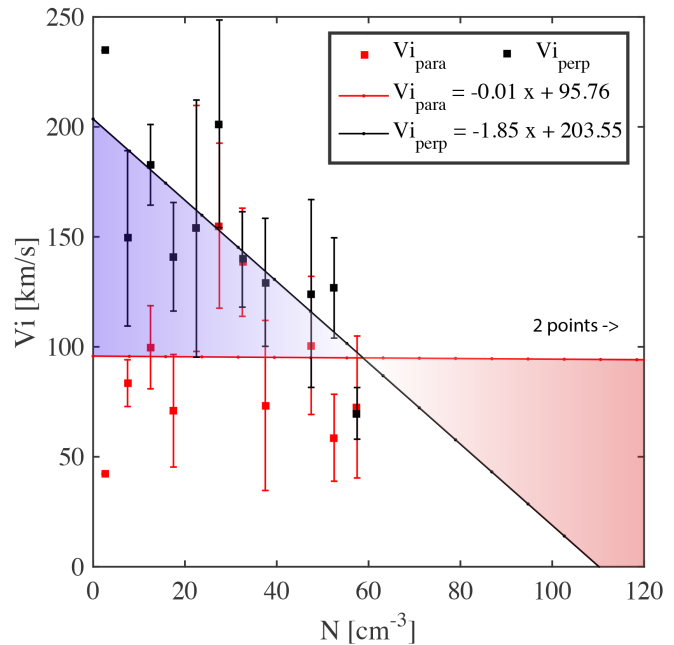
Figure 4-13: Bin-averaged (BW=5 cm^{-3}) linear regressions between the FTEs' averaged number density and parallel (red diamond) and perpendicular ion velocities. Parallel and perpendicular ion flows dominate in the shaded red and blue patches, respectively.

In summary, Figures 4-12 through 4-14 demonstrate that in order for the FTEs to reach their lowest energy states, the excess plasma must be evacuated along the magnetic field, which are signified by parallel flows and field-aligned current densities, while the core magnetic field strengthens (*Saunders et al.*, 1984; *Ma et al.*, 1994; *Zhang et al.*, 2010; *Chen et al.*, 2017). From this perspective, the weakening magnetic pressure gradient and the strengthening core magnetic field imply that the magnetic pressure must increase with increasing FTE size while thermal pressure drops (*Farrugia et al.*, 1998). FTEs are force-free in their core regions. As discussed above, 60% of the cross section of FTEs are force-free. While near the core of the structure magnetic forces cancel out one another, as shown in Figure 4-10.1.g, non-zero net forces at the edges of the FTE drive the evolution of the FTE and are responsible for the large R_J observed across *Event 3*.
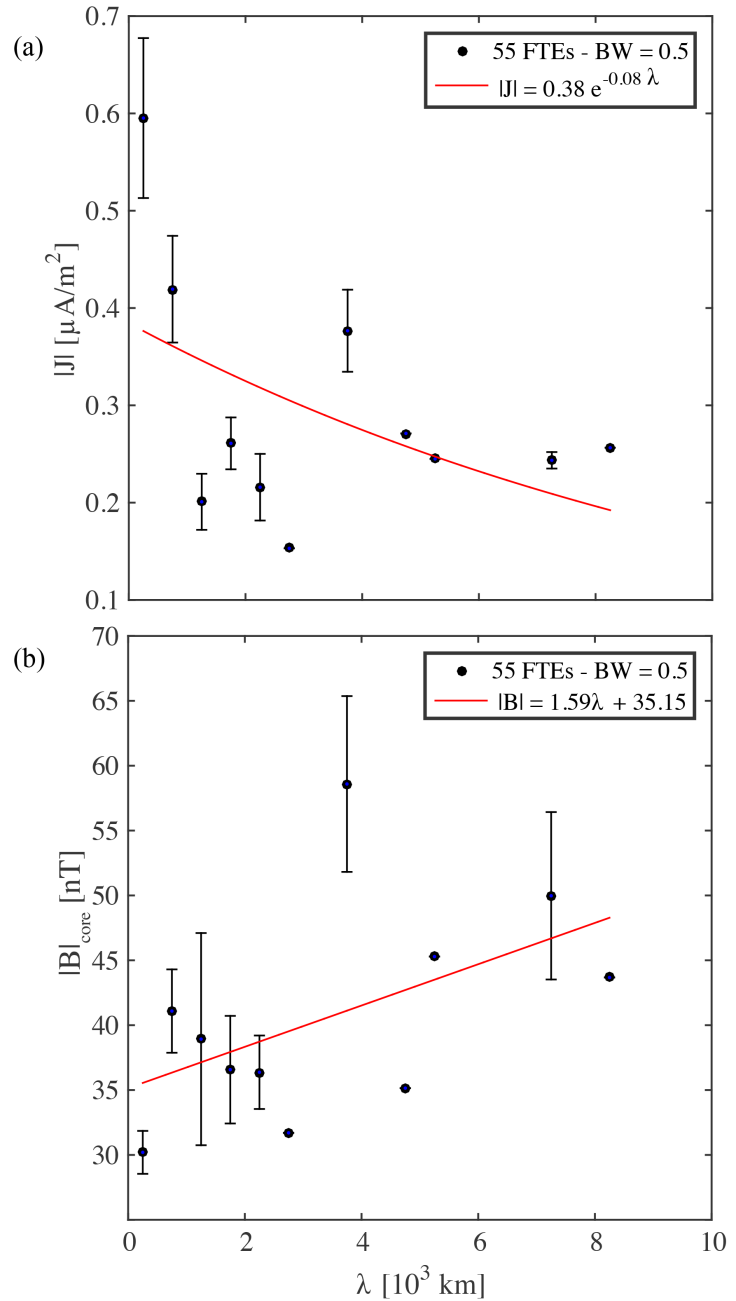
Figure 4-14: Bin-averaged (BW=500 km) *a)* exponential fit between the FTEs' averaged (single-spacecraft FPI) current density magnitude, and *b)* linear regression between the modeled core magnetic field magnitude and the FTE size.

4.4. Conclusions

In this study, we analyzed 55 quasi-force free FTEs observed during 2 months of MMS's Phase-A when the four spacecraft were at near the subsolar magnetopause. These events were identified on the basis of their bipolar B_L, strong core magnetic field signatures, and further screened using the Lepping-Burlaga constant-α flux rope model. The fitting of the MMS magnetic field measurements to this force-free model also allowed us to determine the impact parameter of the spacecraft trajectory relative to the central axis of the flux rope as well as the radius, core magnetic field intensity and magnetic flux content of the FTEs. Only FTEs with MMS impact parameters less than 50% of the radius of the structure were considered. The size and magnetic flux content distributions of the 55 FTEs satisfying this selection criteria fit decaying exponentials and indicate a nominal diameter of 1700 km (equivalent to ~30 ion inertial lengths) and a mean magnetic flux content of 100 kWb. This diameter is by a factor of 3 - 7 smaller than the value reported by *Fermo et al.* (2011) and *Wang et al.* (2005) based upon three years of Cluster data collected at the high-latitude magnetopause and low latitude flanks. The observed non-linear distributions appear consistent with the plasmoid instability theory where coalescence plays a significant role in generating large-scale FTEs (e.g., *Shibata & Tanuma*, 2001; *Loureiro et al.*, 2007; *Samtaney et al.*, 2009; *Daughton et al.*, 2009; *Huang & Bhattacharjee*, 2010; *Fermo et al.*, 2010; *Uzdensky et al.*, 2010).

The difference in the nominal diameter of FTEs at the Earth's dayside magnetopause between MMS and Cluster observations is almost certainly due to their different orbits. Other contributing factors include different dynamic pressures at the two regions (Cluster low-latitude flanks and high-latitude magnetopause and MMS subsolar magnetopause), solar activity cycle for the two studies (Cluster 2001-2003 and MMS 2015), and different sample sizes (Cluster 1098 events and MMS 55 events). Our observations indicate that the ion-scale FTEs observed by MMS in the subsolar region must form locally only a short time before they are detected. These small, newly-formed FTEs are then advected away from the subsolar region toward the flanks and high latitude regions by the anti-sunward magnetosheath flow. During this process FTEs are thought to grow and evolve into larger structures through the coalescence of smaller flux ropes into larger ones (*Fermo et al.*, 2011).

The Cluster's orbit had a perigee of 4 R_E and an apogee of 19.6 R_E with a 90° inclination angle. The plane of Cluster's orbit precesses clockwise looking down from the north, and during planned phases the spacecraft extends outside of the magnetopause during which FTEs can be observed. MMS was launched into a 28° inclination orbit with geocentric perigee and apogee of 1.2 R_E and 12 R_E, respectively. Cluster FTEs are observed at both the high-latitude magnetopause and low-latitude flanks for both southward and northward IMF while the FTEs reported in this study have been observed at the subsolar region where FTEs are believed to be originally formed (*Berchem & Russell*, 1984; *Daly et al.*, 1984; *Russell et al.*, 1985; *Kawano & Russell*, 1997). Hence, Cluster's polar orbit may have contributed to the observation of dominantly larger FTEs. Other missions surveying the magnetopause, such as THEMIS and Double Star, have reported the presence of large-scale FTEs (one to few Earth radii in diameter) farther away from the subsolar magnetopause. In addition, although Cluster is well-equipped to detect small-scale FTEs (sub-second duration) with its high time cadence magnetic field measurements, the spacecraft lacks the high time-resolution MMS/FPI measurements to confidently identify these structures.

Current density, J, is by definition parallel to the local magnetic field in a force-free flux rope. Electric current may be determined using the curlometer technique or directly from plasma ion and electron measurements. We found that, on average, 60% of the cross section of all FTEs are, to a first-order approximation, magnetically force-free. Furthermore, the two current density calculation techniques were juxtaposed to confirm the reliability of the curlometer technique at the subsolar region. It is shown that, in the presence of sharp temporal or spatial magnetic field gradients, the curlometer technique computes slightly larger electric current density than that derived from FPI measurements.

Our inference of an impact parameter for each FTE encounter enables the structure and the evolution of FTEs to be studied as a function of distance from the core. Three ion-scale FTE-type flux ropes with different impact parameters were investigated and the following conclusions are drawn:

i)   Plasma density and plasma beta dip at the core of a quasi-force free FTE-type flux rope, inhibiting instabilities (i.e. sausage or kink-mode instabilities),

ii)   The FTE core magnetic field strengthens as plasma is evacuated,

iii) FTEs are magnetically force-free at the core which is due to the predominately field-aligned current density,

iv) Current density peaks at the core of the structure. In addition, current density decreases with increasing FTE size.

It is also shown that plasma density and plasma beta drop with increasing FTE size and with increasing FTE core magnetic field strength. Electric current density also plummets with increasing structure size. These trends suggest that the factors affecting the force balance inside FTEs change as FTEs evolve. This includes changing the dimension and morphology of the field lines (expansion or contraction (*Drake, Swisdak, Che, et al.*, 2006)) as well as the escape of plasma on the field lines at the time of FTE formation. The variations in plasma moments and magnetic and thermal forces as a function of FTE size and impact parameter are the subjects of future work.

Force-free flux ropes represent the minimum energy state for helical magnetic fields and mark the end point of their evolution (*Priest*, 1990). Weakening current density indicates that the structure is becoming more magnetically force-free as it ages ($J \times B \rightarrow 0$) while the decrease in plasma density with increasing FTE size corresponds to the vanishing of the thermal pressure gradient forces ($\nabla P \rightarrow 0$). A future study will investigate forces inside (*Zhao et al.*, 2016) and outside of FTEs (*Pritchett & Wu*, 1979; *Pritchett*, 1992). Lastly, previous studies have concluded that FTEs extend on one side up through the magnetosheath and connect to the solar wind while their other end reaches into the polar ionosphere (*Fear et al.*, 2007, 2008, 2010; *Owen et al.*, 2008; *Varsani et al.*, 2014). Further work aims to study the evolution in the magnetic connectivity of FTEs as a function of size and impact parameter, using MMS's high time resolution charged particle moments.

Chapter 5: MMS Multi-Point Analysis of FTE Evolution: Physical Characteristics and Dynamics

This Chapter is adopted from Akhavan-Tafti, M., Slavin, J. A., Eastwood, J. P., Cassak, P. A., & Gershman, D. J. (2019). MMS multi-point analysis of FTE evolution: Physical characteristics and dynamics. Journal of Geophysical Research: Space Physics, 124, 5376–5395. https://doi.org/10.1029/2018JA026311.

5.1. Introduction

Magnetic reconnection is the process by which topological rearrangement of field lines relieves stress in magnetized plasmas (e.g., Biskamp, 1996; Yamada et al., 2010a; Gonzalez & Parker, 2016). Magnetic flux ropes are a crucial component of magnetic reconnection (Drake et al., 2006; Daughton et al., 2006). At the Earth's magnetopause, they take the form of FTEs (Russell & Elphic, 1978; Lee & Fu, 1985; Scholer, 1988; Eastwood et al., 2007). Theory suggests that FTEs can begin as small (electron- or ion-scale) flux ropes generated inside the magnetopause current layer as a result of multiple X-line reconnection (e.g., Lee & Fu, 1985; Deng et al., 2004; Daughton et al., 2006; Chen et al., 2008; Daughton et al., 2011).

Kinetic simulations and in-situ observations have suggested that, upon generation, flux ropes in three dimensions evolve in response to their environment moving tailward with the magnetosheath flow and expanding as the external pressure relaxes toward solar wind values (e.g., Berchem & Russell, 1984; Rijnbeek et al., 1984; Zhao et al., 2016; Farrugia et al., 2016; Teh et al., 2017) and coalescence (e.g., Finn & Kaw, 1977; Pritchett, 1992; Karimabadi et al., 2011; Song et al., 2012; Zhou et al., 2014; Wang et al., 2017).

Global magnetohydrodynamic (MHD), kinetic, and Vlasiator simulations indicate that subsolar FTEs tend to grow larger as they travel away from the reconnection site along the magnetopause (*Omidi et al.*, 2006; *Raeder*, 2006; *Omidi & Sibeck*, 2007; *Dorelli & Bhattacharjee*, 2009; *Hoilijoki et al.*, 2017; *Akhavan-Tafti et al.*, 2018; *Hoilijoki et al.*, 2019).

The growth slows down when the FTEs approach their lowest energy state (i.e., 'force-free'; Eastwood et al., 2012). The present study seeks to distinguish between FTE '*expansion*' and '*growth*'. FTE 'expansion' is a type of FTE 'growth' (i.e., increase in diameter) in which magnetic flux remains unchanged throughout the process.

Figure 5- 5-1 illustrates three potential FTE growth mechanisms: *i)* adiabatic expansion, *ii)* continuous reconnection, and *iii)* coalescence. The concentric circles show magnetic islands which are two-dimensional projections of flux ropes. The shading of the islands determine the thermal pressure p inside them with the darkest shades indicating the region of largest p. The number of circles per area indicates magnetic field magnitude and the gradient shading inside the islands shows plasma pressure variability across the structure. The number of black circles represents the islands' magnetic flux content ψ. The X markers indicate X-points at which magnetic field lines reconnect. Due to reconnection, plasma is often heated resulting in an enhanced thermal pressure, i.e., darker shades, and increased magnetic flux content, i.e., more circles. Evolution of the islands is represented with increasing time, $t_1 > t_2$; where subscripts 1 and 2 indicate earlier and later evolution stages, respectively.

In the first scenario, in *panel a*, FTEs grow due to pressure-imbalance across the FTE boundary. As the FTE is carried away from the subsolar region, the external magnetosheath pressure will reduce resulting in the temporal expansion of the FTE. Inside these expanding FTEs, plasma pressure will drop but the magnetic flux content remains constant with time ($\psi = BA$; where ψ and A denote the magnetic flux content and the cross-sectional area of an FTE, respectively).

In the other two scenarios in Figure 5-1, FTEs also grow via reconnection. In one scenario, see Figure 5-1*b*, multiple X-line reconnection may continue after the initial formation of the magnetic island (Lee & Fu, 1985, 1986). Multiple X-line reconnection may or may not be a steady process (*Phan et al.*, 2007). At $t = t_1$, the reconnected magnetic field lines form magnetic islands. But, due to the ongoing magnetic reconnection (*Raeder*, 2006; *Hoilijoki et al.*, 2019), the magnetic islands grow to a size much larger than the original current sheet thickness. During this growth process, plasma is heated due to reconnection (i.e., $p_2 > p_1$). Similarly, ongoing reconnection contributes additional magnetic flux to the original magnetic island (i.e., $\psi_2 > \psi_1$).
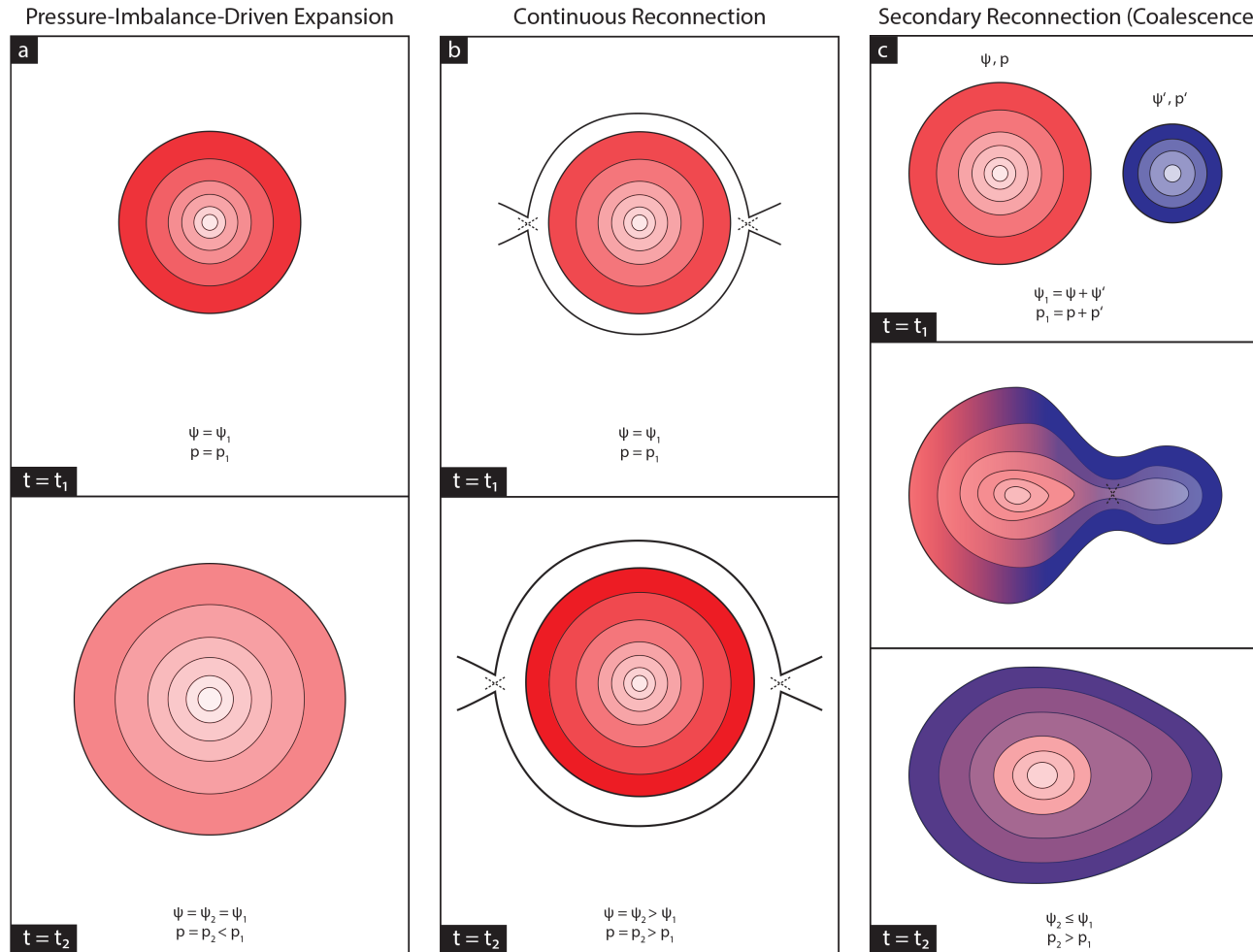
Figure 5-1: Three candidate FTE growth mechanisms: a) Adiabatic Expansion, b) Continuous reconnection, and c) coalescence. The concentric circles show magnetic islands which are two-dimensional projections of flux ropes. The shading of the islands determine the thermal pressure p inside them with the darkest shades indicating the region of largest p. The number of circles per area indicates magnetic field magnitude and the gradient shading inside the islands shows plasma pressure variability across the structure. The number of black circles represents the islands' magnetic flux content ψ. The X markers indicate X-points at which magnetic field lines reconnect. The subscripts 1 and 2 indicate earlier and later evolution stages, respectively.

In the other scenario, depicted in Figure 5-1c, the magnetic islands grow via coalescence. Chains of ion-scale FTEs (*Milan et al.*, 2000; *Slavin et al.*, 2012; *Dong et al.*, 2017; *Teh et al.*, 2017; *Wang et al.*, 2017; *Hwang et al.*, 2018) are formed at the dayside magnetopause due to multiple X-line reconnection (*Lee & Fu*, 1985). In this scenario, the neighboring FTEs are forced to merge, reconnect, and grow into larger structures, a process called 'coalescence' (*Finn & Kaw*, 1977; *Pritchett & Wu*, 1979; *Biskamp*, 1982). Some *in-situ* MMS studies have found evidence for FTE coalescence at the magnetopause (*Alm et al.*, 2017; *Zhou et al.*, 2017; *Wang et al.*, 2017).

As shown in Figure 5-1*c*, repeated formation and convection of magnetic flux ropes during the multiple reconnection process will sometimes force neighboring FTEs to interact and merge via secondary reconnection. This interaction results in heating plasma (i.e., $p_2 > p + p'$; where p and p' represent plasma pressures of individual magnetic islands) and has been the subject of various simulation studies (e.g., *Ding et al.*, 1992 and references therein). In two dimensions (i.e., anti-parallel reconnection), theory suggests that magnetic flux in the two magnetic islands do not add during the coalescence process, $\psi_2 < \psi + \psi'$, where ψ and ψ' represent the flux contents of the two magnetic islands. Rather, the flux in the smaller structure merges with the larger one (*R. L. Fermo et al.*, 2011). In this manner, magnetic flux tubes from the smaller magnetic island connect on both ends to the flux tubes in the larger magnetic island, and in doing so create a larger magnetic island with a greater volume and a larger total mass of plasma.

The three-dimensional picture of coalescing FTEs is more complex (e.g., *Yamada et al.*, 1990). Magnetic helicity, a measure of twist of magnetic field lines inside flux ropes, influences the coalescence process. In particular, the merging FTEs' shear angle, which is controlled by the axial component of their magnetic fields, will determine the rate and the extent to which FTEs coalesce. Correspondingly, the resulting FTE will contain equal, $\psi_2 = \psi < \psi_1$, in the case of anti-parallel reconnection (e.g., *Tian et al.*, 2010), or different magnetic flux than either of the two original FTEs, $\psi - \psi' \le \psi_2 \le \psi + \psi'$, in the case of component or guide-field reconnection (e.g., *Pritchett & Coroniti*, 2004; *Furno et al.*, 2005; *R. Wang et al.*, 2016a; *Stanier et al.*, 2017).

The high temporal and spatial resolution MMS observations enable detailed, multi-point investigations of magnetic reconnection. Here, we use a database of 55 previously identified FTEs (*Akhavan-Tafti et al.*, 2018) to investigate the structure and temporal evolution of FTEs. The previous study used the constant-alpha force-free model to determine the impact parameter, which

is defined as the relative spacecraft distance to the central axis of the flux rope at the closest approach, as well as the radius, core magnetic field intensity, and magnetic flux content of the FTEs. They found that the FTE size distribution followed an exponential law. This result was interpreted as evidence for the plasmoid instability for the onset of fast reconnection. In space and astrophysical environments highly-elongated current sheets are subject to a '*plasmoid instability*' that leads to their breakup and gives rise to an increase in the reconnection rate (collisional plasma regime: *Dieter Biskamp*, 1986; *Loureiro et al.*, 2007; *Bhattacharjee et al.*, 2009; *Cassak et al.*, 2009; *W. Daughton et al.*, 2009; *Y.-M. Huang & Bhattacharjee*, 2010; *Y.-M. Huang et al.*, 2011; *Loureiro et al.*, 2012, 2013; *Murphy et al.*, 2013; *L. Comisso et al.*, 2015; *Ni et al.*, 2015; *L Comisso et al.*, 2016; *Luca Comisso & Grasso*, 2016; and collision-less plasma regime: *William Daughton et al.*, 2006; *Retinò et al.*, 2008; *W Daughton et al.*, 2011; *Baalrud et al.*, 2012; *Y.-M. Huang & Bhattacharjee*, 2013).

FTEs subjected to an external and/or internal driving source evolve dynamically with time. During this evolution, the physical parameters, which characterize the state of the system, become a function of time. Each FTE is observed at a different point in its evolution, and thus the dynamics of growth and expansion can be studied on a statistical basis. In section 3.1, the cross-sectional profiles of the magnetic and plasma characteristics of the 55 FTEs are investigated. Inherently, no forces exist inside perfectly 'force-free' structures (i.e., $\mathbf{J} \times \mathbf{B} \sim \nabla \mathbf{P} \sim 0$). However, residual magnetic and thermal forces are expected inside '*quasi-force-free*' FTEs described here by a goodness of fit (i.e., $\chi^2 \leq 0.1$; *Akhavan-Tafti et al.*, 2018). In fact, the residual forces may contribute to FTEs' temporal evolution. In Section 3.2, the MHD forces are investigated inside the quasi-force-free FTEs. In order to seek evidence for FTE growth and the underlying mechanisms, we evaluate the stress balance inside of these FTE-type flux ropes and their pressure balance with the surrounding magnetosheath. the thermodynamics of FTE growth is studied. In Section 3.3, the force-imbalance across the FTE boundary and the extent to which it may contribute to the expansion of FTEs is discussed. Adiabatic expansion of flux ropes, as suggested by Kumar & Rust (1996), requires plasma pressure inside ion-scale FTEs to drop rapidly with increasing FTE size. However, reconnection slows the rate at which plasma pressure drops with increasing FTE diameter via plasma heating. We conclude that FTE growth in the subsolar region is most likely driven by continuous reconnection at adjacent X-lines and coalescence. This result is important because it underpins the interplay between FTE evolution and adiabatic (e.g., betatron

acceleration) and non-adiabatic (e.g., reconnection, turbulence, wave-particle interaction, etc.) energization of plasmas at the magnetopause (e.g., *Hwang et al.*, 2016).

5.2. Experimental Approach

5.2.1. Methods

Subsolar FTEs are selected from 55 near-equatorial orbital passes (11/03/2015 — 12/28/2015). High spatial and temporal MMS fields (*Torbert, Russell, et al.*, 2016) and plasma suites (Pollock et al., 2016) are used to investigate the structure and dynamics of FTEs. The four MMS spacecraft were maintained at a tetrahedron formation at an average separation of 10 km (*J L Burch, Moore, et al.*, 2016).

FTE identification procedure is done via applying the minimum variance analysis (MVA) on magnetic field measurements where the FTE axis lies in the M (intermediate) direction while N (minimum) and L (maximum) signify the normal and tangential components, respectively (Xiao, 2004). Our event selection criteria only allows FTEs with 1) small impact parameter (IP < 0.5), and 2) cylindrical symmetry (force-free model goodness of fit parameter, $\chi^2 < 0.1$; cf. *Akhavan-Tafti et al.*, 2018).

Taylor expansion of parameters is enabled by the MMS's multi-dimensional measurements and is used here to compute the barycenteric value:

$$\mathbf{V} = \mathbf{V}_\alpha + (\nabla \mathbf{V}_\alpha) \cdot (\overline{\mathbf{r}} - \mathbf{r}_\alpha) \qquad (1)$$

where α indicates the satellite's number ($\alpha = 1, \ldots, 4$), $\overline{\mathbf{r}}$ denotes the barycentric position and is the average of all 4 spacecraft position vectors, $\mathbf{r}_\alpha$, $\mathbf{V}$ is an n-dimensional vector (scalar: $n = 1$ and 3D vector: $n = 3$), and:

$$(\nabla V)_{ij} = \frac{1}{N^2} \left[\sum_{\alpha, \beta \neq \alpha} (V_{\alpha i} - V_{\beta i}) (r_{\alpha k} - r_{\beta k}) \right] R^{-1}_{kj} . \qquad (2)$$

where the symbol $\sum_{\alpha \neq \beta}$ indicates summation over all N(N − 1)/2 independent terms with $\alpha \neq \beta$. Here, r and N signify the position and the number of spacecraft, respectively, and R^{-1}_{kj} is the inverse

of the *volumetric tensor*:

$$R_{kj} = \frac{1}{N} \sum_{\alpha=1}^{N} r_{\alpha k}\, r_{\alpha j}\, , \qquad (3)$$

where *i, j, k* = 1, …, *n* (Harvey, 1998). Equation 2 is also used to calculate the Lorentz force and electron and ion pressure terms in the momentum equation:

$$\rho\, {}^{d\mathbf{u}}/_{dt} = {}^{1}/_{\mu_0}\ (\mathbf{B} \cdot \nabla)\mathbf{B} - \nabla(\frac{\mathbf{B}^2}{2\mu_0}) - \nabla p \qquad (4)$$

where ${}^{du}/_{dt}$ on the left-hand side of the equation is a total convective time derivative. The terms on the right-hand side are magnetic curvature force, magnetic pressure gradient, and (electron and ion) thermal pressure gradient forces, respectively. The thermal pressure gradients are calculated assuming an isotropic (scalar) pressure, *p*.

5.2.2. Assumptions

This study relies on three fundamental assumptions to identify FTEs and to obtain a simple empirical model to investigate FTE structures, dynamics, and evolution. First, FTEs are modeled as force-free flux ropes in order to determine their scale size, impact parameter, and cylindricity (goodness-of-fit; χ^2 < 0.1). Second, FTEs are assumed axisymmetric to obtain radial profiles of their magnetic and plasma characteristics. Third, FTE diameter is used as a proxy to determine their stage of evolution. To accurately study FTE evolution, individual FTEs should be tracked and studied as a function of time and/or distance from their place of origin. However, this is unattainable with present in-situ observational capabilities (i.e., small number of closely-spaced satellites). To address this, Akhavan-Tafti et al. (2018) used FTE diameter as a proxy to determine FTEs' stage of evolution and, therefore, to study how different physical parameters change. The present study will further investigate how FTE characteristics and dynamics evolve as a function of FTE diameter.

In this study, it is further assumed that the internal properties remain relatively constant along the axis of the FTEs. To test this assumption, the 55 subsolar quasi-force-free FTEs are divided into two categories. The first category (35 events) includes only the FTEs that are observed inside the magnetosheath and are labelled as MSH. The second category (20 events) involves FTEs that

are observed at or within <10 seconds from a magnetopause crossing and are labelled as MP. Table 5-1 summarizes the average thermal, P_{th}, and magnetic, P_m, pressures inside and outside each FTE category. The ratio of average pressures is also determined (ratio = P_{inside} / $P_{outside}$); where ratio > 1 indicates that the average pressure inside is larger than the average pressure outside the FTEs. It is shown that thermal pressure averages are nearly similar (i.e., $P_{th, inside}$ = $P_{th, outside}$) inside and outside both MSH and MP FTE categories. However, the average magnetic pressure is found to be larger inside both FTE categories (i.e., $P_{m, inside}$ > $P_{m, outside}$). More importantly, it is revealed that the internal magnetic and thermal properties of an FTE do not necessarily change depending on where along the FTEs' axes observations are made. This suggests that FTEs are closed structures and, therefore, their internal properties remain relatively constant along the axis of the structure making them independent of the spacecraft location. We take advantage of this conclusion to study the properties and the evolution of the 55 FTEs irrespective of where along the axis of each FTE, in the magnetosheath or the magnetosphere, the spacecraft traversed.

Table 5-1: Thermal (P_{th}) and magnetic (P_m) pressure averages inside and outside FTEs observed in the magnetosheath (MSH) and at the magnetopause (MP). The ratio of pressures inside and outside FTEs (ratio = P_{inside} / $P_{outside}$) is determined for each category.

	Inside		Outside		Ratio	
	MSH	**MP**	**MSH**	**MP**	**MSH**	**MP**
P_{th} **[nPa]**	1.95	1.6	2.02	1.56	**0.97**	**1.03**
P_m **[nPa]**	0.79	0.93	0.57	0.69	**1.39**	**1.35**

5.3 Analysis and Results

5.3.1 FTE Physical Properties

Assuming cylindrical symmetry, the constant-α force-free flux rope model is used to infer the size, the core magnetic field strength, the magnetic flux content, and the spacecraft trajectories through the FTEs. Having the knowledge of the trajectory of the spacecraft through the FTE enables statistical study of the structure of quasi-force-free flux ropes as a function of distance from the central axis (Burlaga, 1988; Lepping et al., 1990; Slavin et al., 2003). The model defines impact parameter (IP) as the spacecraft distance from the axis of the flux rope at the closest approach (see Figure 11 in Chapter 4). Figure 5-2 through 5-4 provide single and multi-spacecraft cross-sectional views of the magnetic and plasma characteristics of the 55 FTEs. IP=0 indicates the central region of the FTE and IP=1 denotes the FTE 'edge', beyond which the magnetic field connectivity changes and magnetic fields are no longer bound to the structure (*Rijnbeek et al.*, 1987; *C. J. Farrugia et al.*, 1988, 2016). The assumption here is that variables inside the FTE are axisymmetric.

Physical variables are binned (bin width; BW=0.1) and averaged across all 55 FTEs. Environmental variability such as location can change average parameters inside FTEs. In order to take these variabilities into account, every data point within each FTE was normalized with an assigned 'weight' (i.e., the ratio of FTE-average of a variable to the average of the variable between all 55 FTEs). The detailed procedure is summarized in Appendix B. The error bars indicate the normalized variations of parameters inside individual bins and is known as the standard error, $\sigma_{mean} \equiv \sigma/\sqrt{n}$; where σ and n are the standard deviation and the number of events in each bin, respectively. Furthermore, the contribution from the FPI instrumental measurement errors are negligible compared to the reported plasma moments as suggested by the cross-comparison of magnetic field and plasma moments at the spacecraft barycenter (cf. Figure 9 in *Akhavan-Tafti et al.*, 2018).

Figure 5-2*a-c* shows how plasma moments vary across the FTEs. As shown in *panel a*, plasma density is lower closer to the central region of the flux rope. The plasma density dip suggests that flux ropes are open-ended (three-dimensional) allowing plasma to evacuate upon strengthening magnetic field due to the twisting of the field lines (Ma et al., 1994; Zhang et al., 2010; Øieroset et al., 2016; Akhavan-Tafti et al., 2018). The dashed line indicates that the average plasma density

inside FTEs at the subsolar magnetopause to be $\langle \overline{N} \rangle \pm \sigma_{\overline{N}} = 28 \pm 3$ cm^{-3}. *Panel b* indicates that electron and ion velocities, $\langle \overline{V}_e \rangle = 190$ km/s and $\langle \overline{V}_i \rangle = 230$ km/s, respectively, are independent of the distance from the FTE's central axis. Electron and ion temperatures vary similarly as a function of IP. *Panel c* shows that the temperatures are lowest at the outer edge of the FTE. Electron and ion temperatures reach their maxima at IP=0.5 before dropping to their averages, $\langle \overline{T}_e \rangle = 45$ eV and $\langle \overline{T}_i \rangle = 420$ eV, respectively, near the central axis.

Panel d in Figure 5-2 shows the twisting of the field lines inside an FTE. The magnetic field twist, θ_B, is a function of the ratio of the tangential, B_L, to the axial, B_M, components of magnetic field inside the FTE, $\theta_B = atan(\frac{B_L}{B_M})$. In particular, it indicates that the axial component of the field lines becomes dominant near the central axis. The tangential component of the magnetic field becomes larger near the edges.

Panel e demonstrates the cross-sectional variability of both magnetic, P_m, and thermal, P_{th}, pressures inside quasi-force-free subsolar FTEs. Magnetic pressure, $\langle \overline{P}_m \rangle = 0.65$ nPa, intensifies near the central axis where total magnetic field peaks. In contrast, thermal pressure, $\langle \overline{P}_{th} \rangle = 1.6$ nPa, reaches a minimum near the central axis corresponding to the dip in plasma density. The thermal pressure profile suggests that plasma density variations, not temperature, is the dominant factor determining the plasma pressure profile inside FTEs. More importantly, the pressures are shown to be inversely correlated. A first-order approximation of the pressure gradients inside FTEs (i.e., $\nabla P \sim \frac{\Delta P}{R_{FR}}$, where R_{FR} is the FTE radius) also suggests that the magnetic and thermal pressure gradients point in opposite directions and nearly balance each other.

Panel f further shows that plasma beta, which is the ratio of thermal and magnetic pressures, $\beta = P_{th}/P_m$, dips below its average value of $\langle \overline{\beta} \rangle = 4.3$ near the FTE's central axis. The average plasma beta is larger than those reported inside typical FTEs. This is consistent with Akhavan-Tafti et al. (2018) where newly-born FTEs were shown to contain large plasma density. Over time, plasma will be depleted while magnetic field enhances inside the FTE resulting in lower plasma beta.
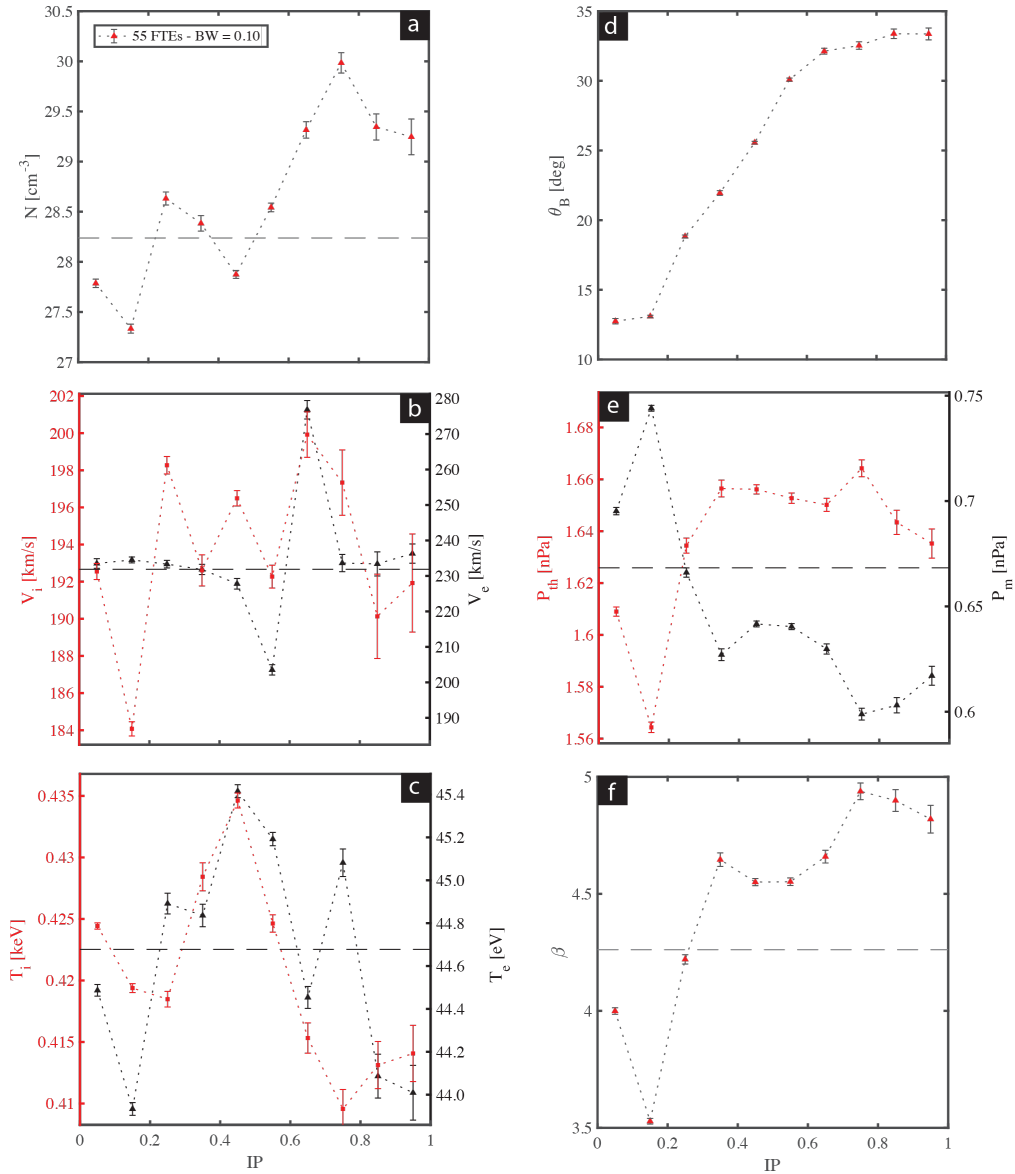
Figure 5-2: Cross-sectional profiles of a) plasma density, b) ion (left axis; red markers) and electron (right axis; black markers) bulk velocity, c) ion (left axis; red markers) and electron (right axis; black markers) temperature, d) magnetic pitch angle, θ_B = atan (B_L/B_M), where B_L and B_M represent tangential and axial magnetic field components, respectively, e) thermal, P_{th}, (left axis; red markers) and magnetic, P_m, pressures (right axis; black markers), and f) plasma beta. All data points across the 55 FTEs are grouped and averaged inside bins (bin-width; BW=0.1). The error bar denotes the standard error σ_{mean} and is defined as the normalized variations of a given parameter inside each individual bin, $\sigma_{mean} \equiv \sigma/\sqrt{n}$; where σ and n are the standard deviation and the number of events in each bin, respectively. Note that the primary and secondary y-axes are different in range and, in the case of plasma temperature, unit.

During (continuous and secondary) reconnection additional magnetic flux and plasma are added to the outer layers of FTEs. Internal magnetic and thermal forces aim to release this stress and bring the structure back to equilibrium. We first investigate the 'frozen-in' condition (i.e., $E \sim -v_i \times B$) for ions inside the 55 FTEs. The Y_{GSE} components of both the electric field measurements (from the Electric Dual Probes (EDP) instrument (*Ergun et al.*, 2016; *Lindqvist et al.*, 2016; *Torbert, Russell, et al.*, 2016)) and the cross product of ion bulk velocity (from the fast plasma investigation (FPI) instrument (*Pollock et al.*, 2016)) and magnetic field measurements (from the fluxgate magnetometer (FGM) instrument (*Russell et al.*, 2016)) are binned into bins (BW=0.5 [mV/m]) and are shown in Figure 5-3*a*. The dashed black line represents a line of slope unity for reference (y=x). The solid red line represents the fit (y=1.01x-0.31) determined using orthogonal linear regression indicating that ions remain frozen-in inside our quasi-force-free FTEs.

Second, the average net force components are investigated across our quasi-force-free FTEs. Here, net force refers to the vector sum of the magnetic, $J \times B$, and thermal pressure, ∇P, forces. Figure 5-3*b* shows the bin-averaged (BW=0.1) values of the *radial* component of the net force on ions, $F_{i, radial}$, across the

Figure 5-3: a) Cross-Comparison of the Y_{GSE} components of -v_i x B and the electric field measurements grouped and counted inside bins (BW=0.5 [mV/m]). The solid red line represents the orthogonal linear regression fit. The cross sectional profile of the b) radial component of the net force, and c) axial component of the net force experienced by ions inside the 55 quasi-force-free FTEs. All data points across the 55 FTEs are grouped and averaged inside bins (BW=0.1). The error bar denotes the standard error inside each individual bin.
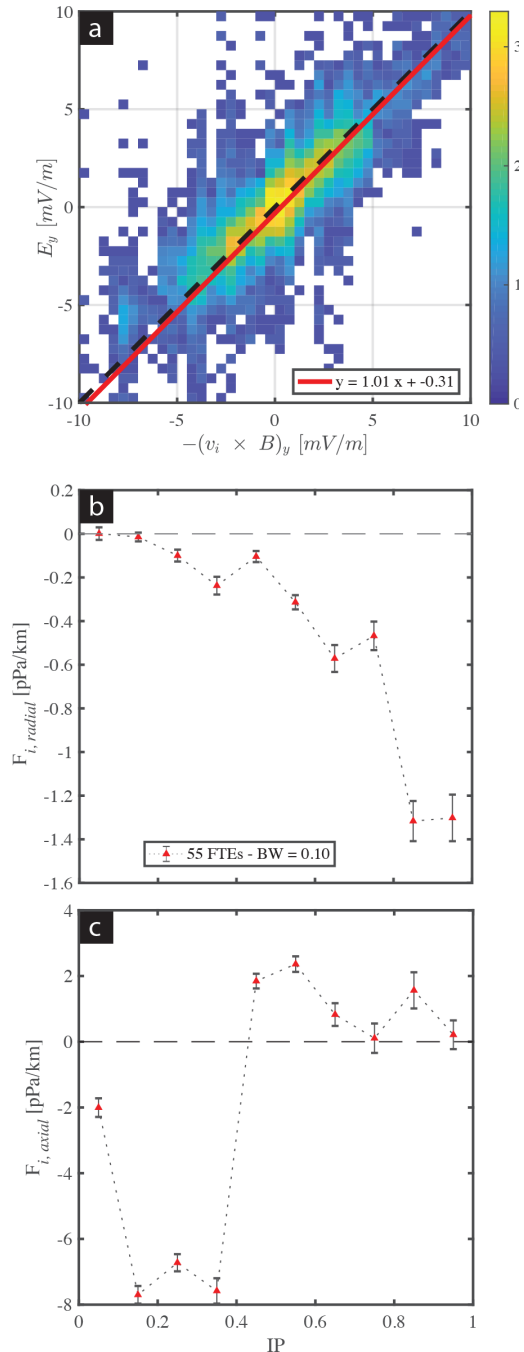
cross sections of the 55 FTEs. The detailed coordinate transformation procedure is summarized in Appendix C. Here, a negative value of $F_{i, radial}$ indicates inward force. We find that the net force is radially inward. Farther away from the FTE axis, the magnitude of the radially-inward net force enhances. The bin-averaged values of the axial component of the net force, $F_{i, axial}$, across the cross section of the FTEs are further shown in Figure 5-3c. In contrast with the radial component, the axial component of the net force is found to enhance significantly near the FTE's central axis, IP < 0.5. In conclusion, the results found in Figure 5-3a-c suggest that the 'frozen-in' magnetic field lines are compressed inward with the plasma giving rise to strengthening core magnetic field. However, due to the strengthening magnetic field the radially-inward net force is reduced near the FTE's central axis while the axial net force enhances. These findings indicate that plasmas are accelerated toward the FTE's central axis, though closer to the FTE's core region the radial force is reduced and the plasma is instead accelerated along the axial direction causing the plasma to escape the stressed region (e.g., *Ma et al.*, 1994).

Figure 5-4 further provides the cross sectional profiles of the radial components of the magnetic and thermal forces across the FTE. The error bars indicate the standard error inside each individual bin. The radial profiles indicate that inside FTEs magnetic pressure gradient (blue shade) and ion thermal pressure gradient (black shade) are dominant near the FTE's central axis. It is also found that magnetic curvature force (red shade) is radially inward and becomes more significant near
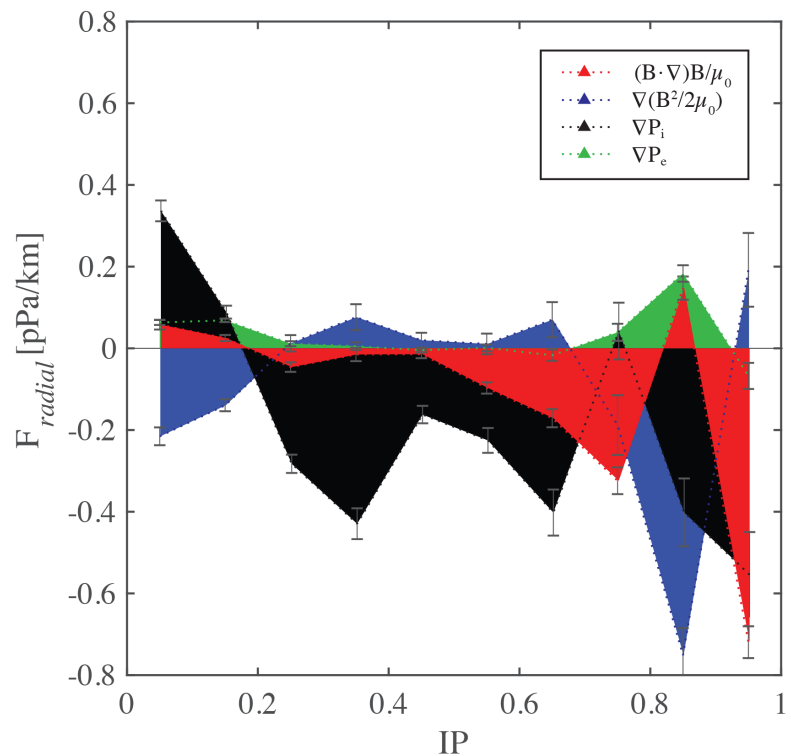
Figure 5-4: The radial components of the magnetic and thermal forces as a function of IP. The magnetic forces include the magnetic curvature force (shown in red) and the magnetic pressure gradient (shown in blue). The thermal forces are the ion (black shade) and electron (green shade) thermal pressure gradients forces. All data points across the 55 FTEs are grouped and averaged inside bins (BW=0.1). The dotted lines show the boundaries of each of the shaded areas.

the FTE's edge. As expected, electron thermal pressure gradient (green shade) is small throughout the structure. On the other hand, ion thermal pressure gradient remains large, relatively steady, and radially inward across the structure.

Figure 5-5*a-d* compare the spatial profiles of perpendicular and parallel components of plasma current density, net force, and electron and ion temperatures. In *panel a*, the ratio of perpendicular to parallel components of the current density is shown to be smaller than unity (i.e., $R_J = J_\perp / J_\parallel < 1$; *Akhavan-Tafti et al.*, 2018). This is a result of our event selection criteria where only quasi-force-free FTE candidates were chosen. *Panel b* shows that the majority of the net force inside the FTE accelerates plasmas perpendicular to the local magnetic field. The relatively large parallel force is consistent with the observed enhanced axial component of the net force inside FTEs. The parallel net force can facilitate the escape of the stressed plasma through accelerating them along the magnetic field. The parallel net force may also affect the helical magnetic structure of the FTEs (*Zhao et al.*, 2016). Temperature anisotropy inside FTEs is evident in *panels c-d*. Parallel electron temperature, $T_{e\parallel}$, and perpendicular ion temperature, $T_{i\perp}$, are observed to be the larger components of the electron and ion temperatures, respectively.
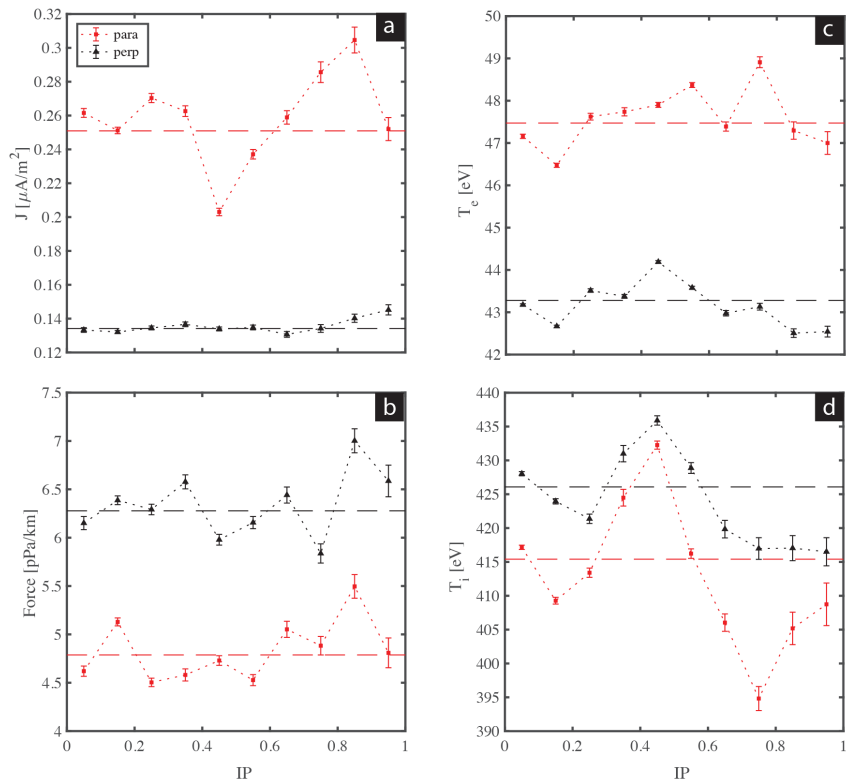
Figure 5-5: Cross sectional profiles of the parallel (red) and perpendicular (black) components of a) current density, b) net force, c) electron and, d) ion temperatures. All data points across the 55 FTEs are grouped and averaged inside bins (BW=0.1). The error bar denotes the standard error inside each individual bin. The dashed line represents the average value of each parameter across all FTEs.

5.3.2 FTE Boundaries

In this section, the physical characteristics and dynamics are studied inside and just outside the 55 quasi-force-free FTEs. As shown in Figure 5-6, the term '*inside*' refers to the cross section of the flux rope (shaded red) that meets the constant-alpha force-free flux rope model criteria *Burlaga*, 1988; *Lepping et al.*, 1990; *Akhavan-Tafti et al.*, 2018, while '*outside,*' shaded as light blue, indicates the outer perimeter of the flux rope (i.e., the draping region *Rijnbeek et al.*, 1987; *Farrugia et al.*, 1988). The thickness of the outer perimeter was selected at 10 local ion-inertial lengths, d_i. This thickness is nearly one-third of the nominal FTE diameter at the dayside magnetopause (*Akhavan-Tafti et al.*, 2018) and is sufficiently large to include reconnection-associated kinetic and MHD effects (*Smith*, 1977; *Tóth et al.*, 2017).

Table 5-2 lists the relative contribution, i.e., percentage of total, of the force terms. The force terms are averaged inside and outside the 55 FTEs. The shading in each row corresponds to the relative contribution of individual force terms with the darkest shading representing the largest contribution. The table indicates that magnetic pressure gradient and ion thermal pressure gradient are the dominant force terms contributing to the total force inside and outside FTEs. Magnetic forces (magnetic curvature force and magnetic pressure gradient) are comparable in magnitude to the ion thermal pressure gradient inside FTEs. The thermal pressure gradient becomes dominant outside the FTEs.
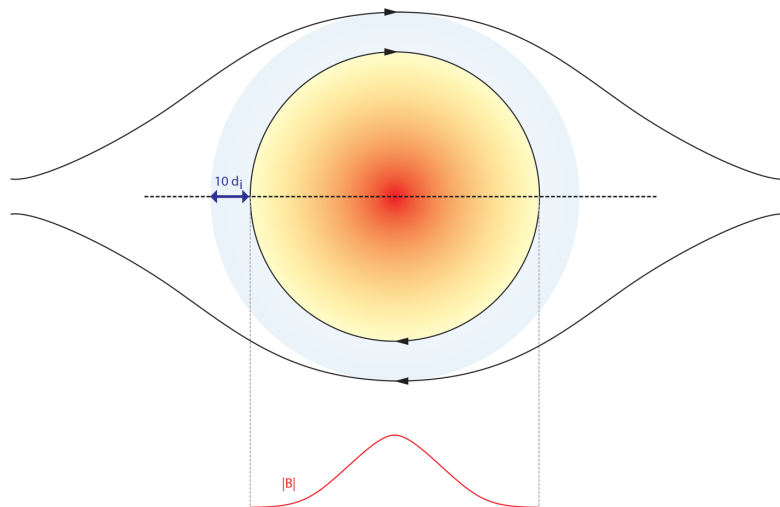
Figure 5-6: The red gradient indicates the magnetic field magnitude inside the FTE, while the light blue shade denotes the outer perimeter of the FTE with a thickness of 10 ion inertial lengths.

Table 5-2: The relative contribution, i.e., the percentage of total, of the force terms inside (blue shade) and outside (red shade) FTEs. The shading in each row corresponds to the relative contribution to the total force average inside all 55 FTEs with the darkest shading representing the largest contribution.

	$\|(\mathbf{B} \cdot \nabla)\mathbf{B}/\mu_0\|$	$\|\nabla(\mathbf{B}^2/2\mu_0)\|$	$\|\nabla\mathbf{P_i}\|$	$\|\nabla\mathbf{P_e}\|$
Inside FTE	15%	33%	43%	9%
Outside FTE	13%	29%	48%	11%

Figure 5-7 compares plasma beta, current density, and net force vector components inside and outside FTEs. Observations outside the 55 FTEs are bin-averaged (BW=1 d_i; where $d_i = c/\omega_{pi} = 2.28 \times 10^7 \, (N_i)^{-1/2}$ cm, is the average local ion inertial length and is a function of average ion density, N_i, outside each FTE). *Panel a* indicates that plasma beta varies quite remarkably across the FTE boundary. This is partly due to the enhanced magnetic pressure inside FTEs. *Panel b* shows that current density is, on average, enhanced by nearly 50% inside FTEs. *Panels c-e* present the net force vector components in the cylindrical coordinate system. The radial component of the vector sum of the magnetic and thermal forces, remains relatively small outside the FTEs suggesting that the radial magnetic and thermal forces are balanced. Furthermore, the magnitude of the tangential component of the net force, defined as $\mathrm{F}_{tangential} = | \mathbf{F} - (\mathrm{F}_{radial} \, \hat{\mathbf{r}} + \mathrm{F}_{axial} \, \hat{\mathbf{M}}) |$, enhances near the FTE edge. Finally, the axial component of the net force remains steady and non-zero outside the FTE. The residual tangential and axial net force components may impact the twist of the field lines at the outer layers of the FTEs (e.g., *Zhao et al.*, 2016).
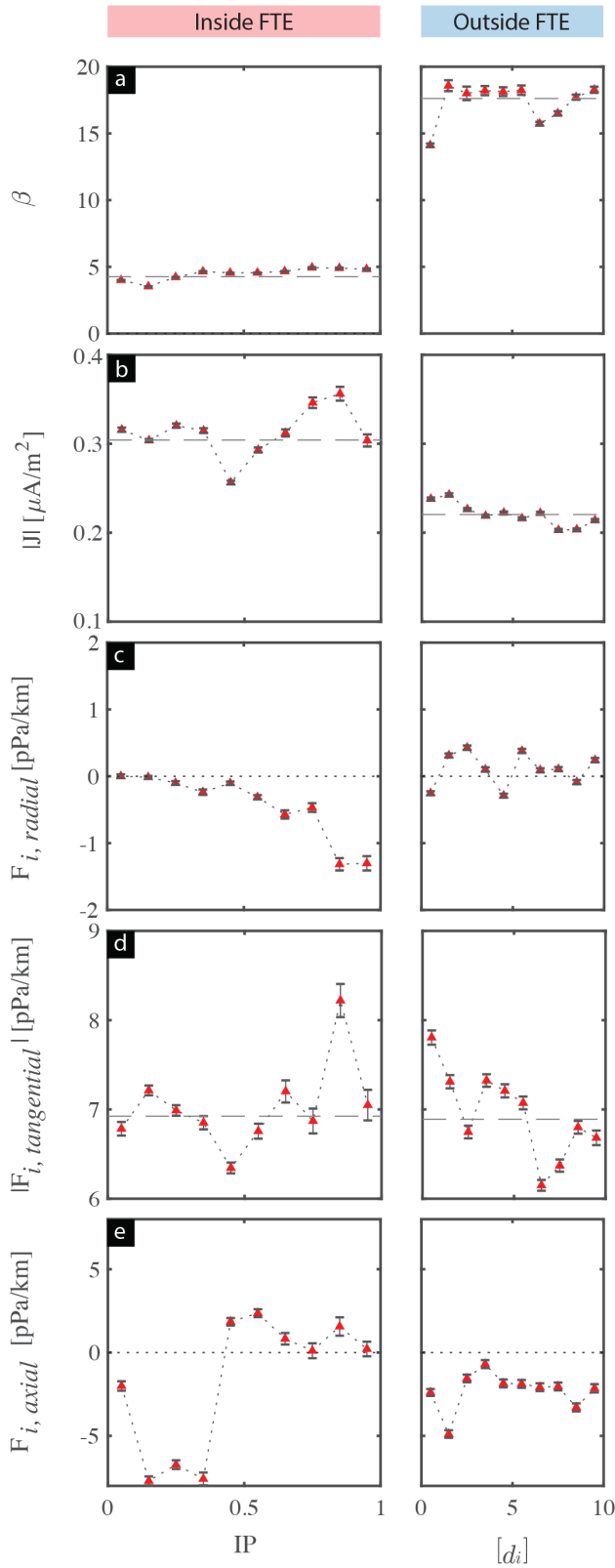
Figure 5-7: The cross-sectional profiles of a) plasma beta, b) current density, c) the radial component of the net force, d) the magnitude of the tangential component of the net force, and e) the axial component of the net force inside and outside (10 local ion inertial lengths from the FTE edge) the 55 FTEs. All data points inside (outside) the 55 FTEs are grouped and averaged inside bins (BW=1 d_i). The error bar denotes the standard error inside each individual bin.

5.3.3 Case Study

The magnetic and thermal force magnitudes inside the 55 quasi-force-free FTEs are non-zero (i.e., $\boldsymbol{J} \times \boldsymbol{B} \neq \boldsymbol{0}$ & $\nabla P \neq \boldsymbol{0}$). Here, we provide two quasi-force free FTEs observed in the magnetosheath with enhanced net force components. Figure 5-8 summarizes the magnetic and plasma moment observations. The panels in the left column include the measurements by MMS2: *a*) total magnetic field, *b*) magnetic field vector components in the GSE coordinate system, *c*) plasma density, *d*) ion velocity, *e*) plasma current density, and *f*) ion temperature. The magnetic and thermal force components are further included in the right column: *g*) total magnetic field, *h*) magnetic and thermal pressure components, *i*) magnetic curvature force, *j*) magnetic pressure gradient force, *k*) ion thermal pressure gradient force, and *l*) net force which is defined as the vector sum of the magnetic and thermal forces. The vector components are presented with respect to the local magnetic field. The component of each vector parallel to B is shown in red, while the magnitude of the perpendicular component of the vector is shown in black. The red gradient and the light-blue solid color shadings represent the areas 'inside' and 'outside' each FTE. The width of the blue shaded area is 10 ion inertial lengths which is determined using the average local ion density, $N_i = 40$ cm^{-3}.

Zhou et al. (2017) reported the presence of an ion jet reversal ($v_{iz, GSM} = \pm 200$ km/s; *panel c*) during a magnetopause crossing (November 17, 2015 — 02:13:40 - 02:14:40 UT) corresponding to a 'dissipative' interaction of two neighboring FTEs. Shortly after this crossing, at the peak of the southward ion velocity, a chain of small-scale FTEs is observed, labeled as 'FTE 1' and 'FTE 2'. In particular, two FTEs centered at 02:20:48 UT and 02:21:24 UT are observed surrounded by two southward v_{iz} peaks (02:17:30 UT and 02:22 UT) which met our selection criteria (*Akhavan-Tafti et al.*, 2018).

Plasma density is shown to dip by 50% at the center of FTE 1 and by 25% inside FTE 2. Parallel current density is further found to enhance inside the two events. Ion temperature anisotropy is observed across both FTEs; however, the parallel ion temperature, $T_{i\parallel}$, is smaller than the perpendicular component, $T_{i\perp}$, inside FTE 1, $T_{i\perp} > T_{i\parallel}$, while $T_{i\perp} < T_{i\parallel}$ inside FTE 2. Magnetic pressure enhances inside both FTEs resulting in increased magnetic pressure gradient force. $\beta = P_{th} / P_m \sim 4$ outside the two FTEs. Plasma beta is reduced inside both structures. Ion thermal pressure gradient force is found dominant inside the two FTEs.
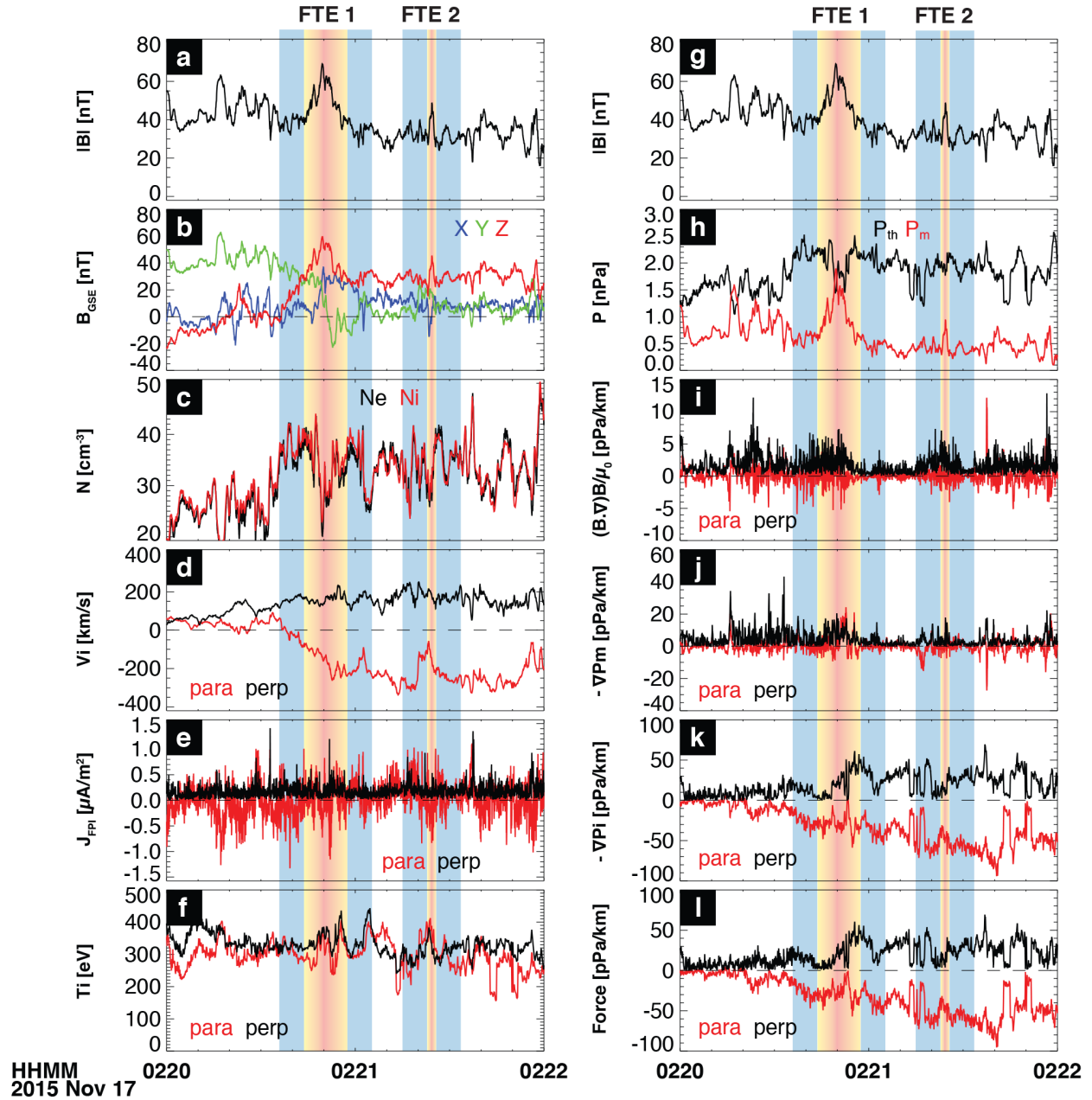
Figure 5-8: The November 17, 2015 magnetopause boundary crossing. Panels include: a&g) magnetic field magnitude, b) magnetic field components in the GSE coordinates, c) ion (red) and electron (black) density, d) ion velocity parallel (red) and perpendicular (black) components, e) plasma current density parallel and perpendicular components, f) ion temperature components, h) ion thermal and magnetic (black) pressures, i) magnetic curvature force parallel and perpendicular components, j) magnetic pressure gradient force parallel and perpendicular components, k) ion thermal pressure gradient force parallel and perpendicular components, and l) net force parallel and perpendicular components. Two quasi-force-free FTEs, labeled as 'FTE 1' and 'FTE 2,' are shown with gradient and solid color shadings corresponding to the observations made 'inside' and 'outside' the FTEs, respectively. The width of the blue solid color shading is 10 ion inertial lengths, $d_i \sim 1400$ km, from an average of $N_i = 40$ cm^{-3}.

94

5.4 Discussion

In this study, we investigate the structural characteristics of the 55 subsolar quasi-force-free FTEs identified and modeled by Akhavan-Tafti et al. (2018). The determination of the impact parameter of the MMS spacecraft trajectories through modeling FTEs as force-free flux ropes with cylindrical geometry allows the study of cross-sectional profiles of physical parameters as a function of distance from the FTEs' central axis. It is revealed that:

i) Plasma density and plasma beta increase with increasing distance from the FTE's central axis.

ii) The radial component of the net force (solid-black arrow in Figure 5-9*a*) at the outer layers of the flux rope points inward. The axial component of the force, shown as an into-the-plane arrow, becomes significant near the FTE's central axis.

As illustrated in Figure 5-9*a*, the continuous supply of magnetic flux and plasma to the FTEs' outer layers, shown as grey-shaded area, by magnetic reconnection at adjacent X-lines and/or coalescence with the neighboring FTEs, shown as X points, drives FTEs to 'grow' (*Hasegawa et al.*, 2010; *Akhavan-Tafti et al.*, 2018) while also contributing to:

a. The observed average decrease in plasma density near the FTE's central axis. Cross-sectional profile of plasma density is represented as a blue and red-shaded area. As discussed above, plasma density drops below average, white-shaded area, near the FTE's core region.

b. The observed radially-inward net force at the outer layers of the FTEs as well as the enhanced axial net force closer to the FTE's central axis.

These observations are consistent with the continuous supply of magnetic flux and plasma heating by magnetic reconnection. As suggested by the radially-inward net force, the additional magnetic flux and plasma, in the reconnection exhaust, is compressed and accelerated, respectively, while being transported toward the FTE's core region. Closer to the FTE's central axis, where B_{axial} enhances, the axial net force component strengthens. The strengthening axial force can then accelerate plasmas along the FTE's axis and cause the 'trapped' plasma population to escape the stressed region (e.g., *Ma et al.*, 1994; *Akhavan-Tafti et al.*, 2018; *Sun et al.*, 2019).
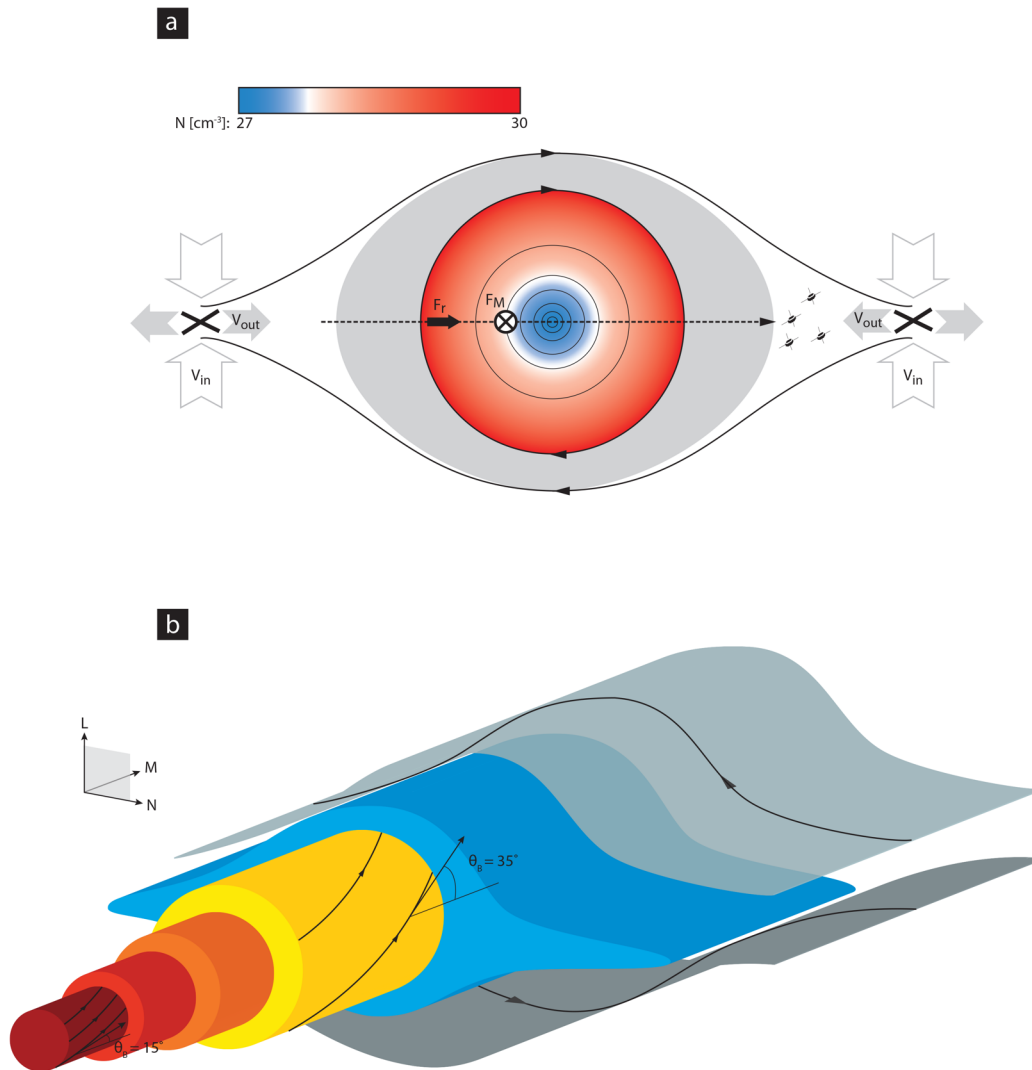
Figure 5-9: Cartoon representation of cross-sectional profiles of a) plasma density profile and the radial (solid black arrow) and the axial (into-the plane arrow) components of the net force, and b) magnetic pitch angle, $\theta_B = \text{atan}(B_L/B_M)$, where B_L and B_M represent tangential and axial magnetic field components, respectively. Plasma density colorbar corresponds to the bin-averaged values reported in this study. The grey shaded area around the flux rope illustrates the magnetic flux and plasma (grey arrows labelled as 'V$_{out}$') continuously added to the FTEs' outer layers by reconnection (shown as 'X').

iii) The tangential component, B_L, of the magnetic field increases farther away from the FTE's central axis. Figure 5-9*b* shows the profile of magnetic pitch angle, $\theta_B = atan(B_L/B_M)$, across the cross section of a typical quasi-force-free FTE. The tangential component of the magnetic field enhances at the FTE's outer layers. The FTEs' magnetic pitch angle may impact the coalescence process (e.g., *Yamada et al.*, 1990).

iv) Ion and electron temperatures are found to be anisotropic throughout the cross section of FTE-type flux ropes observed both inside the magnetosheath and at the magnetopause.

    a. We observe that, on average, $T_{e\parallel} > T_{e\perp}$ throughout the cross section of subsolar FTEs. Firehose, $T_{e\parallel} > T_{e\perp}$, and whistler, $T_{e\perp} > T_{e\parallel}$, instabilities can arise due to electron temperature anisotropy (e.g., *Kennel & Petschek*, 1966; *Hollweg & Völk*, 1970a, 1970b; *Pilipp & Völk*, 1971; *Cuperman*, 1981; *Gary & Madland*, 1985; *Zhao et al.*, 1996; *Drake et al.*, 2010; *Wang et al.*, 2019). Zhao et al. (1996) notes that the former condition is rarely observed in space plasmas and, hence, infrequently reported in the literature, but our analysis suggests that it may occur in FTEs.

    b. We also observe that, on average, $T_{i\perp} > T_{i\parallel}$ inside small-scale subsolar FTEs. In theory, anisotropic ion temperature, $T_{i\perp} > T_{i\parallel}$, can act as a source of free energy for various low-frequency electromagnetic instabilities in the magnetosheath, such as the ion cyclotron anisotropy and instability and the mirror instability (e.g., *Gary et al.*, 1976; *Lee et al.*, 1988; *Midgley & Davis*, 1963; *Remya et al.*, 2013; *Zwan & Wolf*, 1976). A future MMS study will examine anisotropies in the plasma moment distributions and the associated instabilities inside FTEs.

The profiles of the magnetic and plasma properties are further analyzed outside FTEs to gain insight into the role of environmental conditions in impacting the evolution, e.g., growth, of FTEs. In particular, it is shown that, compared to the average properties inside FTEs:

i) Plasma beta enhances significantly, by a factor of >4, outside FTEs. This may be the result of enhanced thermal pressure, and reduced magnetic pressure, at the adjacent X-lines.

ii) Current density is reduced outside FTEs.

iii) The radial component of the net force remains steady and negligible outside FTEs which may be a result of our selection process, i.e., quasi-force-free FTEs. However, the tangential and the axial components of the net force are found to be significant outside FTEs. These observations suggest that the structure of FTEs, in particular, the magnetic field twist at the FTE's outer layers, $\theta_B = atan(B_L/B_M)$, may be affected by environmental net forces (e.g., *Zhao et al.*, 2016).

The observed internal and external magnetic and plasma characteristics suggest that FTEs evolve with time. Previously, the FTEs at the subsolar magnetopause have been found to range between 10^2-10^4 km in diameter. *Akhavan-Tafti et al*. (2018) suggested that FTEs are generated at ion-scale at the subsolar magnetopause and grow as they convect away toward flanks and high-latitude magnetopause where the magnetosheath pressure is much lower (*Sibeck et al*., 1990; *Eastwood et al*., 2012). From the three FTE growth mechanisms discussed in Figure 5-1, a radially-outward net force across the FTE boundary is required to cause the 'expansion' of FTEs as a function of distance from the subsolar region. However, our observations indicate that the net force inside FTEs is radially inward and that the radial component of the net force is negligible, i.e., force balance $\boldsymbol{J} \times \boldsymbol{B} - \nabla\boldsymbol{P} \sim 0$, outside FTEs. To further confirm or deny 'expansion' as an FTE growth mechanism, we examine the plasma pressure inside FTEs as a function of FTE diameter.

In the absence of magnetic reconnection, the irreversible adiabatic expansion of FTEs requires, cf. Appendix D, that the thermal pressure inside an ion-scale FTE to drop by at least two orders of magnitude, i.e., $p < 10^{-4}$ nPa, while the FTE grows macro-scale, >1 R_E in diameter. Figure 5-10*a* shows histograms of thermal ($P_{th} = Nk_BT$; where $T = T_i + T_e$ and k_B is the Boltzmann constant) and magnetic pressures measured inside the 55 FTEs at the subsolar magnetopause. The thermal and magnetic pressure distributions are nearly symmetric about their means at 1.5 nPa (0.3 $< P_{th}$ [nPa] < 5.0) and 0.5 nPa ($0.03 < P_m$ [nPa] < 3), respectively. Therefore, our observations do not confirm FTE growth via expansion.

We further examine the rate at which pressure varies as a function of FTE size. Figure 5-10*b* shows the change in average thermal, P_{th}, and magnetic pressures, P_m, as a function of FTE diameter. Here, pressures are averaged across the cross section of individual FTEs and plotted with respect to the FTE diameter. The 55 FTEs are grouped into bins (bin widths (BW) = 500km) and

the error bars indicate standard error of values inside each bin ($\sigma_{mean} \equiv \sigma/\sqrt{n}$; where n is the number of events in each bin). The solid curves represent power law fits to the data with shaded areas signifying the 95% confidence interval. The dependence of thermal pressure as a function of the FTE diameter, λ, is measured on average as $\lambda^{-0.24}$ compared to $\lambda^{-3.3}$, shown as a grey dashed-line, expected for adiabatic expansion of FTEs. This observed slow decay of the thermal pressure is consistent with plasma undergoing significant heating (Drake et al., 2006) further indicating that adiabatic expansion alone cannot explain the observed FTE range of diameters at the magnetopause. This result suggests that adiabatic FTE expansion in the subsolar magnetosheath is accompanied by processes that add *i)* magnetic flux, and *ii)* thermal pressure to the outer layers of FTEs. Hence, FTE growth can occur via three mechanisms:

1) *Continuous reconnection*: Ongoing multiple X-line reconnection can add magnetic layers to an existing FTE as predicted by simulations (Lee & Fu, 1985; Chen et al., 2017). The
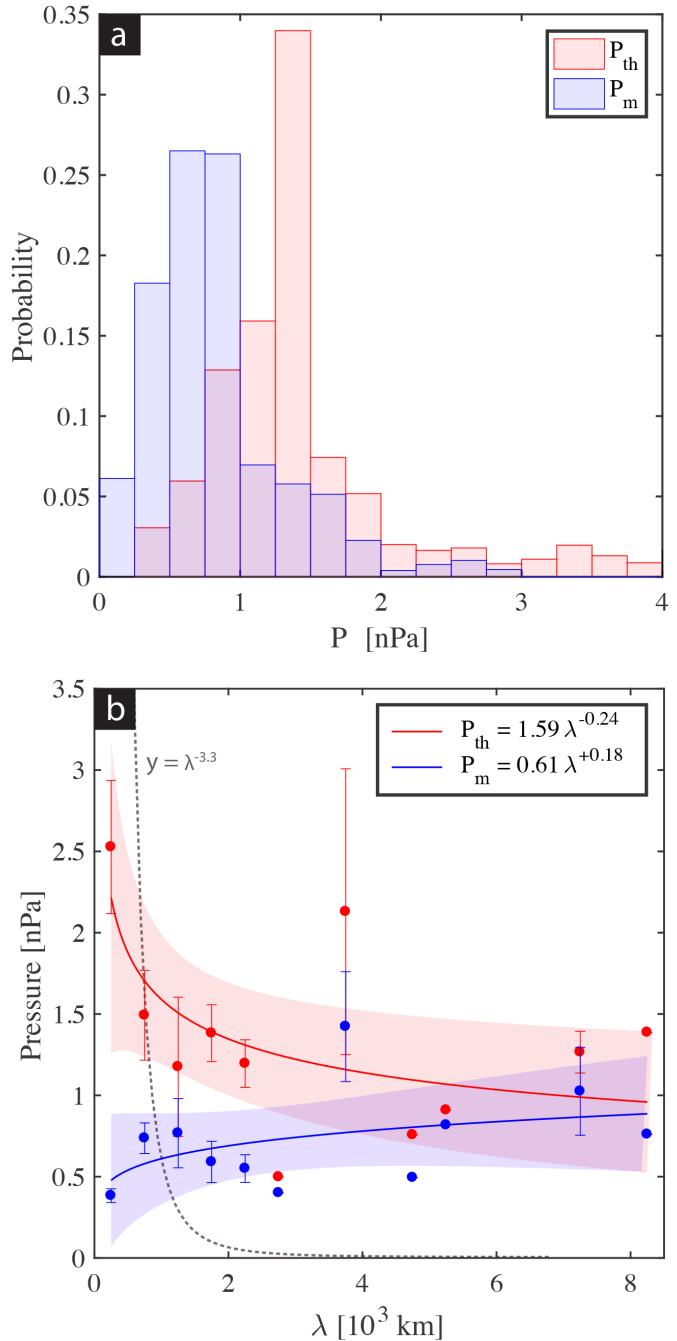
Figure 5-10: a) Histograms of thermal and magnetic pressure data points inside the 55 FTEs. b) Average thermal pressure and magnetic pressure profiles as a function of FTE diameter across the 55 FTEs. The circles indicate the bin-averaged (BW=500 km) values of pressures.

resulting increase in the structures' magnetic flux and plasma content can explain also the exponential distribution of magnetic flux inside subsolar FTEs (*Fermo et al.*, 2011; *Akhavan-Tafti et al.*, 2018). Further, plasma is heated in the exhausts of the primary X-line and plasma pressure is expected to increase in the outer layers of these flux ropes as new layers of helical magnetic flux are added and the FTE grows in size.

2) *Coalescence*: PIC simulations suggest that numerous small-scale flux ropes form in thin current sheets (e.g., *Drake & Lee*, 1977a, 1977b; *Galeev et al.*, 1978; *Hesse et al.*, 1999; *Pritchett*, 2001, 2005; *Ricci et al.*, 2004; *Daughton et al.*, 2011; *Nakamura et al.*, 2016; *Huang et al.*, 2016; *Lapenta et al.*, 2018). Neighboring small-scale flux ropes then reconnect with each other and, as a result, grow into larger merged FTEs (e.g., *Wang et al.*, 2016; *Alm et al.*, 2017; *Zhou et al.*, 2017). Through coalescence, the magnetic flux content of the merged FTE is equal to or greater than the larger of the two (i.e., *R. L. Fermo et al.*, 2011). However, plasma is added to the outer layers of the merged FTE and heating may occur as a result of the reconnection between the outer layers of the two merging FTEs.

3) *Adiabatic expansion due to the pressure-imbalance across the FTE boundary*: Upon formation at the subsolar magnetopause, FTEs advect with the magnetosheath flow toward the flanks and high-latitude regions where the magnetosheath thermal pressure is lower. The pressure-imbalance across the FTE boundary created as they are carried tailward may lead to the expansion of FTEs (*Eastwood et al.*, 2012). The expansion will continue until the internal magnetic forces and plasma pressure gradients are again in balance. FTEs expand to relieve the stress most likely produced by reconnection-driven heating of their outer layers.

5.5 Conclusions

In summary, we have used the high temporal and spatial-resolution MMS magnetic and plasma measurements to investigate the structure and dynamics of 55 subsolar FTEs. The force-free flux rope model was initially used to derive the relative distance of the spacecraft with respect to the FTE's central axis. i.e., the impact parameter. Having knowledge of the impact parameter facilitates the statistical study of cross-sectional profiles of physical parameters inside and outside FTEs. In particular, we observe that plasma density and plasma beta decrease near the FTE's central axis. We also find that the sum of the magnetic and thermal forces points radially inward at the outer layers of FTEs suggesting that plasmas and the frozen-in magnetic flux are accelerated toward the center of the FTE causing the field lines to compress. However, closer to the FTE's central axis, the axial net force is found to dominate and to accelerate the plasma along the FTE's axis and out of the region of compressing field lines.

Magnetic and plasma characteristics are also studied outside FTEs to gain insight into how changing external conditions may impact FTEs. It is observed that plasma beta outside the FTEs is, on average, significantly larger than the values inside. Similarly, the tangential and axial net force components are also found to enhance outside FTEs. Since magnetic field pitch angle is a function of the ratio of the tangential and axial magnetic field components, the enhanced tangential and axial net force components can likely impact the twist of magnetic field lines at the FTEs' outer layers.

We also find that the average thermal pressure inside FTEs decreases with increasing FTE diameter. If the 55 FTEs had started out with similar diameters and external conditions, the observed rate of thermal pressure decrease with increasing FTE diameter is shown to be slower than the rate expected for the adiabatic expansion of FTEs. This result suggests that the adiabatic expansion of FTEs at the subsolar magnetosheath is accompanied by processes, such as magnetic reconnection, that add *i)* magnetic flux, and *ii)* thermal pressure to the outer layers of FTEs. Magnetic reconnection at adjacent X-lines and/or coalescence with the neighboring FTEs is most likely the external source of magnetic flux and plasma. This continuous addition of magnetic flux and plasma, while causing an FTE to grow in size, drives a net radially-inward force which leads to the compression of the magnetic field lines and the acceleration of plasmas inside the FTE. This process leads naturally to the low-beta core region of the FTE as it evolves toward its final relaxed,

force-free state, i.e., the Taylor state (*Taylor*, 1986).

Chapter 6: MMS Observations of Plasma Heating Associated with FTE Growth

This Chapter is adopted from Akhavan-Tafti, M., Slavin, J. A., Sun, W. J., Le, G., & Gershman, D. J. (2019). MMS Observations of Plasma Heating Associated with FTE Growth. Geophysical Research Letters, 46.

6.1   Introduction

Satellite observations have long reported the presence of energetic particles, emanating from the solar corona, in the interplanetary medium and in planetary magnetospheres (e.g., *Murayama & Simpson*, 1968; *Retzler & Simpson*, 1969; *Meng*, 1971; *Meng & Anderson*, 1971; *Sarris et al.*, 1976; *Baker & Stone*, 1977; *Krimigis & Sarris*, 1979; *Retinò et al.*, 2008; *Huang et al.*, 2012; *Dewey et al.*, 2017). The key outstanding questions regard the underlying physical mechanisms producing such energetic particles and their transport. The proposed mechanisms include fast and slow shocks, electromagnetic waves, and magnetic reconnection (e.g., *Miller et al.*, 1997; *Aschwanden*, 2002; *Drake, Swisdak, Che, et al.*, 2006; *Krucker et al.*, 2008; *Guo et al.*, 2015; *Benz*, 2017).

Particle-in-cell (PIC) simulations and in-situ observations have attributed magnetic reconnection-driven plasma acceleration and heating to three major mechanisms (e.g., *Chen, Bhattacharjee, et al.*, 2008; *Dahlin et al.*, 2014, 2015, 2016, 2017; *Kagan et al.*, 2017; *Büchner et al.*, 2018). In the first mechanism, plasma acceleration and heating occur inside or near the diffusion region, where collisionless plasma processes facilitate the changes in magnetic connection through the generation of dissipative electric fields (e.g., *Zenitani & Hoshino*, 2001, 2007, 2008; *Lyubarsky & Liverts*, 2008; *Oka et al.*, 2010; *Uzdensky et al.*, 2011; *Bessho & Bhattacharjee*, 2012; *Cerutti et al.*, 2012). Secondly, acceleration and heating occur in the downstream of the reconnection site, between an adjacent X-line and the edges of a flux rope, where the outflowing plasma first encounters sharp spatial magnetic field variations (i.e., strong magnetic field gradients) (e.g., *Hoshino et al.*, 2001; *Jaroschek et al.*, 2004; *Zenitani & Hoshino*,

2007; *Pritchett*, 2008). Thirdly, acceleration and heating occur inside flux ropes, where the newly-reconnected magnetic flux piles up, particles can become accelerated (*Drake, Swisdak, Che, et al.*, 2006; *Drake et al.*, 2010; *Kowal et al.*, 2011).

Simulations suggest that plasmas are accelerated along reconnecting magnetic field lines due to parallel electric fields and curvature drift, i.e., Fermi acceleration (*Dahlin et al.*, 2014; *Muñoz & Buechner*, 2017). In the guiding-center limit, where the first adiabatic invariant is conserved, plasma acceleration is described by (*Northrop*, 1963; *Drake et al.*, 2019):

$$dU/dt = \dot{U} = E_\parallel J_\parallel + {p_\perp}/{B} \left(\partial B/\partial t + \boldsymbol{u}_E \cdot \boldsymbol{\nabla}\boldsymbol{B}\right) + \left(p_\parallel + \rho\, u_\parallel^2\right) \boldsymbol{u}_E \cdot \boldsymbol{\kappa},$$

where U is the total kinetic energy, $p_\parallel$ and $p_\perp$ are the parallel and perpendicular (with respect to the ambient magnetic field B) thermal pressures, respectively. $\boldsymbol{u}_E$ is the E×B drift velocity. ρ and $u_\parallel$ denote the mass density and the parallel bulk velocity, respectively, and the curvature $\boldsymbol{\kappa} = (\boldsymbol{B} \cdot \boldsymbol{\nabla})\,\boldsymbol{B}/B^2$. Term 1 ($\dot{U}_1$; parallel electric fields) the first term on the right-hand side, describes acceleration due to parallel electric fields and is independent of frame of reference. Conservation of the first adiabatic invariant, μ, is invoked in the second term, Term 2 ($\dot{U}_2$; betatron process). Here, the gradient-B drift accelerates particles via betatron acceleration. The last term, Term 3 ($\dot{U}_3$; first-order Fermi process), describes curvature drift driven by relaxing magnetic field lines which accelerate particles parallel to B through Fermi acceleration.

The simulations by *Egedal et al.* (2012) suggested that parallel electric fields can accelerate electrons over spatial scales larger than the previously-thought electron diffusion regions. Later simulations by *Dahlin et al.* (2016) contradicted these results. Instead, the authors argued that Fermi acceleration dominates electron heating, especially in regimes of strong magnetic shear. These results were re-examined by *Zhou et al.* (2018) using three-dimensional PIC simulations. They concluded that parallel electric fields are the dominant electron acceleration mechanism. More notably, small-scale flux ropes were found to play an essential role in accelerating electrons, in agreement with the Cluster observations by *Fu, Xu, et al.* (2019).

MMS observations (*Akhavan-Tafti et al.*, 2018) and simulations (*Raeder*, 2006; *Fermo et al.*, 2011; *Hoilijoki et al.*, 2019) indicate that FTEs form in the subsolar region and grow as they convect toward the flanks and high-latitude magnetopause. Internal plasma pressure is observed to decrease sub-adiabatically with increasing FTE diameter (*Akhavan-Tafti et al.*, 2019) suggesting the presence of internal plasma acceleration and heating processes. *Akhavan-Tafti et al.* (2019)

further showed the presence of residual net force inside FTEs which can accelerate plasmas. Herein, we quantify the contributions of acceleration mechanisms in the guiding-center approximation using MMS high temporal and spatial-resolution fields and plasma measurements. First, a case study event is presented as a typical example of plasma moments and distributions across and in the environments surrounding two neighboring FTEs of different scale sizes. Next, the contributions of the parallel electric fields, betatron acceleration, and the first-order Fermi acceleration are determined directly from the MMS measurements inside and at the outer perimeters of 55 subsolar, quasi-force-free FTEs, identified by *Akhavan-Tafti et al.* (2018, 2019). It is concluded that magnetic reconnection plays a long-lasting role in accelerating plasmas at the magnetopause by generating FTE-type flux ropes which then grow and further accelerate plasmas.

6.2   Methods

The multi-point analysis techniques are used to calculate spatial gradients, including magnetic gradient $\nabla \boldsymbol{b}$ and curvature $\boldsymbol{\kappa} = (\boldsymbol{b} \cdot \nabla) \, \boldsymbol{b}$ (*Zhao et al.*, 2016; *Akhavan-Tafti et al.*, 2019), at the barycenter of the four MMS spacecraft (*Harvey*, 1998). Plasma current density is determined from the fast plasma investigation (FPI; *Pollock et al.*, 2016) plasma moments at the barycenter (*Akhavan-Tafti et al.*, 2018). The four-spacecraft average plasma and electric field double probe (EDP; *Ergun et al.*, 2016; *Lindqvist et al.*, 2016; *Torbert, Russell, et al.*, 2016) electric field measurements are determined at the barycenter and interpolated to match the flux-gate magnetometer (FGM; *Russell et al.*, 2016) time resolution at 128 samples per second. The induced local magnetic fields is estimated from Faraday's law, $\partial \mathbf{B} / \partial t = -\nabla \times \mathbf{E}$, wherein the component along the E×B drift is calculated as $\partial \mathrm{B} / \partial t = 1/|\boldsymbol{u}_E| \left(\boldsymbol{u}_E \cdot \partial \mathbf{B}/\partial t\right)$, where u_E represents the E×B drift velocity. The four MMS spacecraft were maintained at a tetrahedron formation at an average separation of 10 km throughout the duration of the interval of interest (*Burch, Moore, et al.*, 2016).

FTEs are modeled as force-free flux ropes in order to determine their scale size, impact parameter (IP; defined as the relative distance from the FTE's central axis at the spacecraft closest approach cf. Figure 11 of Chapter 4), and geometry. Fifty-five FTE-type flux ropes are selected based on the following criteria: 1) small impact parameter (IP < 0.5), and 2) cylindrical symmetry (force-free model goodness of fit parameter, $\chi^2 < 0.1$; cf. *Akhavan-Tafti et al.*, 2018; *Akhavan-Tafti et al.*, 2019).

6.3   Analysis and Results

6.3.1   Case Study

The magnetopause crossing of November 17, 2015 was first examined and reported by *Zhou et al.* (2017). The boundary crossing was marked by large ion jet reversals corresponding to a dissipative interaction of two neighboring FTEs. As shown in Figure6-1*a*, the magnetic field magnitude and vector components indicate the presence of two force-free FTEs (e.g., *Russell & Elphic*, 1978; *Akhavan-Tafti et al.*, 2019), labeled as 'FTE 1' and 'FTE 2,' centered at 02:20:48 UT and 02:21:24 UT. The FTEs are identified with their bipolar magnetic signatures coinciding with an enhancement in the axial and total magnetic fields. Plasma distribution along the field lines are used to identify FTE boundaries (e.g., *Lv et al.*, 2016).

FTE 1 is 4000 km in diameter, λ, with a modeled core field magnitude of 60 nT corresponding to a magnetic flux content 300 kWb (*Akhavan-Tafti et al.*, 2018). FTE 2 is much smaller in scale, $\lambda \sim 2000$ km, and has a weaker core magnetic field magnitude, $|B| = 45$ nT, and smaller flux content 40 kWb. Using the timing analysis, it is estimated that FTE 1 and FTE 2 convect at speeds 100 km/s and 180 km/s, respectively. Electrons and ions are found to remain frozen-in throughout the crossings.

The parallel $T_{i\,/\!/}$ and perpendicular $T_{i\perp}$ ion temperature components significantly increase inside the FTEs, $\Delta T_{i\,/\!/} = +150$ eV and $\Delta T_{i\perp} = +100$ eV. *Panel c* represents the acceleration terms which are boxcar averaged in 2-second intervals. The betatron process, $\dot{U}_{i,2}$ (green), is the dominant acceleration mechanism in this particular event. The contribution by the first order Fermi acceleration process (red) is small, $\dot{U}_{i,3} < 0.3$ nW/m^3, and the acceleration due to parallel electric fields (blue), $\dot{U}_{i,1}$, is shown, in *panel c*, to be negligible inside and in the environments surrounding the two FTEs (e.g., *Dahlin et al.*, 2016). The latter may suggest the absence of reconnection-driven dynamics, i.e., parallel electric fields, at the outer layers of the two FTEs. The scalar sum of the three acceleration mechanisms $\dot{U}_{tot}$ closely matches that of the betatron process. In particular, outside FTEs, $\dot{U}_{i,2}$ is negative suggesting that ions (E×B) drift toward a region of weakening magnetic field, i.e., away from the FTE. Inside the FTE, the magnitude of betatron cooling reduces and becomes positive once crossing the FTE's central axis. The Fermi acceleration is negative on the trailing edge of FTE 1, suggesting that the stretched outer magnetic layers at the trailing end

106

of FTE 1 are likely shortening, i.e., reduced curvature. Finally, the acceleration signatures, esp. the betatron process, have similar profiles across FTE 1 and FTE 2. However, the betatron process is larger in magnitude inside and across the smaller FTE.

Panels d-h show the ion energy spectra binned based on their pitch angle distribution (PAD) with respect to the ambient magnetic field direction. Ion bulk velocity is subtracted from the energy spectra. Each PAD bin is 20 degrees in width. At the leading edge of FTE 1, increased low-energy (E_{ion} [keV] < 0.2) ion differential energy fluxes are observed at PAD < 20 degrees and 80 < PAD < 100 degrees. While plasma density drops inside FTE 1, the ion differential energy fluxes with 120 < PAD < 140 degrees and 160 < PAD < 180 degrees increase. At 02:21:00 UT, at the trailing edge of FTE 1, the parallel ion population completely vanishes and the ion distribution becomes predominantly anti-parallel, PAD > 120 degrees. At this point, the spacecraft enter a higher-energy ($0.2 < E_{ion}$ [keV] < 2.0) magnetosheath ion population with PAD > 120 degrees. Once encountering FTE 2, the energy of the anti-parallel ions is significantly reduced and new parallel and perpendicular ion peaks appear, PAD < 100 degrees. After crossing FTE 2, the ion population returns to the higher-energy ($0.2 < E_{ion}$ [keV] < 2.0) magnetosheath ion population with PAD > 120 degrees.

Panels i-j represent the corresponding phase space density (PSD) cuts inside and outside FTE 1 and FTE 2 as a function of ion energy, respectively. The solid lines in *panel i* and *panel j* are the PSD cut averages outside FTE 1 (02:20:30 - 02:20:35 UT) and FTE 2 (02:21:25.5 - 02:21:29.5 UT), respectively. The dashed lines in *panel i* and *panel j* are the PSD cut averages inside FTE 1 (02:20:50 - 02:20:55 UT) and FTE 2 (02:21:24 - 02:21:24.5 UT), respectively. The shift in energy from outside to inside the FTEs are shaded for three energy bins (black: [0-20] degrees, cyan: [80-100] degrees, and red: [160-180] degrees). The energy shift is, on average, more significant in the larger FTE, FTE 1, than FTE 2. The shift in the mid-to-high energy, $0.2 < E_{ion}$ [keV] < 10.0, ions is also found to be, on average, positive from the environments surrounding the two FTEs to the inside, suggesting that these ions may have been accelerated inside FTEs. More importantly, the above two observations indicate that the peak ion acceleration inside the larger FTE is more pronounced than the smaller FTE. This may suggest that the plasma inside the larger FTE has been heated for a longer duration, i.e., cumulative effect, than those inside the smaller, less-developed FTE.
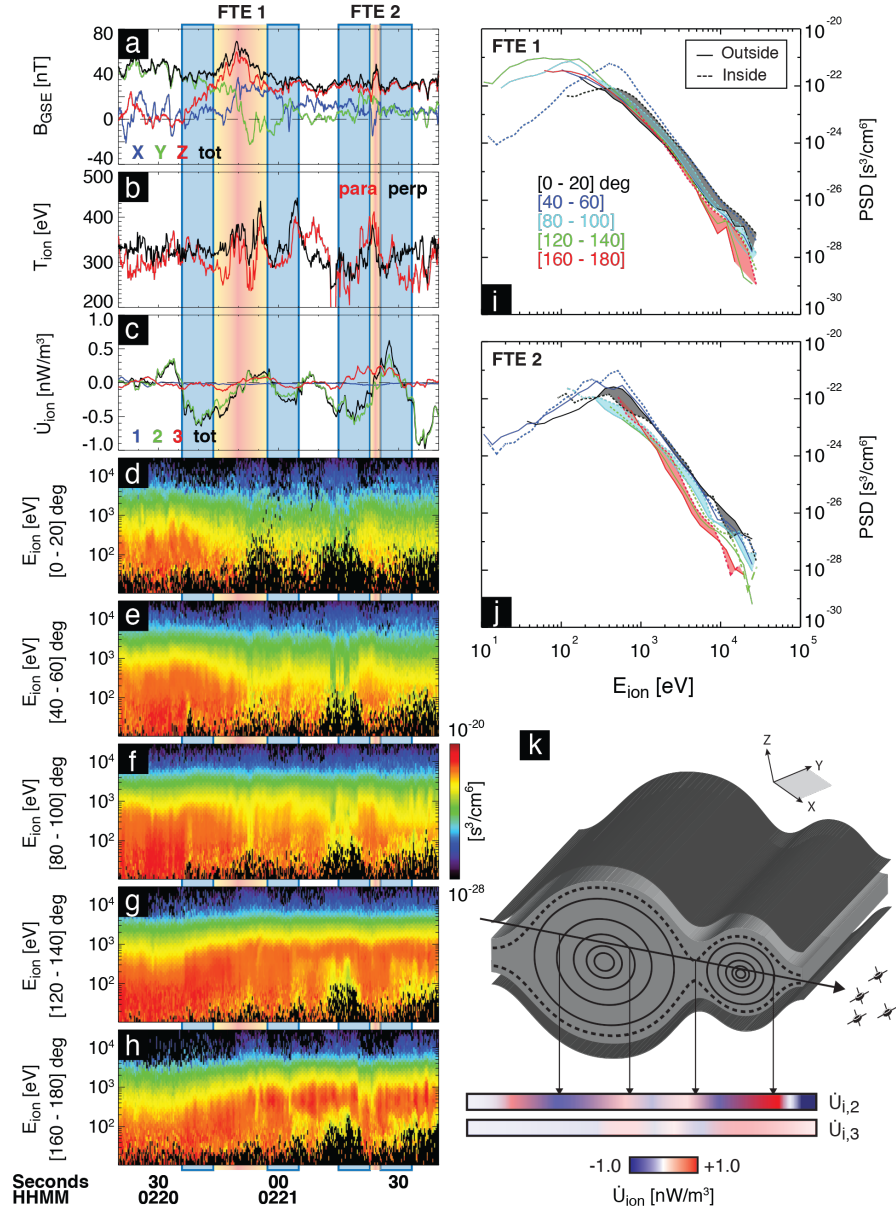
Figure 6-1: Panels include: a) magnetic field magnitude and components in the GSE coordinates, b) ion parallel (red) and perpendicular (black) temperature components, c) box-car averaged (2-seconds) ion acceleration mechanisms, $\dot{U}$, due to parallel electric fields (Term 1; blue), betatron acceleration (Term 2; green), and Fermi acceleration (Term 3; red) as well as the scalar sum of the three terms shown in black. Ion energy spectra (bulk ion velocity subtracted) for pitch angle distributions: d) 0-20 degrees, e) 40-60 degrees, f) 80-100 degrees, g) 120-140 degrees, and h) 160-180 degrees. Time-averaged ion energy spectra inside (dashed line) and outside (solid line) i) FTE 1, and j) FTE 2 at five PADs. The shaded areas represent the shift in ion energy inside and outside each FTE. k) Cartoon schematic of the relative orientations, spacecraft trajectory, and the observed (see panel c) magnitudes and directions of ion acceleration due to betatron and Fermi acceleration across FTE 1 and FTE 2. The gradient and solid color shadings corresponding to the observations made 'inside' and 'outside' the FTEs, respectively.

108

Panel k demonstrates a cartoon illustration of the spacecraft trajectory across FTE 1 & 2. The magnitude and the sign of the betatron, $\dot{U}_{i,2}$, and Fermi, $\dot{U}_{i,3}$, processes are shown as color shades (red: positive and blue: negative). As shown in *panel c*, our observations indicate that the betatron process is larger inside the two FTEs than the Fermi process, therefore, marked in the illustration with darker shades. The contribution from the parallel electric fields is negligible in this particular event, hence, not included in this cartoon illustration. In addition, as the observations suggest, the rate of energization is larger inside and across the smaller FTE.

6.3.2 Statistical Study

Fifty-five quasi-force-free FTEs are selected at the subsolar region within 22 minutes of the magnetic noon during two months of MMS passes near the equatorial region, 11/03/2015 — 12/28/2015. The FTEs are identified based on their helical and flux rope-like structures (e.g., *Russell & Elphic*, 1978; *Akhavan-Tafti et al.*, 2018). Each FTE is initially modeled as a force-free flux rope (*Lepping et al.*, 1990; *Akhavan-Tafti et al.*, 2018) in order to determine the FTE's diameter and the relative distance from its central axis at the closest approach, i.e., impact parameter (IP). These information and the high temporal and spatial-resolution MMS fields and plasma measurements enabled us to determine the contributions of the plasma acceleration mechanisms inside and outside FTEs. Here, the term 'outside' refers to the FTEs' outer perimeters in the draping field region surrounding each FTE within 10 local ion inertial lengths, d_i (*Farrugia et al.*, 1988; *Akhavan-Tafti et al.*, 2019). Outside FTEs include field lines in the magnetosheath which, in many cases, are in the near reconnection exhaust regions of X-lines that generated the FTEs (e.g., *Lee & Fu*, 1985) or contributed to their growth (e.g., *Akhavan-Tafti et al.*, 2019). As shown by *Akhavan-Tafti et al.* (2019), the electrons and ions remained frozen-in inside the 55 FTEs further validating the guiding-center limit.

Figure 6-2 compares averaged cross-sectional profiles of the energization mechanisms, including parallel electric fields and betatron and first-order Fermi processes, inside and outside FTEs. The observations are further divided between two regions: 1) leading (front) half of the FTE, and 2) trailing (rear) half of the FTE. To achieve this, the FTE's convection direction is determined in the spacecraft's frame of reference (*Korotova et al.*, 2009). For instance, the spacecraft encounters the leading edge of the FTE, if $\hat{v}_{\text{FTE}} \cdot \hat{n}_{\text{S/C}} < 0$, where $\hat{v}_{\text{FTE}}$ and $\hat{n}_{\text{S/C}}$ represent FTE displacement and spacecraft trajectory unit vectors, respectively. IP=0 indicates the central region of the FTE and IP=$\pm$1 denote the FTE front and rear 'edges', beyond which the magnetic field connectivity changes and magnetic fields are no longer bound to the structure (*Rijnbeek et al.*, 1987; *C. J. Farrugia et al.*, 1988, 2016). In order to take into account environmental variability between different orbits, all energization terms, $\dot{U}_{i,x}$, are normalized by an analytical weight (Appendix B), defined as the ratio of the magnitudes of the universal average of $\dot{U}_{i,x}$ determined across 55 independent FTE events and inside each individual event.

110

Figure 6-2: Cross sectional profiles of plasma acceleration mechanisms, including parallel electric field ($\dot{U}_1$; blue), betatron acceleration ($\dot{U}_2$; green), and Fermi acceleration ($\dot{U}_3$; red), inside and outside the 55 FTEs for a) ions, and b) electrons. All data points inside the 55 FTEs are grouped and averaged inside impact parameter bins of bin width (BW: IP=0.1). All data points outside the 55 FTEs are grouped and averaged inside bins of BW=1 d_i. Observations are further divided between the leading and trailing halves. The error bar denotes the standard error inside each individual bin. The dashed line represents the universal average of each parameter across 55 FTEs. c) Cartoon illustration of a convecting flux rope interacting with the surrounding environment, based on the observations in panels a and b.
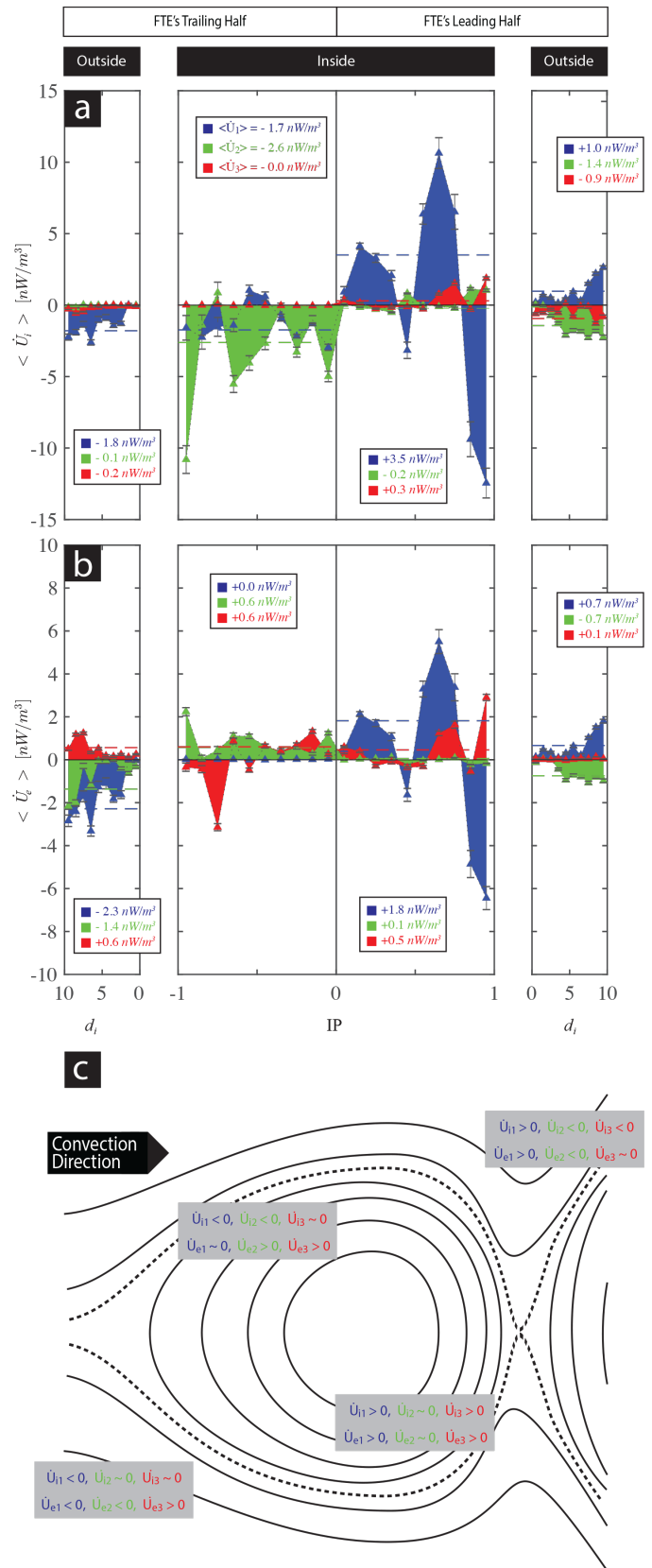
The acceleration mechanisms observed inside FTEs and $|\dot{U}_x|$ [nW/m³] < 30.0 (more than 90% of all observations are within $|\dot{U}_x|$ [nW/m³] < 30.0) are binned independently (bin width (BW): IP=0.1) and averaged across all 55 FTEs. Observations outside the 55 FTEs are bin-averaged (BW=1 d_i; where $d_i = c/\omega_{pi} = 2.28 \times 10^7$ $(N_i)^{-1/2}$ cm, is the average local ion inertial length and is a function of average ion density, N_i, outside each FTE). The error bars indicate the normalized variations of parameters inside individual bins and is known as the standard error, $\sigma_{mean} \equiv \sigma/\sqrt{n}$; where σ and n are the standard deviation and the number of data points in each bin, respectively.

Plasma energization inside and at the outer layers of FTEs is asymmetric. *Panels a and b* show that the acceleration (or deceleration) of ions and electrons is most significant inside FTEs at the leading edge. Ions inside the leading part of the FTEs are, on average, net heated, $\dot{U}_{i,x} > 0$, parallel ($\dot{U}_{i,1}$ = +3.5 nW/m³ and $\dot{U}_{i,3}$ = +0.3 nW/m³) to B. The acceleration magnitude inside the leading part of the FTEs is nearly 3 times larger than those observed outside, at the leading part of the FTE. Ions and electrons are shown to decelerate perpendicular to the ambient magnetosheath B at the leading and trailing edges of FTEs.

Inside FTEs, ions are net-heated parallel to B and net-cooled perpendicular to B, whereas electrons experience net parallel and perpendicular heating. Parallel electric fields become the dominant energization mechanism at the leading part of the FTE, accelerating both ions and electrons parallel to B. The acceleration enhances (and fluctuates) farther away from the FTE's core region, IP=0. Ions are, on average, cooled at the trailing edge of the FTE ($\dot{U}_{i,1}$ = -1.7 nW/m³ and $\dot{U}_{i,2}$ = -2.6 nW/m³). Unlike ions, electrons are, on average, accelerated parallel and perpendicular to B in the trailing half, $\dot{U}_{e,3}$ = +0.6 nW/m³ and $\dot{U}_{e,2}$ = +0.6 nW/m³. The Fermi process is found to steadily accelerate electrons inside FTEs.

Outside FTEs, parallel electric fields remain the most significant of the three energization mechanisms. Parallel electric fields accelerate ions and electrons parallel to B at the leading edge of subsolar FTEs, while they contribute to parallel cooling of the plasma at the trailing edge of the FTE. Outside FTEs at the trailing edge, both ions and electrons are cooled perpendicular to B indicating a region of weakening magnetic field intensity. Similarly, the Fermi process is found to cool both ions and electrons outside the FTEs, suggesting relaxing field lines, i.e., reduced curvature. It is also found that the three energization mechanisms enhance in magnitude farther

away from the FTE front and rear edges.

Panel c provides a cartoon summary of the observations. As the cartoon illustration indicates, one possible explanation is that FTEs convecting away from the subsolar region may reconnect with the surrounding environment (e.g., *Zhou et al.*, 2017; *Akhavan-Tafti et al.*, 2019; *Øieroset et al.*, 2019), therefore, resulting in the formation of strong parallel electric fields which can accelerate plasmas (*Jan Egedal et al.*, 2012). The trailing magnetic field lines, on the other hand, continue to relax resulting in cooling ions and reduced electron heating.

We further examine how the rate at which total acceleration, defined as the magnitude of the sum of the three acceleration mechanisms, varies as a function of FTE diameter. Figure 6-3*a* shows the change in average total acceleration magnitude as a function of FTE diameter. Here, total acceleration magnitudes are averaged inside individual FTEs and plotted with respect to the FTE diameter. The solid curves represent power law fits to the data with shaded areas demonstrating the 95% confidence interval. The dependence of the total acceleration magnitude as a function of the FTE diameter, λ, is measured on average as $\lambda^{-0.55}$ for electrons and $\lambda^{-0.72}$ for ions. These suggest, in agreement with Figure 6-1, that acceleration is most significant inside smaller, and likely younger, FTEs. The observations also show that as FTEs grow larger they become more force-free (e.g., *Taylor*, 1986; *Akhavan-Tafti et al.*, 2018) resulting in reduced plasma acceleration. Another likely contributing factor to the observed decline in average heating with FTE diameter may be the reduced gradient scale length (i.e., $\nabla \propto 1/\lambda$).

Total acceleration is reduced with increasing FTE diameter; however, FTE growth continuously accelerates plasmas inside FTEs resulting in higher energy budget than ions and electrons observed inside smaller FTEs. The table on the right hand corner of Figure 6-3*a* further summarizes the coefficients *a* and *b* for power-law fits for individual electron (grey) and ion (red) acceleration terms as a function of the FTE diameter, $\dot{U} = a\,\lambda^{\,b}$. The values are bin-averaged across all 55 FTEs. In particular, plasma heating by parallel electric fields decreases slowly compared to the betatron and Fermi processes. Fermi acceleration is found to drop fastest, $b = -1.13$, with increasing FTE diameter.

6.4 Discussion and Conclusions

In this letter, we have investigated the contributions of parallel electric fields, betatron, and first-order Fermi processes to plasma acceleration and heating inside FTEs and in the surrounding environments.

First, the MMS plasma and fields measurements are investigated inside a system of two neighboring FTEs with different scale sizes. It is also observed that the betatron process reverses near the FTE's central axis suggesting that ions are decelerated on one side of the FTE, while accelerated on the other side of the FTE, therefore, conserving total energy. As illustrated in Figure 6-3*b*, two scenarios may explain this observation:

1. The interaction of FTE-type flux ropes with the surrounding magnetosheath environment (e.g., *Slavin et al.*, 2003; *Fu et al.*, 2011; *Zhu et al.*, 2019), and/or

2. Reconnection-driven interaction with the surrounding environment (e.g., *Lapenta et al.*, 2016), including FTE coalescence (e.g., *Wang et al.*, 2016a; *Zhou et al.*, 2017), and the associated parallel electric fields (e.g., *Schindler et al.*, 1988; *Ergun et al.*, 2017).

In both scenarios, the field lines at the impacted edge of the FTE will be compressed, while the field lines in the opposite edge expand adiabatically (*Akhavan-Tafti et al.*, 2019). Therefore, in order to conserve the first adiabatic invariant μ, the plasmas in the region of compressing field lines, i.e., enhanced ∇B (e.g., *Øieroset et al.*, 2019), will gain energy while the plasma population in the region of expanding field lines, i.e., weakening B and ∇B, will have reduced total energy. One possible consequence of this local betatron reversal is the energy (e.g., *Matsui et al.*, 2019) and/or distribution bifurcation (e.g., *Artemyev et al.*, 2014; *Zhu et al.*, 2019) of the differential energy flux of the seed plasma population, wherein part of the seed plasma population is accelerated while others decelerate.

Next, we determine the average contributions of the acceleration processes inside an ensemble of 55 subsolar, quasi-force free FTEs including the region at their outer perimeters. This region just outside of the FTEs in the magnetosheath is important because, in many cases, it is in the near-reconnection exhaust of adjacent X-line.

$\dot{U}_{tot}(\lambda) = a\,\lambda^{\,b}$				
	a	b	a	b
$\dot{U}_1$	0.06	-0.75	0.06	-0.74
$\dot{U}_2$	0.02	-0.77	0.17	-0.77
$\dot{U}_3$	0.01	-1.13	0.09	-1.13
$\dot{U}_{tot}$	0.07	-0.77	0.21	-0.80

$< |\dot{U}_e| > = 0.13\ \lambda^{-0.55}$
$< |\dot{U}_i| > = 0.68\ \lambda^{-0.72}$

Scenario 1) Environmental Impact

Scenario 2) Adjacent X-line
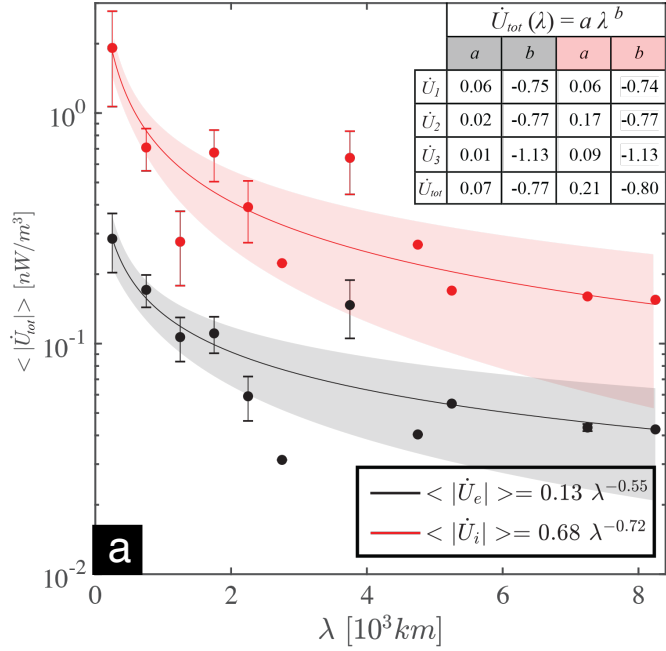
Figure 6-3: a) Ion (red) and electron (black) total acceleration magnitudes as a function of FTE diameter across the 55 FTEs. The circles indicate the bin-averaged (BW = 500 km) values of total acceleration. The table represents the dependence of bin-averaged acceleration mechanisms as a function of FTE diameter for both electrons (grey) and ions (red), and b) Cartoon illustrations of two potential scenarios to explain the observed reversal in plasma acceleration near the FTE's central axis. The shading suggests the magnitude and the direction of plasma acceleration wherein red and blue indicate positive and negative values, respectively. The dashed lines represent a reconnection separatrix (and X-line).
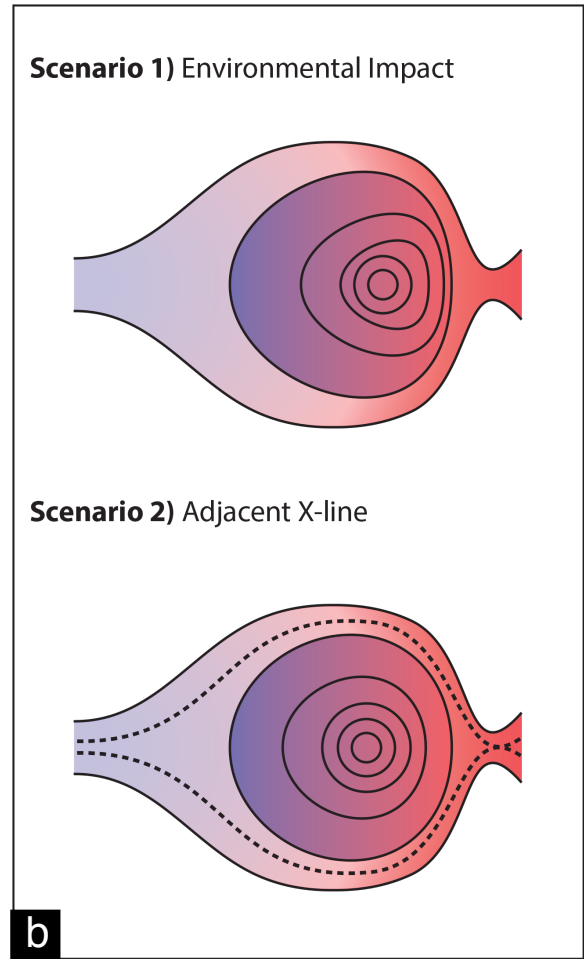
Our results show that plasma energization inside and at the outer layers of FTEs is found to be asymmetric. It is further shown that:

I. Ions and electrons are, on average, net heated, $\dot{U} > 0$, inside and just outside FTEs. We find that, on average, parallel electric fields are the dominant heating mechanism (70 - 90% of $\dot{U}_{tot}$) for both ions and electrons, at the leading half of FTEs, in agreement with the kinetic simulation runs by *Egedal et al.* (2012) and *Zhou et al.* (2018). At the leading part of the structure, ions and electrons gain further parallel energy via the Fermi process.

As listed in the table in Figure 6-3*a*, electron heating due to Fermi acceleration is negligible. In contrast, ion heating due to the Fermi process is significant at small FTE scales, though it decreases sharply with increasing FTE diameter. The betatron heating of ions is dominant at small FTE scales. These results and the observed dominant plasma heating by parallel electric fields may indicate the occurrence of secondary reconnection, including FTE coalescence, inside and/or between neighboring FTEs (e.g., *Fermo et al.*, 2011; *Wang et al.*, 2016; *Zhou et al.*, 2017).

II. Inside FTEs, at the leading edge of FTEs, ions and electrons are preferentially accelerated parallel to B (e.g., *Shay et al.*, 2014), farther away from the FTE's central axis, where |B| is reduced. Plasma energization drops by ~75% across the FTE's leading boundary. At the trailing part of FTEs, ions are cooled mainly by the betatron process and the electron net heating is reduced.

III. Outside FTEs, at the leading edge of FTEs, ions and electrons are accelerated parallel to B by parallel electric fields. Ions are shown to gain, on average, 30% more energy than electrons from parallel electric fields (*Pritchett*, 2008; *Haggerty et al.*, 2015). At the trailing edge of the FTEs, both ions and electrons are cooled perpendicular to B, indicating a region of relaxing field topology.

IV. MMS observations suggest that acceleration mechanisms are enhanced farther away from the FTEs' outer edge. This suggests:

a. Farther away from the FTE edge, most likely nearer to the reconnection X-line(s) (e.g., *Dahlin et al.*, 2015; *Fu et al.*, 2019), parallel electric fields and magnetic field gradients are most effective in plasma acceleration (see Figure 8 in *Zhou et al.*,

2018), and/or

    b. Force-free FTEs may slow down the rate at which plasmas are accelerated in the reconnection exhaust (e.g., *Taylor*, 1974). As FTEs grow, they seek to reach a lower energy state by re-arranging magnetic field lines. At lower magnetic energy-state, the trapped plasma population will experience small acceleration compared to the plasmas at the outer boundaries of FTEs near the reconnection exhaust.

V.   Statistical analysis of the MMS observations show that the magnitude of the total ion acceleration inside FTEs is proportional to $\lambda^{-0.7}$. However, energetic ions are more often observed inside FTEs of larger diameter. These results suggest that the plasmas inside smaller FTEs are continuously accelerated while the FTEs grow. Even though, the rate at which plasmas are accelerated slows down inside larger FTEs, the total plasma energy budget continues to increase with time, resulting in increased differential flux of energetic ions (e.g., $0.2 < E_{ion}$ [keV] < 10.0) inside FTEs. Similar long-lasting, evolutionary processes may also contribute to the generation of energetic plasmas observed in other plasma environments (e.g., *Ji et al.*, 1998; *Milan et al.*, 2000; *Øieroset et al.*, 2002; *Lin et al.*, 2003; *Angelopoulos et al.*, 2008; *Dewey et al.*, 2017; *Fu et al.*, 2019).

The present study focuses on the contributions of parallel electric fields, betatron, and first-order Fermi processes to plasma acceleration and heating inside FTEs and in the surrounding environments. Future studies will further include other key terms such as polarization drift associated with ion acceleration across reconnecting fields with a shear angle (e.g., *Kleva et al.*, 1995; *Pritchett & Coroniti*, 2004; *Eastwood et al.*, 2018) and ion inertial drift (e.g., *Drake et al.*, 2009; *Phan et al.*, 2014; *Haggerty et al.*, 2015). Global simulations are also essential in understanding the FTE evolution and its role in magnetosheath heating (e.g., *Chen et al.*, 2017; *Jarvinen et al.*, 2018).

Chapter 7: Comparative Analysis of the Vlasiator Simulations and MMS Observations of Multiple X-Line Reconnection and Flux Transfer Events

This Chapter is adopted from Akhavan-Tafti, M., Palmroth, M., Slavin, J. A., Battarbee, M., Ganse, U., Grandin, M., Le, G., Gershman, D. J., Eastwood, J. P., Stawarz, J. E., Comparative Analysis of the Vlasiator Simulations and MMS Observations of Multiple X-Line Reconnection and Flux Transfer Events, submitted to the Journal of Geophysical Research: Space Physics.

7.1 Introduction

Akhavan-Tafti et al. (2019) classified FTE growth mechanisms into two main categories: 1) FTE growth via adiabatic expansion due to decreasing external pressure away from the reconnection region, and 2) magnetic reconnection. In the latter category, FTE growth occurs via continuous supply of magnetic flux and plasma to the outer layers of FTEs by reconnection at adjacent X-lines and/or coalescence with the neighboring FTEs.

Figure 7-1 shows a magnetic island which is a 2D projection of a flux rope generated due to primary multiple X-lines reconnection. The magnetic island can grow via continuous reconnection (Akhavan-Tafti et al., 2019) at adjacent X-lines. The X-lines at the two ends of the magnetic island are represented as ion diffusion regions (IDR). Inside IDR, inflowing ions (V_{in}; green arrows) are demagnetized and accelerated outward as perpendicular jets (solid red arrows) and field-aligned currents (FACs; red-stroke arrows). The electron diffusion region (EDR), not shown here, is located inside the IDR (*Burch et al.*, 2016). Electrons become demagnetized inside the EDR before becoming energized by the reconnection's magnetic-to-kinetic energy conversion.

At the subsolar magnetopause, where FTEs are likely generated (e.g., *Lee & Fu*, 1985; *Akhavan-Tafti et al.*, 2018), the magnetic field strength and plasma properties of reconnecting field lines are asymmetric across the X-line. Theory and observations have linked this asymmetry to non-Maxwellian anisotropic ion and electron velocity distribution functions (VDFs) in the inflow

and outflow regions (e.g., *Egedal et al.*, 2011; *Hesse et al.*, 2014; *Bessho et al.*, 2016; *Burch et al.*, 2016).

Sharp spatial gradients, sub-gyro-period temporal variations, or sources and sinks in phase space can give rise to non-gyrotropic distribution functions. Gyrotropy is a measure of a distribution function's weighted average of variances of velocities perpendicular to the local field direction (*Swisdak*, 2016; *Che et al.*, 2018). Non-gyrotropic plasma populations depend on gyro-phase angle and, therefore, they are not in thermal equilibrium. They carry excess energy and may excite unstable waves (e.g., *Motschmann et al.*, 1999). Crescent-shaped VDFs are a class of non-gyrotropic plasma distributions. They are indicative of the reconnection diffusion region and are often observed in spacecraft measurements (*Nagai et al.*, 2015; *Burch et al.*, 2016) and simulations (e.g., *Hesse et al.*, 2014; *Bessho et al.*, 2016).

Magnetic islands, which are, to a first-order approximation, two-dimensional projections of flux ropes, can grow due to magnetic reconnection (e.g., Akhavan-Tafti et al., 2019). Simulations and observations have also indicated that the cross section of a magnetic island can be reduced due to reconnection (e.g., *Øieroset et al.*, 2011; *Hiroshi Hasegawa et al.*, 2016). The role of reconnection in determining magnetic island dynamics can be divided into four main categories: 1) coalescence, 2) continuous reconnection, 3) erosion, and 4) division.
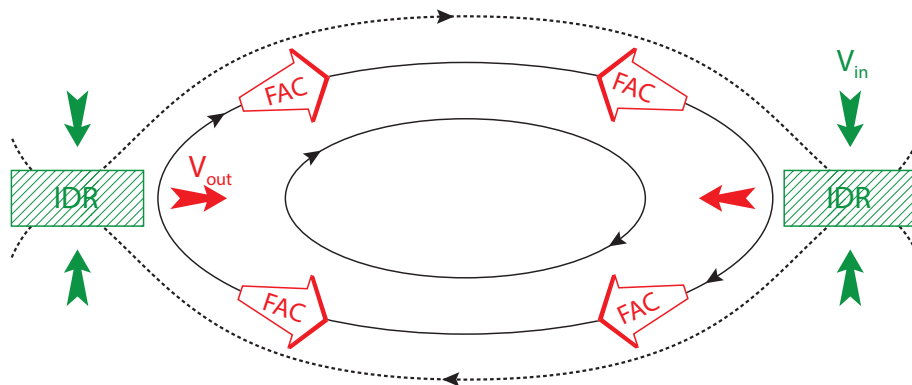
Figure 7-1: Two dimensional schematics of ion flows in a typical FTE forming due to multiple X-line reconnection. Field-aligned currents (FACs; white-red arrows) are generated due to reconnection. Inflowing ions (V_{in}; green arrow) are also accelerated inside the ion diffusion region (IDR) perpendicular to the magnetic field (V_{out}; red arrow) downstream of an X-line. The reconnecting field lines, i.e., separatrix, are shown as dashed lines.

Figure 7-2 represents schematics of the four categories. Individual magnetic islands are represented with concentric circles. The last reconnected-field lines are depicted with bold solid lines and the newly-reconnecting field lines, i.e., magnetic separatrix, are shown with dashed lines. The solid and hollow arrows determine the convection speed flowing into and out of the reconnection site, respectively.

In the first category, labelled as Q1, two magnetic islands coalesce. The two neighboring islands merge and create one island whose area, A, is larger than either of the two islands. However, reconnection at the outer layers of the two merging islands will reduce the overall magnetic flux, ψ. Therefore, the resulting magnetic island has a larger cross section ($A_{product} > A_2$, A_1) and contains equal or greater magnetic flux ($\psi_{product} = \psi_{larger\ island} > \psi_{smaller\ island}$ in the two-dimensional case and $\psi_{product} > \psi_{larger\ island} > \psi_{smaller\ island}$ in three-dimensional coalescing flux ropes with a shear angle) than at least one of the two original islands (cf. Figure 1 in Chapter 5). The second category, Q2, involves island growth due to continuous reconnection at the adjacent X-lines. Here, the continuous supply of magnetic flux to the outer layers of the magnetic island enlarges the structure, both in terms of magnetic flux and area ($\Delta\psi > 0$ and $\Delta A > 0$).

In the other two categories, the overall cross-sectional area of the magnetic island is reduced over time, due to magnetic reconnection. In these categories, magnetic reconnection either peels off the outer most layers of a magnetic island, called 'erosion,' Q3, or it divides a magnetic island into two smaller magnetic islands, known as 'division,' Q4 (e.g., *Øieroset et al.*, 2011; *Hiroshi Hasegawa et al.*, 2016). In both cases, the area of the original magnetic island(s) decreases with time. For instance, during the coalescence process, the smaller island will be eroded by the larger of the two merging islands. Similar processes are also reported in the magnetotail wherein an earthward-moving flux rope is eroded when interacting with the geomagnetic field (e.g., *Lu et al.*, 2015; *Man et al.*, 2018; *Poh et al.*, 2019).

Theory and simulation have attempted to determine the dynamics of magnetic islands that are generated by multiple X-lines reconnection (e.g., *Daughton et al.*, 2009; *Dorelli & Bhattacharjee*, 2009; *Fermo et al.*, 2010; *Uzdensky et al.*, 2010). In particular, it is essential to understand how these islands develop from birth at small spatial scales to macroscale objects. In practice, simulating long current layers inside which magnetic islands are generated has proven computationally expensive. Global fluid simulations (e.g., *Raeder*, 2006; *Dorelli & Bhattacharjee*,

2009) have successfully resolved these large spatial scales. However, until recently (*Y. Chen et al.*, 2017), these simulations were not capable of capturing the small-scale physics of reconnection and island formation. Global hybrid-Vlasov simulations of the magnetopause have also demonstrated the small-scale physics of magnetic island formation and growth (e.g., *Hoilijoki et al.*, 2017).
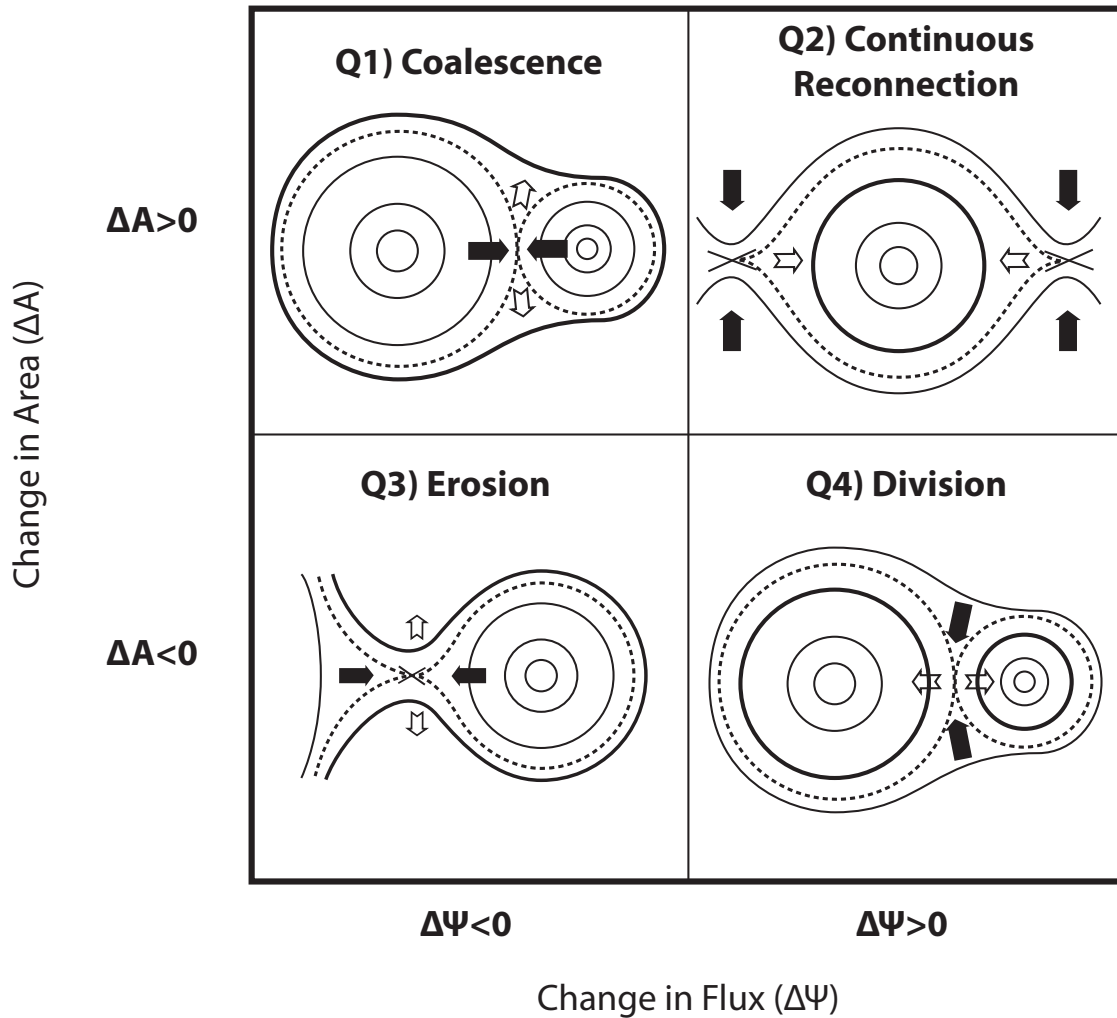
Figure 7-2: Schematic of magnetic island dynamics driven by magnetic reconnection. The enclosed area, A, inside magnetic islands increases due to coalescence and continuous reconnection at adjacent X-lines. The island's magnetic flux content, ψ, changes due to magnetic reconnection. The arrows indicate island convection flows, wherein the inflow is shown in black solid arrows and the outflows are presented as white arrows. Last reconnected field lines are indicated as bold solid lines. The dashed lines represent magnetic separatrices which embody reconnecting field lines.

In the context of FTE growth, the correlation between the observed normalized reconnection rate and the change in an FTE's magnetic flux content is essential in understanding the rate at which FTEs grow from micro-scale (*Eastwood et al.*, 2016; *Akhavan-Tafti et al.*, 2018) to macro-scale (e.g., *Walker & Russell*, 1985; *Eastwood et al.*, 2012; *Imber et al.*, 2014; *Jasinski et al.*, 2016) due to reconnection. Normalized reconnection rate is defined as the electric field pointing out of the reconnection plane that drives the reconnection normalized to the reconnecting magnetic field and the local Alfvén speed. However, the normalized reconnection rate from in-situ observations cannot determine the rate at which magnetic flux is reconnected globally. The global normalized rate of reconnection is approximately 0.1 (e.g., *Cassak et al.*, 2017) and in-situ magnetospheric observations of magnetic reconnection have reported reconnection rates up to 0.2 (e.g., *Mozer et al.*, 2002; *Fuselier et al.*, 2005; *Phan et al.*, 2007; *Slavin et al.*, 2009; *Chen et al.*, 2017; *Genestreti et al.*, 2018), consistent with theory (*Cassak & Shay*, 2007; *Liu et al.*, 2017).

In the present study, we take advantage of the hybrid-Vlasov code Vlasiator to study the evolution of magnetic islands at the magnetopause. First, the ion kinetics inside and around two adjacent X-points are investigated. A first X-point is selected to demonstrate ion dynamics at a typical magnetopause reconnection. Another X-point is located in the vicinity and in the downstream of the first X-point. The second X-point demonstrates the ion dynamics in the vicinity of an X-point sandwiched between two magnetic islands. Velocity distribution functions are compared between the two X-points. Next, all magnetic islands, defined as a bundle of magnetic flux function, i.e., 'O-point,' positioned between two saddle points, i.e., 'X-points', are automatically identified with an algorithm. The identified islands are then grouped into four main quadrants based on their temporal change in enclosed magnetic flux and cross-sectional area, as discussed in Figure 7-2. The algorithm also tracks individual islands to determine the rate of reconnection at each individual dominant X-point. The temporal evolution of magnetic islands' enclosed flux and cross sectional area is further investigated to estimate the rate of FTE growth at the magnetopause. Lastly, the Vlasiator simulation results are compared with high-temporal and spatial-resolution magnetic and plasma measurements of an FTE at the magnetopause. It is concluded that, i) Vlasiator resolves the ion kinetics at and in the vicinity of X-points, as previously predicted (e.g., *Hesse et al.*, 2014) and observationally supported (e.g., *Burch et al.*, 2016; *Wang et al.*, 2016), and ii) the global magnetospheric Vlasiator simulations confirm that the recently-

formed, subsolar small-scale FTEs can grow macroscale while being transported to the high-latitude magnetopause.

7.2   Methods

7.2.1   Global Hybrid-Vlasov Simulation Code Vlasiator

The hybrid-Vlasov code Vlasiator (http://www.helsinki.fi/en/researchgroups/vlasiator) has been developed to investigate global magnetospheric dynamics at ion scales (*Von Alfthan et al.*, 2014; *Palmroth et al.*, 2018). Vlasiator solves the Vlasov equation, evolving ions (protons) as distribution functions in three velocity-space dimensions, tracked on a cartesian grid. Electrons are treated as a cold massless charge-neutralizing fluid, and closure is provided by the generalized Ohm's law including the Hall term. The simulation used in this study is two-dimensional in real space and three-dimensional in velocity space (*Palmroth et al.*, 2013; *Palmroth et al.*, 2017; *Hoilijoki et al.*, 2017; *Jarvinen et al.*, 2018; *Juusola, Hoilijoki, et al.*, 2018; *Juusola, Pfau-Kempf, et al.*, 2018).

The simulation domain extends within -94 R_E < X < +48 R_E and -56 R_E < Z < +56 R_E in the z-direction, where R_E = 6371 km is the Earth's radius. The geocentric solar ecliptic (GSE) coordinates are used in which X points sunward, Y points opposite Earth's motion about the Sun, and Z points normal to the ecliptic plane. The inner boundary with a radius of 5 R_E is modelled as an ideal conducting sphere. Due to the two-dimensional nature of the simulation in the ordinary space, the dipole field is implemented as a 2-D line-dipole with a strength resulting in a realistic magnetopause standoff distance (*Daldorff et al.*, 2014). The simulation initialization process involves distributing plasma with a stationary Maxwellian distribution within the simulation domain's inner boundary.

We model a steady solar wind inflow at the +x boundary, with a fast solar wind of $\mathbf{v}$ [km/s] = -750 $\hat{\mathbf{x}}$, a density of n_{sw}=1 cm^{-3}, a proton temperature of T_p = 0.5 MK, and a purely southward IMF of magnitude 5 nT. The fast solar wind is intended to speed up the initialization of the simulation run. The spatial grid resolution is 300 km in each direction and the velocity space grid is 30 km/s in each direction. Despite not resolving the ion inertial length (~200 km at the magnetopause under the stated upstream conditions), kinetic effects at the Earth's bow shock are captured in the Vlasiator's simulation grid (*Pfau-Kempf et al.*, 2018). The simulation is carried out

for 2150 seconds of simulation time. The analysis provided in this study only includes the final 1050 seconds of the simulation run.

7.2.2   Observational Instrumentation:

The four identical MMS spacecraft were launched in 2015 and are designed to unravel the physics of magnetic reconnection (*Burch & Phan*, 2016). The high temporal and spatial plasma measurements (Fast Plasma Investigation (FPI); *Pollock et al.*, 2016) provide three-dimensional electron and ion distributions. Plasma moments are constructed from all-sky FPI electron and ion distributions at 30 ms and 150 ms cadence, respectively. The fields instrument suites (*Torbert, Russell, et al.*, 2016) including the fluxgate magnetometers (FGM; *Russell et al.*, 2016) and the electric dual probes (EDP) (*Ergun et al.*, 2016; *Lindqvist et al.*, 2016; *Torbert, Russell, et al.*, 2016) are used for magnetic and electric field measurements. Multi-point analysis techniques (*Harvey*, 1998) are used to determine spatial gradients in fields and plasma measurements. The spacecraft separation was, on average, 10 km for our events (Phase 1a; *Burch, Moore, et al.*, 2016).

7.3 Results

7.3.1 Hybrid-Vlasov Simulation Results

7.3.1.1 Vlasiator Case Studies

As Vlasiator simulations operate directly on a mesh-based representation of 6D phase space, velocity space plots are taken straight from the instantaneous simulation state. The VDF plots are constructed within a single simulation grid cell at each individual timestep. The VDF plots presented here show re-binned slices of velocity space in the local magnetic frames, with the local plasma bulk velocity subtracted, identical to the MMS spacecraft measurements.

Due to the sparse velocity space representation in Vlasiator (*von Alfthan et al.*, 2014), cells with a phase space density of less than 10^{-15} s^3 m^{-6} are dropped from the simulation, except when neighbouring denser regions are present. Dropped regions are displayed as empty areas in the VDF plots.

Two virtual passes across a magnetic island (diameter ~ 1 R_E) in the northern hemisphere magnetosheath are displayed in Figure 7-3 and Figure 7-4. The magnetic island is embedded within the exhaust region south of an X-point (labeled herein as 'Northern X-point'). Both the island and the northern X-point are located in the exhaust region of a subsequent X-point, the 'Southern X-point.' The Southern X-point does not reconnect all of the magnetic flux that reconnects at the Northern X-point.

The panels include: a) a Vlasiator simulation plot in which the contours indicate the magnetic flux function and the colormap shows the component of electric field in the X_{GSE} direction, E_x, and the red dashed line indicates a virtual spacecraft trajectory, b) the profile of E_x along the virtual spacecraft moving direction, and c) velocity distribution functions (VDFs) sliced in the V_B - $V_{B \times V}$ (left column) and $V_{B \times V}$ - $V_{B \times (B \times V)}$ (right column) planes, where V_B represents the velocity along the magnetic field orientation, $V_{B \times V}$ and $V_{B \times (B \times V)}$, respectively, along $(B \times V)$ and $B \times (B \times V)$ directions, where V is the ion bulk velocity. The VDFs correspond to the local extrema in the one-dimensional E_x profile of panel b and are identified with numbers 1-5.

The trajectory at the southern edge of the island, in Figure 7-3, demonstrates signatures that are of a nominal magnetosheath X-point. There exists a local minimum along the E_x line profile on the magnetospheric side of the X-point, labeled as '1.' The corresponding V_B - $V_{B \times V}$ VDF shows an intense and uniform core cold ion population, $V_B < 250$ km/s, due to the hot solar

wind inflow. At this extremum, a bi-directional 'butterfly' distribution of higher-energy ions, $\mathbf{V}_{B \times V}$ >250 km/s, starts to form.

A perpendicular crescent-shaped ion distribution is identified coinciding with the local E_x minimum on the magnetospheric side of the X-point. Closer to the separatrix, where E_x reaches a maximum, both the butterfly- and crescent-shaped distributions of the higher-energy ions, $\mathbf{V}_{B \times V}$ > 250 km/s, become clearer. At extrema '3' and '4', the spacecraft crosses the reconnecting current sheet inside which E_x sharply changes direction and fluctuates between 6 mV/m and -5 mV/m. Inside the current sheet, the VDFs retain some structure, though the ions are largely diffused, i.e., heated. Finally, at '5,' symmetric higher energies, $\mathbf{V}_{B \times V}$ >250 km/s, ion population peaks are detected in all four quadrants. We also find ions with velocities $\mathbf{V}_{B \times V}$ > 500 km/s to appear non-gyrotropic.

The trajectory across the northern side of the magnetic island is demonstrated in Figure 7-4. The most significant difference between the northern and southern trajectories is the environments in which the X-points are located. In contrast to the southern X-point, which is located near subsolar magnetopause, the northern X-point is positioned between two northward-propagating islands.
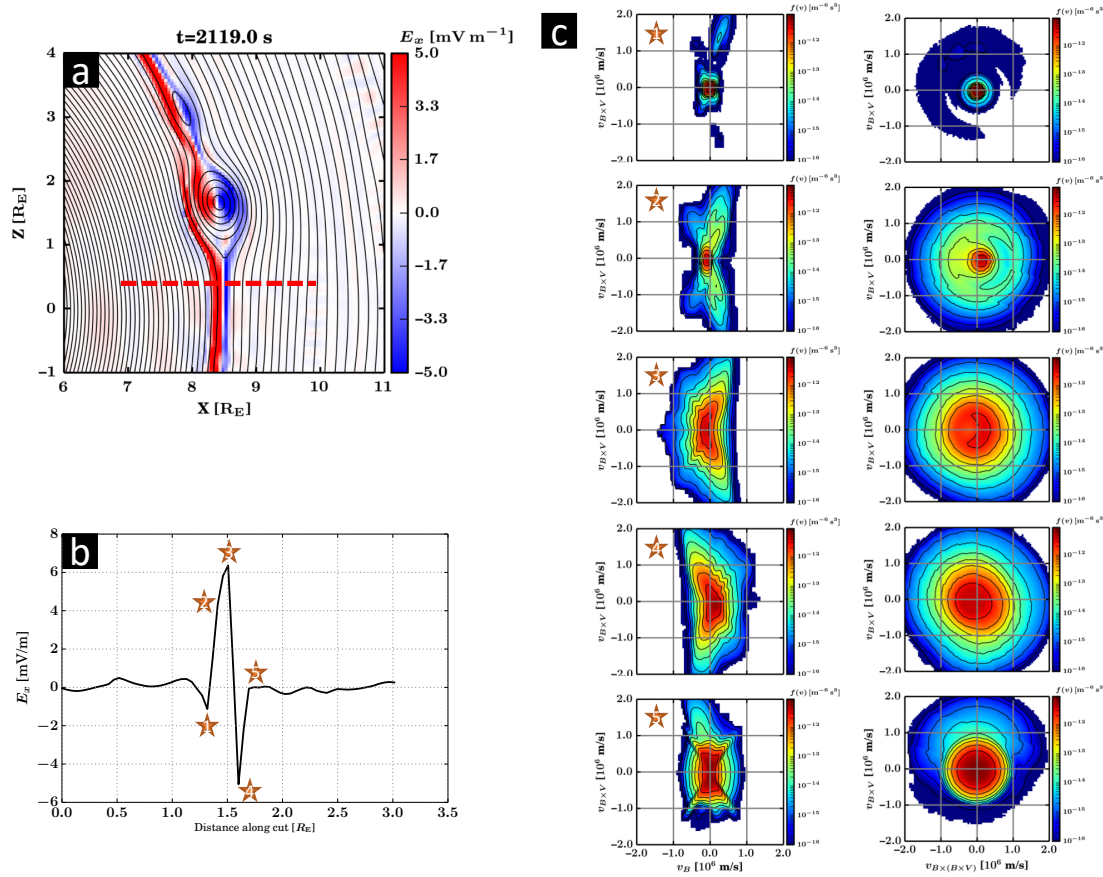
Figure 7-3: Vlasiator electric field profile and ion velocity distribution functions across a nominal magnetopause X-point. The panels include: a) Simulation frame of a magnetic island located in the northern hemisphere. The contours represent the XZ-plane magnetic field and the color bar shows the magnitude and the direction of electric field along X_{GSM}. The red dashed line denotes a virtual spacecraft outbound trajectory through the X-point. b) One-dimensional E_x profile along the virtual spacecraft's trajectory. The local extrema (except #2 & 5) are selected and labeled as '1'-'5'. c) VDF cuts at the five selected E_x values in V_B - $V_{B \times V}$ (left column) and $V_{B \times V}$ - $V_{B \times (B \times V)}$ (right column) diagrams, where V_B represents the velocity along the magnetic field orientation. $V_{B \times V}$ and $V_{B \times (B \times V)}$ are along $(B \times V)$ and $B \times (B \times V)$ directions, respectively, where V is the ion bulk velocity.
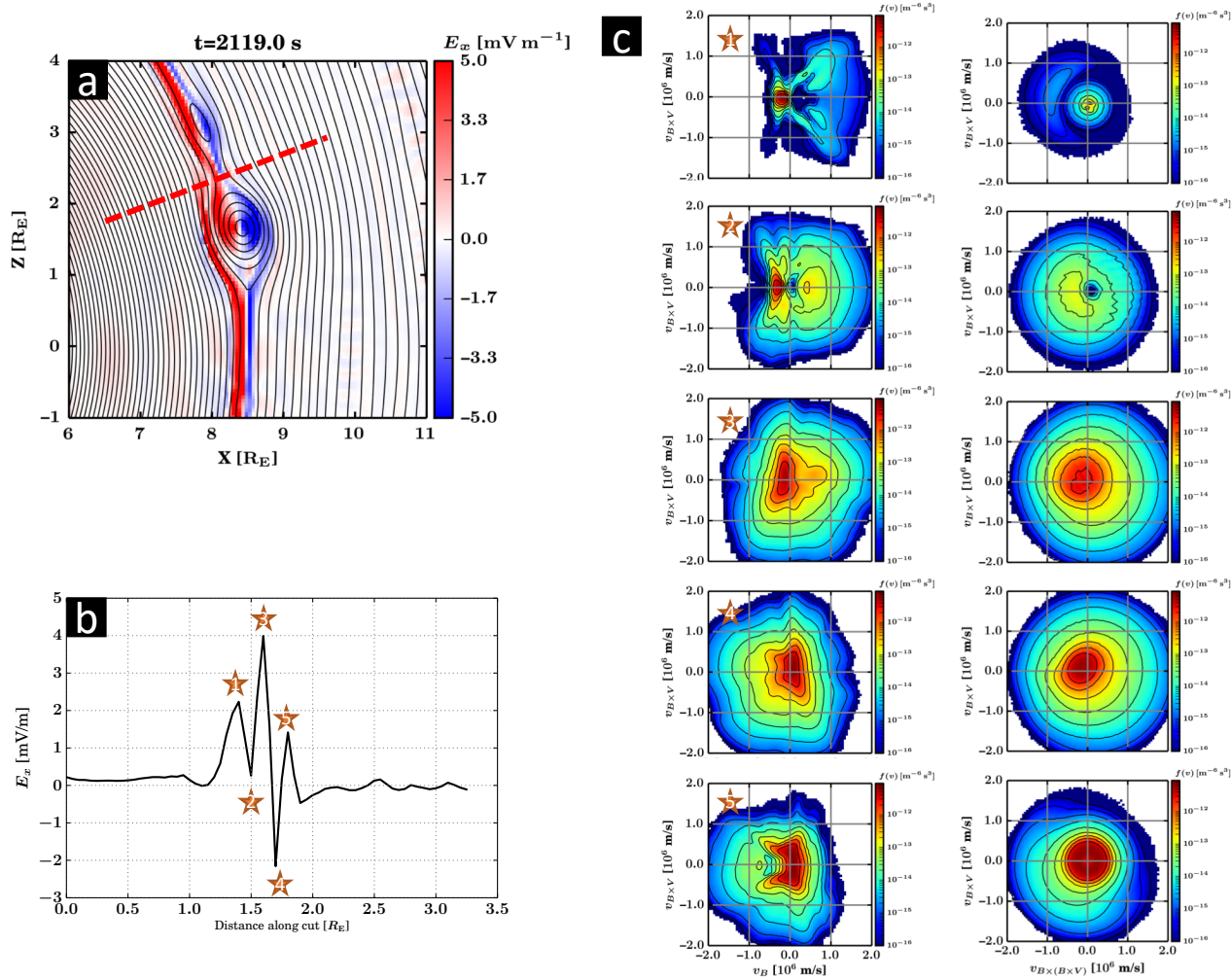
Figure 7-4: Vlasiator electric field profile and ion velocity distribution functions across an X-point located between two magnetic islands. The panels include: a) Simulation frame of a magnetic island located in the northern hemisphere. The contours represent the XZ-plane magnetic field and the color bar shows the magnitude and the direction of electric field along X_{GSM}. The red dashed line denotes a virtual spacecraft outbound trajectory through the X-point. b) One-dimensional E_x profile along the virtual spacecraft's trajectory. Five extrema are selected and labeled as '1'-'5'. c) VDF cuts at the five E_x extrema in V_B - $V_{B \times V}$ (left column) and $V_{B \times V}$ - $V_{B \times (B \times V)}$ (right column) diagrams, where V_B represents the velocity along the magnetic field orientation. $V_{B \times V}$ and $V_{B \times (B \times V)}$ are along $(B \times V)$ and $B \times (B \times V)$ directions, respectively, where V is the ion bulk velocity.

129

At extremum '1,' on the magnetospheric side of the northern X-point, an anti-parallel intense cold ion beam, V_B < 250 km/s, and a high-energy, $V_{B\times V}$ > 250 km/s, butterfly ion distribution are found. Compared to the VDFs on the magnetospheric side of the southern X-point discussed above, the core ion population is off center, i.e., anti-parallel to B, and the butterfly distribution is diffused suggesting the presence of significant heating. This may also be due to the fact that the virtual spacecraft location is farther away from the southern X-point. A crescent-shaped ion distribution is also formed at the magnetospheric E_x extremum '1'. Closer to the separatrix, on the magnetospheric side, a parallel D-shaped ion distribution is observed. D-shaped ion VDFs are often observed in the reconnection exhaust region (e.g., *Cowley*, 1995; *Phan et al.*, 2004). The parallel D-shaped ion distribution indicates that the northern X-point is located within and is influenced by the southern X-point's outflow exhaust. While in the reconnecting current sheet, at extrema '3' & '4', the VDFs transition from magnetospheric-type into magnetosheath-type as suggested by the high abundance of energetic ions, $V_{B\times V}$ > 500 km/s. Farther away from the magnetopause, in the extremum '5' in the magnetosheath side of the X-point, parallel ion crescent-shaped-like distribution and non-gyrotropic perpendicular ions are identified.

The presence of magnetic islands near the northern X-point may impact the rate at which field lines enter the diffusion region. This can be done via: 1) building-up pressure in the reconnection exhaust, i.e., inside islands, and/or 2) thickening the current sheet layer within which the islands propagate. The latter can result in increasing magnetic field tension along the highly-bent reconnecting field lines, therefore, introducing stress against the inflow flux. Figure 7-5 shows the rates of reconnection at the northern and southern X-points as a function of simulation time. The same two X-points, i.e., saddle points in the magnetic flux function, are tracked between simulation frames and their reconnection rates are determined at each time frame, similar to *Hoilijoki et al.* (2017). The normalized reconnection rate here is defined as the out-of-plane electric field component, E_y, at the X-point, normalized by the inflow plasma Alfvén speed, v_{Ai}, and magnetic field magnitude, B, given thus as,

$$\mathcal{R} = E_y^{x\text{-}point} \, v_{Ai}^{-1} \, B^{-1}$$

where the inflow values are gathered from the simulation just upstream of the X-point. The out-of-plane component of the electric field, E_y, are offset ($E_y^{x\text{-}point} = E_y + V_{X\text{-}point} \times B$) by the convection term, $E = - V_{X\text{-}point} \times B$, where $V_{X\text{-}point}$ refers to the X-point's convection speed at the

magnetopause. $V_{\text{X-point}}$ is calculated by assuming the instantaneous plasma bulk velocity to describe the motion of the X-point in space. In order to smooth out the normalization impact of magnetosheath fluctuations such as mirror modes, visible in B and $v_{\text{A}i}$ signatures (not shown here), the inflow values are averaged over 5 consecutive simulation cells in the radial direction, at least 1 R_{E} outwards from each X-point. Consistent with the latest kinetic predictions (e.g., *Y.-H. Liu et al.*, 2017), it is discovered that normalized reconnection rate can surpass the magnetohydrodynamic (MHD) threshold normalized reconnection rate of 0.1 (*Cassak et al.*, 2017). It is further revealed that the normalized reconnection rate at the older,

Figure 7-5: Temporal profile of the normalized reconnection rate, $\mathcal{R} = E_y^{x\text{-}point}\, v_{\text{A}i}^{-1}\, B^{-1}$, at the northern (solid black line) and southern (solid green line) X-points, in the reference frame of the X-points. The vertical grey line indicates the simulation timeframe t = 2119.0 s.

northern X-point, which is located in the exhaust region of a newly-formed X-point and sandwiched between two islands is larger than the newly-formed, southern X-point. In addition, the normalized reconnection rate at the northern X-point increases with time while the normalized reconnection rate slowly decreases at the southern X-point.

7.3.2 Statistical Analysis

Magnetic islands within the simulation are identified by searching for maxima and saddle points of the magnetic flux function (*Yeates & Hornig*, 2011; *Hoilijoki et al.*, 2017). A magnetic island is defined as encapsulated loops of magnetic field lines, identified as a local maximum of the magnetic flux function (an 'O-point') positioned between two saddle points ('X-points'). In other words, we require magnetic islands to be bounded by at least two X-points (*Hoilijoki et al.*, 2019). Figure 7-6a illustrates an example simulation timeframe of the dayside magnetosphere in which the 'X'-points and 'O'-points are automatically identified with an algorithm. The algorithm is also capable of determining the magnetic flux, ψ, and the cross-sectional area, A, for the magnetic islands. The algorithm can further track the merging of islands, the process known as coalescence, and can distinguish X-points within the islands. We focus on subsolar magnetic islands, tracking only those where the island O-point is within polar angle, $|\theta| < 30$ degrees from the X_{GSE}-axis.

Magnetic islands are categorized based on the relative significance of the X-points and the O-points. For each island, i.e., O-point, the two dominant X-points are defined as the two saddle points with lowest flux function value, i.e., which have reconnected the most. O-points of an island, defined as a local maxima in the magnetic flux function, are located between two dominant X-points. The dominant O-point is defined as the O-point with the highest flux function value. There may exist additional X-points between two dominant X-points indicating the presence of interior islands within the dominant structure. Similar structures have been postulated (e.g., *Fermo et al.*, 2011) and were recently observed by MMS (e.g., *Hwang et al.*, 2018). Additionally, the relative location of dominant O-points and X-points are tracked between simulation frames. This enabled the identification of island coalescence events in which two neighboring O-points merge to create one larger island. During this process, the innermost of three dominant X-points describing two islands becomes a non-dominant inner X-point. The coalescence process is of great practical significance, hence, it has been the subject of numerous theoretical (e.g., *Pritchett & Wu*, 1979), experimental (e.g., *Yamada et al.*, 1990), and observational (e.g., *Wang et al.*, 2016; *Zhao et al.*, 2016; *Zhou et al.*, 2017) studies.

Table 7-1 summarizes the distribution of the two-dimensional magnetic islands identified at the magnetopause. A total of 4786 magnetic islands, defined as an O-point positioned between two X-points, are independently identified in one simulation run at different locations ($|\theta| < 30$

degrees) and different timeframes. This approach is different from *Hoilijoki et al.* (2019), wherein individual magnetic islands were tracked across all timeframes. The O-points are divided by the algorithm into four main categories depending on their structure and evolution: 1) '2 X-points' wherein reconnection at two dominant X-points forms a magnetic island, 2) '>2 X-points' in which reconnection at two dominant X-points forms an O-point inside which multiple smaller O-points and one or more additional X-points exist, 3) 'Coalescence' which describes the merging of two independent O-points during which three dominant X-points, i.e., '>2 X-points,' are reduced to two dominant X-points, and 4) 'Division' which describes the process through which one O-point is divided into two independent magnetic islands, therefore, two dominant X-points become three dominant X-points. The categories 3 and 4 are subcategories of the categories 2 and 1, respectively.

Table 7-1: The number of islands included in this study (4786) partitioned into four main categories depending on their structure and evolution.

Quadrants [b]	Structure Categories [a]			
	Category 1 2 X-Points	**Category 2** >2 X-Points	**Category 3** Coalescence	**Category 4** Division
Q1 ($\Delta A > 0$ & $\Delta\psi < 0$)	205	40	4	15
Q2 ($\Delta A > 0$ & $\Delta\psi > 0$)	1716 [c]	888	23	72
Q3 ($\Delta A < 0$ & $\Delta\psi < 0$)	406	46	24	12
Q4 ($\Delta A < 0$ & $\Delta\psi > 0$)	477	191	15	4
$\Delta A = 0$ or $\Delta\psi = 0$	669	42	0	3
Total	**3473**	**1207**	**66**	**106**

[a] The four categories include: 1) '2 X-points' wherein reconnection at two dominant X-points forms a magnetic island, 2) '>2 X-points' in which reconnection at two dominant X-points forms a magnetic island inside which multiple smaller islands and X-points exist, 3) 'Coalescence' which describes the merging of two independent magnetic islands during which three dominant X-points are reduced to two dominant X-points, and 4) 'Division' which describes the process through which one magnetic island is divided into two independent magnetic islands, therefore, two dominant X-points become three dominant X-points.

[b] The structures are further divided into based on their evolution, describing the change in individual magnetic island's magnetic flux, $\Delta\psi$, and area, ΔA.

[c] The shade of red indicates the relative magnitude of each cell compared to the column's total counts (bottom row), with bright red signifying the largest value.

In this part of the study, we focus on the evolution of magnetic islands. In particular, we are interested in reconnection-associated processes that contribute to a change in an O-point's dimensions and/or flux content between two consecutive timeframes. This is achieved by identifying all O-points in a given simulation timeframe, independent of other timeframes, and tracking the identified O-points in a subsequent timeframe to study the change in dimensions and/or flux content between timeframes. In practice, the evolution of an island through its lifetime can involve a multitude of the above mechanisms. However, for the purposes of this study, only the evolution processes between two consecutive timeframes are considered. The O-points are split into four main quadrants, Q1-4, based on the temporal change in magnetic flux content, $\Delta\psi$, and cross-sectional area, ΔA, as described in Figure 7-2. To achieve this, the flux content and the cross-sectional area of magnetic islands in each simulation frame are compared with the previous frame (or subsequent frame; in the case of island 'division'). There remains a sub-population of islands whose cross-sectional area does not change between two consecutive time frames. The islands in which the magnetic flux content and/or the cross-sectional area does not change between simulation frames are separated from the four quadrants and listed in the table as ($\Delta A = 0$ and/or $\Delta\psi = 0$). Our observations include:

1. Continuous reconnection at adjacent dominant X-points supplies additional magnetic flux, $\Delta\psi > 0$, to the outer layers of the majority of 'uniform' magnetic islands, defined as islands with no substructure, (Category 1, Q2 & Q4; 2193/3473 ~ 60%), and those with substructure (Category 2, Q2 & Q4; 1079/1207 ~ 90%). The sizes of these islands also increase, ($\Delta A > 0$; Q1 & Q2), in nearly 60 and 80 percent of islands in Categories 1 and 2, respectively.

2. Nearly 20% of islands with substructure (Category 2) exhibit simultaneous increase of magnetic flux content and reduction of cross-sectional area, $\Delta A < 0$ (Q4).

3. The coalescence process, Category 3, is more complex. In 40% of the cases (Q1 & Q2), it involves the growth of the total enclosed area ($\Delta A > 0$, $A_{coalescence} > A_{pre,\,1}$ & $A_{pre,\,2}$, where $A_{coalescence}$, $A_{pre,\,1}$, and $A_{pre,\,2}$ represent cross sectional areas of islands after and before the coalescence process, respectively). Similarly, 40% of the islands are found to 'erode' when coalescing with larger islands, $\Delta A < 0$ & $\Delta\psi < 0$ (Q3).

4. Magnetic island division, Category 4, involves the splitting of one magnetic island into two smaller islands (and in one case, three islands). The likelihood of identifying island division events is nearly twice that of island coalescence events suggesting that the division of magnetic islands is more common than coalescence (e.g., *Øieroset et al.*, 2011, 2019).

5. Magnetic flux and area of dividing islands are found to increase ($\Delta A > 0$ & $\Delta\psi > 0$) in the majority of cases, in contrary to the proposed classification in Figure 7-2. Similarly, magnetic flux is found to increase in more than 50% of the coalescing islands. Island area decreases in nearly 60% of the coalescing islands. As discussed above, when coalescing, the minor island erodes ($\Delta A < 0$ & $\Delta\psi < 0$), contributing to the growth, in both area and magnetic flux content, of the larger island.

6. Most importantly, >70% of the islands evolve due to continuous reconnection only, Category 1, further emphasizing the significance of magnetopause reconnection with the interplanetary magnetic field.

Next, the evolution of magnetic islands is investigated. First, in accordance with Figure 7-2, islands are categorized into four quadrants, Q1-4, as shown in Figure 7-6b. The upper right corner, of the plot ($\Delta A > 0$ & $\Delta\psi > 0$) contains islands whose relative cross-sectional area increases with growth of relative magnetic flux content, as suggested by the linear fit shown in dashed black line, $\Delta A/A$ [s^{-1}] = 2.16 ($\pm\bar{\sigma}_S$) $\Delta\psi/\psi$ [s^{-1}] $-$ 0.03 ($\pm\bar{\sigma}_I$), where $\pm\bar{\sigma}_S$ = 6.4 $\times10^{-2}$ s and $\pm\bar{\sigma}_I$ = 1.9 $\times10^{-3}$ s^{-1} are the standard errors ($\bar{\sigma} = \sigma / \sqrt{n}$, where σ and n respectively represent the standard deviation and bin population size (*Akhavan-Tafti, Slavin, Eastwood, et al.*, 2019)) for the derived slope and intercept values, respectively. The linear fits were found using an orthogonal distance regression method using visible data points only. Here, the magnetic flux content and cross-sectional area are normalized to account for variations in island physical properties associated with island size (*Akhavan-Tafti et al.*, 2018, 2019; *Hoilijoki et al.*, 2019).

In Figure 7-6c, the relative change in the magnetic islands' magnetic flux is investigated as a function of normalized reconnection rate, $\mathcal{R}$. The normalized reconnection rate is determined at the dominant X-point, i.e., lowest magnetic flux function. We find that the majority of magnetic islands experience normalized reconnection rates between 0.05 and 0.15 and that the average reconnection rate is about 0.07. We also find that most coalescence events, shown in red circles, are located within this region. At lower reconnection rates, $\mathcal{R} < 0.05$, magnetic flux is reduced due

to reconnection, i.e., 'erosion.' In contrast, the islands' normalized magnetic flux content, $\Delta\psi/\Delta t > 0$, is enhanced at higher reconnection rates, $\mathcal{R} > 0.08$. The linear fit, shown in black dashed line, further indicates that, as expected, the island's magnetic flux content increases with increasing reconnection rate, $\Delta\psi/\Delta t$ [Wb/km-s] = 8.6 ($\pm\bar{\sigma}_S$) $\mathcal{R}$ + 0.5 ($\pm\bar{\sigma}_I$), where $\bar{\sigma}_S = 3.4 \times 10^{-1}$ and $\bar{\sigma}_I = 3.9 \times 10^{-2}$ Wb/km-s.
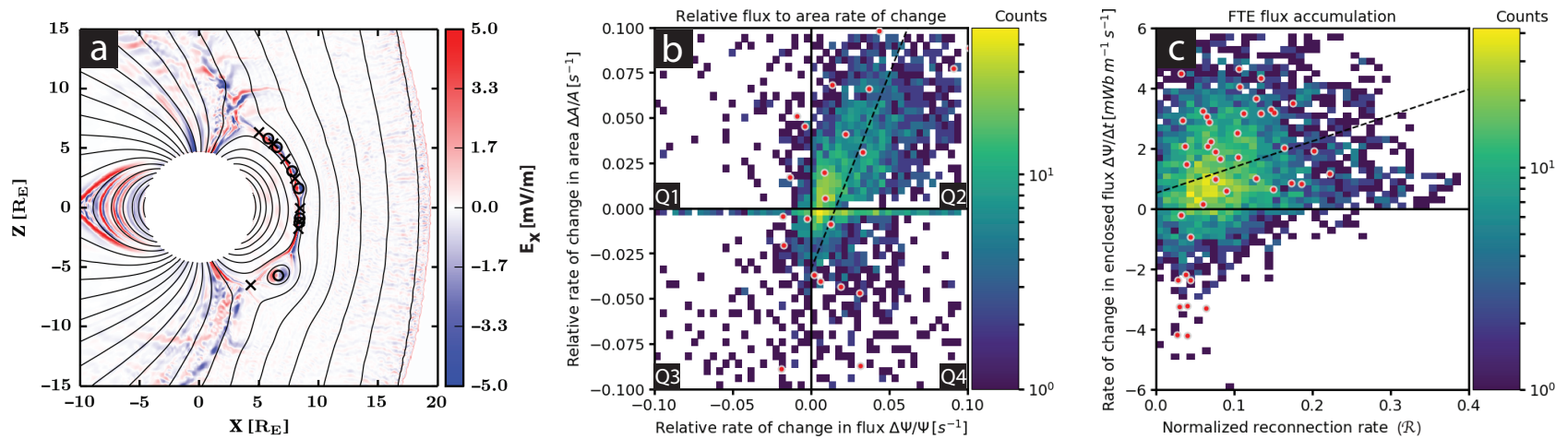
Figure 7-6: a) Example snapshot (simulation timeframe: t = 2119.0 s) of the Vlasiator magnetopause. The 'X'-points and 'O'-points are automatically identified by the algorithm. The color bar indicates the electric field along the X_{GSM} axis, Ex [mV/m]. b) Magnetic islands categorized into four quadrants, Q1-4, based on their temporal change in enclosed magnetic flux, $\Delta\psi$, and cross-sectional area, ΔA. The linear fit from the orthogonal distance regression, shown as dashed black line, is y = 2.16 x − 0.03. The color bars indicate the count of events per bin. c) The change in the enclosed magnetic flux as a function of normalized reconnection rate, $\mathcal{R} = E_y^{x\text{-}point} \, v_{Ai}^{-1} \, B^{-1}$. The linear fit from the orthogonal distance regression, shown as dashed black line, is y = 8.6 x − 0.5. The red circles denote coalescing magnetic islands wherein two neighboring magnetic islands merge and create one larger island.

7.3.3   MMS Case Study

7.3.3.1   Fields and Plasma Moments:

On 14 December 2015 at 0058-0100 UT, the MMS spacecraft were located dawnward of the subsolar magnetopause, at [9.8, -4.3, -0.8] $R_{E, GSE}$ on an outbound trajectory. As shown in magenta, a sudden pressure enhancement is observed shortly before the magnetopause crossing interval. The IMF remains steadily southward throughout the interval.

In-situ magnetic and plasma measurements are shown in Figure 7-7. From top to bottom, the panels include the following parameters (at the barycenter in the GSE coordinates): a) total magnetic field, b) magnetic field components, c) ion plasma density, d) ion velocity components, e) electron velocity components, f) parallel (red solid line) and perpendicular (black solid line) current density, g) parallel (red solid line) and perpendicular (black solid line) ion temperature, h) plasma beta, β, defined as the ratio of plasma thermal pressure to magnetic pressure. This magnetopause crossing is described in detail by *Hwang et al.* (2018).

At least five localized peaks in the total magnetic field are observed, as shown in magenta bars. The peaks correspond to enhancements in B_y and a bipolar signature in the tangential component of the magnetic field (not shown here). These signatures, together with, plasma density dips (panel c), parallel current density enhancements (panel f), and localized plasma beta dips (panel h) suggest the presence of d_i-scale FTE-type flux ropes (*Eastwood et al.*, 2016; *Akhavan-Tafti et al.*, 2018; *Akhavan-Tafti, Slavin, Eastwood, et al.*, 2019). *Hwang et al.* (2018) states that the observed FTEs have diameters ranging between, $2.5 < \lambda [d_i] < 6.8$, where λ and d_i (= 75 km) denote the FTE diameter and the local ion inertial length, respectively.

Multiple localized dips in the total magnetic field were also observed dispersed adjacent to the above FTEs. Ion-scale FTEs are smaller in size than the local ion gyro-radius, $r_{gi} \sim 400$ km. Therefore, the frozen-in condition in the generalized Ohm's law (i.e., $\mathbf{E} + \mathbf{v}_i \times \mathbf{B} = 0$) is naturally violated inside FTEs and the thin current layers within which FTEs are generated. Figure 7-7i-l juxtapose the boxcar averaged EDP electric field measurements and the cross product of the bulk FPI ion and electron velocities and the FGM magnetic field vectors at the location of MMS1 within a magnetic field dip at the leading edge of one of the observed FTEs, marked with a cyan bar. High-resolution electric field measurements are boxcar averaged to match the cadence of the FPI electron measurements, i.e., 30 ms. The FPI ion bulk velocity measurements are also interpolated

to the FPI electron measurements. The x component of the electric field is negative at the magnetic dip. Ions are found to become demagnetized within the magnetic dip, but not the electrons. Ions remain demagnetized inside the adjacent FTEs.

The localized dips in magnetic field total coincide with ion flow enhancements and localized field-aligned current density peaks. The presence of ion jets and the observed demagnetized ions suggest that the MMS spacecraft traversed near multiple X-lines (*Gosling et al.*, 1990, 2005; *Hwang et al.*, 2018). Based on the above observations, *Hwang et al.* (2018) proposes a magnetic field topology involving multiple ion-scale FTEs sandwiched between two active X-lines. Figure 7-8 provides a schematic illustration of the field geometry. Here, the MMS spacecraft are shown to traverse across a reconnecting magnetopause current sheet within which multiple FTEs are spotted.

7.3.3.2 Ion Velocity Distribution Functions:

Figure 7-8 illustrates the approximate locations and geometry of the observed ion-scale FTEs and the X-lines. The orientation of the FTEs (and the orientation of X-lines) is along the intermediate eigen vector (M) derived from applying the minimum variance analysis (MVA) on the magnetopause crossing. The eigen vectors (in the GSM coordinates) include: $\mathbf{n}$ = [0.84, -0.36, -0.41], $\mathbf{m}$ = [-0.46, -0.87, -0.17], and $\mathbf{l}$ = [0.30, -0.33, 0.89]. We further investigate the MMS observations of ion VDFs in the vicinity of two independent X-lines. The VDFs are projected onto the parallel (i.e., field-aligned ion population) and perpendicular planes.

In Figure 7-8 the ion VDFs at the X-lines are displayed in the ion bulk velocity frame of reference. To achieve this, the components of the bulk ion velocity, $\mathbf{v_i}$, are subtracted from velocity distribution components. The top and bottom rows in each panel show VDF cuts in the $\mathbf{V_B}$ - $\mathbf{V_{B\times V}}$ and $\mathbf{V_{B\times V}}$ - $\mathbf{V_{B\times(B\times V)}}$ planes, where $\mathbf{V_B}$ represents the velocity along the magnetic field orientation, and $\mathbf{V_{B\times V}}$ and $\mathbf{V_{B\times(B\times V)}}$, respectively, along the $(\mathbf{B} \times \mathbf{V})$ and $\mathbf{B} \times (\mathbf{B} \times \mathbf{V})$ directions, where $\mathbf{V}$ is the ion bulk velocity. The VDF cuts are also organized on the basis of ion energy range. From left to right, the columns represent ions measurements of 1) all energy bins (1 eV – 30 keV), 2) low-energy ions (1 eV – 3 keV), mid-energy ions (3 – 6 keV), and high-energy ions (6 – 30 keV).
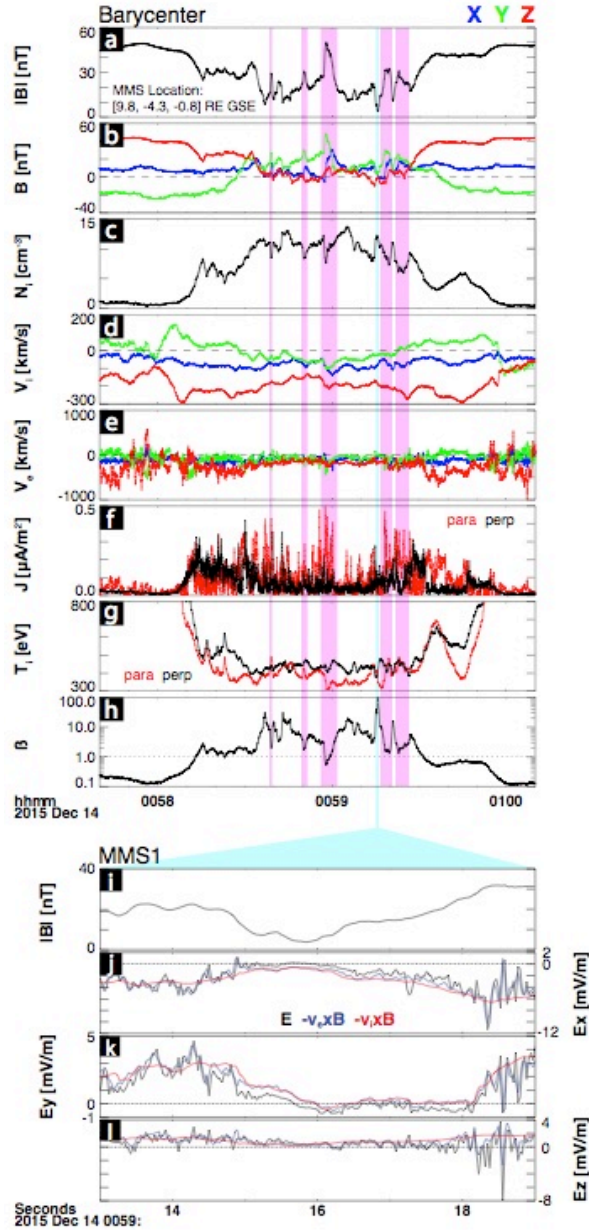
Figure 7-7: Magnetic field and plasma moments as observed at the barycenter of the four MMS spacecraft for a magnetopause crossing of December 14, 2015 — 00:57:40 - 01:00:10 UT. The panels include: a) total magnetic field, b) magnetic field components in the Geocentric Solar Ecliptic (GSE) coordinates, c) ion plasma density, d) ion velocity components, e) electron velocity components, f) parallel (red solid line) and perpendicular (black solid line) current density components, g) parallel (red solid line) and perpendicular (black solid line) ion temperature components, h) plasma beta, β, defined as the ratio of plasma thermal pressure to magnetic pressure. The frozen-in condition of the ions and electrons at 00:59:13-19 UT are also represented as observed by MMS1 in the following panels: i) magnetic field total, and the components of the electric field measured directly using the EDP instrument (black solid line) and derived from the cross product of the bulk FPI electron (blue) and ion (red) velocities and the FGM magnetic field vectors (red solid line) along the j) X_{GSE}, k) Y_{GSE}, and l) Z_{GSE}.

Figure 7-8: Schematic of the approximate locations and orientations of the observed ion-scale FTEs, shown as out-of-plane cylinders wherein the magnetic field intensity enhances (darker shade) near the FTE core regions, and the adjacent reconnection X-lines, in the FTE's frame of reference and in the LMN coordinates. The X-lines are marked by dashed lines. The magnetosheath and magnetospheric magnetic flux are distinguished and shown as red and blue-shaded surfaces, respectively. The MMS spacecraft trajectory, shown as a black arrow traversing across the structures is estimated based on the MMS observations. The green and black arrows/panels represent ion velocity distributions in the vicinity of the two observed X-lines at 00:58:26 and 00:59:15 UT, respectively. The energy bins are divided into four energy bins organized in two rows: *top row*) the $\mathbf{V}_B$ - $\mathbf{V}_{B \times V}$ slice, and *bottom row*) the $\mathbf{V}_{B \times V}$ - $\mathbf{V}_{B \times (B \times V)}$ slice, where $\mathbf{V}_B$ represents the velocity along the magnetic field orientation. $\mathbf{V}_{B \times V}$ and $\mathbf{V}_{B \times (B \times V)}$ are along $(\mathbf{B} \times \mathbf{V})$ and $\mathbf{B} \times (\mathbf{B} \times \mathbf{V})$ directions, where $\mathbf{V}$ is the ion bulk velocity. The energy bins from left to right include: a) 1 eV-30 keV, b) 1 eV – 3 keV, c) 3-6 keV, and d) 6-30 keV. The bulk velocity is subtracted from the velocity distribution function slices.

In the vicinity of a first possible X-line encounter, marked by a green arrow, in the V_B - $V_{B \times V}$ slice for low-energy ions (1 eV − 3 keV), there exists a non-isotropic population of ions moving anti-parallel to B. The low-energy ions are population appears gyrotropic in the $V_{B \times V}$ and $V_{B \times (B \times V)}$ slice. However, there exists a non-gyrotropic mid-energy ion population, $3 < E_i$ [keV] < 6, with a clear shift in negative V_B direction in the V_B - $V_{B \times V}$ plane, i.e., parallel crescent-shaped population (e.g., *Hesse et al.*, 2014; *Wang et al.*, 2016). The high-energy ion population, $6 < E_i$ [keV] < 30, appears sparse and scattered in the velocity space with peaks along V_B.

At a second possible X-line, marked by a black arrow, the low-energy ions population is found to be isotropic in the V_B - $V_{B \times V}$ plane, but non-gyrotropic, in the $V_{B \times V}$ - $V_{B \times (B \times V)}$ plane. The mid-energy ions, $3 < E_i$ [keV] < 6, show an isotropic distribution in the V_B - $V_{B \times V}$ plane. However, in the $V_{B \times V}$ - $V_{B \times (B \times V)}$ plane, the ions form an non-gyrotropic, perpendicular crescent-shaped distribution. The high-energy ion population, $6 < E_i$ [keV] < 30, remains sparse with peaks along $V_{\parallel}$ and $V_{\perp 2}$.

7.4 Discussion

The hybrid-Vlasov Vlasiator simulation results and MMS observations are juxtaposed at the magnetopause. We find that:

1. Multiple X-point reconnection: The magnetic island depicted in Figure 7-3&4 is generated between two adjacent X-points. The formation mechanism for the two X-points is sequential in nature, similar to the sequential multiple X-line reconnection (SMXR) model proposed by *Raeder* (2006) under southward IMF conditions. The SMXR model suggests that an initial X-point reconnects field lines, analogous to the elbow-shaped FTEs, proposed by *Russell & Elphic* (1979). The initial X-point relocates which allows for the formation of a second X-point at the subsolar region. The old X-point does not reconnect all of the magnetic flux that reconnects at the new X-point, as shown in Figure 7-7.

    Spacecraft observations (e.g., *Trattner et al.*, 2012) have provided evidence for the multiple X-line reconnection model by *Lee & Fu* (1985). For instance, *Fear et al.* (2008) used Cluster observations to show that the azimuthal extension of an observed FTE could not be explained by the elbow-shaped FTE model. THEMIS observations have similarly found bi-directional electron flows inside FTEs further suggesting the need for a second X-line to close the field lines (*Hasegawa et al.*, 2010). Recently, MMS observations provided further evidence for multiple X-line reconnection at the magnetopause. In particular, *Fuselier et al.* (2018) showed the presence of adjacent X-lines at the magnetopause under southward IMF conditions, i.e., large IMF clock angles, similar to our simulations' upstream conditions.

    Multiple localized total magnetic field extrema are observed in the in-situ magnetic field measurements. Further investigation of plasma measurements suggests that |B|-peaks are ion-scale FTEs dispersed within a thin reconnection current sheet, as indicated by the ion jet reversals and current density enhancements. The FTEs are likely generated via multiple X-line reconnection and the associated tearing-mode instability (e.g., *Lee & Fu*, 1985; *Akhavan-Tafti et al.*, 2018; *Fuselier et al.*, 2018; *Hwang et al.*, 2018). In the proposed topology, in agreement with the SMXR model and the Vlasiator simulation results, a second X-line is formed at the location of an earlier X-line. The older X-line is then located in the exhaust region of the second X-line.

144

The upstream solar wind conditions and the spacecraft location at the time of the encounter are somewhat different between in-situ observations and the Vlasiator simulations results. In particular, our simulated upstream solar wind conditions lack the observed IMF B_y (out-of-plane) component, which is an essential contributor to the formation of 3D flux ropes' core field (e.g., *Daughton et al.*, 2011), and IMF B_x. The latter was addressed by *Hoilijoki et al.* (2019) wherein the authors showed that, compared to a purely-southward IMF, the simulation run with an IMF B_x tilt, the reconnection x-points are slightly shifted in longitude, in agreement with Cluster observations (*Wang et al.*, 2006). In the case of southward IMF, the simulated X-points are often initiated at the local magnetic noon while the MMS observed X-lines are situated in the prenoon sector. This can be the result of IMF B_y component, i.e., IMF clock angle. *Fuselier et al.* (2018) provided a list of possible MMS observed multiple reconnection events under southward IMF conditions that are located at the subsolar region, in agreement with our simulation results.

In addition, the two-dimensional simulations generate magnetic islands whose central region are characterized by high density (*Markidis et al.*, 2013) and low magnetic field magnitude, contrary to the observed profiles inside flux ropes (*Akhavan-Tafti, Slavin, Eastwood, et al.*, 2019). In fact, magnetic islands collect much of the outflow plasma from adjacent reconnection X-points. In three dimensions, the outflowing plasma in an x-line's exhaust region can flow along the out-of-plane component of the magnetic field at the outer layers of flux ropes (*Ma et al.*, 1994; *Zhang et al.*, 2010; *Chen et al.*, 2017). Future Vlasiator simulations will further investigate the three-dimensional aspects of FTEs at the magnetopause.

2. Butterfly pitch angle distributions: Similar to the Vlasiator VDFs, butterfly pitch angle distributions are observed in the magnetospheric-side of the MMS X-lines (not shown here) and are often attributed to a combination of betatron and Fermi processes (e.g., *Ebihara et al.*, 2008). In this case, the depression of magnetic field lines near the X-point, along the separatrix, can cause betatron cooling of ions. Furthermore, the compression of field lines surrounding the convecting island can also accelerate ions perpendicular to the local magnetic field and/or create new mirror points within which ions are accelerated via Fermi acceleration, as discussed in Chapter 6.

The simulated strong parallel peaks may be the result of the 2D nature of the islands in which field-aligned bulk flow can only propagate in the simulation plane. In this case, the ions trapped inside an island with a closed-field geometry will continuously gain or lose energy, unlike 3D flux ropes wherein plasmas can escape the stressed region along the axis (e.g., cf. Figure 9a in Chapter 5).

3. Larmor electric field: *Malakit et al.* (2013) proposed the formation of a Larmor electric field, defined as an in-plane electric field in collisionless asymmetric magnetic reconnection, associated with finite Larmor radius effects. Larmor electric field is independent of the Hall electric field (i.e., $\mathbf{J} \times \mathbf{B} / n_i q_i$; where n_i and q_i represent the ion desnity and electric charge, respectively). The Larmor electric field is located in the inflow region of the dissipation region, which is the region where electromagnetic energy conversion occurs (*Pritchett & Mozer*, 2009), just upstream of the Hall electric field region.

Larmor electric field is proposed to exist on the magnetospheric side of a collisionless asymmetric magnetic reconnection pointing toward Earth away from the X-line, i.e., $E_x<0$. The Vlasiator simulation results indicate the presence of an Earthward electric field extremum, $E_x < -1$ mV/m located upstream and on the magnetospheric side of the southern X-point (see Figure 7-3*b*, marked as #1). The theoretical magnitude of the Larmor electric field is estimated to be: $E_x \sim k_B T_i / q_i r_i = 2$ mV/m (*Malakit et al.*, 2013), where k_B, T_i, q_i, and r_i respectively represent the Boltzmann constant and ion temperature, electric charge, and gyroradius. The derived theoretical Larmor electric field magnitude is comparable to the simulated $E_x = -0.5$ mV/m at extremum #1, offset by the Hall electric field term (see Supplemental Figure S1, panel a3). The Vlasiator estimated Larmor electric field can be directly compared with observations with no additional scaling factor.

Further particle tracing is required to confirm the relationship between the simulated earthward-pointing and Larmor electric fields. Similarly, the electric field measurements within the magnetic dip in Figure 7-7j shows negative E_x (peaking at -4 mV/m). We also find that the Larmor electric field is absent at the older of the two X-points located in the exhaust region of a second X-point. The magnitude of the Larmor electric field in the northern trajectory at the older X-point is exceeded by a stronger and oppositely-directed Hall electric field along the separatrix of the second X-point.

Our simulated electric field signatures are in agreement with the global 3D MHD with embedded PIC model simulation of the Earth's dayside reconnection by *Chen et al.* (2017) where similar localized Earthward-pointing electric field is identified accompanying a strong sunward electric field. The strong positive E_x pointing toward the Sun along the magnetopause is the Hall electric field. Farther away from the reconnection X-point, on the magnetospheric inflow region, a localized negative field pointing toward the Earth is the Larmor electric field (*Malakit et al.*, 2013; *Chen et al.*, 2017), consistent with in-situ observations (*Daniel B Graham et al.*, 2017).

4. Parallel and perpendicular ion crescent-shaped distributions in the magnetospheric side of the X-point, where E_x approaches a local minimum. This finding agrees with particle-in-cell (PIC) simulations of asymmetric reconnection (*Hesse et al.*, 2014) and MMS observations. The Vlasiator ion VDFs agree with our MMS-observed ion distributions:

   a. Isotropic distribution of low-energy magnetospheric ions (1 eV – 3 keV) farther away from the X-line. Closer to the X-line, in both locations in Figure 7-8, the low-energy ions form either an anisotropic distribution or a non-gyrotropic distribution. These signatures are also evident in the VDFs in Figure 7-3 and Figure 7-4 where the low-energy ions shift along $\mathbf{V_B}$.

   b. Non-gyrotropic and/or non-isotropic distribution of mid-energy ions at the X-point. Parallel and/or perpendicular distributions of mid-energy ions, $3 < E_i \,[\text{keV}] < 6$, are observed by MMS in the vicinity of possible X-lines.

5. The Vlasiator simulations further indicate the formation of perpendicular ion crescent-shaped distributions in the upstream region of the northern X-point on the magnetospheric side where E_x reaches a local maximum. In other words, we identify a perpendicular ion-crescent-shaped distribution which coincides with a sunward E_x maximum. This finding contradicts with the theory suggesting that crescent-shaped ion VDFs are associated with Earthward Larmor electric field (e.g., *Malakit et al.*, 2013; *Phan et al.*, 2016). The inconsistency may be due to the type of reconnection observed at the northern X-point, i.e., symmetric vs. asymmetric. It may also suggest that the crescent-shaped ion distributions are independent of the ($\mathbf{E} \times \mathbf{B}$) drift and are likely the result of magnetic field gradient, i.e., tension, in the upstream region of the X-point.

Non-gyrotropic, crescent-shaped ions are observed at the |B|-dip indicating that the MMS spacecraft may have passed through an IDR. The lower-energy non-isotropic ion population is drifted less than the non-gyrotropic mid-energy population, suggesting that the two populations are distinct. In a ($\mathbf{E} \times \mathbf{B}$)-drifted distribution in plasma, lower energy particles are more affected due to the relative velocity drift (e.g., *Nagai et al.*, 2015). Therefore, our observations may indicate that the two distinct ion populations are likely formed independent of the ($\mathbf{E} \times \mathbf{B}$) drift (e.g., *Lapenta et al.*, 2017).

Lastly, it is possible that the simulated non-gyrotropic ion distributions are numerical and a result the simulation grid specifications. However, as discussed by *Pfau-Kempf et al.* (2018), ion kinetics are well-captured by global Vlasiator simulations despite the code not resolving the ion inertial length (~100 km at the magnetopause).

Other noteworthy Vlasiator simulation results, though not confirmed in this study by MMS observations, include:

1. Sunward E_x in the upstream region of the X-point on the magnetosheath side: In addition to Earthward pointing E_x on the magnetospheric inflow region, we find a Sunward E_x peak, $E_x > +1.5$ mV/m in the upstream of the older of the two X-points located in the exhaust region of a second X-point on the magnetosheath-side (see Figure 7-4 at extremum '5'). These fluctuations are different from the proposed Larmor electric field and Hall electric field (Earthward on the magnetosheath side). To our knowledge no theory predicts the existence of this type of electric field.

2. Parallel and perpendicular ion crescent-shaped distributions in the magnetosheath side of the X-point, co-located with the simulated sunward E_x in the upstream region of the X-point. While unprecedented, these simulation results are consistent with theory linking crescent-shaped distributions to particle drift due to the magnetic field gradients in the upstream region and not an ($\mathbf{E} \times \mathbf{B}$) drift.

It is possible that the sunward E_x and non-gyrotropic ion population are simulation artifacts. However, these signatures may be the result of:

a. Formation of a sunward electric field in the reconnection upstream region, likely supported by ion pressure divergence and contributing to energy conversion at/near the X-point (e.g., *Genestreti, Varsani, et al.*, 2018).

b. Ion energization obtained over a single ion interaction with the reconnection region. Ions can be substantially energized by reflection from a magnetic field discontinuity, in this case at a separatrix in the vicinity of which magnetic field amplitude is significantly reduced resulting in a sharp magnetic field gradient (e.g., *Akhavan-Tafti, Slavin, Sun, et al.*, 2019).

Similar non-gyrotropic ion populations have been observed in the magnetosheath and are attributed to a mixing process of meandering ions (e.g., *Speiser et al.*, 1996; *Hoshino et al.*, 1998; *Hesse et al.*, 2011). Non-gyrotropic, reflected plasma populations have also been reported in association with dipolarization fronts (e.g., *Zhou et al.*, 2010, 2011; *Birn et al.*, 2012) and quasi-perpendicular shocks (e.g., *Gosling et al.*, 1982). Future investigation will further examine the source of the magnetosheath sunward E_x and the associated crescent-shaped ion distributions. MMS observations in the magnetosheath-side of X-lines will also be investigated to search for similar non-isotropic, non-gyrotropic ion distributions in the magnetosheath side of X-lines to support these simulation results.

3. Reconnection rate at an X-point ('Northern X-point', located in the exhaust region of a second X-point ('Southern X-point'), increases with time while the reconnection rate at the Southern X-point is reduced. This may be due to the reconnection exhaust geometry. The Northern X-point is sandwiched between two magnetic islands of different scales, while the Southern island is surrounded by one island and a semi-infinite current sheet. This finding may further underpin the significant role of flux ropes in reconnection dynamics by unblocking the exhaust region and providing a path along which the outflowing plasma can efficiently propagate.

A total of 4786 subsolar islands ($|\theta| < 30$ degrees) are identified across time frames. The islands are divided into four main categories depending on their structure and evolution: 1) '2 X-points', 2) '>2 X-points', 3) 'Coalescence,' and 4) 'Division.' It is concluded that:

1. On average, continuous reconnection at adjacent dominant X-points supplies additional magnetic flux, $\Delta\psi > 0$, to the outer layers of magnetic islands. The additional supply of

magnetic flux further causes an increase ($\Delta A > 0$) in the cross-sectional areas of the majority of these islands, as proposed by *Akhavan-Tafti et al.* (2019; cf. Figure 1).

2. In 20% of the islands belonging to Category 2, magnetic flux content increases while the islands' cross-sectional area is reduced. This suggests that the internal X-points may contribute to dividing the dominant island into at least two smaller islands, i.e., island division. Another possible scenario, as postulated by *Akhavan-Tafti et al.* (2019), may include the compression of the island due to the radially-inward force from the continuous supply of magnetic flux at adjacent X-points ($\Delta A < 0$ & $\Delta \psi > 0$), before the island grows in dimensions.

3. In the Coalescence category, 40% of the magnetic islands grow in dimensions while 40% are eroded, i.e., reduction in cross-sectional area. These suggest that, as discussed by *Fermo et al.* (2011), the coalesce process involves the merging of two neighboring islands wherein the smaller of two islands is consumed, i.e., eroded ($\Delta A < 0$), by the larger island ($\Delta A > 0$).

4. The likelihood of identifying island division events is nearly twice that of island coalescence events suggesting that the division of magnetic islands is more common than coalescence (e.g., *Øieroset et al.*, 2011, 2019). While identifying the two processes in spacecraft observations is challenging, one approach in distinguishing flux rope coalescence from division is to investigate the relative structure velocities. In the coalescence process, the two neighboring flux ropes approach each other (in the flux ropes' frame of reference), whereas in the division process the structure velocity vectors point in opposite directions (moving away from one another).

5. The proposed classification in Figure 7-2 oversimplifies the island dynamics by neglecting the fact that one or two of the processes could occur concurrently. For instance, in Category 3, the two X-points on the outer edges of the two coalescing islands can and do continue to supply additional magnetic flux and plasma to the outer layers of the two islands.

6. Continuous reconnection, Category 1, is the dominant contributor to island evolution (e.g., *G. Paschmann et al.*, 1982; *Akhavan-Tafti, Slavin, Eastwood, et al.*, 2019). However, this result may also be an artifact of our island selection criteria wherein islands are defined as 'O-points' sandwiched between two 'X-points.'

7. Based on the above statistics, the cross-sectional areas of subsolar islands evolve, on average, as:

$$\Delta A / \Delta t \ \left[km^2/s\right] \cong A \left[km^2\right] (\psi \ [Wb])^{-1} (2.2 \ (8.6 \ \mathcal{R} + 0.5) \pm \bar{\sigma}) \times 10^3 (Eq. \ 1)$$

where A, ψ, and $\mathcal{R}$ denote respectively the FTE cross sectional area (in units of km^2) and magnetic flux content and the normalized reconnection rate at an adjacent X-line, assuming steady and continuous reconnection X-line. The propagated standard error $\bar{\sigma} = 1.5$ Wb/s.

Equation 1 provides an *upper threshold* for the rate of change of the cross-sectional area of subsolar magnetopause FTEs. The 2D nature of the simulation grid requires all interplanetary magnetic flux to reconnect with the magnetosphere at the magnetopause. Therefore, the amount of reconnected flux in 2D simulations is over-estimated, resulting in larger normalized reconnection rate and faster FTE growth.

The purely-southward and fast upstream IMF condition may impact the above statistics and average normalized reconnection rates. *Hoilijoki et al.* (2019) compared Vlasiator island evolution under southward IMF conditions with and without a B_x-component and found that magnetopause reconnection dynamics and island frequency and size change across the northern and southern hemispheres under different upstream IMF conditions. Therefore, future analyses shall investigate island statistics under various upstream IMF conditions to further compare with spacecraft observations (*Wang et al.*, 2006).

Finally, the Vlasiator simulations indicate that the change in magnetic island magnetic flux content, $\Delta\psi$, due to continuous reconnection at adjacent X-lines is a function of normalized reconnection rate. In 2D, the magnetic flux content is described as the enclosed in-plane flux within an area and, therefore, it is, in practice, different from in-situ observations. However, the rate of change in magnetic flux, $\Delta\psi$ [Wb/s-km], is, to a first-order approximation, similar in 2D simulation results and spacecraft observations. The rate of change in magnetic flux is determined in the reconnection plane (per X-line length) along the X-line.

The MMS multi-spacecraft fields and plasma measurements are used to estimate the temporal change in magnetic flux content of the observed d_i-scale FTEs, discussed in Section 7.3.2. Figure 7-9 shows the observed FGM magnetic field vectors, the bulk FPI ion and electron velocities and the EDP electric field vectors at the location of MMS1 in the vicinity of a possible

X-line encounter sandwiched between two of the observed FTEs, marked with a cyan bar in Figure 7-7. The vectors are transformed into the LMN coordinate system where the lmn eigen vectors (in the GSM coordinates) are: $\mathbf{n}$ = [0.84, -0.36, -0.41], $\mathbf{m}$ = [-0.46, -0.87, -0.17], and $\mathbf{l}$ = [0.30, -0.33, 0.89] (*Hwang et al.*, 2018). High-resolution electric field measurements are boxcar-averaged to match the cadence of the FPI electron measurements, i.e., 30 ms. The X-line is found to convect at a normal velocity $\mathbf{v}_{structure}$ [km/s] = 130 * [-0.96, 0.29, 0.06] LMN. Therefore, the electric field vector in the X-line's frame of reference can be estimated as $\mathbf{E}_{X\text{-}line}$ = $\mathbf{E}$ + $\mathbf{v}_{X\text{-}line}$ x $\mathbf{B}$ (panel f).

The observed MMS estimated out-of-plane component of electric field, E_M, averaged at the vicinity of the X-line within the purple-shaded interval is $E_{M,\,obsv}$ = 0.2 mV/m. This corresponds to an averaged normalized reconnection rate, $\mathcal{R}$ = E_M / $V_{Ai}\,B_{MSH}$ = 0.18, where V_{Ai} and B_{MSH} are the average upstream Alfvén velocity (panel g) and magnetic field magnitude (panel a), respectively (e.g., *Liu et al.*, 2017; *Genestreti et al.*, 2018). Based on the Vlasiator simulation fit of $\Delta\psi/\Delta t$ [Wb/km-s] = 8.6 $\mathcal{R}$ + 0.5, where $\mathcal{R}$ represents the rate of reconnection, it is concluded that, to a first-order approximation, the observed d_i-scale FTE (ψ = 4.4 kWb) can gain magnetic flux at rate <+9.0 kWb/s-km due to continuous supply of magnetic flux at the adjacent X-line. At this rate, this FTE will contain 1 MWb of magnetic flux (e.g., *Wang et al.*, 2005) in less than 2 minutes.
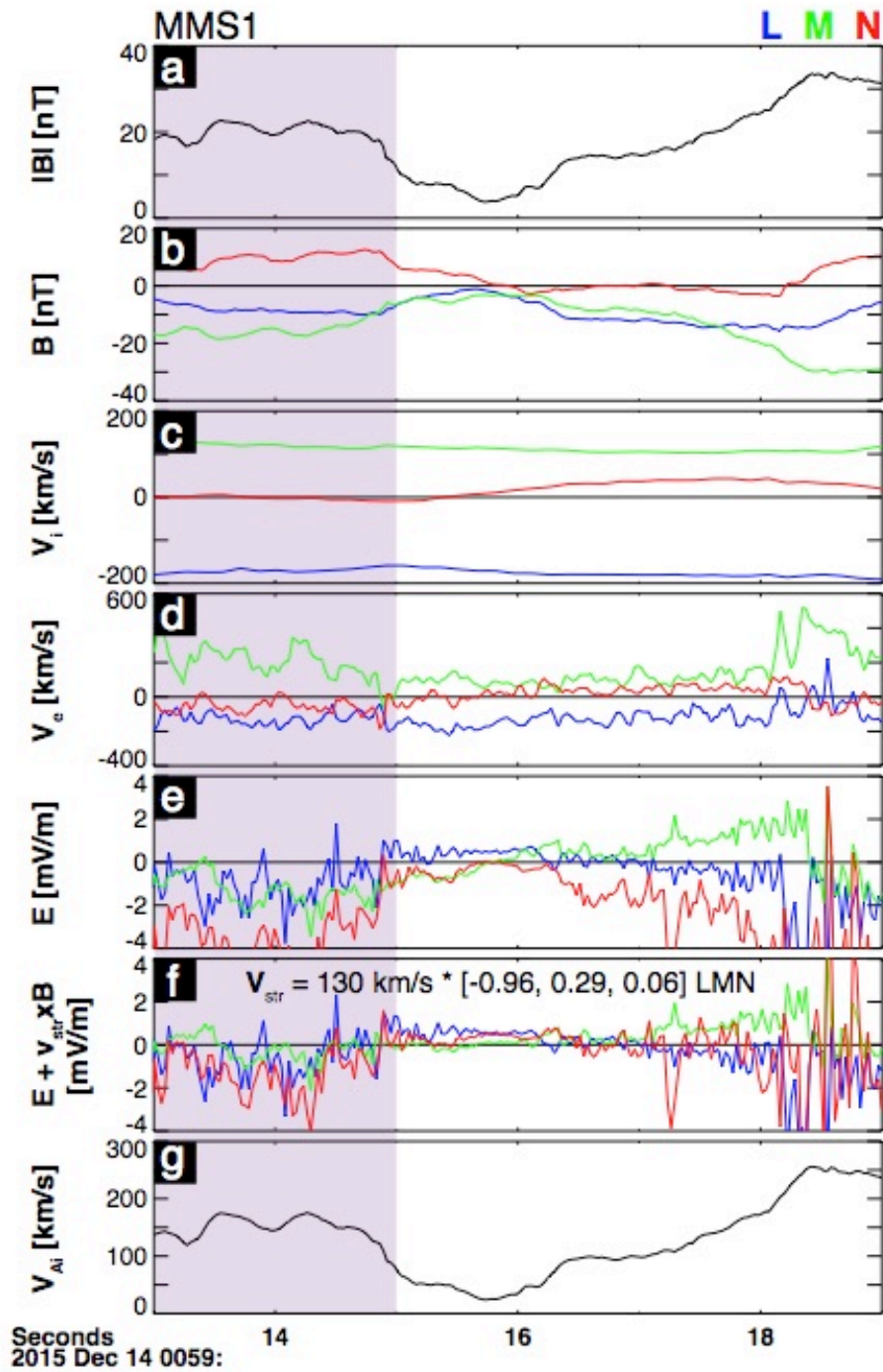
Figure 7-9: Fields and plasma moments in the vicinity of a candidate IDR crossing in LMN coordinates as observed by MMS 1: a) magnetic field magnitude, |B|, b) magnetic field components, c) ion velocity components, d) electron velocity components, e) electric field components in the spacecraft's frame of reference, f) corrected electric field components in the X-line's frame of reference, and g) Alfvèn velocity. The normalized reconnection rate is estimated from the fields and plasma signatures in the purple-shaded region.

153

The global Vlasiator simulations results are further utilized to determine the average rate at which FTEs grow at the magnetopause. From the MMS-observed normalized rate of reconnection rate, $\mathcal{R} = 0.18$, and ion-scale FTE sizes and magnetic flux contents, it is determined that the ion-scale FTE observed in the vicinity of an X-line may grow in size at rate:

$$\Delta A/\Delta t \ (\lambda = 6.8 \ d_i, \ \mathcal{R}=0.18, \ \psi=4.4 \ \mathrm{kWb}) \leq +2.1(\pm0.7)\times10^5 \left[\mathrm{km}^2/\mathrm{s}\right] = +3.1 \ (\pm0.1)\times10^{-1} \left[R_E^2/\mathrm{min}\right].$$

At this growth rate, the ion-scale FTE will grow Earth-sized, $r = 1 \ R_E$ (e.g., *Eastwood et al.*, 2012), in 10^{+5}_{-2} minutes due to steady and continuous reconnection at the adjacent X-line while convecting away from the subsolar region along the magnetopause. This estimated growth duration is comparable to the transport time for an FTE forming at the subsolar magnetopause to reach the high-latitude magnetopause, i.e., $\sim$ 10 minutes (e.g., *Owen et al.*, 2001). The underlying assumption here is that only one actively-reconnecting X-line is contributing to the growth of the FTE. A second X-line will expedite this growth process, such that an ion-scale FTE will become Earth-sized in nearly half the time estimated for one continuous reconnection X-line. Similarly, ion-scale (e.g., *Sun et al.*, 2019) and large-scale flux ropes with strong core fields (e.g., *Slavin et al.*, 1995; *Slavin, et al.*, 2003) are observed in the Earth's magnetotail, which is the focus of a future comparative analysis.

It is concluded that the difference between the average FTE size observed at the subsolar magnetopause by MMS (*Akhavan-Tafti et al.*, 2018) and at high-latitude and flank regions by Cluster (e.g., *Wang et al.*, 2005; *Fermo et al.*, 2011) is most likely due to their orbits and different FTE sampling populations. As suggested by *Akhavan-Tafti et al.* (2018), FTEs grow while convecting away from the subsolar region where they are most likely formed. Therefore, MMS, due to its near-equatorial orbit, is expected to observe smaller-scale FTEs soon after formation, hence, smaller average FTE size compared to Cluster, due to its polar orbit. Further investigation of the Cluster magnetic field data is required to confirm this conclusion, since the study by *Wang et al.* (2005) did not account for small-scale FTEs (4s cadence magnetometer data).

7.5   Conclusion

The hybrid-Vlasov Vlasiator simulations of multiple X-point reconnection at the subsolar region are compared with MMS observations of two neighboring X-lines within which at least five ion-scale FTEs are identified. In both the simulations and the observations, one X-line is located in the exhaust region of a second X-line, consistent with the sequential multiple X-line reconnection model. The drift of an initial X-point allows for the formation of a second X-point at the subsolar region. The old X-point does not reconnect all of the magnetic flux that reconnects at the new X-point. The crescent-shaped ion distributions observed at the leading X-line indicate that the MMS spacecraft may have traversed the ion diffusion regions. These crescent-shaped ion distributions are in good agreement with the Vlasiator simulations. The Vlasiator crescent-shaped ion distributions are spotted at the location of the Larmor electric field, on the magnetospheric inflow region of the second X-point and behind the Hall electric field, in agreement with global MHD-EPIC simulations and MMS observations.

We further investigate the evolution of the Vlasiator's two-dimensional magnetic islands due to magnetic reconnection. Magnetic islands at the low-latitude magnetopause (polar angle, $|\theta|$ < 30 degrees) are found to grow mainly due to continuous reconnection at adjacent X-points. It is also shown that magnetic islands further evolve due to coalescence, erosion, and division. The relationship between the normalized rate of reconnection at an adjacent X-point and the change in the islands' enclosed magnetic flux are determined.

The average rate at which magnetic flux is added to the outer layers of magnetic islands due to continuous reconnection at adjacent X-points is determined. Based on our statistical analysis of magnetic islands in the Vlasiator code, magnetic islands grow at +0.3 R_E^2/min. At this rate, a subsolar MMS-observed d_i-scale FTE is estimated to grow Earth-sized within ~10 minutes, by a single X-line, while convecting away from the reconnection site along the magnetopause. The estimated growth time is comparable to the average transport time for FTEs formed in the subsolar region to reach the high-latitude magnetopause and flanks.

Finally, it is concluded that the discrepancy in the average FTE size at the magnetopause between the Cluster and MMS observations is most likely the result of their different orbits, wherein MMS mainly observes the newly-formed FTEs at the subsolar region near the magnetic equator while Cluster detects grown FTEs farther away from the subsolar region at higher-latitude

magnetopause and flanks. Further investigation of the Cluster magnetic field measurements are required to confirm this conclusion.

Chapter 8: MMS Observations and Global Vlasiator Simulations of the FTE Coalescence Process

This Chapter is adopted from Akhavan-Tafti, M., Palmroth, M., Slavin, J. A., Dubart, M., Johlander, A., Grandin, M., Ganse, U., MMS Observations and Global Vlasiator Simulations of the FTE Coalescence Process, to be submitted to the Geophysical Research Letters.

8.1 Introduction

Magnetic reconnection is a process through which magnetic field lines break and reform. Magnetic reconnection can convert energy from the magnetic fields into kinetic energy of plasmas in space, astrophysical, and laboratory environments (e.g., *Yamada et al.*, 2010, 2014). Magnetic reconnection can develop in multiple X-lines (*Lee & Fu*, 1985, 1986) and generate multiple flux ropes. Tearing instability can further drive the current sheets between two neighboring X-lines unstable and result in the formation of ion-scale flux ropes (*Biskamp*, 1982; *Daughton et al.*, 2011; *Eastwood et al.*, 2016). Flux ropes, such as flux transfer events (FTEs) at the magnetopause (*Russell & Elphic*, 1979; *Akhavan-Tafti et al.*, 2018), are highly dynamic (*Akhavan-Tafti, Slavin, Eastwood, et al.*, 2019) and can evolve via continuous reconnection at the adjacent X-lines, coalescence, erosion, and division (Akhavan-Tafti et al., *submitted*), as observed in planetary magnetospheres (*Fuselier et al.*, 2018; *Hwang et al.*, 2018; *Sun et al.*, 2019), the solar wind (*Song et al.*, 2012), and in the solar corona (*Su et al.*, 2013).

In a typical dayside magnetopause reconnection, the magnetospheric field lines with strong magnetic field and low plasma density come in contact with the magnetosheath field lines whose magnetic fields are weaker and a plasma density that is nearly an order of magnitude greater (*Burch et al.*, 2016). This asymmetry in fields and plasma parameters differentiates magnetopause reconnection from magnetotail reconnection where the lobe magnetic field lines are often of similar magnetic field magnitude and plasma density (*Eastwood, Phan, et al.*, 2010; *Torbert et al.*, 2018). One contributing factor to the observed differences between the two environments is plasma

beta β (*Swisdak et al.*, 2010), defined as the ratio of thermal pressure to magnetic pressure, as supported by the observations of *DiBraccio et al.* (2013) at Mercury (low-beta) and at Saturn (high-beta) by *Masters et al.* (2012).

Thin current sheets, whose thickness is a fraction of an ion inertial length, d_i, have been observed on the magnetospheric side ($\beta_{MSP} < \beta_{MSH}$) of asymmetric magnetopause reconnection and in the vicinity of the electron diffusion region (e.g., *Burch et al.*, 2016; *Ergun et al.*, 2017; *Chen et al.*, 2017). The current sheet is believed to stabilize the ion pressure asymmetry across the reconnection region via generating a strong electric field component perpendicular to the current sheet plane (e.g., *Cassak & Shay*, 2007; *Pritchett et al.*, 2012; *Price et al.*, 2016; *Ergun et al.*, 2017). The strong E×B drift associated with the generated electric field forms an in-plane current, known as the 'Hall' term in the generalized Ohm's law ($E_{Hall} \propto J \times B$).

The FTE coalescence process involves the merging of two (or more) neighboring FTE-type flux ropes (*Pritchett & Wu*, 1979; *Pritchett*, 1992, 2007). While merging, a current sheet is formed between the merging FTEs (*Wang et al.*, 2016a). The sheet layer can become susceptible to reconnection. In a reconnecting current sheet, the field lines of the two neighboring FTEs break and reorganize in order to create a larger FTE. MMS measurements have recently discovered thin reconnecting current sheets at the interface of interacting magnetic environments at the dayside magnetopause (*Zhou et al.*, 2017; *Kacem et al.*, 2018; *Phan et al.*, 2018; *Øieroset et al.*, 2019) and in the magnetotail (*Man et al.*, 2018; *Poh et al.*, 2019) with unprecedented details.

The coalescence current sheet is generated and controlled by the shear angle between the outer magnetic layers of the two merging FTEs (*Markidis et al.*, 2013). Two-dimensional, fully kinetic, particle-in-cell (PIC) simulations suggest that before (or, in some cases, during) the reconnection onset, magnetic flux may pile up within the current sheet (*Karimabadi et al.*, 2011). The flux pileup is shown to be a function of island size. Magnetic islands are the 2D equivalents of three-dimensional flux ropes. Plasma beta reduces with increasing magnetic flux pile up between the merging FTEs. In low-beta environments, such as the solar corona, magnetotail (*Øieroset et al.*, 2002; *Dewey et al.*, 2017), or the interaction region between colliding coronal mass ejections (*Gopalswamy et al.*, 2001), plasmas are accelerated by magnetic reconnection (e.g., *Egedal et al.*, 2009).

The temporal evolution of merging flux ropes is shown in Figure 8-1. The net environmental forces cause the merging of neighboring flux ropes. Before coalescence at $t = t_1$, a spacecraft (grey lines) traversing across the two approaching flux ropes, will observe two independent flux ropes, identified by bipolar magnetic field coinciding with peaks in the axial and total magnetic field (e.g., *Slavin et al.*, 2003). The magnetic field signatures are presented in the flux ropes' frame of reference, where the out-of-plane component, B_y, indicates the axial component of the magnetic field. Magnetic flux piles up between the two flux ropes approach one another ($t_2 > t_1$; *Karimabadi et al.*, 2011). Next, a current sheet is formed between the oppositely-directed field lines at the outer layers (shown in bold black arrows) of the two merging flux ropes, i.e., the Ampere's law. Inside this current sheet, the flux ropes' outer magnetic field lines reconnect, creating a larger flux rope within which coalescence proceeds, as indicated by two coalescing concentric ovals embedded inside a relaxing ellipse ($t_3 > t_2$). The resulting structure can be identified as a quadrupolar magnetic field signature, B_z, corresponding to the two adjacent flux ropes. The coalescence process may continue ($t_4 > t_3$) until the two flux ropes have created one larger flux rope. However, *Karimabadi et al.* (2011) proposed an upper threshold for the extent to which larger magnetic structures (scale size $> 100\ d_i$) may coalesce.

The reconnection separatrix, defined as a surface separating the plasma entering the reconnection region from the plasma already processed by the reconnection process (*Lapenta et al.*, 2016), are identified with numerous key features, including the strong parallel current density, the density cavity (*Shay et al.*, 2001; *Wang et al.*, 2013), and the Hall signatures (e.g., *Rogers et al.*, 2003; *Eastwood et al.*, 2010). Electrons, as is also shown for this coalescence event in the cartoon schematic by *Zhou et al.* (2017; Figure 2g), mainly stream along the separatrix toward the X-line. *Lapenta et al.* (2015) showed that ions, on the other hand, cross the separatrix.

The early accounts of reconnection electromagnetic patterns including the Hall field polarity and symmetry are summarized by *Rogers et al.* (2003). The patterns are believed to be generated by the reconnection electric field, the out-of-plane component E_M, which causes the out-of-plane acceleration of magnetized electrons and, with them, the magnetic field lines, B_M. Since ions are demagnetized in this region, they do not partake in this process. Another characteristic Hall signature is the in-plane electric field component, E_N. *Ma & Feng* (2008) proposed that E_N is a result of the density imbalance caused by differential motions of electrons and ions in asymmetric

reconnection. Using Hall MHD simulations, they found that the E_N and plasma density are greater at the reconnection inflow region with the lower density or/and higher magnetic field magnitude.
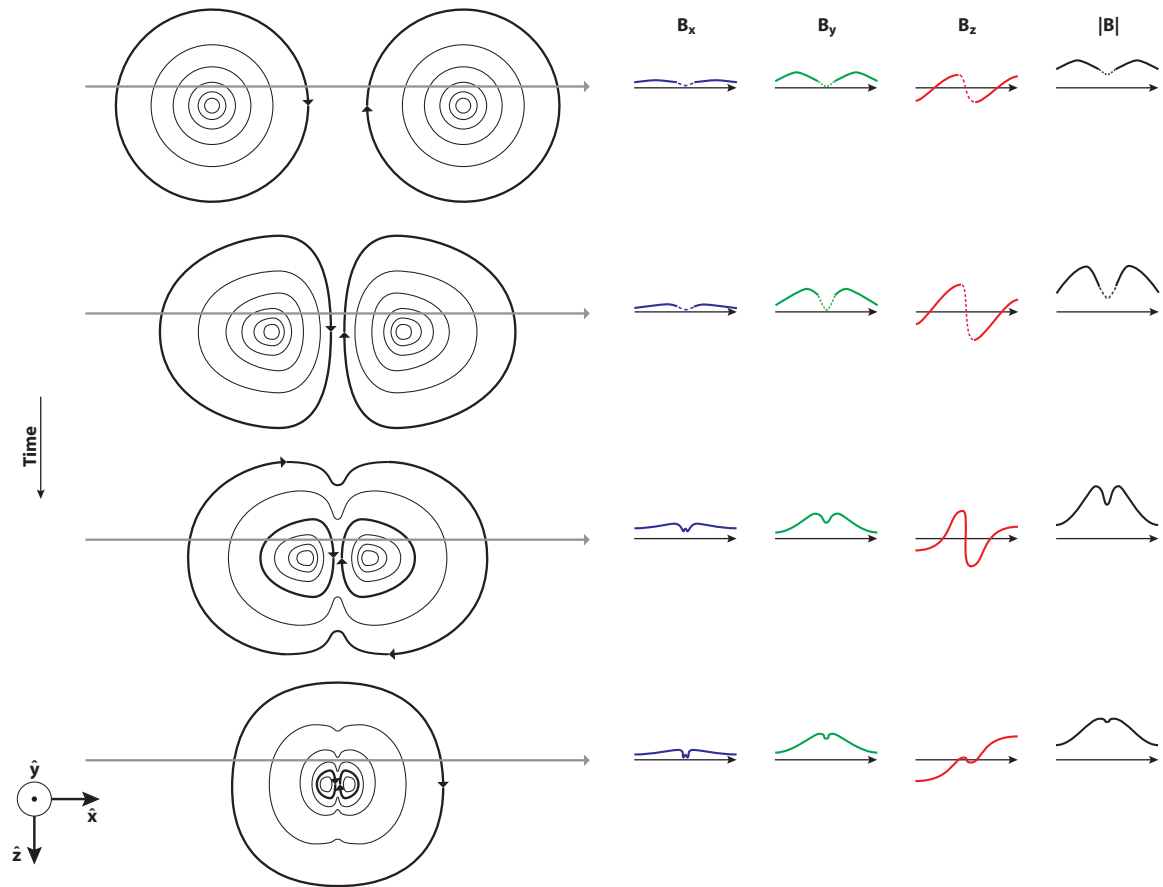
Figure 8-1: The cartoon schematic of the temporal evolution of the coalescence process. Flux ropes are represented as concentric black contours. Time stamps t_n denote progressing time.

161

Swisdak et al. (2003) studied magnetic reconnection with a large density asymmetry across the reconnecting field regimes using 3D PIC simulations. It was concluded that the density gradient, in the presence of a shear angle, gives rise to the generation of a diamagnetic drift that can advect the reconnecting field region. Under extreme upstream conditions, where the relative diamagnetic electron and ion drifts exceed the local Alfven velocity, the diamagnetic drift can stabilize the reconnecting current sheet and, by doing so, suppress reconnection.

In the present study, we examine the FTE coalescence event of November 17, 2015 (*Zhou et al.*, 2017). We first investigate the relationship between the observed plasma density non-uniformity, diamagnetic current, and Hall signatures (*Eastwood et al.*, 2007) at the interface of the two coalescing FTEs. Next, we provide the first global view of island coalescence at the dayside magnetopause using the hybrid-vlasov Vlasiator simulation code (*von Alfthan et al.*, 2014; *Palmroth et al.*, 2018). The Vlasiator coalescence events are used to study the temporal evolution of diamagnetic currents between coalescing magnetic islands. It is concluded that the diamagnetic current loops generated from the observed plasma density between two asymmetric FTEs create the observed Hall signatures.

8.2 MMS Observations

During the outbound magnetopause crossing of 17 November, 2015, the MMS spacecraft were located at (X, Y, Z) = (9.7, -0.9, -0.3) R_E in the geocentric solar magnetospheric (GSM) coordinates. The interplanetary magnetic field (IMF) was steadily southward ($B_z \sim$ -2 nT) with a relative large dawn-dusk component ($B_y \sim$ +4 nT). The spacecraft separation was nearly 20 km ($\sim$ 2 d_i; assuming average ion density 40 cm^{-3}). The magnetopause crossing was marked by an ion jet reversal ($|\frac{\Delta v_{iz}}{v_{iz}}| > 4$), likely reconnection flows from two reconnection exhausts located northward and southward of the MMS spacecraft. Similar jet reversals associated with adjacent X-lines have been reported at the magnetopause (*Fuselier et al.*, 2018; *Hwang et al.*, 2018), in correspondence with the multiple X-line reconnection model (*Lee & Fu*, 1986) and, likely, the sequential multiple X-line reconnection model (*Raeder*, 2006).

As reported by *Zhou et al.* (2017), shortly after the magnetopause crossing, the MMS spacecraft encountered a system of two coalescing FTEs at 02:16:30 — 02:16:40 UT. The coalescence process includes a quadrupolar signature, similar to trajectory t=t$_3$ in Figure 8-1, in

the tangential component of the magnetic field, B_L. The LMN coordinate system is determined by applying the minimum variance analysis (MVA) on magnetic field components across the grey-shaded region 02:16:06.2 – 09.6 UT encompassing the bimodal peaks in plasma density, panel b. The LMN eigen values and eigen vectors are included in Table 8-1.

As shown in Figure 8-2a, the sharp bipolar B_L (negative to positive) observed by MMS2 at the center of the two FTE-type flux ropes is sandwiched between the two plasma density extrema. Magnetic field magnitude and the out-of-plane component, B_M, are found to decrease when n increases and vice versa. The tangential component of normalized (relative to the Alfvèn velocity, v_A) ion velocity in the current sheet frame of reference, $v_{iCS, L}$, is quadrupolar modulating in-phase with $|B|$. The parallel and perpendicular components (relative to **B**) of current density are shown in panel d to suddenly jump to extreme values at $n = n_{min}$. The modulations in plasma density (negligible ∇T) and $|B|$ result in perturbations in thermal and magnetic pressures, therefore, creating a bimodal β signature within the grey-shaded region. Ion beta, $\beta_i < 1$ at $n = n_{min}$.

In the present study, we focus on the perpendicular current layer (PCL) at the interface of the two coalescing FTEs between the two plasma density peaks at 02:16:06 – 10 UT. Figure 8-2 provides a summary of the fields and plasma properties within the . In panel *a*, the out-of-plane magnetic field, B_M, offset by the background guide field ($B_G = 60$ nT, suggesting a large shear angle between the merging field lines, <180 degrees), is bipolar. The in-plane current density, J_L, and electric field, E_N, components are also bipolar in this region, presented in panels *b* and *c*. Simulations and observations of reconnection have shown characteristic bipolar and quadrupolar signatures in the in-plane electric field and the out-of-plane magnetic field, respectively (*Øieroset et al.*, 2001; *Mozer et al.*, 2002; *Borg et al.*, 2005; *Eastwood et al.*, 2009). These signatures indicate the creation of a Hall region within which ions decouple from magnetic field in a greater scale than electrons. The Hall signatures in Figure 8-2 are quite distorted, which, as previous studies have suggested, can be a result of the observed large guide field, i.e., asymmetric Hall signatures in guide field reconnection (i.e., *Eastwood et al.*, 2010).

Table 8-1: The LMN coordinate system determined by applying the minimum variance analysis (MVA) on magnetic field components across the grey-shaded region.

	L (max)	**M** (int)	**N** (min)
Eigen values	217	16	3
Eigen vectors	[-0.96, 0.01, 0.29]	[0.20, 0.75, 0.63]	[-0.21, 0.66, 0.72]

In addition, the plasma density and magnetic field asymmetries across the coalescence region are expected to alter the reconnection dynamics. In particular, plasma pressure (or plasma beta) asymmetry across the PCL can facilitate the diamagnetic drift of ions and electrons. Electrons and ions will experience different drifts resulting in a diamagnetic current, $\mathbf{J}_{dia} \sim (\mathbf{B} \times \nabla\mathbf{P}) / \mathrm{B}^2$, where the inertial term ($\propto du/dt$) is assumed negligible. Panel *d* provides the components of ion diamagnetic current. The in-plane component of diamagnetic current, $J_{dia, L}$, calculated at the spacecraft barycenter, shows a bipolar signature similar to the observed Hall current, though slightly smaller in magnitude (at 150 ms cadence). Panel e provides the in-plane components of current density at the spacecraft barycenter derived from thermal pressure gradients (J_{dia}), averaged time-shifted FPI moments ($<J>$), and the curlometer technique (J_{curl}; *Harvey*, 1998). The three independent techniques produce matching J_L. The diamagnetic ion and electron currents are further provided in panel *e* and show that ions account for ~90% of the observed PCL.
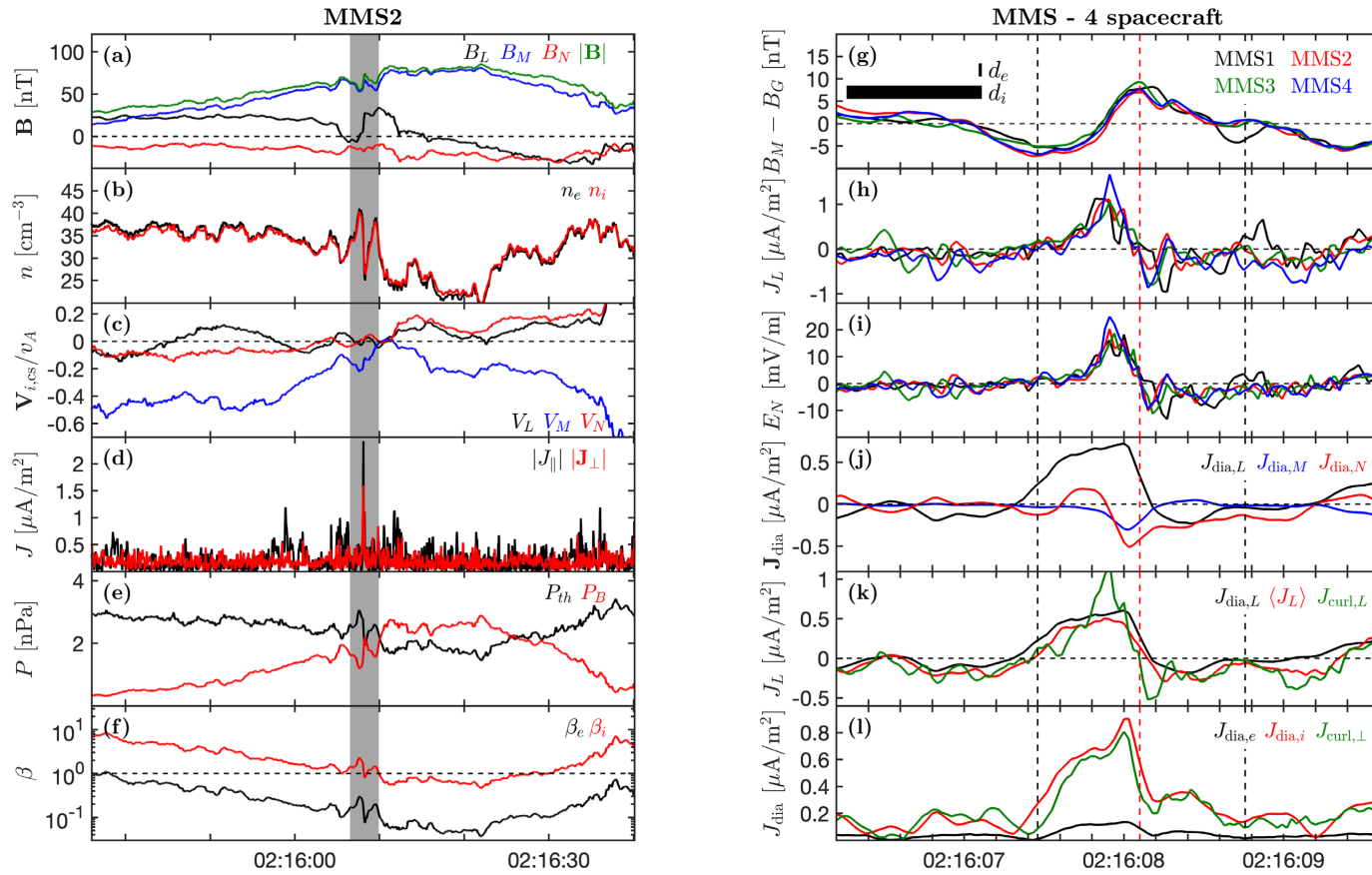
Figure 8-2: MMS observations of a flux rope merger on 2015-11-17 as identified by Zhou et al. (2017). (a-f) MMS3 observations. The yellow time interval shows the times of panels (g-k). (g-k) Multi-spacecraft observations. The gray time interval shows the current sheet. (a) Magnetic field in geocentric solar ecliptic (GSE) coordinates. (b) Electric field. (c) Electron (black) and ion (red) number density. (d) Ion flow velocity. (e) Current measured with the curlometer technique. (f) Electron (black) and ion (red) plasma beta. (g) Four-spacecraft magnetic field in the intermediate variance direction subtracted with the guide field, $B_G = 62$ nT. The traversal time of the electron and ion inertial lengths obtained from the timing analysis are indicated. (h) Currents in the maximum variance directions measured by FPI. (i) Electric field in the normal direction. (j) Total diamagnetic current in the LMN coordinate system. (k) Magnitude of electron (black) and ion (red) diamagnetic current and perpendicular current measured with the curlometer technique (green). All data have 30 ms cadence and in (g-i) are time-shifted to the center of the spacecraft tetrahedron.

8.3 Vlasiator Simulations

The hybrid-Vlasov code Vlasiator (http://www.helsinki.fi/en/researchgroups/vlasiator) has been developed to investigate global magnetospheric dynamics at ion scales (*Von Alfthan et al.*, 2014; *Palmroth et al.*, 2018). Vlasiator solves the Vlasov equation, evolving ions (protons) as distribution functions in three velocity-space dimensions, tracked on a cartesian grid. Electrons are treated as a cold massless charge-neutralizing fluid, and closure is provided by the generalized Ohm's law including the Hall term. The simulation used in this study is two-dimensional in real space (resolution=300 km) and three-dimensional in velocity space (resolution=30 km/s) (*Palmroth et al.*, 2013; *Palmroth et al.*, 2017; *Hoilijoki et al.*, 2017; *Jarvinen et al.*, 2018; *Juusola et al.*, 2018; *Juusola et al.*, 2018).

For the sake of brevity, the details of the simulation run are not included here and the reader is referred to Chapter 7. It is important to note that 1) the simulation d_i~200 km at the magnetopause under our upstream conditions (fast solar wind of $\mathbf{v}$ [km/s] = -750 $\hat{\mathbf{x}}$, a density of n_{sw}=1 cm^{-3}, a proton temperature of T_p = 0.5 MK, and a purely southward IMF of magnitude 5 nT), and 2) despite not resolving d_i, kinetic effects at the Earth's dayside are captured in the Vlasiator's simulation grid (*Pfau-Kempf et al.*, 2018).

At simulation time t=1678.5 s, as shown in Figure 8-3, an anti-sunward-moving magnetic island catches up to a larger magnetic island that is slowly convecting northward. The smaller island has a smaller magnetic pressure and larger thermal pressure. At the interface of the two islands inside an out-of-plane current sheet $\mathbf{J}_2$, magnetic field lines break and reconnect, as shown by enhanced ion jets, $\mathbf{v}_{i1,2}$, in the outflow region. The reconnection results in the formation of a large, closed magnetic island within which the two islands are embedded, hence referred to as island coalescence. The reconnection between the two islands is described as asymmetric due both the magnetic and density imbalance across the reconnecting inflow regions. The coalescence process is further characterized by a strong, diamagnetic current density.

As time progresses, at t=1686.5 s and then t=1692.0 s, the magnetic field lines between the two merging islands are compressed, magnetic field pileup. Inside the field pileup region, the curvature of the reconnecting field lines is reduced resulting in flattened reconnection inflow regions. The outflow region, on the other hand, experiences increased curvature, as indicated by stretched field lines. At later time frames, the diamagnetic current is found to become longer in

extent, l, while the separation, w, between the two J_{DM} peaks remains constant. In addition, the J_{DM} magnitude remains stronger on the side of the current sheet with lower β.
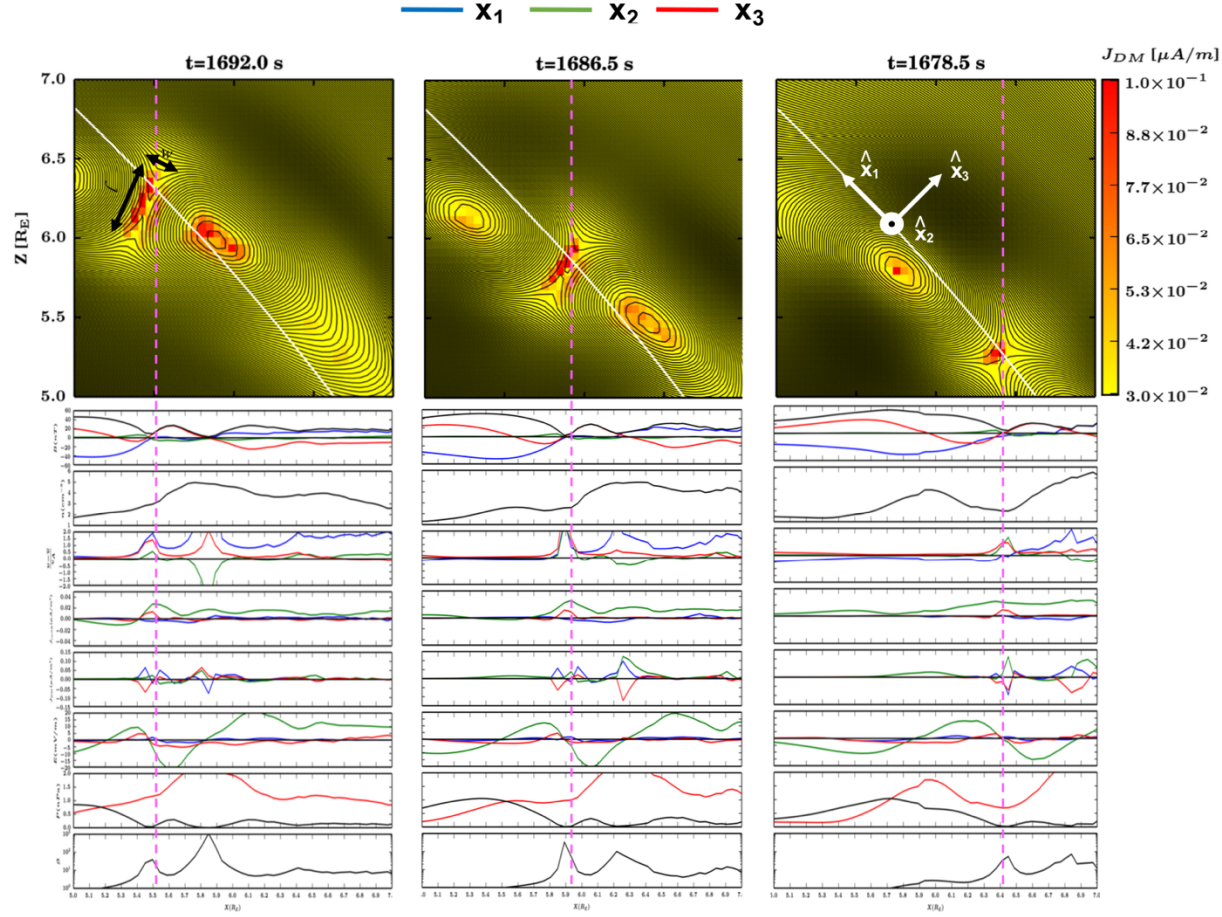
Figure 8-3: The temporal evolution of the Vlasiator coalescence process. The rows include: a) simulation frames of diamagnetic current total, $\mathbf{J}_{DM} = \frac{\mathbf{B}}{B^2} \times \rho \frac{d\mathbf{u}}{dt} + \frac{\mathbf{B}}{B^2} \times \nabla P$, between two coalescing magnetic islands located in the northern hemisphere. The contours represent the XZ-plane magnetic field and the color bar shows the magnitude of J_{DM}. The white line denotes a virtual spacecraft inbound trajectory through the coalescence region. The spacecraft trajectory is the average magnetopause distance and, therefore, used to derive the magnetopause normal boundary coordinates, $\mathbf{x}_i$. b) magnetic field components, c) plasma density, d) ion velocity components in the structures' frame of reference, e) current density components, $\mathbf{J} \propto \nabla \times \mathbf{B}$, f) diamagnetic current components, $\mathbf{J}_{DM}$, g) electric field components, magnetic and thermal pressures, h) plasma beta.

8.4   Summary and Conclusions

MMS observations indicate that the thermal pressure difference between the two coalescing magnetic structures, $P_{th,FTE2} / P_{th,FTE1} \sim 1.5$ as shown in Figure 8-2a, causes diamagnetic currents in within the current sheet. Figure 8-4a represents a simple slab model comprising charged particles frozen into an infinitely-long, uniform static out-of-plane magnetic field, B_G. In the collisionless regime in which scattering force is too small compared to the magnitude of the magnetic force, the charged particles gyrate around B_G, as depicted by clockwise circular arrows showing ion gyration.

In the presence of the observed non-uniform plasma at the coalescence region, there will be more charged particles with a finite Larmor radius traversing from the region of higher plasma density (low |B|) into the lower plasma density region (high |B|). This, in turn, results in a net counterclockwise (clockwise) drift of ions from the lower (higher) pressure region into the higher (lower) pressure region, $v_{iD} \propto \nabla P_{\perp}$. The electrons' net diamagnetic drift is opposite to that of ions, thus, causing diamagnetic currents. As illustrated in Figure 8-4a, the diamagnetic currents can be modeled as a series of infinitely-long rectangular solenoids (*Hallock & Meier*, 2018). The induced, out-of-plane magnetic field perturbations, B_{DM}, from each of the solenoids are parallel to B_G. The B_{DM} and J_{DM} perturbations are out-of-phase by 90 degrees. The resulting magnetic pressure perturbations, δP_B, and δP_{th} perturbations are anti-phase, resulting in the observed $\delta\beta$ perturbations. The anti-phase relationship between magnetic and thermal pressures resemble the mirror-mode instability (e.g., *Southwood & Kivelson*, 1993; *Wang et al.*, 2010).

Figure 8-4b provides a schematic illustration of an asymmetric reconnection with a significant guide field ($B_G \sim$ |B|), based on the MMS observations. While exiting the FTE with lower magnetic pressure, MMS spacecraft observe a peak (red shade) followed by a sharp drop (blue shade) in plasma density. The plasma density signatures correspond to the PIC simulations of guide field reconnection (cf. Figure 8.1*n* in *Lapenta et al.*, 2016). The large gradient in plasma density results in strong, in-plane diamagnetic current loops whose magnitude can be estimated as, $J_{DM, max} \sim {}^1/_B \left({}^{\Delta P}/_{\Delta x} \right) \sim (1/60 \text{ nT}) (1.5 \text{ nPa}/60 \text{ km}) = 0.45 \, \mu A/m^2$. This diamagnetic current loop creates the Hall current signatures, as indicated by $J_{dia, L} \sim J_{curl, L}$ in MMS observations. The diamagnetic loops can generate out-of-plane, bipolar Hall magnetic field signatures, with

magnitudes approaching $B_{DM, max} \sim \mu_0 (\Delta P/B) = 30$ nT. The diamagnetic current loops can further generate an in-plane electric field, E_{DM}, as described by the generalized Ohm's law.

Vlasiator simulations produce diamagnetic currents that are in agreement with in-situ observations. Both MMS observations and Vlasiator simulations indicate that J_{DM} peaks at the side with lower β. They also show that the diamagnetic current forms in the reconnection plane, LN-plane in MMS observations and $\mathbf{x}_{1,3}$-plane in Vlasiator simulations. The Vlasiator simulations further reveal that the area, $l \times w$, occupied by the diamagnetic current loops can extend far from the reconnection region, developing at speed $\frac{\partial l}{\partial t} \sim (0.5\text{-}0.1\ R_E)/(13.5\ s) = 3\times10^{-2}\ R_E/s \sim 200$ km/s. Previous studies have also shown that the expansion of the Hall region along the separatrix can develop at speeds exceeding the local Alfvèn velocity (*Shay et al.*, 2011).

Future research will investigate the roles of coalescing FTEs' relative size, plasma beta, and convection speed in the generation and controlling the asymmetry of diamagnetic current signatures. Further investigation is also needed to analyze the relationship between the observed diamagnetic current signatures and plasma instabilities. Vlasiator simulations will also be re-examined to search for plasma energization and heating mechanisms associated with the coalescence process.
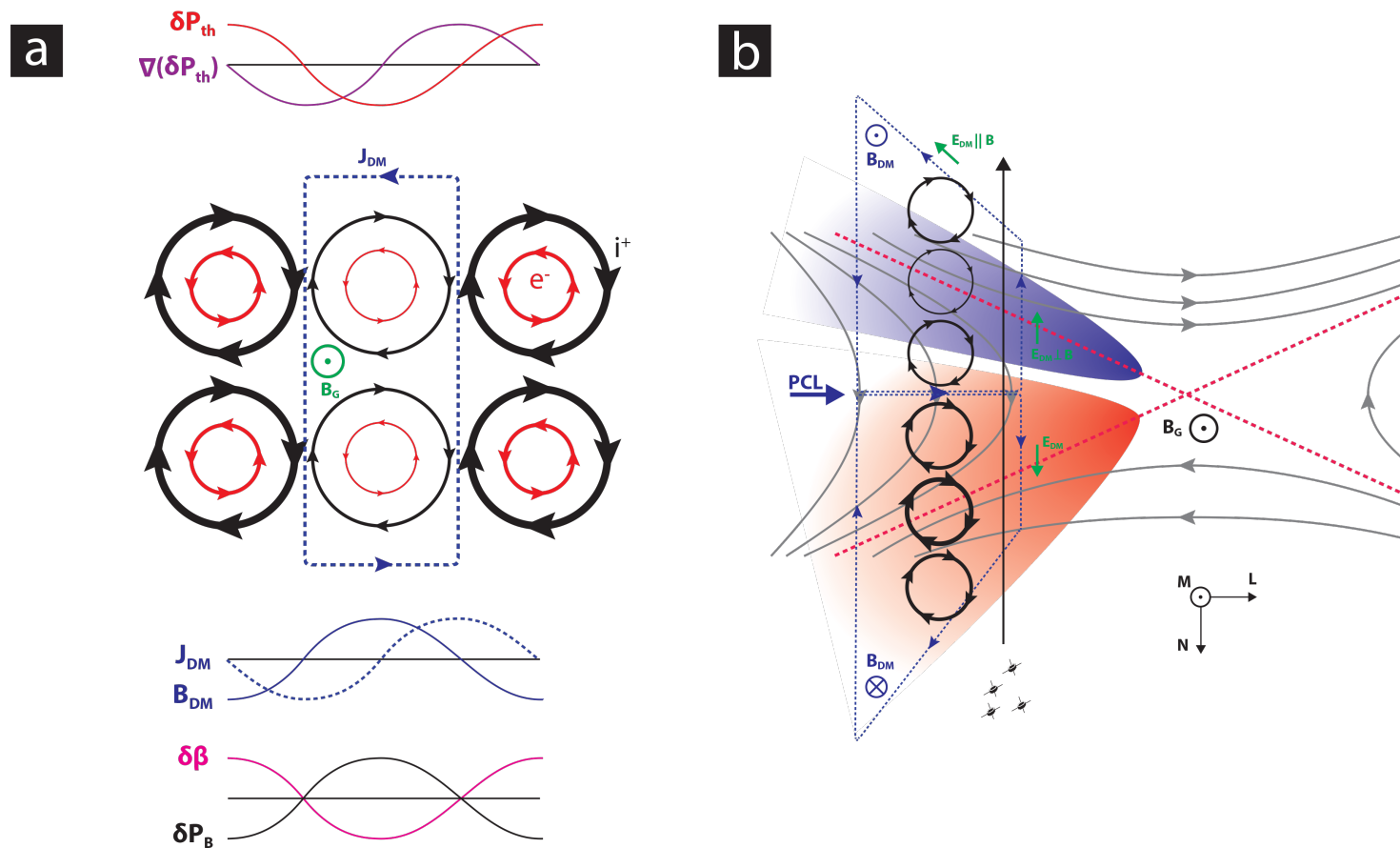
Figure 8-4: The cartoon schematics of the generation of and the role of diamagnetic current loops in asymmetric magnetic reconnection: a) the generation of diamagnetic current loops from plasma non-uniformity, and b) the location and orientation of MMS-observed diamagnetic current loops with respect to the reconnection region. The shaded red and blue regions indicate the plasma density peak and valley, respectively. The separatrix is marked by a red dashed line.

Chapter 9: Conclusions and Future Direction

9.1　Conclusions

As discussed in Section 1.3, this dissertation aims to address five overarching science objectives. In this section, we review our in-situ MMS analyses and global hybrid-Vlasov Vlasiator simulations at the Earth's magnetopause to advance our understanding of these science objectives.

1) What is the size distribution of FTEs at the Earth's subsolar magnetopause? How do FTEs evolve along the magnetopause?

Determining the magnetic field structure, electric currents, and plasma distributions within FTE-type flux ropes is critical to the understanding of their origin, evolution, and dynamics. Here, the Magnetospheric Multiscale (MMS) high-resolution magnetic field and plasma measurements are used to identify FTEs in the vicinity of the subsolar magnetopause. The constant-α flux rope model is used to identify quasi-force free flux ropes and to infer the size, the core magnetic field strength, the magnetic flux content, and the spacecraft trajectories through these structures. Our statistical analysis determines a mean diameter of 1,700 ± 400 km ($\sim$30 ± 9 d_i) and an average magnetic flux content of 100 ± 30 kWb for the quasi-force free FTEs at the Earth's subsolar magnetopause which are smaller than values reported by Cluster at high latitudes. These observed nonlinear size and magnetic flux content distributions of FTEs appear consistent with the plasmoid instability theory, which relies on the merging of neighboring, small-scale FTEs to generate larger structures. The ratio of the perpendicular to parallel components of current density, R_J, indicates that our FTEs are magnetically force-free, defined as $R_J < 1$, in their core regions (<0.6 $R_{flux\ rope}$). Plasma density is shown to be larger in smaller, newly formed FTEs and dropping with increasing FTE size. It is also shown that parallel ion velocity dominates inside FTEs with largest plasma density. Field-aligned flow facilitates the evacuation of plasma inside newly formed FTEs, while their core magnetic field strengthens with increasing FTE size.

2) *What are the radial profiles of plasma moments and net MHD forces inside subsolar FTEs? How do they impact plasma thermodynamics inside FTEs?*

Previous studies have indicated that FTEs grow as they convect away from the reconnection site along the magnetopause. This increase in FTE diameter may occur via adiabatic expansion in response to decreasing external pressure away from the subsolar region or due to a continuous supply of magnetic flux and plasma to the FTEs' outer layers by magnetic reconnection. Here, we investigate an ensemble of 55 FTEs at the subsolar magnetopause using MMS multi-point measurements. The FTEs are initially modeled as quasi-force-free flux ropes in order to infer their geometry and the spacecraft trajectory relative to their central axis. The MMS observations reveal a radially-inward net force at the outer layers of FTEs which can accelerate plasmas and fields toward the FTE's core region. Inside the FTEs, near the central axis, plasma density is found to decrease as the axial net force increases. It is interpreted that the axial net force accelerates plasmas along the axis in the region of compressing field lines. Statistical analysis of the MMS observations of the 55 FTEs indicates that plasma pressure, P_{th}, decreases with increasing FTE diameter, λ, as $P_{th,\,obsv} \propto \lambda^{-0.24}$. Assuming that all 55 FTEs started out with similar diameters, this rate of plasma pressure decrease with increasing FTE diameter is at least an order of magnitude slower than the theoretical rate for adiabatic expansion (i.e., $P_{th,\,adiab.} \propto \lambda^{-3.3}$), suggesting the presence of efficient plasma heating mechanisms, such as magnetic reconnection, to facilitate FTE growth.

3) *Can FTE evolution cause the energization and/or heating of plasmas at the magnetopause? If so, what are the relative contributions of different energization mechanisms?*

Upon formation, FTEs in the subsolar magnetosheath have been observed to grow in diameter, λ, while convecting along the magnetopause. Plasma pressure has also been found to decrease sub-adiabatically with increasing λ, indicating the presence of internal plasma acceleration and heating processes. Here, the MMS fields and plasma measurements are used to determine the relative roles of parallel electric fields, betatron, and Fermi processes in plasma heating inside an ensemble of 55 subsolar FTEs. Plasma heating is shown asymmetric inside FTEs. Parallel electric fields

dominate (>75%) ion and electron heating at the leading edge of FTEs. At the trailing edge, betatron and Fermi processes overtake (>50%), resulting in ion cooling and electron heating, respectively. The observed strong net-heatings inside FTEs are proportional to $\lambda^{-1/2}$. It is concluded that reconnection-driven heating continues inside FTEs far from the subsolar electron and ion diffusion regions.

4) *What are the processes through which FTEs evolve? What can global simulations tell us about the average rate at which subsolar FTEs grow at the magnetopause?*

The Vlasiator hybrid-Vlasov code was developed to investigate global magnetospheric dynamics at ion-inertial scales. Here, we focus on the role of magnetic reconnection in the formation and evolution of the magnetic islands at the low-latitude magnetopause, under southward interplanetary magnetic field (IMF) conditions. The simulation results indicate that: 1) the ion kinetics inside the reconnection ion diffusion region, including the Earthward-pointing Larmor electric field on the magnetospheric-side of an X-point and the corresponding three-dimensional crescent-shaped ion distributions, are well-captured by the Vlasiator code, 2) magnetic islands evolve due to continuous reconnection at the adjacent X-points, 'coalescence' which refers to the merging of neighboring islands to create a larger island, 'erosion' during which an island loses magnetic flux due to reconnection, and 'division' which involves the splitting of an island into smaller islands, and 3) continuous reconnection at the adjacent X-points is the dominant source of magnetic flux and plasma to the outer layers of magnetic islands resulting in cross-sectional growth rates up to +0.2 R_E^2/min. The simulation results are validated by comparison to MMS measurements of a chain of ion-scale FTEs sandwiched between two dominant X-lines observed on 14 December, 2015. The MMS measurements reveal: 1) crescent-shaped ion populations, and 2) normalized reconnection rates up to 0.18, in agreement with theory and the Vlasiator predictions. Based on the simulation results and the MMS measurements, it is estimated that the observed ion-scale FTEs can grow Earth-sized within ~10 minutes, which is comparable to the average transport time for FTEs formed in the subsolar region to the high-latitude magnetopause.

5) *What are the characteristic signatures of FTE coalescence? What is the temporal evolution of coalescing FTEs based on global simulations?*

FTEs at the dayside magnetopause is believed to grow via FTE coalescence. During the coalescence process, two neighboring FTEs merge and reconnect to create one larger FTE. Here, we focus on the perpendicular current layer (PCL) forming between the two merging FTEs. MMS observations show Hall signatures within the sub-ion-scale PCL. The Hall current is found to be largely supported by the ion diamagnetic current generated from a density asymmetry across PCL. We provide the first global simulations of coalescing magnetic islands at the magnetopause which predict the formation of a magnetic field pileup region between the two merging islands. Inside the pile-up region, plasma gradients facilitate diamagnetic drift of ions which, in turn, creates the observed Hall current. Global hybrid-Vlasov Vlasiator simulations further suggest that the magnitude and asymmetry of diamagnetic and Hall current enhance at later stages of the coalescence process with increasing pressure gradient across PCL.

9.2   Future Direction

This dissertation focused on FTE-type flux ropes as important byproducts of magnetopause magnetic reconnection. The average physical properties and the thermodynamics of fields and plasmas were investigated inside FTEs. FTE-type flux ropes were further found to contribute significantly to plasma heating at the magnetopause, far from the primary reconnection exhausts.

Our findings using in-situ MMS measurements and global Vlasiator simulations advanced our understanding of FTE-type flux rope generation mechanisms and evolution processes. Future efforts to extend the conclusions of this dissertation's findings shall explore three key science questions:

Science Question 1) Are plasmas inside and at the outer layers of FTEs conducive to instabilities? If so, what do plasma instabilities tell us about the FTE evolution at the magnetopause?

As shown in Chapter 5, it was revealed that electron and ion temperatures are, on average, anisotropic inside FTEs at the subsolar magnetopause. Departures from the Maxwellian particle distribution functions can serve as a free source of energy (*Hellinger et al.*, 2006). The free energy can give rise to various plasma instabilities. In collisionless plasmas, thermalization due to Coulomb relaxation is insufficient. However, pressure-anisotropy instabilities can act to pitch-angle scatter the plasma back towards isotropy (*Eviatar & Schulz*, 1970). In the solar wind, the instabilities have been shown to constrain the shape of particle distribution functions, as a feedback mechanism (e.g., *Gary et al.*, 1976, 2001; *Kasper et al.*, 2002, 2003, 2006; *Cranmer et al.*, 2009).

Proton temperature anisotropy is divided into two sub-categories: $T_{\perp p} > T_{\parallel p}$ and $T_{\parallel p} > T_{\perp p}$. The subscripts $\perp$ and $\parallel$ denote the perpendicular and parallel proton temperatures with respect to the ambient magnetic field. The former anisotropy is associated with the proton cyclotron and the mirror mode instabilities (e.g., *Gary et al.*, 1994; *Pokhotelov et al.*, 2004). The latter anisotropy is linked to the firehose instabilities (e.g., *Quest & Shapiro*, 1996; *Farrugia et al.*, 1998; *Gary et al.*, 1998; *Hellinger & Matsumoto*, 2000; *Matteini et al.*, 2005). *Hellinger et al.* (2006) showed that, in a weakly magnetized plasma consisting of protons and electrons, an instability threshold can be derived for values of parallel plasma beta, $\beta_{\parallel}$ $[= n_p k_b T_{\parallel}/(B^2/2\mu_0)]$:

$$\frac{T_{\perp p}}{T_{\parallel p}} = 1 + \frac{a}{\left(\beta_{\parallel p} - \beta_0\right)^{b}}.$$

where a, b, and β_0 are constants corresponding to the parallel firehose ($[a, b, \beta_0] = [-0.47, 0.53, 0.59]$) and mirror mode ($[a, b, \beta_0] = [077, 0.76, -0.016]$) instabilities. The magnetic fields and plasmas inside subsolar FTEs will be examined to search for evidence for firehose and/or mirror-mode instabilities.

Pressure-anisotropy instabilities can drive electromagnetic fluctuations (e.g., *Štverák et al.*, 2008). The field fluctuations are proportional to the extent to which the instability threshold is crossed. In other words, field fluctuations can isotropize the plasma distribution function via wave-particle scattering, hence, placing constraints on (electrons: *Phillips et al.*, 1989; *Gary et al.*, 1999 and ions: *Kasper et al.*, 2003; *Marsch et al.*, 2006; *Hellinger et al.*, 2006) temperature anisotropies. The magnetic field fluctuations (*Bale et al.*, 2009) shall be investigated inside and at the outer layers of FTEs.

Science Question 2) What is the role of the shear angle between the merging flux tubes in the formation and the strength of diamagnetic currents observed at the interface of coalescing FTEs? What is the role of plasma beta in the magnetic field pileup region between coalescing FTEs?

Magnetic helicity, K, a measure of 'twist' in magnetic fields (*Woltjer*, 1958), is closely related to field line topology (*Berger & Field*, 1984). It is defined by:

$$K = \int \mathbf{A} \cdot \mathbf{B} \, dV$$

where $\mathbf{A}$ is the vector potential of the magnetic field $\mathbf{B}$ and the integration is over a volume V. In a perfectly conducting plasma, the magnetic helicity is conserved within a flux tube.

As shown in Figure 9-1a, reconnection theories in two dimensions are based on three different field topology configurations (*Vasyliunas*, 1975; *Biskamp*, 1993; *Ji*, 1999). The main difference between the three field topologies is the out-of-plane magnetic field component, i.e., B_M. Also known as the guide field, B_M is responsible not only for the helicity content of the

merging flux tubes, but also the local shear angle at the reconnection site, as shown in Figure 9-1b. Magnetic shear angle is defined as the angle between two merging flux tubes and is believed to be responsible for controlling the reconnection dynamics (e.g., *Yamada et al.*, 1997; *Lapenta et al.*, 2016).

In the absence of B_M, reconnection is defined as 'anti-parallel,' as illustrated in configuration *i*. In the presence of a B_M component, the field lines reconnect either at an angle when parallel B_M components across the merging interface, as shown in configuration *ii*, or anti-parallel when oppositely-directed B_M, such as configuration *iii*. As shown, the reconnection is anti-parallel in both null- and counter-helicity field topology configurations.

The MMS-observed FTE coalescence of November 17, 2015 discussed in Chapter 8 is an example of co-helicity reconnection. Both FTEs are oriented with their axes in the same direction, i.e., same helicity. We reported, for the first time, that the plasma density gradient across the two merging FTEs resulted in the formation of a strong diamagnetic current that generated the observed Hall signatures. The MMS observations of diamagnetic currents between coalescing FTEs was further supported by Vlasiator simulations of magnetic islands at the magnetopause. However, the two-dimensional magnetic island coalescence event by Vlasiator depicts an anti-parallel, null-helicity reconnection. To better understand the role of magnetic shear, B_M, in the formation and strength of diamagnetic currents between coalescing FTEs, simulations with three spatial dimensions are required to resolve the different helicities.
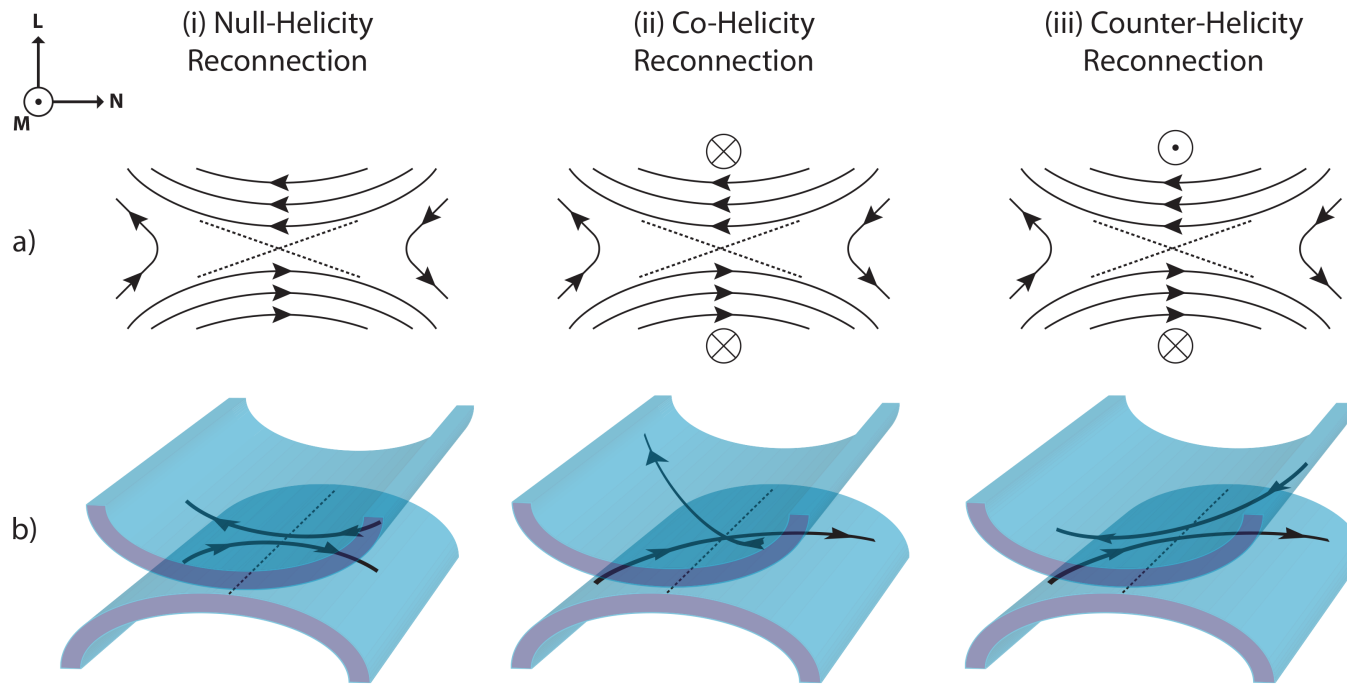
Figure 9-1: a) Two-, and b) three-dimensional schematic views of magnetic reconnection for three cases: (i) null-helicity, (ii) co-helicity, and (iii) counter-helicity.

In addition, the FTE coalescence observations and simulations confirmed that the diamagnetic currents are strongest at the side with lower plasma beta, suggesting that reconnection is favored where plasma beta is reduced. Future investigation shall study the role of plasma beta in controlling the magnitude and asymmetry of diamagnetic currents between coalescing FTEs. In theory, enhanced diamagnetic effects can suppress reconnection (e.g., *Swisdak et al.*, 2003). Further observations and simulations are needed to study the coalescence process in three dimensions and under various plasma and fields conditions.

Science Question 3) Does FTE coalescence energize and/or heat plasmas? Are there plasma instabilities associated with the FTE coalescence process?

As discussed in Chapter 6, plasmas are found to energize inside FTEs. The energization is dominated by parallel electric fields at the leading edge of FTEs which suggests that FTEs reconnect with their surrounding environment while convecting along the magnetopause.

The magnetic reconnection-associated particle acceleration can be divided into two sub-categories: X-type and O-type (e.g., *Kliem et al.*, 2000; *Hoshino et al.*, 2001; *Hoshino*, 2005, 2012; *Karlicky & Bárta*, 2007; *Bárta et al.*, 2008; *Oka et al.*, 2010; *Oka et al.*, 2010; *Tanaka et al.*, 2010). In the vicinity of the reconnection site, un-magnetized plasmas can be energized via the X-type acceleration (e.g., *Scholer & Jamitzky*, 1987; *Kliem*, 1994; *Hoshino et al.*, 2001; *Hoshino*, 2005). Inside the geometrically-closed structures of magnetic islands, particles are energized via the O-type acceleration mechanisms (e.g., *Stern*, 1979; *Scholer & Jamitzky*, 1987; *Kliem*, 1994; *Drake, Swisdak, Che, et al.*, 2006; *Guidoni et al.*, 2016). Magnetic islands are 2D structures bounded by two X-lines at each end and represent flux ropes in 3D. Particle energization inside coalescing magnetic islands involves both the X-type and the O-type acceleration mechanisms.

Newman (1990) hypothesized that *impulsive field events* (IFEs) can energize ions. In the ion reference frame, an IFE is viewed as a narrow spatial structure on the order of the ion gyro-radius, r_i. They suggest that sudden impulsive changes within the ambient electric and magnetic field can disrupt ion gyro-motion. Impulsive external forces over timescales shorter than the local ion cyclotron period violate the adiabatic invariants of motion. Through this non-adiabatic (and non-resonant) process, some of the energy from E×B drift may transfer into the ion gyration motion. Hence, the resulting ion velocity-space distribution is broadened (i.e., non-adiabatic diffusion) due to the increased gyration speed (e.g., *Moore et al.*, 1986; *Artemyev et al.*, 2017). In

the context of laboratory plasmas, IFEs and the associated instabilities have also been extensively studied (e.g., *Rechester & Rosenbluth*, 1978; *Rechester & Stix*, 1979; *Khalilzadeh et al.*, 2017).

It was reported in Chapter 8 that the thickness of the perpendicular current sheet is of the order of one ion inertial length. We found that within this region ions and electrons decouple giving rise to diamagnetic currents. Future investigation will investigate the role of the FTE coalescence in decoupling and energizing plasmas. In addition, preferential energization of plasmas along and/or perpendicular to the field lines can further drive plasmas unstable. In particular, future investigations shall examine mirror-mode unstable ions and the generation of whistler waves from electron temperature anisotropies at the outer layers of coalescing FTEs (e.g., *Shimou Wang et al.*, 2019).

In addition, our FTE analyses can be applied to flux ropes in other collisionless plasma regimes. Two main flux rope categories are flux ropes in planetary magnetotails as well as coronal mass ejections (CMEs) and corotating interaction regions (CIRs) in the interplanetary medium. In particular, two main science questions shall need to be addressed:

1) What is the size distribution of flux ropes in the magnetotail? How do Earthward-moving and tailward-moving flux ropes evolve upon generation?

2) How does CME growth in the interplanetary medium compare with FTE growth at the magnetopause and plasmoid growth in the magnetotail? What can we learn about the coalescence process from CIRs' magnetic field and plasma properties?

In summary, this dissertation explored the role of magnetic reconnection in controlling the evolution and thermodynamics of magnetic fields and plasmas through the lens of FTE-type flux ropes. Our findings shed light on the extent to which reconnection contributes to the energization and heating of plasmas at the magnetopause. New science frontiers are revealed for further exploring the physics of magnetic reconnection and flux rope dynamics, both in planetary and interplanetary environments.

Appendix A: Force-Free Flux Rope Model

The steps involved in determining the size and flux content of FTEs from the Lepping-Burlaga constant-α flux rope model:

i) To enable comparison of FTE observation with modeled values, observation magnetic field data is transformed from LMN to (radial-axial-tangential) RAT coordinate system:

$$B_{A\text{-}Obsrv} = \frac{B_M}{|B|},$$

$$B_{T\text{-}obsrv} = \sqrt{\left[\frac{B_L}{|\boldsymbol{B}|}\right]^2 + \left[\frac{B_N}{|\boldsymbol{B}|}\right]^2}.$$

ii) The *closest approach* (CA) is defined as the point across the structure where $B_{A\text{-}Obsrv}$ reaches the peak magnitude. At CA, the ratio:

$$\frac{Y_0}{R_0} = \frac{B_{A\text{-}Obsrv}}{B_{T\text{-}Obsrv}}$$

is used to determine the *impact parameter*. The impact parameter is the fractional distance that the spacecraft has passed from the flux rope core at CA, where Y_0 is the distance from the flux rope center and R_0 is the radius of the flux rope, both of which are unknown at this point.

iii) The velocity of the FTE is that of total ion velocity as measured by FPI outside the structure ($V_0 \sim V_i$). The spacecraft are assumed stationary (i.e. $V_0 \gg V_{S/C}$). The distance, X_0, between the edge of the flux rope and the CA is $X_0 = V_0 t_0$, where t_0 is the time it takes the spacecraft to traverse from the edge of the flux rope to the CA:

$$t_0 = \frac{1}{2} \Delta t_{peak\text{-}to\text{-}peak}.$$

Here, $\Delta t_{peak\text{-}to\text{-}peak}$ is the duration of the flux rope.

iv) Axial and tangential components of observed magnetic field data are incrementally stepped through in order to compute X_i. Increments are equivalent to the resolution of the magnetic field

measurements (i.e. 128 vectors/s).

v) For increasing values of X_i (from 0 to X_0), the fractional radial distance, r', is calculated using the Pythagorean theorem normalized with the flux rope radius R_0:

$$R_0^2 = X_0^2 + Y_0^2$$

and,

$$r' = R_i/R_0 = \sqrt{\left(Y_0/R_0\right)^2 + \left(X_i/R_0\right)^2}$$

where impact parameter and R_0 are constants. $B_{A\text{-}Model}$ and $B_{T\text{-}Model}$ are the modeled components of magnetic field:

$$B_{A\text{-}Model} = J_0(\alpha \sqrt{\left(Y_0/R_0\right)^2 + \left(X_i/R_0\right)^2})B_0$$

$$B_{T\text{-}Model} = J_1(\alpha \sqrt{\left(Y_0/R_0\right)^2 + \left(X_i/R_0\right)^2})B_0 H$$

assuming B_0 and H are equal to unity, for simplicity. The actual value of B_0 will be determined later.

vi) Chi-square statistical test (i.e. goodness of fit) is applied to compare observed and modeled values of B_A and B_T:

$$\chi^2 = 1/N \sum_{i=1}^{N} [(B_{A\text{-}Model}\text{-}B_{A\text{-}Obsrv})^2 + (B_{T\text{-}Model}\text{-}B_{T\text{-}Obsrv})^2]$$

where N is the number of data points.

vii) The flux rope radius, R_i, resulting in the minimization of χ^2 represents the best fit for the force-free flux rope model (i.e. $R_i = R_0$ at $\min(\chi^2)$). At this point, impact parameter is used to determine the absolute value of Y_0. Similarly, the flux rope's core field strength, B_0, at CA is:

$$B_0 = B_M \left(B_{A\text{-}Obsrv}/B_{A\text{-}Model}\right)$$

Figure 2j represents the chi-squared profile of the ion-scale FTE. The curve has a minimum at R_0

~ 430 km.

viii) Determination of R_0 and B_0 enable estimating the flux transported across the dayside magnetopause by a given FTE [*Eastwood et al., 2012*]:

$$\Phi = \left(\frac{2\pi \, B_0 \, R_0^2}{\alpha} \right) J_1(\alpha) \ .$$

Appendix B: Analytical Weight Determination

An analytical weight determines that the i_{th} observation comes from a sub-population with a particular mean and variance, σ^2/w_i, where σ^2 is a common variance and w_i is the weight of the i_{th} observation. Analytical weights are commonly used in meta-analyses where each *observation* is the mean of a sample (Kish, 1992). In this study, each observed data point, $X_{i,n}$, is weighted with:

$$w_n = \langle X \rangle \Big/ \overline{X}_n ,$$

where w_n is the analytical weight assigned to data points inside the n_{th} FTE. Here, $\langle X \rangle \equiv \frac{1}{P} \sum_{n=1}^{P} \overline{X}_n$, where $P = 55$ and is the total number of FTEs used in this study. $\overline{X}_n$ indicates the average value of variable X across the cross section of the n_{th} FTE, hence it is defined as:

$$\overline{X}_n \equiv \frac{1}{N} \sum_{i=1}^{N} X_{i,n} ,$$

where subscript $i = 1, ..., N$ denotes individual data points inside an FTE with total N measurements.

Appendix C: LMN to Cylindrical Coordinate Transformation

In order to determine the radial component of a vector in a force-free flux rope, the vector is projected from the LMN coordinates into the cylindrical coordinates. Figure C-1 demonstrates that the vector, A, is first projected into the flux rope cross section plane (LN-plane). The vector can then be written in terms of the in-plane components, $A(\widehat{N}, \widehat{L}) = A_N\,\widehat{N} + A_L\,\widehat{L}$; where unit vector $\widehat{N}$ points along the spacecraft trajectory and $\widehat{L} = \widehat{M} \times \widehat{N}$. The transformation into the cylindrical coordinates requires the knowledge of angle $\boldsymbol{\theta}$ which is a function of 1) the distance of the spacecraft location along its trajectory ($0 < X < d$; where d indicates the distance between the two flux rope edges) from the flux rope's central axis, and 2) the closest approach ($d_{closest\ approach} = r_{flux\ rope} \times$ IP):

$$\theta = \ tan^{-1}\left(\frac{\left(\frac{X - d/2}{r_{flux\ rope}}\right)}{\boldsymbol{IP}}\right)$$

where $r_{flux\ rope}$ is the flux rope radius as determined by the force-free flux rope model. The radial component of the vector can be written as:

$$A_r = A_N\ sin(\theta).$$

It is important to note that for statistical analyses, all flux ropes should be rotated into the same LMN coordinates. To achieve this, all flux ropes are rotated with respect to the $\widehat{N}$ axis for their axes, $\widehat{M}$, to point in the same (e.g., dawn-dusk) direction. Because we are only interested in the radial component of the vector the different flux rope helicities (e.g., right-hand helicity) will not impact the results.
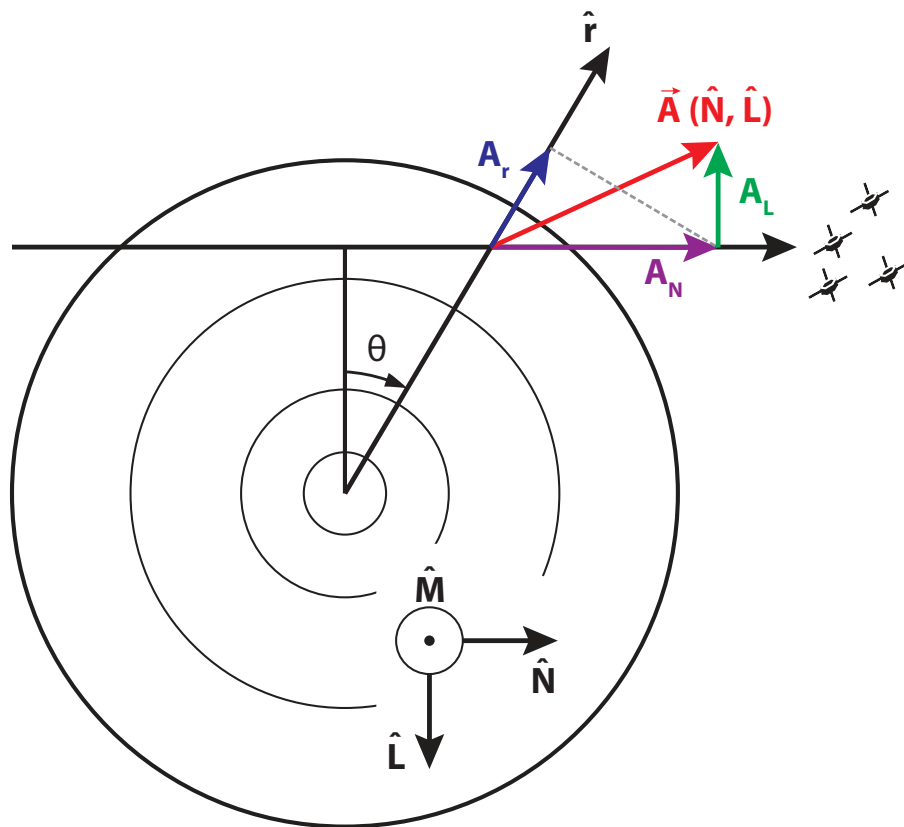
Figure C-1: Coordinate transformation between flux rope's LMN and cylindrical coordinate systems.

Appendix D: Adiabatic and Double-Adiabatic Approximations of FTE State

The second law of thermodynamics states that the entropy inside an irreversibly expanding FTE must not decrease:

$$p_2 V_2^\gamma \geq p_1 V_1^\gamma$$

where pressure $p \propto N\,T$, where N and T are zeroth (density) and second (temperature) plasma moments, respectively. V denotes the flux rope volume, hence, proportional to the square of the FTE diameter ($V \propto \lambda^2 H$; where λ is the FTE diameter and H is the FTE length, assuming cylindrical symmetry) (e.g., *Lingam & Comisso*, 2018). The length, H, of the FTE is assumed to remain constant. It is important to note that recent observational evidence suggest that reconnection sites can expand, though primarily in local time along the boundary, which may result in a change in H (Zou et al., 2018). The subscripts indicate the stage of evolution (t_1 and $t_2 \gg t_1$) and $\gamma = 5/3$ is the adiabatic specific heat ratio for monoatomic gases. Thereby, the equation above can be written as:

$$p_2/p_1 \geq \left(\lambda_2/\lambda_1\right)^{-3.3},$$

where λ is the FTE diameter.

The role of magnetic field in the above approximation can also be included by using the double-adiabatic approximation (e.g., *Baumjohann & Treumann*, 2012). This approximation takes into account the different variations in the parallel and perpendicular pressures in the presence of a sufficiently strong magnetic field. The perpendicular thermal pressure $P_\perp$ is a linear function of plasma density n and magnetic field magnitude B as suggested by the conservation of magnetic moment, $\mu = P_\perp/nB$, in systems wherein plasma gyration takes longer than temporal variations of the plasma. In the absence of any dissipative mechanisms and heat transfer, the parallel component of thermal pressure is also found to be a function of both plasma density and magnetic field:

$$P_\perp \propto n\,B$$

$$P_\parallel \propto n^3 \, B^{-2}$$

It is further shown that the parallel $\gamma_\parallel$ and the perpendicular $\gamma_\perp$ adiabatic indices are defined in the double-adiabatic equations of state as:

$$\gamma_\perp = 1 + \frac{\ln(B_2 / B_1)}{\ln(n_2 / n_1)} \text{ , and}$$

$$\gamma_\parallel = 3 - 2 \, \frac{\ln(B_2 / B_1)}{\ln(n_2 / n_1)} \text{ .}$$

Therefore, inside an adiabatically growing flux rope, wherein no heat transfer is assumed, the thermal pressure becomes increasingly anisotropic, i.e., $P_\perp / P_\parallel \neq 1$. Plasma pressure components can then be written as:

$$p_{\perp 2}/p_{\perp 1} \geq \left(\lambda_2/\lambda_1\right)^{-2\gamma_\perp} \text{ , and}$$

$$p_{\parallel 2}/p_{\parallel 1} \geq \left(\lambda_2/\lambda_1\right)^{-2\gamma_\parallel} \text{ .}$$

Given the MMS observations, *Akhavan-Tafti et al.* (2018) found that plasma density of subsolar FTEs is, to a first-order approximation, a linear function of the flux rope core magnetic field, n [cm^{-3}] = -0.36 |B| [nT] + 43.81. Here, we find that:

$$p_{\perp 2}/p_{\perp 1} \geq \left(\lambda_2/\lambda_1\right)^{-5.9} \text{ , and}$$

$$p_{\parallel 2}/p_{\parallel 1} \geq \left(\lambda_2/\lambda_1\right)^{+1.9} \text{ ,}$$

which suggests that for small-scale FTEs to grow macro-scale via adiabatic expansion their internal pressure must become dominantly parallel. This is not physically possible since the strong anisotropy will trigger plasma instabilities, e.g., firehose instability, to return the plasma population to a lower energy state. Dissipative mechanisms and/or plasma energization mechanisms including magnetic reconnection can further thermalize plasma and prevent anisotropy.

Bibliography

Akhavan-Tafti, M., Slavin, J. A., Le, G., Eastwood, J. P., Strangeway, R. J., Russell, C. T., … Burch, J. L. (2018). MMS Examination of FTEs at the Earth's Subsolar Magnetopause. *Journal of Geophysical Research: Space Physics*. https://doi.org/10.1002/2017JA024681

Akhavan-Tafti, M., Slavin, J. A., Eastwood, J. P., Cassak, P. A., & Gershman, D. J. (2019). MMS Multi-Point Analysis of FTE Evolution: Physical Characteristics and Dynamics. *Journal of Geophysical Research: Space Physics*. https://doi.org/10.1029/2018JA026311

Akhavan-Tafti, M., Slavin, J. A., Sun, W. J., Le, G., & Gershman, D. J. (2019). MMS Observations of Plasma Heating Associated with FTE Growth. *Geophysical Research Letters*, *46*.

von Alfthan, S., Pokhotelov, D., Kempf, Y., Hoilijoki, S., Honkonen, I., Sandroos, A., & Palmroth, M. (2014). Vlasiator: First global hybrid-Vlasov simulations of Earth's foreshock and magnetosheath. *Journal of Atmospheric and Solar-Terrestrial Physics*, *120*, 24–35.

Allen, J. A. Van. (1958). Observation of high intensity radiation by satellites 1958 Alpha and Gamma. *Journal of Jet Propulsion*, *28*(9), 588–592.

Alm, L., Farrugia, C. J., Paulson, K. W., Argall, M. R., Torbert, R. B., Burch, J. L., … Giles, B. L. (2017). Differing properties of two ion-scale magnetopause flux ropes. *Journal of Geophysical Research: Space Physics*. https://doi.org/10.1002/2017JA024525

De Angelis, A. (2011). *L'enigma dei raggi cosmici: le più grandi energie dell'universo*. Springer Science & Business Media.

Angelopoulos, V., McFadden, J. P., Larson, D., Carlson, C. W., Mende, S. B., Frey, H., … others. (2008). Tail reconnection triggering substorm onset. *Science*, *321*(5891), 931–935.

Artemyev, A. V, Mourenas, D., Agapitov, O. V, & Blum, L. (2017). Transverse eV ion heating by random electric field fluctuations in the plasmasphere. *Physics of Plasmas*, *24*(2), 22903.

Artemyev, A. V, Walsh, A. P., Petrukovich, A. A., Baumjohann, W., Nakamura, R., & Fazakerley, A. N. (2014). Electron pitch angle/energy distribution in the magnetotail. *Journal of Geophysical Research: Space Physics*, *119*(9), 7214–7227.

Aschwanden, M. J. (2002). Particle acceleration and kinematics in solar flares. In *Particle Acceleration and Kinematics in Solar Flares* (pp. 1–227). Springer.

Baalrud, S. D., Bhattacharjee, A., & Huang, Y.-M. (2012). Reduced magnetohydrodynamic theory of oblique plasmoid instabilities. *Physics of Plasmas*, *19*(2), 22101.

Baker, D. N., & Stone, E. C. (1977). Observations of energetic electrons (E 200 keV) in the earth's magnetotail: Plasma sheet and fireball observations. *Journal of Geophysical Research*, *82*(10), 1532–1546.

Bale, S. D., Kasper, J. C., Howes, G. G., Quataert, E., Salem, C., & Sundkvist, D. (2009). Magnetic

fluctuation power near proton temperature anisotropy instability thresholds in the solar wind. *Physical Review Letters*, *103*(21), 211101.

Barta, M., Vršnak, B., & Karlick\`y, M. (2008). Dynamics of plasmoids formed by the current sheet tearing. *Astronomy & Astrophysics*, *477*(2), 649–655.

Baumjohann, W., & Treumann, R. A. (2012). *Basic space plasma physics*. World Scientific Publishing Company.

Benz, A. O. (2017). Flare observations. *Living Reviews in Solar Physics*, *14*(1), 2.

Berchem, J., & Russell, C. T. (1984). Flux transfer events on the magnetopause: Spatial distribution and controlling factors. *Journal of Geophysical Research: Space Physics*, *89*(A8), 6689–6703.

Berger, M. A., & Field, G. B. (1984). The topological properties of magnetic helicity. *Journal of Fluid Mechanics*, *147*, 133–148.

Bessho, N., & Bhattacharjee, A. (2012). FAST MAGNETIC RECONNECTION AND PARTICLE ACCELERATION IN RELATIVISTIC LOW-DENSITY ELECTRON-POSITRON PLASMAS WITHOUT GUIDE FIELD. *The Astrophysical Journal*, *750*(2), 129. https://doi.org/10.1088/0004-637X/750/2/129

Bessho, N., Chen, L.-J., & Hesse, M. (2016). Electron distribution functions in the diffusion region of asymmetric magnetic reconnection. *Geophysical Research Letters*, *43*(5), 1828–1836.

Bhattacharjee, A., Huang, Y.-M., Yang, H., & Rogers, B. (2009). Fast reconnection in high-Lundquist-number plasmas due to the plasmoid instability. *Physics of Plasmas*, *16*(11), 112102.

Birn, J., Artemyev, A. V, Baker, D. N., Echim, M., Hoshino, M., & Zelenyi, L. M. (2012). Particle acceleration in the magnetotail and aurora. *Space Science Reviews*, *173*(1–4), 49–102.

Biskamp, D. (1982). Effect of secondary tearing instability on the coalescence of magnetic islands. *Physics Letters A*, *87*(7), 357–360.

Biskamp, D. (1993). Nonlinear Magnetohydrodynamics. Chap.

Biskamp, Dieter. (1986). Magnetic reconnection via current sheets. *The Physics of Fluids*, *29*(5), 1520–1531.

Biskamp, Dieter. (1996). Magnetic reconnection in plasmas. *Astrophysics and Space Science*, *242*(1–2), 165–207.

Biskamp, Dieter. (2000). Magnetic reconnection in plasmas, Cambridge monographs on plasma physics Vol. 3. Cambridge University Press, Cambridge, UK.

Borg, A. L., Øieroset, M., Phan, T. D., Mozer, F. S., Pedersen, A., Mouikis, C., … Rème, H. (2005). Cluster encounter of a magnetic reconnection diffusion region in the near-Earth magnetotail on September 19, 2003. *Geophysical Research Letters*, *32*(19).

Briggs, J. A., Brain, D. A., Cartwright, M. L., Eastwood, J. P., & Halekas, J. S. (2011). A statistical study of flux ropes in the Martian magnetosphere. *Planetary and Space Science*, *59*(13), 1498–1505.

Büchner, J., Kilian, P., Muñoz, P. A., Spanier, F., Widmer, F., Zhou, X., & Jain, N. (2018). Kinetic

simulations of electron acceleration at mercury. In *Magnetic Fields in the Solar System* (pp. 201–240). Springer.

Burch, J. L., & Phan, T. D. (2016). Magnetic reconnection at the dayside magnetopause: Advances with MMS. *Geophysical Research Letters*. https://doi.org/10.1002/2016GL069787

Burch, J L, Moore, T. E., Torbert, R. B., & Giles, B. L. (2016). Magnetospheric multiscale overview and science objectives. *Space Science Reviews*, *199*(1–4), 5–21.

Burch, J L, Torbert, R. B., Phan, T. D., Chen, L., Moore, T. E., Ergun, R. E., … Goodrich, K. A. (2016). Electron-scale measurements of magnetic reconnection in space, *2939*(May).

Burch, James L., Torbert, R. B., Phan, T. D., Chen, L.-J., Moore, T. E., Ergun, R. E., … Others. (2016). Electron-scale measurements of magnetic reconnection in space. *Science*, *352*(6290), aaf2939.

Burlaga, L. F. (1988). Magnetic clouds and force-free fields with constant alpha. *Journal of Geophysical Research*, *93*(7), 7217. https://doi.org/10.1029/JA093iA07p07217

Burlaga, L. F., Ness, N. F., & Stone, E. C. (2013). Magnetic field observations as Voyager 1 entered the heliosheath depletion region. *Science*, *341*(6142), 147–150.

Cahill, L. J. (1963). Magnetic field measurements in space. *Space Science Reviews*, *1*(3), 399–414.

Cassak, P. A., & Drake, J. F. (2009). The impact of microscopic magnetic reconnection on pre-flare energy storage. *The Astrophysical Journal Letters*, *707*(2), L158.

Cassak, P. A., Shay, M. A., & Drake, J. F. (2009). Scaling of Sweet--Parker reconnection with secondary islands. *Physics of Plasmas*, *16*(12), 120702.

Cassak, P. A., & Shay, M. A. (2007). Scaling of asymmetric magnetic reconnection: General theory and collisional simulations. *Physics of Plasmas*, *14*(10), 102114.

Cassak, P. A., Liu, Y.-H., & Shay, M. A. (2017). A review of the 0.1 reconnection rate problem. *Journal of Plasma Physics*, *83*(5).

Cazzola, E., Innocenti, M. E., Markidis, S., Goldman, M. V., Newman, D. L., & Lapenta, G. (2015). On the electron dynamics during island coalescence in asymmetric magnetic reconnection. *Physics of Plasmas*, *22*(9). https://doi.org/10.1063/1.4929847

Cerutti, B., Werner, G. R., Uzdensky, D. A., & Begelman, M. C. (2012). BEAMING AND RAPID VARIABILITY OF HIGH-ENERGY RADIATION FROM RELATIVISTIC PAIR PLASMA RECONNECTION. *The Astrophysical Journal*, *754*(2), L33. https://doi.org/10.1088/2041-8205/754/2/L33

Chapman, S., & Ferraro, V. C. A. (1931). A new theory of magnetic storms. *Terrestrial Magnetism and Atmospheric Electricity*, *36*(2), 77–97.

Che, H., Schiff, C., Le, G., Dorelli, J. C., Giles, B. L., & Moore, T. E. (2018). Quantifying the effect of non-Larmor motion of electrons on the pressure tensor. *Physics of Plasmas*, *25*(3), 32101.

Chen, L.-J., Bessho, N., Lefebvre, B., Vaith, H., Fazakerley, A., Bhattacharjee, A., … others. (2008). Evidence of an extended electron current sheet and its neighboring magnetic island during magnetotail reconnection. *Journal of Geophysical Research: Space Physics*, *113*(A12).

Chen, L.-J., Bhattacharjee, A., Puhl-Quinn, P. A., Yang, H., Bessho, N., Imada, S., … others. (2008). Observation of energetic electrons within magnetic islands. *Nature Physics*, *4*(1), 19.

Chen, L.-J., Hesse, M., Wang, S., Gershman, D., Ergun, R. E., Burch, J., … others. (2017). Electron diffusion region during magnetopause reconnection with an intermediate guide field: Magnetospheric multiscale observations. *Journal of Geophysical Research: Space Physics*, *122*(5), 5235–5246.

Chen, Y., Tóth, G., Cassak, P., Jia, X., Gombosi, T. I., Slavin, J. A., … Henderson, M. G. (2017). Global Three-Dimensional Simulation of Earth's Dayside Reconnection Using a Two-Way Coupled Magnetohydrodynamics With Embedded Particle-in-Cell Model: Initial Results. *Journal of Geophysical Research: Space Physics*, *122*(10), 10,318-10,335. https://doi.org/10.1002/2017JA024186

Comisso, L., Grasso, D., & Waelbroeck, F. L. (2015). Phase diagrams of forced magnetic reconnection in Taylor's model. *Journal of Plasma Physics*, *81*(5).

Comisso, L, Lingam, M., Huang, Y.-M., & Bhattacharjee, A. (2016). General theory of the plasmoid instability. *Physics of Plasmas*, *23*(10), 100702.

Comisso, Luca, & Grasso, D. (2016). Visco-resistive plasmoid instability. *Physics of Plasmas*, *23*(3), 32111.

Coulomb, A. (1935). First memoir on electricity and magnetism. *A Source Book in Physics*, 408–413.

Cowley, S. W. H. (1995). Theoretical perspectives of the magnetopause: A tutorial review. *Physics of the Magnetopause*, *90*, 29–43.

Cranmer, S. R., Matthaeus, W. H., Breech, B. A., & Kasper, J. C. (2009). Empirical constraints on proton and electron heating in the fast solar wind. *The Astrophysical Journal*, *702*(2), 1604.

Cuperman, S. (1981). Electromagnetic kinetic instabilities in multicomponent space plasmas: Theoretical predictions and computer simulation experiments. *Reviews of Geophysics*, *19*(2), 307–343.

Dahlin, J. T., Drake, J. F., & Swisdak, M. (2014). The mechanisms of electron heating and acceleration during magnetic reconnection. *Physics of Plasmas*, *21*(9), 92304. https://doi.org/10.1063/1.4894484

Dahlin, J. T., Drake, J. F., & Swisdak, M. (2015). Electron acceleration in three-dimensional magnetic reconnection with a guide field. *Physics of Plasmas*, *22*(10), 100704.

Dahlin, J. T., Drake, J. F., & Swisdak, M. (2016). Parallel electric fields are inefficient drivers of energetic electrons in magnetic reconnection. *Physics of Plasmas*, *23*(12), 120704.

Dahlin, J. T., Drake, J. F., & Swisdak, M. (2017). The role of three-dimensional transport in driving enhanced electron acceleration during magnetic reconnection. *Physics of Plasmas*, *24*(9), 92110.

Daldorff, L. K. S., Tóth, G., Gombosi, T. I., Lapenta, G., Amaya, J., Markidis, S., & Brackbill, J. U. (2014). Two-way coupling of a global Hall magnetohydrodynamics model with a local implicit particle-in-cell model. *Journal of Computational Physics*, *268*, 236–254.

Daly, P. W., Saunders, M. A., Rijnbeek, R. P., Sckopke, N., & Russell, C. T. (1984). The

distribution of reconnection geometry in flux transfer events using energetic ion, plasma and magnetic data. *Journal of Geophysical Research: Space Physics*, *89*(A6), 3843–3854.

Daughton, W., Roytershteyn, V., Albright, B. J., Karimabadi, H., Yin, L., & Bowers, K. J. (2009). Transition from collisional to kinetic regimes in large-scale reconnection layers. *Physical Review Letters*, *103*(6), 065004. https://doi.org/10.1103/PhysRevLett.103.065004

Daughton, W., Roytershteyn, V., Karimabadi, H., Yin, L., Albright, B. J., Bergen, B., & Bowers, K. J. (2011). Role of electron physics in the development of turbulent magnetic reconnection in collisionless plasmas. *Nature Physics*, *7*(7), 539–542. https://doi.org/10.1038/nphys1965

Daughton, W, Roytershteyn, V., Karimabadi, H., Yin, L., Albright, B. J., Gary, S. P., & Bowers, K. J. (2011). Secondary island formation in collisional and collisionless kinetic simulations of magnetic reconnection. In *AIP Conference Proceedings* (Vol. 1320, pp. 144–159).

Daughton, William, Scudder, J., & Karimabadi, H. (2006). Fully kinetic simulations of undriven magnetic reconnection with open boundary conditions. *Physics of Plasmas*, *13*(7), 72101.

Deng, X. H., Matsumoto, H., Kojima, H., Mukai, T., Anderson, R. R., Baumjohann, W., & Nakamura, R. (2004). Geotail encounter with reconnection diffusion region in the Earth's magnetotail: Evidence of multiple X lines collisionless reconnection? *Journal of Geophysical Research: Space Physics*, *109*(A5).

Dewey, R. M., Slavin, J. A., Raines, J. M., Baker, D. N., & Lawrence, D. J. (2017). Energetic Electron Acceleration and Injection During Dipolarization Events in Mercury's Magnetotail. *Journal of Geophysical Research: Space Physics*.

DiBraccio, G. A., Slavin, J. A., Boardsen, S. A., Anderson, B. J., Korth, H., Zurbuchen, T. H., … Solomon, S. C. (2013). MESSENGER observations of magnetopause structure and dynamics at Mercury. *Journal of Geophysical Research: Space Physics*, *118*(3), 997–1008.

Ding, D. Q., Lee, L. C., & Swift, D. W. (1992). Particle simulations of driven collisionless magnetic reconnection at the dayside magnetopause. *Journal of Geophysical Research: Space Physics*, *97*(A6), 8453–8481.

Divin, A. V, Sitnov, M. I., Swisdak, M., & Drake, J. F. (2007). Reconnection onset in the magnetotail: Particle simulations with open boundary conditions. *Geophysical Research Letters*, *34*(9).

Dong, C., Wang, L., Hakim, A., Bhattacharjee, A., Slavin, J. A., DiBraccio, G. A., & Germaschewski, K. (2019). A Novel Ten-Moment Multifluid Model for Mercury: From the Planetary Conducting Core to the Dynamic Magnetosphere. *Geophysical Research Letters*, 2019GL083180. https://doi.org/10.1029/2019GL083180

Dong, X.-C., Dunlop, M. W., Trattner, K. J., Phan, T. D., Fu, H.-S., Cao, J.-B., … others. (2017). Structure and evolution of flux transfer events near dayside magnetic reconnection dissipation region: MMS observations. *Geophysical Research Letters*.

Dorelli, J. C., & Bhattacharjee, A. (2009). On the generation and topology of flux transfer events. *Journal of Geophysical Research: Space Physics*, *114*(6), 1–21. https://doi.org/10.1029/2008JA013410

Drake, J. F., Opher, M., Swisdak, M., & Chamoun, J. N. (2010). A magnetic reconnection mechanism for the generation of anomalous cosmic rays. *The Astrophysical Journal*, *709*(2),

963–974. https://doi.org/10.1088/0004-637X/709/2/963

Drake, J. F., Arnold, H., Swisdak, M., & Dahlin, J. T. (2019). A computational model for exploring particle acceleration during reconnection in macroscale systems. *Physics of Plasmas*, *26*(1), 12901.

Drake, J. F., Swisdak, M., Schoeffler, K. M., Rogers, B. N., & Kobayashi, S. (2006). Formation of secondary islands during magnetic reconnection. *Geophysical Research Letters*, *33*(13), 10–13. https://doi.org/10.1029/2006GL025957

Drake, J. F., & Lee, Y. C. (1977a). Kinetic theory of tearing instabilities. *The Physics of Fluids*, *20*(8), 1341–1353.

Drake, J. F., & Lee, Y. C. (1977b). Nonlinear evolution of collisionless and semicollisional tearing modes. *Physical Review Letters*, *39*(8), 453.

Drake, J. F., Swisdak, M., Che, H., & Shay, M. A. (2006). Electron acceleration from contracting magnetic islands during reconnection. *Nature*, *443*(7111), 553. https://doi.org/10.1038/nature05116

Drake, J. F., Swisdak, M., Phan, T. D., Cassak, P. A., Shay, M. A., Lepri, S. T., … Zurbuchen, T. H. (2009). Ion heating resulting from pickup in magnetic reconnection exhausts. *Journal of Geophysical Research: Space Physics*, *114*(A5).

Dungey, J. W. (1954). Electrodynamics of the outer atmospheres, Rep. 69, Ions. *Res. Lab. Pa. State Univ., University Park*.

Dunlop, M. W., Balogh, A., Southwood, D. J., Elphic, R. C., Glassmeier, K.-H., & Neubauer, F. M. (1990). Configurational sensitivity of multipoint magnetic field measurements. *Space Plasma Physics Investigation by Cluster and Regatta*.

Dunlop, M. W., Taylor, M., Davies, J. A., Owen, C. J., Pitout, F., Fazakerley, A. N., … others. (2005). Coordinated Cluster/Double Star observations of dayside reconnection signatures. In *Annales Geophysicae* (Vol. 23, pp. 2867–2875).

Eastwood, J. P., Phan, T. D., Mozer, F. S., Shay, M. A., Fujimoto, M., Retin??, A., … Dandouras, I. (2007). Multi-point observations of the Hall electromagnetic field and secondary island formation during magnetic reconnection. *Journal of Geophysical Research: Space Physics*, *112*(6), 1–13. https://doi.org/10.1029/2006JA012158

Eastwood, J. P., Shay, M. A., Phan, T. D., & Øieroset, M. (2010). Asymmetry of the ion diffusion region Hall electric and magnetic fields during guide field reconnection: Observations and comparison with simulations. *Physical Review Letters*, *104*(20), 205001.

Eastwood, J. P., Mistry, R., Phan, T. D., Schwartz, S. J., Ergun, R. E., Drake, J. F., … others. (2018). Guide field reconnection: Exhaust structure and heating. *Geophysical Research Letters*, *45*(10), 4569–4577.

Eastwood, J. P., Phan, T. D., Øieroset, M., & Shay, M. A. (2010). Average properties of the magnetic reconnection ion diffusion region in the Earth's magnetotail: The 2001--2005 Cluster observations and comparison with simulations. *Journal of Geophysical Research: Space Physics*, *115*(A8).

Eastwood, J. P., Phan, T. D., Fear, R. C., Sibeck, D. G., Angelopoulos, V., Ieroset, M., … Shay,

M. A. (2012). Survival of flux transfer event (FTE) flux ropes far along the tail magnetopause. *Journal of Geophysical Research: Space Physics*, *117*(8), 1–9. https://doi.org/10.1029/2012JA017722

Eastwood, J. P., Phan, T. D., Bale, S. D., & Tjulin, A. (2009). Observations of turbulence generated by magnetic reconnection. *Physical Review Letters*, *102*(3), 35001.

Eastwood, J. P., Phan, T. D., Cassak, P. A., Gershman, D. J., Haggerty, C., Malakit, K., … Wang, S. (2016). Ion-scale secondary flux-ropes generated by magnetopause reconnection as resolved by MMS. *Geophysical Research Letters*, *43*(10), 1–9. https://doi.org/10.1002/2016GL068747

Ebihara, Y., Fok, M.-C., Blake, J. B., & Fennell, J. F. (2008). Magnetic coupling of the ring current and the radiation belt. *Journal of Geophysical Research: Space Physics*, *113*(A7).

Egedal, J, Le, A., Pritchett, P. L., & Daughton, W. (2011). Electron dynamics in two-dimensional asymmetric anti-parallel reconnection. *Physics of Plasmas*, *18*(10), 102901.

Egedal, J, Daughton, W., Drake, J. F., Katz, N., & Lê, A. (2009). Formation of a localized acceleration potential during magnetic reconnection with a guide field. *Physics of Plasmas*, *16*(5), 50701.

Egedal, Jan, Daughton, W., & Le, A. (2012). Large-scale electron acceleration by parallel electric fields during magnetic reconnection. *Nature Physics*, *8*(4), 321.

Ergun, R. E., Tucker, S., Westfall, J., Goodrich, K. A., Malaspina, D. M., Summers, D., … Cully, C. M. (2016). The axial double probe and fields signal processing for the MMS mission. *Space Science Reviews*, *199*(1–4), 167–188. https://doi.org/10.1007/s11214-014-0115-x

Ergun, R. E., Chen, L.-J., Wilder, F. D., Ahmadi, N., Eriksson, S., Usanova, M. E., … others. (2017). Drift waves, intense parallel electric fields, and turbulence associated with asymmetric magnetic reconnection at the magnetopause. *Geophysical Research Letters*, *44*(7), 2978–2986.

Escoubet, C. P., Pedersen, A., Schmidt, R., & Lindqvist, P. A. (1997). Density in the magnetosphere inferred from ISEE 1 spacecraft potential. *Journal of Geophysical Research: Space Physics*, *102*(A8), 17595–17609. https://doi.org/10.1029/97JA00290

Eviatar, A., & Schulz, M. (1970). Ion-temperature anisotropies and the structure of the solar wind. *Planetary and Space Science*, *18*(3), 321–332.

Farrugia, C. J., Lavraud, B., Torbert, R. B., Argall, M., Kacem, I., Yu, W., … Strangeway, R. J. (2016). MMS Observations and Non-Force Free Modeling of a Flux Transfer Event Immersed in a Super-Alfvénic Flow. *Geophysical Research Letters*, *43*(12), 1–8. https://doi.org/10.1002/2016GL068758

Farrugia, C. J., Rijnbeek, R. P., Saunders, M. A., Southwood, D. J., Rodgers, D. J., Smith, M. F., … Woolliscroft, L. J. C. (1988). A multi-instrument study of flux transfer event structure. *Journal of Geophysical Research*, *93*(A12), 14465. https://doi.org/10.1029/JA093iA12p14465

Farrugia, Charles J, Gratton, F. T., Gnavi, G., & Ogilvie, K. W. (1998). On the possible excitation of electromagnetic ion cyclotron waves in solar ejecta. *Journal of Geophysical Research: Space Physics*, *103*(A4), 6543–6550.

Fear, R. C., Milan, S. E., Fazakerley, A. N., Owen, C. J., Asikainen, T., Taylor, M. G. G. T., … Daly, P. W. (2007). Motion of flux transfer events: a test of the Cooling model. *Ann. Geophys*, *25*, 1669–1690. Retrieved from www.ann-geophys.net/25/1669/2007/

Fear, R. C., Milan, S. E., Fazakerley, A. N., Lucek, E. A., Cowley, S. W. H., & Dandouras, I. (2008). The azimuthal extent of three flux transfer events. *Annales Geophysicae*, *26*(8), 2353–2369. https://doi.org/10.5194/angeo-26-2353-2008

Fear, R. C., Milan, S. E., Lucek, E. A., Cowley, S. W. H., & Fazakerley, A. N. (2010). Mixed azimuthal scales of flux transfer events. In *The Cluster Active Archive* (pp. 389–398). Springer.

Fermo, R. ~L. L., Drake, J. ~F. F., & Swisdak, M. (2010). A statistical model of magnetic islands in a current layer. *Physics of Plasmas*, *17*(1), 10702. https://doi.org/10.1063/1.3286437

Fermo, R. L., Drake, J. F., Swisdak, M., & Hwang, K. J. (2011). Comparison of a statistical model for magnetic islands in large current layers with Hall MHD simulations and Cluster FTE observations. *Journal of Geophysical Research: Space Physics*, *116*(A9), n/a-n/a. https://doi.org/10.1029/2010ja016271

Finn, J. M., & Kaw, P. K. (1977). Coalescence instability of magnetic islands. *The Physics of Fluids*, *20*(1), 72–78.

Fu, H. S., Khotyaintsev, Y. V., André, M., & Vaivads, A. (2011). Fermi and betatron acceleration of suprathermal electrons behind dipolarization fronts. *Geophysical Research Letters*, *38*(16). https://doi.org/10.1029/2011GL048528

Fu, H S, Khotyaintsev, Y. V, Vaivads, A., Retinò, A., & André, M. (2013). Energetic electron acceleration by unsteady magnetic reconnection. *Nature Physics*, *9*(7), 426.

Fu, H S, Peng, F. Z., Liu, C. M., Burch, J. L., Gershman, D. G., & Le Contel, O. (2019). Evidence of electron acceleration at a reconnecting magnetopause. *Geophysical Research Letters*.

Fu, H S, Xu, Y., Vaivads, A., & Khotyaintsev, Y. V. (2019). Super-efficient Electron Acceleration by an Isolated Magnetic Reconnection. *The Astrophysical Journal Letters*, *870*(2), L22.

Fu, Huishan S, Khotyaintsev, Y. V, André, M., & Vaivads, A. (2011). Fermi and betatron acceleration of suprathermal electrons behind dipolarization fronts. *Geophysical Research Letters*, *38*(16).

Fujimoto, K. (2006). Time evolution of the electron diffusion region and the reconnection rate in fully kinetic and large system. *Physics of Plasmas*, *13*(7), 72904.

Furno, I., Intrator, T. P., Hemsing, E. W., Hsu, S. C., Abbate, S., Ricci, P., & Lapenta, G. (2005). Coalescence of two magnetic flux ropes via collisional magnetic reconnection. *Physics of Plasmas*, *12*(5), 55702.

Furth, H. P., Killeen, J., & Rosenbluth, M. N. (1963). Finite-resistivity instabilities of a sheet pinch. *The Physics of Fluids*, *6*(4), 459–484.

Fuselier, S. A., Petrinec, S. M., Trattner, K. J., Broll, J. M., Burch, J. L., Giles, B. L., … others. (2018). Observational Evidence of Large-Scale Multiple Reconnection at the Earth's Dayside Magnetopause. *Journal of Geophysical Research: Space Physics*, *123*(10), 8407–8421.

Fuselier, S. A., Trattner, K. J., Petrinec, S. M., Owen, C. J., & Rème, H. (2005). Computing the

reconnection rate at the Earth's magnetopause using two spacecraft observations. *Journal of Geophysical Research: Space Physics*, *110*(A6).

Fuselier, S. A., Lewis, W. S., Schiff, C., Ergun, R., Burch, J. L., Petrinec, S. M., & Trattner, K. J. (2016). Magnetospheric multiscale science mission profile and operations. *Space Science Reviews*, *199*(1–4), 77–103.

Galeev, A. A., Coroniti, F. V, & Ashour-Abdalla, M. (1978). Explosive tearing mode reconnection in the magnetospheric tail. *Geophysical Research Letters*, *5*(8), 707–710.

Gary, S. P., Montgomery, M. D., Feldman, W. C., & Forslund, D. W. (1976). Proton temperature anisotropy instabilities in the solar wind. *Journal of Geophysical Research*, *81*(7), 1241–1246. https://doi.org/10.1029/JA081i007p01241

Gary, S. P., McKean, M. E., Winske, D., Anderson, B. J., Denton, R. E., & Fuselier, S. A. (1994). The proton cyclotron instability and the anisotropy/β inverse correlation. *Journal of Geophysical Research: Space Physics*, *99*(A4), 5903–5914.

Gary, S. P., Neagu, E., Skoug, R. M., & Goldstein, B. E. (1999). Solar wind electrons: Parametric constraints. *Journal of Geophysical Research: Space Physics*, *104*(A9), 19843–19849.

Gary, S. P., & Madland, C. D. (1985). Electromagnetic electron temperature anisotropy instabilities. *Journal of Geophysical Research: Space Physics*, *90*(A8), 7607–7610.

Gary, S. P., Skoug, R. M., Steinberg, J. T., & Smith, C. W. (2001). Proton temperature anisotropy constraint in the solar wind: ACE observations. *Geophysical Research Letters*, *28*(14), 2759–2762.

Gary, S. P., Li, H., O'Rourke, S., & Winske, D. (1998). Proton resonant firehose instability: Temperature anisotropy and fluctuating field constraints. *Journal of Geophysical Research: Space Physics*, *103*(A7), 14567–14574.

Genestreti, K. J., Nakamura, T. K. M., Nakamura, R., Denton, R. E., Torbert, R. B., Burch, J. L., … others. (2018). How Accurately Can We Measure the Reconnection Rate EM for the MMS Diffusion Region Event of 11 July 2017? *Journal of Geophysical Research: Space Physics*, *123*(11), 9130–9149.

Genestreti, K. J., Varsani, A., Burch, J. L., Cassak, P. A., Torbert, R. B., Nakamura, R., … others. (2018). MMS observation of asymmetric reconnection supported by 3-D electron pressure divergence. *Journal of Geophysical Research: Space Physics*, *123*(3), 1806–1821.

Gilbert, W. (1958). *De magnete*. Courier Corporation.

Gombosi, T. I., De Zeeuw, D. L., Häberli, R. M., & Powell, K. G. (1996). Three-dimensional multiscale MHD model of cometary plasma environments. *Journal of Geophysical Research: Space Physics*, *101*(A7), 15233–15253.

Gombosi, T. I., Powell, K. G., & De Zeeuw, D. L. (1994). Axisymmetric modeling of cometary mass loading on an adaptively refined grid: MHD results. *Journal of Geophysical Research: Space Physics*, *99*(A11), 21525–21539.

Gonzalez, W., & Parker, E. (2016a). *Magnetic Reconnection: Concepts and Applications* (Vol. 427). Springer.

Gonzalez, W., & Parker, E. (2016b). Magnetic reconnection. *Astrophysics and Space Science*

Library, *427*, 10–1007.

Gopalswamy, N., Yashiro, S., Kaiser, M. L., Howard, R. A., & Bougeret, J.-L. (2001). Radio signatures of coronal mass ejection interaction: Coronal mass ejection cannibalism? *The Astrophysical Journal Letters*, *548*(1), L91.

Gosling, J. T., Thomsen, M. F., Bame, S. J., Onsager, T. G., & Russell, C. T. (1990). The electron edge of low latitude boundary layer during accelerated flow events. *Geophysical Research Letters*, *17*(11), 1833–1836.

Gosling, J. T., Thomsen, M. F., Bame, S. J., Feldman, W. C., Paschmann, G., & Sckopke, N. (1982). Evidence for specularly reflected ions upstream from the quasi-parallel bow shock. *Geophysical Research Letters*, *9*(12), 1333–1336.

Gosling, J. T., Skoug, R. M., McComas, D. J., & Smith, C. W. (2005). Direct evidence for magnetic reconnection in the solar wind near 1 AU. *Journal of Geophysical Research: Space Physics*, *110*(A1).

Graham, D. B., Khotyaintsev, Y. V., Norgren, C., Vaivads, A., André, M., Lindqvist, P.-A., … Burch, J. L. (2016). Electron currents and heating in the ion diffusion region of asymmetric reconnection. *Geophysical Research Letters*, *43*(10), 4691–4700. https://doi.org/10.1002/2016GL068613

Graham, Daniel B, Khotyaintsev, Y. V, Norgren, C., Vaivads, A., André, M., Toledo-Redondo, S., … others. (2017). Lower hybrid waves in the ion diffusion and magnetospheric inflow regions. *Journal of Geophysical Research: Space Physics*, *122*(1), 517–533.

Guidoni, S. E., DeVore, C. R., Karpen, J. T., & Lynch, B. J. (2016). Magnetic-Island Contraction and Particle Acceleration in Simulated Eruptive Solar Flares. *The Astrophysical Journal*, *820*(1), 60.

Guo, F., Liu, Y.-H., Daughton, W., & Li, H. (2015). Particle Acceleration and Plasma Dynamics during Magnetic Reconnection in the Magnetically-dominated Regime. Retrieved from https://arxiv.org/abs/1504.02193

Haerendel, G., Lüst, R., & Rieger, E. (1967). Motion of artificial ion clouds in the upper atmosphere. *Planetary and Space Science*, *15*(1), 1–18.

Haggerty, C. C., Shay, M. A., Drake, J. F., Phan, T. D., & McHugh, C. T. (2015). The competition of electron and ion heating during magnetic reconnection. *Geophysical Research Letters*, *42*(22), 9657–9665.

Hakim, A. H. (2008). Extended MHD modelling with the ten-moment equations. *Journal of Fusion Energy*, *27*(1–2), 36–43.

Hallock, G. A., & Meier, M. A. (2018). Diamagnetic current measurements in a solid-state plasma. *Review of Scientific Instruments*, *89*(8), 83505.

Harvey, C. C. (1998). Spatial Gradients and the Volumetric Tensor. Retrieved from http://www.issibern.ch/forads/sr-001-12.pdf

Hasegawa, H., Wang, J., Dunlop, M. W., Pu, Z. Y., Zhang, Q.-H. Q.-H. H., Lavraud, B., … Bogdanova, Y. V. (2010). Evidence for a flux transfer event generated by multiple X-line reconnection at the magnetopause. *Geophysical Research Letters*, *37*(16), 1–6.

https://doi.org/10.1029/2010GL044219

Hasegawa, H, Sonnerup, B. U. Ö., Owen, C. J., Klecker, B., Paschmann, G., Balogh, A., & Rème, H. (2006). The structure of flux transfer events recovered from Cluster data. In *Annales Geophysicae* (Vol. 24, pp. 603–618).

Hasegawa, Hiroshi, Kitamura, N., Saito, Y., Nagai, T., Shinohara, I., Yokota, S., … others. (2016). Decay of mesoscale flux transfer events during quasi-continuous spatially extended reconnection at the magnetopause. *Geophysical Research Letters*, *43*(10), 4755–4762. https://doi.org/10.1002/2016GL069225

Hellinger, P, & Matsumoto, H. (2000). New kinetic instability: Oblique Alfvén fire hose. *Journal of Geophysical Research: Space Physics*, *105*(A5), 10519–10526.

Hellinger, Petr, Trávn\'\iček, P., Kasper, J. C., Lazarus, A. J., Trávníček, P., Kasper, J. C., & Lazarus, A. J. (2006). Solar wind proton temperature anisotropy: Linear theory and WIND/SWE observations. *Geophysical Research Letters*, *33*(9), L09101. https://doi.org/10.1029/2006GL025925

Hesse, M., Aunai, N., Sibeck, D., & Birn, J. (2014). On the electron diffusion region in planar, asymmetric, systems. *Geophysical Research Letters*, *41*(24), 8673–8680. https://doi.org/10.1002/2014GL061586

Hesse, M., Schindler, K., Birn, J., & Kuznetsova, M. (1999). The diffusion region in collisionless magnetic reconnection. *Physics of Plasmas*, *6*(5), 1781–1795.

Hesse, M., Neukirch, T., Schindler, K., Kuznetsova, M., & Zenitani, S. (2011). The diffusion region in collisionless magnetic reconnection. *Space Science Reviews*, *160*(1–4), 3–23. https://doi.org/10.1007/s11214-010-9740-1

Hoilijoki, S, Ganse, U., Sibeck, D. G., Cassak, P. A., Turc, L., Battarbee, M., … others. (2019). Properties of magnetic reconnection and FTEs on the dayside magnetopause with and without positive IMF B component during southward IMF. *Journal of Geophysical Research: Space Physics*.

Hoilijoki, Sanni, Ganse, U., Pfau-Kempf, Y., Cassak, P. A., Walsh, B. M., Hietala, H., … Palmroth, M. (2017). Reconnection rates and X line motion at the magnetopause: Global 2D-3V hybrid-Vlasov simulation results. *Journal of Geophysical Research: Space Physics*, *122*(3), 2877–2888.

Hollweg, J. V., & Völk, H. J. (1970a). Two New Plasma Instabilities in the Solar Wind. *Nature*, *225*(5231), 441–443. https://doi.org/10.1038/225441a0

Hollweg, J. V, & Völk, H. J. (1970b). New plasma instabilities in the solar wind. *Journal of Geophysical Research*, *75*(28), 5297–5309.

Hoshino, M., Mukai, T., Terasawa, T., & Shinohara, I. (2001). Suprathermal electron acceleration in magnetic reconnection. *Journal of Geophysical Research: Space Physics*, *106*(A11), 25979–25997. https://doi.org/10.1029/2001JA900052

Hoshino, M, Mukai, T., Yamamoto, T., & Kokubun, S. (1998). Ion dynamics in magnetic reconnection: Comparison between numerical simulation and Geotail observations. *Journal of Geophysical Research: Space Physics*, *103*(A3), 4509–4530.

Hoshino, Masahiro. (2005). Electron surfing acceleration in magnetic reconnection. *Journal of Geophysical Research: Space Physics*, *110*(A10).

Hoshino, Masahiro. (2012). Stochastic particle acceleration in multiple magnetic islands during reconnection. *Physical Review Letters*, *108*(13), 135003.

Huang, S. Y., Sahraoui, F., Retino, A., Le Contel, O., Yuan, Z. G., Chasapis, A., … Burch, J. L. (2016). MMS observations of ion-scale magnetic island in the magnetosheath turbulent plasma. *Geophysical Research Letters*, *43*(15), 7850–7858. https://doi.org/10.1002/2016GL070033

Huang, S. Y., Vaivads, A., Khotyaintsev, Y. V, Zhou, M., Fu, H. S., Retinò, A., … others. (2012). Electron acceleration in the reconnection diffusion region: Cluster observations. *Geophysical Research Letters*, *39*(11).

Huang, Y.-M., & Bhattacharjee, A. (2010). Scaling laws of resistive magnetohydrodynamic reconnection in the high-Lundquist-number, plasmoid-unstable regime. *Physics of Plasmas*, *17*(6), 62104. https://doi.org/10.1063/1.3420208

Huang, Y.-M., & Bhattacharjee, A. (2013). Plasmoid instability in high-Lundquist-number magnetic reconnection a. *Physics of Plasmas*, *20*(5), 55702.

Huang, Y.-M., Bhattacharjee, A., & Sullivan, B. P. (2011). Onset of fast reconnection in Hall magnetohydrodynamics mediated by the plasmoid instability. *Physics of Plasmas*, *18*(7), 72109.

Hwang, K-J, Sibeck, D. G., Burch, J. L., Choi, E., Fear, R. C., Lavraud, B., … others. (2018). Small-scale flux transfer events formed in the reconnection exhaust region between two X-lines. *Journal of Geophysical Research: Space Physics*.

Hwang, K.-J., Sibeck, D. G., Giles, B. L., Pollock, C. J., Gershman, D., Avanov, L., … Burch, J. L. (2016). The substructure of a flux transfer event observed by the MMS spacecraft. *Geophysical Research Letters*, *43*(18), 9434–9443. https://doi.org/10.1002/2016GL070934

Hwang, K. J., Sibeck, D. G., Burch, J. L., Choi, E., Fear, R. C., Lavraud, B., … Strangeway, R. J. (2018). Small-Scale Flux Transfer Events Formed in the Reconnection Exhaust Region Between Two X Lines. *Journal of Geophysical Research: Space Physics*, *123*(10), 8473–8488. https://doi.org/10.1029/2018JA025611

Imber, S. M., Slavin, J. A., Boardsen, S. A., Anderson, B. J., Korth, H., McNutt, R. L., & Solomon, S. C. (2014). MESSENGER observations of large dayside flux transfer events: Do they drive Mercury's substorm cycle? *Journal of Geophysical Research: Space Physics*, *119*(7), 5613–5623. https://doi.org/10.1002/2014JA019884

Jaroschek, C. H., Lesch, H., & Treumann, R. A. (2004). Self-consistent Diffusive Lifetimes of Weibel Magnetic Fields in Gamma-Ray Bursts. *The Astrophysical Journal*, *616*(2), 1065–1071. https://doi.org/10.1086/424923

Jarvinen, R., Vainio, R., Palmroth, M., Juusola, L., Hoilijoki, S., Pfau-Kempf, Y., … von Alfthan, S. (2018). Ion Acceleration by Flux Transfer Events in the Terrestrial Magnetosheath. *Geophysical Research Letters*, *45*(4), 1723–1731.

Jasinski, J. M., Slavin, J. A., Arridge, C. S., Poh, G., Jia, X., Sergis, N., … Waite, J. H. (2016). Flux transfer event observation at Saturn's dayside magnetopause by the Cassini spacecraft.

Geophysical Research Letters, *43*(13), 6713–6723.

Ji, H. (1999). Helicity, reconnection, and dynamo effects. *GEOPHYSICAL MONOGRAPH-AMERICAN GEOPHYSICAL UNION*, *111*, 167–178.

Ji, H., & Daughton, W. (2011). Phase diagram for magnetic reconnection in heliophysical, astrophysical, and laboratory plasmas. *Physics of Plasmas*, *18*(11). https://doi.org/10.1063/1.3647505

Ji, H., Yamada, M., Hsu, S., & Kulsrud, R. (1998). Experimental test of the Sweet-Parker model of magnetic reconnection. *Physical Review Letters*, *80*(15), 3256.

Juusola, L., Pfau-Kempf, Y., Ganse, U., Battarbee, M., Brito, T., Grandin, M., … others. (2018). A possible source mechanism for magnetotail current sheet flapping. In *Annales Geophysicae*.

Juusola, L., Hoilijoki, S., Pfau-Kempf, Y., Ganse, U., Järvinen, R., Battarbee, M., … others. (2018). Fast plasma sheet flows and X line motion in the Earth's magnetotail. In *Annales Geophysicae*.

Kacem, I., Jacquey, C., Génot, V., Lavraud, B., Vernisse, Y., Marchaudon, A., … others. (2018). Magnetic reconnection at a thin current sheet separating two interlaced flux tubes at the Earth's magnetopause. *Journal of Geophysical Research: Space Physics*.

Kagan, D., Nakar, E., & Piran, T. (2017). Physics of the saturation of particle acceleration in relativistic magnetic reconnection. *ArXiv Preprint ArXiv:1711.08701*.

Karimabadi, H., Dorelli, J., Roytershteyn, V., Daughton, W., & Chacón, L. (2011). Flux Pileup in Collisionless Magnetic Reconnection: Bursty Interaction of Large Flux Ropes. *Physical Review Letters*, *107*(2), 025002. https://doi.org/10.1103/PhysRevLett.107.025002

Karimabadi, H., Daughton, W., & Scudder, J. (2007). Multi-scale structure of the electron diffusion region. *Geophysical Research Letters*, *34*(13).

Karimabadi, H., Krauss-Varban, D., Omidi, N., & Vu, @bullet H X. (1999). Magnetic structure of the reconnection layer and core field generation in plasmoids. *JOURNAL OF GEOPHYSICAL RESEARCH*, *104326*(1), 313–12. https://doi.org/10.1029/1999JA900089

Karimabadi, H., Krauss-Varban, D., Omidi, N., & Vu, H. X. (1999). Magnetic structure of the reconnection layer and core field generation in plasmoids. *Journal of Geophysical Research: Space Physics*, *104*(A6), 12313–12326. https://doi.org/10.1029/1999JA900089

Karlick\`y, M., & Bárta, M. (2007). Drifting pulsating structures generated during tearing and coalescence processes in a flare current sheet. *Astronomy & Astrophysics*, *464*(2), 735–740.

Kasper, J C, Lazarus, A. J., Gary, S. P., & Szabo, A. (2003). Solar wind temperature anisotropies. In *AIP Conference Proceedings* (Vol. 679, pp. 538–541).

Kasper, J C, Lazarus, A. J., Steinberg, J. T., Ogilvie, K. W., & Szabo, A. (2006). Physics-based tests to identify the accuracy of solar wind ion measurements: A case study with the Wind Faraday Cups. *Journal of Geophysical Research: Space Physics*, *111*(A3).

Kasper, Justin C, Lazarus, A. J., & Gary, S. P. (2002). Wind/SWE observations of firehose constraint on solar wind proton temperature anisotropy. *Geophysical Research Letters*, *29*(17).

Kawano, H., & Russell, C. T. (1997). Survey of flux transfer events observed with the ISEE 1 spacecraft: Dependence on the interplanetary magnetic field. *Journal of Geophysical Research: Space Physics*, *102*(A6), 11307–11313. https://doi.org/10.1029/97JA00481

Kennel, C. F., & Petschek, H. E. (1966). Limit on stably trapped particle fluxes. *Journal of Geophysical Research*, *71*(1), 1–28.

Khalilzadeh, E., Chakhmachi, A., & Yazdanpanah, J. (2017). Stochastic behavior of electrons in high intensity laser--plasma interaction. *Plasma Physics and Controlled Fusion*, *59*(12), 125004.

Kish, L. (1992). Weighting for unequal Pi. *Journal of Official Statistics*, *8*(2), 183.

Kivelson, M. G., Khurana, K. K., Russell, C. T., Volwerk, M., Walker, R. J., & Zimmer, C. (2000). Galileo magnetometer measurements: A stronger case for a subsurface ocean at Europa. *Science*, *289*(5483), 1340–1343.

Kleva, R. G., Drake, J. F., & Waelbroeck, F. L. (1995). Fast reconnection in high temperature plasmas. *Physics of Plasmas*, *2*(1), 23–34.

Kliem, B. (1994). Particle orbits, trapping, and acceleration in a filamentary current sheet model. In *International Astronomical Union Colloquium* (Vol. 142, pp. 719–728).

Kliem, B., Karlicky, M., & Benz, A. O. (2000). Solar flare radio pulsations as a signature of dynamic magnetic reconnection. *ArXiv Preprint Astro-Ph/0006324*.

Klumpar, D. M., Fuselier, S. A., & Shelley, E. G. (1990). Ion composition measurements within magnetospheric flux transfer events. *Geophysical Research Letters*, *17*(13), 2305–2308.

Korotova, G. I., Sibeck, D. G., & Rosenberg, T. (2009). Geotail observations of FTE velocities. In *Annales Geophysicae* (Vol. 27, pp. 83–92).

Kowal, G., Dal Pino, E. M. de G., & Lazarian, A. (2011). Magnetohydrodynamic simulations of reconnection and particle acceleration: three-dimensional effects. *The Astrophysical Journal*, *735*(2), 102.

Krimigis, S. M., & Sarris, E. T. (1979). Energetic particle bursts in the Earth's magnetotail. In *Dynamics of the Magnetosphere* (pp. 599–630). Springer.

Krucker, S., Battaglia, M., Cargill, P. J., Fletcher, L., Hudson, H. S., MacKinnon, A. L., … others. (2008). Hard X-ray emission from the solar corona. *The Astronomy and Astrophysics Review*, *16*(3–4), 155–208.

Kumar, A., & Rust, D. M. (1996). Interplanetary magnetic clouds, helicity conservation, and current-core flux-ropes. *Journal of Geophysical Research: Space Physics*, *101*(A7), 15667–15684.

Lapenta, G., Berchem, J., Zhou, M., Walker, R. J., El-Alaoui, M., Goldstein, M. L., … Burch, J. L. (2017). On the origin of the crescent-shaped distributions observed by MMS at the magnetopause. *Journal of Geophysical Research: Space Physics*, *122*(2), 2024–2039. https://doi.org/10.1002/2016JA023290

Lapenta, G, Goldman, M., Newman, D., & Markidis, S. (2016). Where should MMS look for electron diffusion regions? In *Journal of Physics: Conference Series* (Vol. 719, p. 12011).

Lapenta, Giovanni, Wang, R., & Cazzola, E. (2016). Reconnection separatrix: Simulations and

spacecraft measurements. In *Magnetic reconnection* (pp. 315–344). Springer.

Lapenta, Giovanni, Markidis, S., Divin, A., Newman, D., & Goldman, M. (2015). Separatrices: The crux of reconnection. *Journal of Plasma Physics*, *81*(1).

Lapenta, Giovanni, Pucci, F., Olshevsky, V., Servidio, S., Sorriso-Valvo, L., Newman, D. L., & Goldman, M. V. (2018). Nonlinear waves and instabilities leading to secondary reconnection in reconnection outflows. *Journal of Plasma Physics*, *84*(1).

Lee, L. C., & Fu, Z. F. (1985). A theory of magnetic flux transfer at the Earth's magnetopause. *Geophysical Research Letters*, *12*(2), 105–108. https://doi.org/10.1029/GL012i002p00105

Lee, L. C., & Fu, Z. F. (1986). Multiple X line reconnection: 1. A criterion for the transition from a single X line to a multiple X line reconnection. *Journal of Geophysical Research: Space Physics*, *91*(A6), 6807–6815.

Lee, L. C., Price, C. P., Wu, C. S., & Mandt, M. E. (1988). A study of mirror waves generated downstream of a quasi-perpendicular shock. *Journal of Geophysical Research: Space Physics*, *93*(A1), 247–250.

Lepping, R. P., Jones, J. A., & Burlaga, L. F. (1990). Magnetic field structure of interplanetary magnetic clouds at 1 AU. *Journal of Geophysical Research*, *95*(A8), 11957. https://doi.org/10.1029/JA095iA08p11957

Li, X., Guo, F., Li, H., & Li, G. (2017). Particle Acceleration during Magnetic Reconnection in a Low-beta Plasma. *The Astrophysical Journal*, *843*(1), 21. https://doi.org/10.3847/1538-4357/aa745e

Lin, R. P. c, Krucker, S., Hurford, G. J., Smith, D. M., Hudson, H. S., Holman, G. D., … others. (2003). RHESSI observations of particle acceleration and energy release in an intense solar gamma-ray line flare. *The Astrophysical Journal Letters*, *595*(2), L69.

Lin, Y. (2003). Global-scale simulation of foreshock structures at the quasi-parallel bow shock. *Journal of Geophysical Research: Space Physics*, *108*(A11).

Lin, Y., & Wang, X. Y. (2005). Three-dimensional global hybrid simulation of dayside dynamics associated with the quasi-parallel bow shock. *Journal of Geophysical Research: Space Physics*, *110*(A12).

Lindqvist, P.-A. P.-A., Olsson, G., Torbert, R. B., King, B., Granoff, M., Rau, D., … others. (2016). The spin-plane double probe electric field instrument for MMS. *Space Science Reviews*, *199*(1–4), 137–165. https://doi.org/10.1007/s11214-014-0116-9

Lingam, M., & Comisso, L. (2018). A maximum entropy principle for inferring the distribution of 3D plasmoids. *Physics of Plasmas*, *25*(1), 12114.

Liu, C. X., Jin, S. P., Wei, F. S., Lu, Q. M., & Yang, H. A. (2009). Plasmoid-like structures in multiple X line Hall MHD reconnection. *Journal of Geophysical Research: Space Physics*, *114*(10), 1–16. https://doi.org/10.1029/2009JA014257

Liu, Y.-H., Hesse, M., Guo, F., Daughton, W., Li, H., Cassak, P. A., & Shay, M. A. (2017). Why does steady-state magnetic reconnection have a maximum local rate of order 0.1? *Physical Review Letters*, *118*(8), 85101.

Lockwood, M., & Hapgood, M. A. (1998). On the cause of a magnetospheric flux transfer event.

Journal of Geophysical Research: Space Physics, *103*(A11), 26453–26478.

Loureiro, N. F., Schekochihin, A. A., & Cowley, S. C. (2007). Instability of current sheets and formation of plasmoid chains. *Physics of Plasmas*, *14*(10), 100703. https://doi.org/10.1063/1.2783986

Loureiro, N. F., Schekochihin, A. A., & Uzdensky, D. A. (2013). Plasmoid and Kelvin-Helmholtz instabilities in Sweet-Parker current sheets. *Physical Review E*, *87*(1), 13102.

Loureiro, N. F., Samtaney, R., Schekochihin, A. A., & Uzdensky, D. A. (2012). Magnetic reconnection and stochastic plasmoid chains in high-Lundquist-number plasmas. *Physics of Plasmas*, *19*(4), 42303.

Lu, S., Lu, Q., Lin, Y., Wang, X., Ge, Y., Wang, R., … others. (2015). Dipolarization fronts as earthward propagating flux ropes: A three-dimensional global hybrid simulation. *Journal of Geophysical Research: Space Physics*, *120*(8), 6286–6300.

Lundquist, S. (1950). Magnetohydrostatic fields. *Ark. Fys.*, *2*, 361–365.

Lv, L., Pu, Z., & Xie, L. (2016). Multiple magnetic topologies in flux transfer events: THEMIS measurements. *Science China Technological Sciences*, *59*(8), 1283–1293. https://doi.org/10.1007/s11431-016-6071-9

Lyubarsky, Y., & Liverts, M. (2008). Particle Acceleration in the Driven Relativistic Reconnection. *The Astrophysical Journal*, *682*(2), 1436–1442. https://doi.org/10.1086/589640

Ma, Z., & Feng, S. L. (2008). Generation of electric field and net charge in hall reconnection. *Chinese Physics Letters*, *25*(8), 2934.

Ma, Z. W. T., Otto, A., & Lee, L. C. (1994). Core magnetic field enhancement in single X line, multiple X line and patchy reconnection. *Journal of Geophysical Research: Space Physics*, *99*(A4), 6125–6136.

Malakit, K., Shay, M. A., Cassak, P. A., & Ruffolo, D. (2013). New electric field in asymmetric magnetic reconnection. *Physical Review Letters*, *111*(13), 135001.

Man, H. Y., Zhou, M., Deng, X. H., Fu, H. S., Zhong, Z. H., Chen, Z. Z., … others. (2018). In situ observation of magnetic reconnection between an earthward propagating flux rope and the geomagnetic field. *Geophysical Research Letters*, *45*(17), 8729–8737.

Manheimer, W. M., & Lashmore-Davies, C. (1984). *MHD instabilities in simple plasma configuration*.

Markidis, S., Henri, P., Lapenta, G., Divin, A., Goldman, M., Newman, D., & Laure, E. (2013). Kinetic simulations of plasmoid chain dynamics. *Physics of Plasmas*, *20*(8), 82105.

Markidis, S., Lapenta, G., & others. (2010). Multi-scale simulations of plasma with iPIC3D. *Mathematics and Computers in Simulation*, *80*(7), 1509–1519.

Marsch, E., Zhao, L., & Tu, C.-Y. (2006). Limits on the core temperature anisotropy of solar wind protons. In *Annales Geophysicae* (Vol. 24, pp. 2057–2063).

Masters, A., Eastwood, J. P., Swisdak, M., Thomsen, M. F., Russell, C. T., Sergis, N., … Krimigis, S. M. (2012). The importance of plasma β conditions for magnetic reconnection at Saturn's magnetopause. *Geophysical Research Letters*, *39*(8).

Matsui, H., Farrugia, C. J., Goldstein, J., Torbert, R. B., Argall, M. R., Vaith, H., … others. (2019). Velocity Rotation Events in the Outer Magnetosphere Near the Magnetopause. *Journal of Geophysical Research: Space Physics*.

Matteini, L., Landi, S., Hellinger, P., & Velli, M. (2005). Proton fire hose instability in the expanding solar wind. In *Solar Wind 11/SOHO 16, Connecting Sun and Heliosphere* (Vol. 592, p. 503).

Mauk, B. H., Blake, J. B., Baker, D. N., Clemmons, J. H., Reeves, G. D., Spence, H. E., … others. (2016). The energetic particle detector (EPD) investigation and the energetic ion spectrometer (EIS) for the magnetospheric multiscale (MMS) mission. *Space Science Reviews*, *199*(1–4), 471–514.

Meng, C.-I. (1971). Energetic electrons in the magnetotail at 60RE. *Journal of Geophysical Research*, *76*(4), 862–872.

Meng, C.-I., & Anderson, K. A. (1971). Energetic electrons in the plasma sheet out to 40 RE. *Journal of Geophysical Research*, *76*(4), 873–882.

Midgley, J. E., & Davis, L. (1963). Calculation by a moment technique of the perturbation of the geomagnetic field by the solar wind. *Journal of Geophysical Research*, *68*(18), 5111–5123.

Milan, S. E., Lester, M., Cowley, S. W. H., & Brittnacher, M. (2000). Convection and auroral response to a southward turning of the IMF: Polar UVI, CUTLASS, and IMAGE signatures of transient magnetic flux transfer at the magnetopause. *J. Geophys. Res.*, *105*(A7), 15741–15755. https://doi.org/10.1029/2000JA900022

Miller, J. A., Cargill, P. J., Emslie, A. G., Holman, G. D., Dennis, B. R., LaRosa, T. N., … Tsuneta, S. (1997). Critical issues for understanding particle acceleration in impulsive solar flares. *Journal of Geophysical Research: Space Physics*, *102*(A7), 14631–14659.

Moore, T. E., Waite, J. H., Lockwood, M., & Chappell, C. R. (1986). Observations of coherent transverse ion acceleration. *Ion Acceleration in the Magnetosphere and Ionosphere*, 50–55.

Moser, A. L., & Bellan, P. M. (2012). Magnetic reconnection from a multiscale instability cascade. *Nature*, *482*(7385), 379–381.

Motschmann, U., Glassmeier, K. H., & Brinca, A. L. (1999). Nongyrotropic particle distributions in space plasmas. In *Annales Geophysicae* (Vol. 17, pp. 613–622).

Mozer, F. S. (2016). DC and low-frequency double probe electric field measurements in space. *Journal of Geophysical Research: Space Physics*, *121*(11), 10–942.

Mozer, F. S., Bale, S. D., & Phan, T. D. (2002). Evidence of diffusion regions at a subsolar magnetopause crossing. *Physical Review Letters*, *89*(1), 15002.

Muñoz, P. A., & Buechner, J. (2017). Two-stage electron acceleration by 3D collisionless guide field magnetic reconnection. *ArXiv Preprint ArXiv:1705.01066*.

Murayama, T., & Simpson, J. A. (1968). Electrons within the neutral sheet of the magnetospheric tail. *Journal of Geophysical Research*, *73*(3), 891–905.

Murphy, N. A., Young, A. K., Shen, C., Lin, J., & Ni, L. (2013). The plasmoid instability during asymmetric inflow magnetic reconnection. *Physics of Plasmas*, *20*(6), 61211.

Nagai, T., Shinohara, I., & Zenitani, S. (2015). Ion acceleration processes in magnetic

reconnection: Geotail observations in the magnetotail. *Journal of Geophysical Research: Space Physics*, *120*(3), 1766–1783. https://doi.org/10.1002/2014JA020737

Nakamura, T. K. M., Nakamura, R., Narita, Y., Baumjohann, W., & Daughton, W. (2016). Multi-scale structures of turbulent magnetic reconnection. *Physics of Plasmas*, *23*(5), 52116.

Newman, A. L. (1990). Thermal energization of ions during impulsive field events. *Geophysical Research Letters*, *17*(8), 1061–1064.

Ni, L., Kliem, B., Lin, J., & Wu, N. (2015). Fast magnetic reconnection in the solar chromosphere mediated by the plasmoid instability. *The Astrophysical Journal*, *799*(1), 79.

Northrop, T. G. (1963). Adiabatic charged-particle motion. *Reviews of Geophysics*, *1*(3), 283. https://doi.org/10.1029/RG001i003p00283

Øieroset, M., Lin, R. P., Phan, T. D., Larson, D. E., & Bale, S. D. (2002). Evidence for Electron Acceleration up to ~300 keV in the Magnetic Reconnection Diffusion Region of Earth's Magnetotail. *Physical Review Letters*, *89*(19), 195001. https://doi.org/10.1103/PhysRevLett.89.195001

Øieroset, M., Phan, T. D., Eastwood, J. P., Fujimoto, M., Daughton, W., Shay, M. A., … Glassmeier, K.-H. H. (2011). Direct evidence for a three-dimensional magnetic flux rope flanked by two active magnetic reconnection X lines at earth's magnetopause. *Physical Review Letters*, *107*(16), 165007. https://doi.org/10.1103/PhysRevLett.107.165007

Oieroset, M., Phan, T. D., Fujimoto, M., Lin, R. P., & Lepping, R. P. (2001). In situ detection of collisionless reconnection in the Earth's magnetotail. *Nature*, *412*(6845), 414–417. Retrieved from http://dx.doi.org/10.1038/35086520

Øieroset, M., Phan, T. D., Haggerty, C., Shay, M. A., Eastwood, J. P., Gershman, D. J., … Malakit, K. (2016). MMS observations of large guide field symmetric reconnection between colliding reconnection jets at the center of a magnetic flux rope at the magnetopause. *Geophysical Research Letters*, *43*(11), 5536–5544. https://doi.org/10.1002/2016GL069166

Øieroset, M., Phan, T. D., Drake, J. F., Eastwood, J. P., Fuselier, S. A., Strangeway, R. J., … others. (2019). Reconnection With Magnetic Flux Pileup at the Interface of Converging Jets at the Magnetopause. *Geophysical Research Letters*, *46*(4), 1937–1946.

Oka, M., Fujimoto, M., Shinohara, I., & Phan, T. D. (2010). "Island surfing" mechanism of electron acceleration during magnetic reconnection. *J. Geophys. Res*, *115*. https://doi.org/10.1029/2010JA015392

Oka, M., Phan, T.-D.-D. T.-D., Krucker, S., Fujimoto, M., & Shinohara, I. (2010). Electron acceleration by multi-island coalescence. *The Astrophysical Journal*, *714*(1), 915. https://doi.org/10.1088/0004-637X/714/1/915

Omidi, N., Blanco-Cano, X., Russell, C. T., & Karimabadi, H. (2006). Global hybrid simulations of solar wind interaction with Mercury: Magnetosperic boundaries. *Advances in Space Research*, *38*(4), 632–638.

Omidi, N., & Sibeck, D. G. (2007). Flux transfer events in the cusp. *Geophysical Research Letters*, *34*(4), L04106. https://doi.org/10.1029/2006GL028698

Owen, C. J., Fazakerley, A. N., Carter, P. J., Coates, A. J., Krauklis, I. C., Szita, S., … Dunlop, M.

W. (2001). Cluster PEACE observations of electrons during magnetospheric flux transfer events. *Annales Geophysicae*, *19*(10/12), 1509–1522. Retrieved from https://hal.archives-ouvertes.fr/hal-00316948/#.VdJIssFtcS8.mendeley

Owen, C. J., Marchaudon, A., Dunlop, M. W., Fazakerley, A. N., Bosqued, J.-M., Dewhurst, J. P., … Rème, H. (2008). Cluster observations of "crater" flux transfer events at the dayside high-latitude magnetopause. *Journal of Geophysical Research*, *113*(A7), A07S04. https://doi.org/10.1029/2007JA012701

Palmroth, M, Honkonen, I., Sandroos, A., Kempf, Y., von Alfthan, S., & Pokhotelov, D. (2013). Preliminary testing of global hybrid-Vlasov simulation: Magnetosheath and cusps under northward interplanetary magnetic field. *Journal of Atmospheric and Solar-Terrestrial Physics*, *99*, 41–46.

Palmroth, Minna, Ganse, U., Pfau-Kempf, Y., Battarbee, M., Turc, L., Brito, T., … von Alfthan, S. (2018). Vlasov methods in space physics and astrophysics. *Living Reviews in Computational Astrophysics*, *4*(1), 1.

Palmroth, Minna, Hoilijoki, S., Juusola, L., Pulkkinen, T. I., Hietala, H., Pfau-Kempf, Y., … others. (2017). Tail reconnection in the global magnetospheric context. In *Annales Geophysicae*.

Parker, E N. (1958). Interaction of the solar wind with the geomagnetic field. *The Physics of Fluids*, *1*(3), 171–187.

Parker, Eugene N. (1957). Sweet's mechanism for merging magnetic fields in conducting fluids. *Journal of Geophysical Research*, *62*(4), 509–520.

Paschmann, G., Haerendel, G., Papamastorakis, I., Sckopke, N., Bame, S. J., Gosling, J. T., & Russell, C. T. (1982). Plasma and magnetic field characteristics of magnetic flux transfer events. *Journal of Geophysical Research*, *87*(A4), 2159. https://doi.org/10.1029/JA087iA04p02159

Paschmann, Götz, McIlwain, C. E., Quinn, J. M., Torbert, R. B., Whipple, E. C., & Christensen, J. (1998). The electron drift technique for measuring electric and magnetic fields.

Perri, S., Valentini, F., Sorriso-Valvo, L., Reda, A., & Malara, F. (2017). On the estimation of the current density in space plasmas: Multi-versus single-point techniques. *Planetary and Space Science*, *140*, 6–10.

Pfau-Kempf, Y., & others. (2016). Vlasiator From local to global magnetospheric hybrid-Vlasov simulations.

Pfau-Kempf, Y., Battarbee, M., Ganse, U., Hoilijoki, S., Turc, L., von Alfthan, S., … Palmroth, M. (2018). On the importance of spatial and velocity resolution in the hybrid-Vlasov modeling of collisionless shocks. *Frontiers in Physics*, *6*, 44.

Phan, T. D., Drake, J. F., Shay, M. A., Gosling, J. T., Paschmann, G., Eastwood, J. P., … Angelopoulos, V. (2014). Ion bulk heating in magnetic reconnection exhausts at Earth's magnetopause: Dependence on the inflow Alfvén speed and magnetic shear angle. *Geophysical Research Letters*, *41*(20), 7002–7010.

Phan, T. D., Gosling, J. T., Paschmann, G., Pasma, C., Drake, J. F., Øieroset, M., … Davis, M. S. (2010). The dependence of magnetic reconnection on plasma β and magnetic shear:

Evidence from solar wind observations. *The Astrophysical Journal Letters*, *719*(2), L199.

Phan, T. D., Dunlop, M. W., Paschmann, G., Klecker, B., Bosqued, J. M., Reme, H., … Kistler, L. M. (2004). Cluster observations of continuous reconnection at the magnetopause under steady interplanetary magnetic field conditions. In *Annales Geophysicae* (Vol. 22, pp. 2355–2367). Copernicus GmbH. https://doi.org/10.5194/angeo-22-2355-2004

Phan, T. D., Paschmann, G., Twitty, C., Mozer, F. S., Gosling, J. T., Eastwood, J. P., … Lucek, E. A. (2007). Evidence for magnetic reconnection initiated in the magnetosheath. *Geophysical Research Letters*, *34*(14).

Phan, T. D., Shay, M. A., Haggerty, C. C., Gosling, J. T., Eastwood, J. P., Fujimoto, M., … others. (2016). Ion Larmor radius effects near a reconnection X line at the magnetopause: THEMIS observations and simulation comparison. *Geophysical Research Letters*, *43*(17), 8844–8852.

Phan, T. D., Eastwood, J. P., Shay, M. A., Drake, J. F., Sonnerup, B. U. Ö., Fujimoto, M., … others. (2018). Electron magnetic reconnection without ion coupling in Earth s turbulent magnetosheath. *Nature*, *557*(7704), 202.

Phillips, J. L., Gosling, J. T., McComas, D. J., Bame, S. J., Gary, S. P., & Smith, E. J. (1989). Anisotropic thermal electron distributions in the solar wind. *Journal of Geophysical Research: Space Physics*, *94*(A6), 6563–6579.

Pilipp, W., & Völk, H. J. (1971). Analysis of electromagnetic instabilities parallel to the magnetic field. *Journal of Plasma Physics*, *6*(1), 1–17.

Poh, G., Slavin, J. A., Lu, S., Le, G., Ozturk, D. S., Sun, W.-J., … Burch, J. L. (2019). Dissipation of Earthward Propagating Flux Rope Through Re-reconnection with Geomagnetic Field: An MMS Case Study. *Journal of Geophysical Research: Space Physics*. https://doi.org/10.1029/2018JA026451

Pokhotelov, O. A., Sagdeev, R. Z., Balikhin, M. A., & Treumann, R. A. (2004). Mirror instability at finite ion-Larmor radius wavelengths. *Journal of Geophysical Research: Space Physics*, *109*(A9).

Pollock, C., Moore, T., Jacques, A., Burch, J., Gliese, U., Saito, Y., … Zeuch, M. (2016). Fast Plasma Investigation for Magnetospheric Multiscale. *Space Science Reviews*, *199*(1–4), 331–406. https://doi.org/10.1007/s11214-016-0245-4

Powell, K. G., Roe, P. L., Linde, T. J., Gombosi, T. I., & De Zeeuw, D. L. (1999). A solution-adaptive upwind scheme for ideal magnetohydrodynamics. *Journal of Computational Physics*, *154*(2), 284–309.

Price, L., Swisdak, M., Drake, J. F., Cassak, P. A., Dahlin, J. T., & Ergun, R. E. (2016). The effects of turbulence on three-dimensional magnetic reconnection at the magnetopause. *Geophysical Research Letters*, *43*(12), 6020–6027.

Priest, E. R. (1990). The equilibrium of magnetic flux ropes (Tutorial lecture). *Physics of Magnetic Flux Ropes*, *58*, 1–22.

Pritchett, P. L. (1992). The coalescence instability in collisionless plasmas. *Physics of Fluids B: Plasma Physics*, *4*(10), 3371–3381.

Pritchett, P. L. (2001). Collisionless magnetic reconnection in a three-dimensional open system.

Journal of Geophysical Research: Space Physics, *106*(A11), 25961–25977.

Pritchett, P. L. (2005). Onset and saturation of guide-field magnetic reconnection. *Physics of Plasmas*, *12*(6), 62301.

Pritchett, P. L. (2007). Kinetic properties of magnetic merging in the coalescence process. *Physics of Plasmas*, *14*(5), 052102. https://doi.org/10.1063/1.2727458

Pritchett, P. L. (2008). Energetic electron acceleration during multi-island coalescence. *Physics of Plasmas*, *15*(10), 102105. https://doi.org/10.1063/1.2996321

Pritchett, P. L., & Coroniti, F. V. (2004). Three-dimensional collisionless magnetic reconnection in the presence of a guide field. *Journal of Geophysical Research: Space Physics*, *109*(A1).

Pritchett, P. L., & Mozer, F. S. (2009). The magnetic field reconnection site and dissipation region. *Physics of Plasmas*, *16*(8), 80702.

Pritchett, P. L., Mozer, F. S., & Wilber, M. (2012). Intense perpendicular electric fields associated with three-dimensional magnetic reconnection at the subsolar magnetopause. *Journal of Geophysical Research: Space Physics*, *117*(A6).

Pritchett, P. L., & Wu, C. C. (1979). Coalescence of magnetic islands. *The Physics of Fluids*, *22*(11), 2140–2146.

Pu, Z. Y., Raeder, J., Zhong, J., Bogdanova, Y. V., Dunlop, M., Xiao, C. J., … Fazakerley, A. (2013). Magnetic topologies of an in vivo FTE observed by Double Star/TC-1 at Earth's magnetopause. *Geophysical Research Letters*, *40*(14), 3502–3506. https://doi.org/10.1002/grl.50714

Quest, K. B., & Shapiro, V. D. (1996). Evolution of the fire-hose instability: Linear theory and wave-wave coupling. *Journal of Geophysical Research: Space Physics*, *101*(A11), 24457–24469.

Raeder, J. (2006). Flux transfer events: 1. Generation mechanism for strong southward IMF. In *Annales Geophysicae* (Vol. 24, pp. 381–392).

Rechester, A B, & Rosenbluth, M. N. (1978). Electron heat transport in a tokamak with destroyed magnetic surfaces. *Physical Review Letters*, *40*(1), 38.

Rechester, Alexander B, & Stix, T. H. (1979). Stochastic instability of a nonlinear oscillator. *Physical Review A*, *19*(4), 1656.

Remya, B., Reddy, R. V., Tsurutani, B. T., Lakhina, G. S., & Echer, E. (2013). Ion temperature anisotropy instabilities in planetary magnetosheaths. *Journal of Geophysical Research: Space Physics*, *118*(2), 785–793. https://doi.org/10.1002/jgra.50091

Retinò, A., Nakamura, R., Vaivads, A., Khotyaintsev, Y., Hayakawa, T., Tanaka, K., … others. (2008). Cluster observations of energetic electrons and electromagnetic fields within a reconnecting thin current sheet in the Earth's magnetotail. *Journal of Geophysical Research: Space Physics*, *113*(A12).

Retzler, J., & Simpson, J. A. (1969). Relativistic electrons confined within the neutral sheet of the geomagnetic tail. *Journal of Geophysical Research*, *74*(9), 2149–2160.

Ricci, P., Brackbill, J. U., Daughton, W., & Lapenta, G. (2004). Collisionless magnetic reconnection in the presence of a guide field. *Physics of Plasmas*, *11*(8), 4102–4114.

Richard, R. L., Walker, R. J., Sydora, R. D., & Ashour-Abdalla, M. (1989). The coalescence of magnetic flux ropes and reconnection in the magnetotail. *Journal of Geophysical Research: Space Physics*, *94*(A3), 2471–2483. https://doi.org/10.1029/JA094iA03p02471

Rijnbeek, R. P., Cowley, S. W. H., Southwood, D. J., & Russell, C. T. (1984). A survey of dayside flux transfer events observed by ISEE 1 and 2 magnetometers. *Journal of Geophysical Research: Space Physics*, *89*(A2), 786–800.

Rijnbeek, R. P., Farrugia, C. J., Southwood, D. J., Dunlop, M. W., Mier-Jedrzejowicz, W. A. C., Chaloner, C. P., … Smith, M. F. (1987). A magnetic boundary signature within flux transfer events. *Planetary and Space Science*, *35*(7), 871–878. https://doi.org/10.1016/0032-0633(87)90065-1

Rogers, B. N., Denton, R. E., & Drake, J. F. (2003). Signatures of collisionless magnetic reconnection. *Journal of Geophysical Research: Space Physics*, *108*(A3).

Russell, C. T., & Elphic, R. C. (1979). ISEE observations of flux transfer events at the dayside magnetopause. *Geophysical Research Letters*, *6*(1), 33–36. https://doi.org/10.1029/GL006i001p00033

Russell, C. T., Anderson, B. J., Baumjohann, W., Bromund, K. R., Dearborn, D., Fischer, D., … Richter, I. (2016). The Magnetospheric Multiscale Magnetometers. *Space Science Reviews*, *199*(1–4), 189–256. https://doi.org/10.1007/s11214-014-0057-3

Russell, C T, Berchem, J., & Luhmann, J. G. (1985). On the source region of flux transfer events. *Advances in Space Research*, *5*(4), 363–368.

Russell, Christopher T, & Elphic, R. C. (1978). Initial ISEE magnetometer results: Magnetopause observations. *Space Science Reviews*, *22*(6), 681–715.

Russell, Christopher T, & Elphic, R. C. (1979). Observation of magnetic flux ropes in the Venus ionosphere. *Nature*, *279*(5714), 616–618.

Samtaney, R., Loureiro, N. F., Uzdensky, D. A., Schekochihin, A. A., & Cowley, S. C. (2009). Formation of Plasmoid Chains in Magnetic Reconnection. *Physical Review Letters*, *103*(10), 105004. https://doi.org/10.1103/PhysRevLett.103.105004

Sarris, E. T., Krimigis, S. M., & Armstrong, T. P. (1976). Observations of magnetospheric bursts of high-energy protons and electrons at~ 35 RE with Imp 7. *Journal of Geophysical Research*, *81*(13), 2341–2355.

Saunders, M. A., Russell, C. T., & Sckopke, N. (1984). FLUX TRANSFER EVENTS: SCALE SIZE AND INTERIOR STRUCTURE. *GEOPHYSICAL RESEARCH LETTERS*, *11*(2), 131–134. Retrieved from http://onlinelibrary.wiley.com/store/10.1029/GL011i002p00131/asset/grl2533.pdf?v=1&t=j18efdev&s=f967f765e783279551398ce9bf31de189dacddf9

Schindler, K. (1979). On the role of irregularities in plasma entry into the magnetosphere. *Journal of Geophysical Research: Space Physics*, *84*(A12), 7257–7266.

Schindler, K., Hesse, M., & Birn, J. (1988). General magnetic reconnection, parallel electric fields, and helicity. *Journal of Geophysical Research: Space Physics*, *93*(A6), 5547–5557.

Schmidt, H. U., & Wegmann, R. (1981). Plasma flow and magnetic fields in comets. In *Scientific*

and Experimental Aspects of the Giotto Mission.

Schoeffler, K. M., Drake, J. F., & Swisdak, M. (2011). THE EFFECTS OF PLASMA BETA AND ANISOTROPY INSTABILITIES ON THE DYNAMICS OF RECONNECTING MAGNETIC FIELDS IN THE HELIOSHEATH. *The Astrophysical Journal*, *743*(1), 70. https://doi.org/10.1088/0004-637X/743/1/70

Scholer, M, & Jamitzky, F. (1987). Particle orbits during the development of plasmoids. *Journal of Geophysical Research: Space Physics*, *92*(A11), 12181–12186.

Scholer, Manfred. (1988). Magnetic flux transfer at the magnetopause based on single X line bursty reconnection. *Geophysical Research Letters*, *15*(4), 291–294.

Shay, M. A., Drake, J. F., Rogers, B. N., & Denton, R. E. (2001). Alfvénic collisionless magnetic reconnection and the Hall term. *Journal of Geophysical Research: Space Physics*, *106*(A3), 3759–3772.

Shay, M. A., Haggerty, C. C., Phan, T. D., Drake, J. F., Cassak, P. A., Wu, P., … Malakit, K. (2014). Electron heating during magnetic reconnection: A simulation scaling study. *Physics of Plasmas*, *21*(12), 122902.

Shay, M. A., Drake, J. F., Eastwood, J. P., & Phan, T. D. (2011). Super-Alfvénic propagation of substorm reconnection signatures and Poynting flux. *Physical Review Letters*, *107*(6), 65001.

Shibata, K., & Tanuma, S. (2001). Plasmoid-induced-reconnection and fractal reconnection. *Earth, Planets and Space*, *53*(6), 473–482. https://doi.org/10.1186/BF03353258

Shue, J.-H., Song, P., Russell, C. T., Steinberg, J. T., Chao, J. K., Zastenker, G., … Kawano, H. (1998). Magnetopause location under extreme solar wind conditions. *Journal of Geophysical Research*, *103*(A8), 17691. https://doi.org/10.1029/98JA01103

Sibeck, D. G., Lepping, R. P., & Lazarus, A. J. (1990). Magnetic Field Line Draping in the Plasma Depletion Layer. *JOURNAL OF GEOPHYSICAL RESEARCH*, *95*(1), 2433–2440. https://doi.org/10.1029/JA095iA03p02433

Simakov, A. N., & Chacón, L. (2008). Quantitative, comprehensive, analytical model for magnetic reconnection in hall magnetohydrodynamics. *Physical Review Letters*, *101*(10), 105003.

Sitnov, M. I., Swisdak, M., & Divin, A. V. (2009). Dipolarization fronts as a signature of transient reconnection in the magnetotail. *Journal of Geophysical Research: Space Physics*, *114*(A4).

Slavin, J. A., Lepping, R. P., Gjerloev, J., Goldstein, M. L., Fairfield, D. H., Acuña, M. H., … Bosqued, J. M. (2003). Cluster electric current density measurements within a magnetic flux rope in the plasma sheet. *Geophysical Research Letters*, *30*(7), 11–14. https://doi.org/10.1029/2002GL016411

Slavin, J. A., Lepping, R. P., Gjerloev, J., Fairfield, D. H., Hesse, M., Owen, C. J., … Mukai, T. (2003). Geotail observations of magnetic flux ropes in the plasma sheet. *Journal of Geophysical Research*, *108*(A1), 1015. https://doi.org/10.1029/2002JA009557

Slavin, J A, Owen, C. J., Kuznetsova, M. M., & Hesse, M. (1995). ISEE 3 observations of plasmoids with flux rope magnectic topologies. *Geophysical Research Letters*, *22*(15), 2061–2064.

Slavin, James A, Acuña, M. H., Anderson, B. J., Baker, D. N., Benna, M., Boardsen, S. A., …

others. (2009). MESSENGER observations of magnetic reconnection in Mercury's magnetosphere. *Science*, *324*(5927), 606–610.

Slavin, James A, Imber, S. M., Boardsen, S. A., DiBraccio, G. A., Sundberg, T., Sarantos, M., … others. (2012). MESSENGER observations of a flux-transfer-event shower at Mercury. *Journal of Geophysical Research: Space Physics*, *117*(A12).

Smith, D. F. (1977). Current instability in reconnecting current sheets. *Journal of Geophysical Research*, *82*(4), 704–708.

Song, H.-Q., Chen, Y., Li, G., Kong, X.-L., Feng, S.-W., & others. (2012). Coalescence of macroscopic magnetic islands and electron acceleration from STEREO observation. *Physical Review X*, *2*(2), 21015. https://doi.org/10.1103/PhysRevX.2.021015

Sonnerup, B. U. Ö., & Cahill Jr, L. J. (1967). Magnetopause structure and attitude from Explorer 12 observations. *Journal of Geophysical Research*, *72*(1), 171–183.

Sonnerup, B. U. O., & Scheible, M. (1998). Minimum and maximum variance analysis. *Analysis Methods for Multi-Spacecraft Data*, 185–220.

Southwood, D. J. J., Farrugia, C. J. J., Saunders, M. a. A., & FARRIJGIA, C. J. (1988). What are flux transfer events? *Planetary and Space Science*, *36*(5), 503–508. https://doi.org/10.1016/0032-0633(88)90109-2

Southwood, D. J., & Kivelson, M. G. (1993). Mirror instability: 1. Physical mechanism of linear instability. *Journal of Geophysical Research: Space Physics*, *98*(A6), 9181–9187.

Speiser, T., Martin, R., & others. (1996). Remote sensing of the geomagnetic tail current sheet topology using energetic ions: Neutral lines versus weak field regions. *Journal of Geomagnetism and Geoelectricity*, *48*(5–6), 799–807.

Speiser, T. W., & Williams, D. J. (1982). Magnetopause modeling: Flux transfer events and magnetosheath quasi-trapped distributions. *Journal of Geophysical Research: Space Physics*, *87*(A4), 2177–2186.

Stanier, A., Daughton, W., Simakov, A. N., Chacón, L., Le, A., Karimabadi, H., … Bhattacharjee, A. (2017). The role of guide field in magnetic reconnection driven by island coalescence. *Physics of Plasmas*, *24*(2), 022124. https://doi.org/10.1063/1.4976712

Stern, D. P. (1979). The role of O-type neutral lines in magnetic merging during substorms and solar flares. *Journal of Geophysical Research: Space Physics*, *84*(A1), 63–71.

Štverák, Š., Trávn\'\iček, P., Maksimovic, M., Marsch, E., Fazakerley, A. N., & Scime, E. E. (2008). Electron temperature anisotropy constraints in the solar wind. *Journal of Geophysical Research: Space Physics*, *113*(A3).

Su, Y., Veronig, A. M., Holman, G. D., Dennis, B. R., Wang, T., Temmer, M., & Gan, W. (2013). Imaging coronal magnetic-field reconnection in a solar flare. https://doi.org/10.1038/NPHYS2675

Sun, W. J., Slavin, J. A., Tian, A. M., Bai, S. C., Poh, G. K., Akhavan-Tafti, M., … others. (2019). MMS study of the structure of ion-scale flux ropes in the Earth's cross-tail current sheet. *Geophysical Research Letters*.

Swisdak, M. (2016). Quantifying gyrotropy in magnetic reconnection. *Geophysical Research*

Letters, *43*(1), 43–49.

Swisdak, M., Opher, M., Drake, J. F., & Bibi, F. A. (2010). The vector direction of the interstellar magnetic field outside the heliosphere. *The Astrophysical Journal*, *710*(2), 1769.

Swisdak, M., Rogers, B. N., Drake, J. F., & Shay, M. A. (2003). Diamagnetic suppression of component magnetic reconnection at the magnetopause. *Journal of Geophysical Research: Space Physics*, *108*(A5).

Tanaka, K. G., Yumura, T., Fujimoto, M., Shinohara, I., Badman, S. V, & Grocott, A. (2010). Merging of magnetic islands as an efficient accelerator of electrons. *Physics of Plasmas*, *17*(10), 102902.

Taylor, J. B. (1974). Relaxation of toroidal plasma and generation of reverse magnetic fields. *Physical Review Letters*, *33*(19), 1139.

Taylor, Jb. (1986). Relaxation and magnetic reconnection in plasmas. *Reviews of Modern Physics*, *58*(3), 741.

Teh, W.-L. W.-L., Nakamura, T. K. M., Nakamura, R., Baumjohann, W., Russell, C. T., Pollock, C., … others. (2017). Evolution of a typical ion-scale magnetic flux rope caused by thermal pressure enhancement. *Journal of Geophysical Research: Space Physics*, *122*(2), 2040–2050. https://doi.org/10.1002/2016JA023777

Teh, W. -L., Denton, R. E., Sonnerup, B. U. Ö., & Pollock, C. (2017). MMS observations of oblique small-scale magnetopause flux ropes near the ion diffusion region during weak guide-field reconnection. *Geophysical Research Letters*, *44*(13), 6517–6524. https://doi.org/10.1002/2017GL074291

Tian, H., Yao, S., Zong, Q., He, J., & Qi, Y. (2010). Signatures of magnetic reconnection at boundaries of interplanetary small-scale magnetic flux ropes. *The Astrophysical Journal*, *720*(1), 454.

Torbert, R. B., Russell, C. T., Magnes, W., Ergun, R. E., Lindqvist, P.-A., LeContel, O., … Lappalainen, K. (2016). The FIELDS Instrument Suite on MMS: Scientific Objectives, Measurements, and Data Products. *Space Science Reviews*, *199*(1–4), 105–135. https://doi.org/10.1007/s11214-014-0109-8

Torbert, R. B., Vaith, H., Granoff, M., Widholm, M., Gaidos, J. A., Briggs, B. H., … others. (2016). The electron drift instrument for MMS. *Space Science Reviews*, *199*(1–4), 283–305.

Torbert, R. B., Burch, J. L., Phan, T. D., Hesse, M., Argall, M. R., Shuster, J., … others. (2018). Electron-scale dynamics of the diffusion region during symmetric magnetic reconnection in space. *Science*, *362*(6421), 1391–1395.

Tóth, G., Sokolov, I. V, Gombosi, T. I., Chesney, D. R., Clauer, C. R., De Zeeuw, D. L., … others. (2005). Space Weather Modeling Framework: A new tool for the space science community. *Journal of Geophysical Research: Space Physics*, *110*(A12).

Tóth, G., Jia, X., Markidis, S., Peng, I. B., Chen, Y., Daldorff, L. K. S., … others. (2016). Extended magnetohydrodynamics with embedded particle-in-cell simulation of Ganymede's magnetosphere. *Journal of Geophysical Research: Space Physics*, *121*(2), 1273–1293.

Tóth, G., Chen, Y., Gombosi, T. I., Cassak, P., Markidis, S., & Peng, I. B. (2017). Scaling the ion

inertial length and its implications for modeling reconnection in global simulations. *Journal of Geophysical Research: Space Physics*, *122*(10).

Trattner, K. J., Petrinec, S. M., Fuselier, S. A., Omidi, N., & Sibeck, D. G. (2012). Evidence of multiple reconnection lines at the magnetopause from cusp observations. *Journal of Geophysical Research: Space Physics*, *117*(A1).

Trenchi, L., Marcucci, M. F., Rème, H., Carr, C. M., & Cao, J. B. (2011). TC-1 observations of a flux rope: Generation by multiple X line reconnection. *Journal of Geophysical Research: Space Physics*, *116*(A5).

Uzdensky, D. A., Loureiro, N. F., & Schekochihin, A. A. (2010). Fast Magnetic Reconnection in the Plasmoid-Dominated Regime. *Physical Review Letters*, *105*(23), 235002. https://doi.org/10.1103/PhysRevLett.105.235002

Uzdensky, Dmitri A., Cerutti, B., & Begelman, M. C. (2011). RECONNECTION-POWERED LINEAR ACCELERATOR AND GAMMA-RAY FLARES IN THE CRAB NEBULA. *The Astrophysical Journal*, *737*(2), L40. https://doi.org/10.1088/2041-8205/737/2/L40

Varsani, A., Owen, C. J., Fazakerley, A. N., Forsyth, C., Walsh, A. P., André, M., … Carr, C. M. (2014). Cluster observations of the substructure of a flux transfer event: analysis of high-time-resolution particle data. *Annales Geophysicae*, *32*(9), 1093–1117. https://doi.org/10.5194/angeo-32-1093-2014

Vasyliunas, V. M. (1975). Theoretical models of magnetic field line merging. *Reviews of Geophysics*, *13*(1), 303–336.

Vishniac, E. T. (1995). Magnetohydrodynamic turbulence in accretion disks. *ArXiv Preprint Astro-Ph/9508085*.

Walker, R. J., & Russell, C. T. (1985). Flux transfer events at the Jovian magnetopause. *Journal of Geophysical Research: Space Physics*, *90*(A8), 7397–7404.

Wang, L., Germaschewski, K., Hakim, A., Dong, C., Raeder, J., & Bhattacharjee, A. (2018). Electron Physics in 3-D Two-Fluid 10-Moment Modeling of Ganymede's Magnetosphere. *Journal of Geophysical Research: Space Physics*, *123*(4), 2815–2830.

Wang, R., Du, A., Nakamura, R., Lu, Q., Khotyaintsev, Y. V, Volwerk, M., … Fazakerley, A. N. (2013). Observation of multiple sub-cavities adjacent to single separatrix. *Geophysical Research Letters*, *40*(11), 2511–2517.

Wang, R., Lu, Q., Nakamura, R., Baumjohann, W., Russell, C. T., Burch, J. L., … others. (2017). Interaction of magnetic flux ropes via magnetic reconnection observed at the magnetopause. *Journal of Geophysical Research: Space Physics*, *122*(10).

Wang, R., Lu, Q., Huang, C., & Wang, S. (2010). Multispacecraft observation of electron pitch angle distributions in magnetotail reconnection. *Journal of Geophysical Research: Space Physics*, *115*(A1).

Wang, R., Lu, Q., Nakamura, R., Huang, C., Du, A., Guo, F., … Wang, S. (2016a). Coalescence of magnetic flux ropes in the ion diffusion region of magnetic reconnection. *Nature Physics*, *12*(3), 263–267. https://doi.org/10.1038/nphys3578

Wang, R., Lu, Q., Nakamura, R., Huang, C., Du, A., Guo, F., … Wang, S. (2016b). Coalescence

of magnetic flux ropes in the ion diffusion region of magnetic reconnection. *Nat Phys*, *12*(3), 263–267. Retrieved from http://dx.doi.org/10.1038/nphys3578

Wang, Shan, Chen, L.-J., Hesse, M., Bessho, N., Gershman, D. J., Dorelli, J., … others. (2016a). Two-scale ion meandering caused by the polarization electric field during asymmetric reconnection. *Geophysical Research Letters*, *43*(15), 7831–7839.

Wang, Shan, Chen, L. J., Hesse, M., Bessho, N., Gershman, D. J., Dorelli, J., … Saito, Y. (2016b). Two-scale ion meandering caused by the polarization electric field during asymmetric reconnection. *Geophysical Research Letters*, *43*(15), 7831–7839. https://doi.org/10.1002/2016GL069842

Wang, Shimou, Wang, R., Yao, S. T., Lu, Q., Russell, C. T., & Wang, S. (2019). Anisotropic Electron Distributions and Whistler Waves in a Series of the Flux Transfer Events at the Magnetopause. *Journal of Geophysical Research: Space Physics*, *124*(3), 1753–1769.

Wang, X., Bhattacharjee, A., & Ma, Z. W. (2000). Collisionless reconnection: Effects of Hall current and electron pressure gradient. *Journal of Geophysical Research: Space Physics*, *105*(A12), 27633–27648.

Wang, Y. L., Elphic, R. C., Lavraud, B., Taylor, M. G. G. T., Birn, J., Raeder, J., … Friedel, R. H. (2005). Initial results of high-latitude magnetopause and low-latitude flank flux transfer events from 3 years of Cluster observations. *Journal of Geophysical Research: Space Physics*, *110*(A11), 1–10. https://doi.org/10.1029/2005JA011150

Wang, Y. L., Elphic, R. C., Lavraud, B., Taylor, M., Birn, J., Russell, C. T., … Zhang, X. X. (2006). Dependence of flux transfer events on solar wind conditions from 3 years of Cluster observations. *Journal of Geophysical Research: Space Physics*, *111*(A4).

Weibel, E. S. (1959). Spontaneously Growing Transverse Waves in a Plasma Due to an Anisotropic Velocity Distribution. *Physical Review Letters*, *2*(3), 83–84. https://doi.org/10.1103/PhysRevLett.2.83

Winske, D., Yin, L., Omidi, N., Karimabadi, H., & Quest, K. (2003). Hybrid Simulation Codes: Past, Present and Future—A Tutorial. In *Space Plasma Simulation* (pp. 136–165). Berlin, Heidelberg: Springer Berlin Heidelberg. https://doi.org/10.1007/3-540-36530-3_8

Woltjer, L. (1958). The Stability of Force-Free Magnetic Fields. *The Astrophysical Journal*, *128*, 384.

Xiao, C. J., Pu, Z. Y., Ma, Z. W., Fu, S. Y., Huang, Z. Y., & Zong, Q. G. (2004). Inferring of flux rope orientation with the minimum variance analysis technique. *Journal of Geophysical Research*, *109*(A11), A11218. https://doi.org/10.1029/2004JA010594

Yamada, M, Ono, Y., Hayakawa, A., Katsurai, M., & Perkins, F. W. (1990). Magnetic reconnection of plasma toroids with cohelicity and counterhelicity. *Physical Review Letters*, *65*(6), 721.

Yamada, Masaaki, Kulsrud, R., & Ji, H. (2010). Magnetic reconnection. *REVIEWS OF MODERN PHYSICS*, *82*(JANUARY–MARCH), 603–664. https://doi.org/10.1103/RevModPhys.82.603

Yamada, Masaaki, Yoo, J., Jara-Almonte, J., Ji, H., Kulsrud, R. M., & Myers, C. E. (2014). Conversion of magnetic energy in the magnetic reconnection layer of a laboratory plasma.

Nature Communications, *5*, 4774.

Yamada, Masaaki, Ji, H., Hsu, S., Carter, T., Kulsrud, R., Bretz, N., … Perkins, F. (1997). Study of driven magnetic reconnection in a laboratory plasma. *Physics of Plasmas*, *4*(5), 1936–1944.

Yeates, A. R., & Hornig, G. (2011). Dynamical constraints from field line topology in magnetic flux tubes. *Journal of Physics A: Mathematical and Theoretical*, *44*(26), 265501.

Young, D. T., Burch, J. L., Gomez, R. G., De Los Santos, A., Miller, G. P., Wilson, P., … others. (2016). Hot plasma composition analyzer for the magnetospheric multiscale mission. *Space Science Reviews*, *199*(1–4), 407–470.

Zenitani, S., & Hoshino, M. (2001). The Generation of Nonthermal Particles in the Relativistic Magnetic Reconnection of Pair Plasmas. *The Astrophysical Journal*, *562*(1), L63–L66. https://doi.org/10.1086/337972

Zenitani, S., & Hoshino, M. (2007). Particle Acceleration and Magnetic Dissipation in Relativistic Current Sheet of Pair Plasmas. *The Astrophysical Journal*, *670*(1), 702–726. https://doi.org/10.1086/522226

Zenitani, S., & Hoshino, M. (2008). The Role of the Guide Field in Relativistic Pair Plasma Reconnection. *The Astrophysical Journal*, *677*(1), 530–544. https://doi.org/10.1086/528708

Zhang, H., Kivelson, M. G., Khurana, K. K., McFadden, J., Walker, R. J., Angelopoulos, V., … others. (2010). Evidence that crater flux transfer events are initial stages of typical flux transfer events. *Journal of Geophysical Research: Space Physics*, *115*(A8). https://doi.org/10.1029/2009JA015013

Zhang, H., Khurana, K. K., Kivelson, M. G., Angelopoulos, V., Pu, Z. Y., Zong, Q.-G., … Zhou, X.-Z. (2008). Modeling a force-free flux transfer event probed by multiple Time History of Events and Macroscale Interactions during Substorms (THEMIS) spacecraft. *Journal of Geophysical Research: Space Physics*, *113*(A1), n/a--n/a. https://doi.org/10.1029/2008JA013451

Zhao, A., Wang, Y., Chi, Y., Liu, J., Shen, C., & Liu, R. (2017). Main cause of the poloidal plasma motion inside a magnetic cloud inferred from multiple-spacecraft observations. *Solar Physics*, *292*(4), 58.

Zhao, C., Russell, C. T., Strangeway, R. J., Petrinec, S. M., Paterson, W. R., Zhou, M., … others. (2016). Force balance at the magnetopause determined with MMS: Application to flux transfer events. *Geophysical Research Letters*, *43*(23). https://doi.org/10.1002/2016GL071568

Zhao, J., Sakai, J.-I., & Nishikawa, K.-I. (1996). Excitation of whistler waves driven by an electron temperature anisotropy. *Solar Physics*, *168*(2), 345–355. https://doi.org/10.1007/BF00148060

Zhao, Y., Wang, R., Lu, Q., Du, A., Yao, Z., & Wu, M. (2016). Coalescence of magnetic flux ropes observed in the tailward high-speed flows. *Journal of Geophysical Research: Space Physics*, *121*(11), 10,898-10,909. https://doi.org/10.1002/2016JA023526

Zhou, M., Berchem, J., Walker, R. J. J., El-Alaoui, M., Deng, X., Cazzola, E., … Burch, J. L. (2017). Coalescence of Macroscopic Flux Ropes at the Subsolar Magnetopause:

Magnetospheric Multiscale Observations. *Physical Review Letters*, *119*(5), 055101. https://doi.org/10.1103/PhysRevLett.119.055101

Zhou, Meng, Pang, Y., Deng, X., Huang, S., & Lai, X. (2014). Plasma physics of magnetic island coalescence during magnetic reconnection. *Journal of Geophysical Research: Space Physics*, *119*(8), 6177–6189. https://doi.org/10.1002/2013JA019483

Zhou, Meng, El-Alaoui, M., Lapenta, G., Berchem, J., Richard, R. L., Schriver, D., & Walker, R. J. (2018). Suprathermal Electron Acceleration in a Reconnecting Magnetotail: Large-Scale Kinetic Simulation. *Journal of Geophysical Research: Space Physics*, *123*(10), 8087–8108.

Zhou, X.-Z., Angelopoulos, V., Sergeev, V. A., & Runov, A. (2010). Accelerated ions ahead of earthward propagating dipolarization fronts. *Journal of Geophysical Research: Space Physics*, *115*(A5).

Zhou, X.-Z., Angelopoulos, V., Sergeev, V. A., & Runov, A. (2011). On the nature of precursor flows upstream of advancing dipolarization fronts. *Journal of Geophysical Research: Space Physics*, *116*(A3).

Zhu, C., Zhang, H., Fu, S., Ni, B., Strangeway, R. J., Giles, B. L., … Le, H. (2019). Trapped and Accelerated Electrons within a Magnetic Mirror behind a Flux Rope on the Magnetopause. *Journal of Geophysical Research: Space Physics*.

Zou, Y., Walsh, B. M., Nishimura, Y., Angelopoulos, V., Ruohoniemi, J. M., McWilliams, K. A., & Nishitani, N. (2018). Spreading Speed of Magnetopause Reconnection X-Lines Using Ground-Satellite Coordination. *Geophysical Research Letters*, *45*(1), 80–89.

Zwan, B. J., & Wolf, R. A. (1976). Depletion of solar wind plasma near a planetary boundary. *Journal of Geophysical Research*, *81*(10), 1636–1648.